Attack on Tissue
Uncovering Invasion Strategies of Cancer Cells

van der Net, J.J.P.

DOI
10.4233/uuid:2c064b1e-8c0d-4131-adda-38d728cb277f

Publication date
2025

Document Version
Final published version

Citation (APA)
van der Net, J. J. P. (2025). *Attack on Tissue: Uncovering Invasion Strategies of Cancer Cells*. [Dissertation (TU Delft), Delft University of Technology]. https://doi.org/10.4233/uuid:2c064b1e-8c0d-4131-adda-38d728cb277f

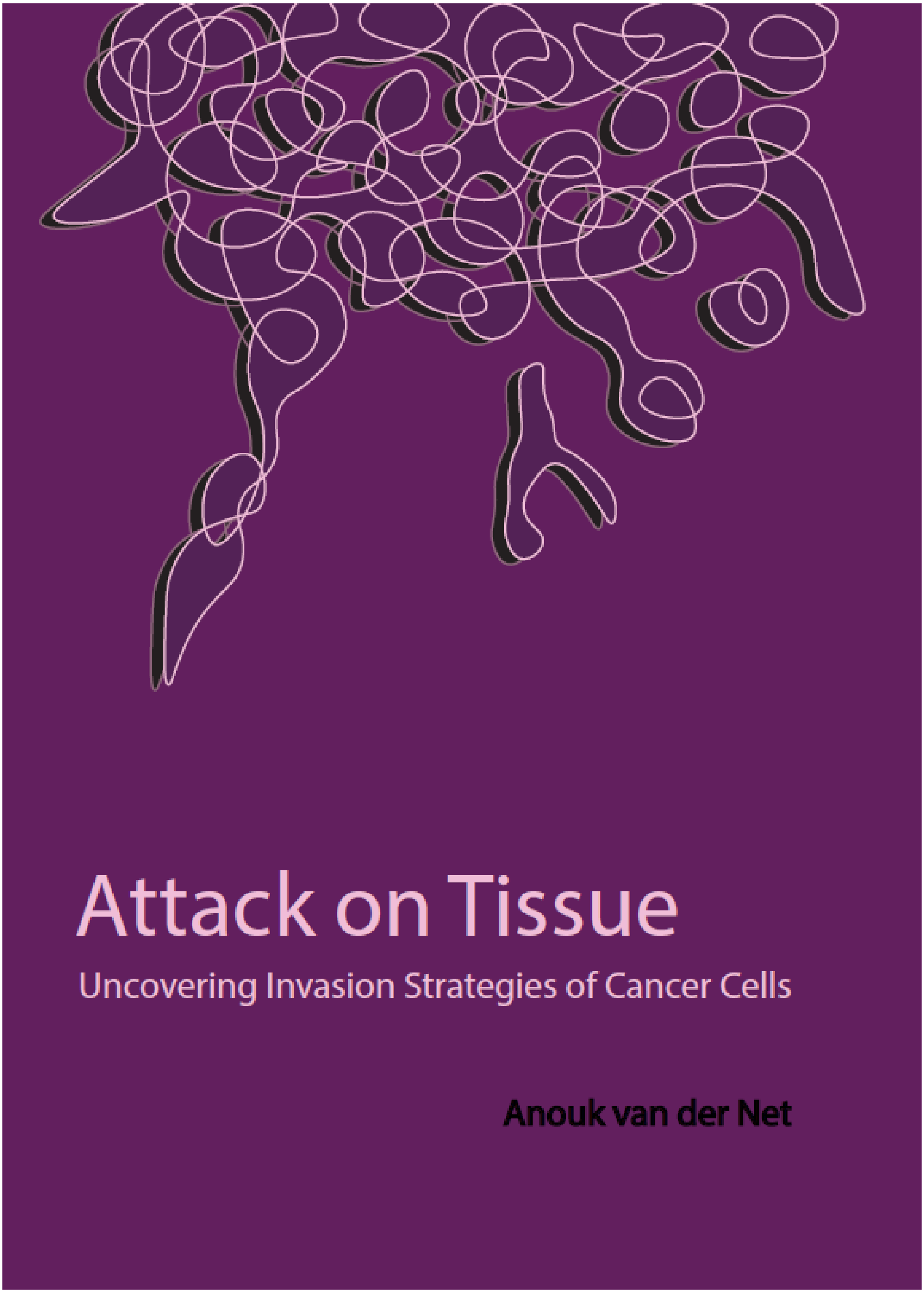

Attack on Tissue

Uncovering Invasion Strategies of Cancer Cells

Anouk van der Net

ATTACK ON TISSUE

UNCOVERING INVASION STRATEGIES OF CANCER CELLS

ATTACK ON TISSUE

UNCOVERING INVASION STRATEGIES OF CANCER CELLS

Dissertation

for the purpose of obtaining the degree of doctor
at Delft University of Technology
by the authority of the Rector Magnificus, prof. dr. ir. T.H.J.J. van der Hagen, chair of the
Board for Doctorates to be defended publicly on Wednesday 29 October 2025 at 15:00
o'clock

by

Anouk VAN DER NET

Master of Science in Biomedical Engineering,
Technical University of Eindhoven, the Netherlands

born in Dordrecht, the Netherlands

This dissertation has been approved by the promotors.

Composition of the doctoral committee:

Rector Magnificus,	chairperson
Prof. Dr. G. H. Koenderink,	Delft University of Technology, promotor
Prof. Dr. E. H. J. Danen,	Leiden University, promotor
Independent members:	
Prof. Dr. M.E. Tanenbaum,	Delft University of Technology
Prof. Dr. L. Janssen,	Eindhoven University of Technology
Dr. M. Mavrakis,	Institut Fresnel (France)
Dr. N. Kurniawan,	Eindhoven University of Technology
Dr. M. Gloerich,	Utrecht University
Prof. Dr. Ir. S.J.J. Brouns,	Delft University of Technology, reserve member

ISBN 978-94-6384-843-5

An electronic version of this dissertation is available at
`http://repository.tudelft.nl/`.

The difference in judgement between you and me originates from different rules derived from past experience.

- Levi Ackerman, Attack on Titan

CONTENTS

SUMMARY

Cell migration refers to the movement of cells from one location to another. This process is fundamental for directing immune cells to harmful agents to defend us against infections, closing wounds to prevent infections and restore tissue structures, and guiding healthy embryonic development. In malignant tumors, however, cell migration is used by tumor cells of non-motile origin to leave the tumor and invade local tissues. The ability of tumor cells to invade is one of the deadliest aspects of cancer, because invaded tumor cells can evade therapy and seed new metastatic tumors in distant organs. Metastatic tumors will eventually disrupt tissue structure and impair organ function at different locations throughout the body, resulting in poor survival prognosis. Because cell migration is the underlying process of cancer development, understanding how exactly tumor cells migrate can help us find new targets to treat and potentially even prevent cancer.

The composition of the local tissue around a tumor, known as the tumor microenvironment (TME), is an important factor in cancer cell invasion. The TME mainly consists of different cell types (e.g. specific tissue cells, immune cells) and the extracellular matrix (ECM); a network of macromolecules and minerals produced by cells that fill the intercellular spaces. Cells can interact with the ECM by adhering to matrix proteins, depositing new components or secreting enzymes that degrade matrix proteins. These interactions can lead to changes in ECM alignment, porosity, stiffness, and more, which can both restrict and promote invasion. Cells can sense these parameters and adapt their internal processes in response, which includes the strategies cancer cells deploy for invasion.

The internal cellular processes that determine invasion strategies are mostly regulated by the cytoskeleton: the skeleton of the cell that is composed of protein filaments that form networks. The main components are actin, microtubules, intermediate filaments and septins. These networks provide cell shape, stiffness and the ability to contract, which are essential during migration. The cytoskeletal networks also form connections with cell-matrix adhesions, known as focal adhesions, that mediate connections between the ECM and the cytoskeleton. Through these adhesions, the cytoskeleton can sense and transmit extracellular stimuli into the cell, which are converted into biochemical signals that regulate cellular adaptations, such as cytoskeletal remodeling. This process is known as mechanotransduction and controls how cells can respond to their environment, including their migration strategies in response to different environments. Furthermore, the different mechanisms that drive migration are often fine-tuned by crosstalk between the cytoskeletal networks, which is generally mediated by cytolinkers that can bind to two or more cytoskeletal components.

In summary, cell-matrix interactions as well as cytoskeletal crosstalk affect cancer cell invasion, but their complexity and dynamic nature make them difficult to study and fully understand. Therefore, these processes are often studied using simplified models

in the lab, so-called *in vitro* live-cell experiments (outside of the body), where cancer cell invasion is reproduced by placing cancer cell line cultures in artificial environments that mimic parts of the tumor microenvironment. In this thesis, we perform several variations of *in vitro* live-cell experiments where we can directly study how cell-matrix interactions and cytoskeletal crosstalk impact cancer cell invasion strategies. The cancer invasion models we use in this thesis are microfluidic chips, hydrogels and 3D spheroid invasion. Microfluidic chips consist of micron-sized designs molded into a material where we can control the geometry of the areas cells migrate in, to study how cancer cells respond to these geometries. Hydrogels are made of complex networks of polymers that absorb a lot of water, and closely resemble important elements of the tumor microenvironment. Spheroids are multicellular aggregates that we make from tumor cells and are used as miniature tumors, which we use to study multicellular migration.

In this thesis, we first explain the different migration modes of cancer cell invasion and how these are influenced by cell-matrix interactions and cytoskeletal crosstalk in **Chapter 1**. We introduce the intricate interplay between cells and ECM, and discuss different ECM remodeling mechanisms. We summarize the current understanding of cytoskeletal crosstalk events that mediate migration, and introduce important cytoskeletal crosstalk mediators such as septin and plectin. Finally **Chapter 1** presents the *in vitro* live-cell invasion assays we deploy and summarizes the central aim and structure of this thesis.

We start the first research part of this thesis by investigating the effect of cell-ECM interplay in **Chapter 2** and **3**. We explore the relationship between cancer cell deformability and confined migration using microfluidic devices in **Chapter 2**. By measuring the deformability of cancer cell lines with a microfluidic aspiration assay, we find a clear correlation between mechanical properties and migration efficiency through narrow constrictions. These results demonstrate how cell mechanics directly influence invasive behaviour in confined environments.

To investigate how ECM remodelling affects invasion, we analyse 3D spheroid invasion into collagen-based hydrogels in **Chapter 3**. We use cancer cell lines with varying EMT status (which describes how much a cell has switched from a stationary cell type to a more mobile cell type) and study their invasion into hydrogels with different stiffness and pore sizes. We discovered that matrix porosity and vimentin expression regulate the onset of cancer cell invasion, while invasion rates are influenced by matrix porosity and the expression of matrix-degrading enzymes. These findings thus highlight how reciprocal cell-ECM interactions connect EMT and unjamming-based invasion mechanisms.

We then shift our focus to the second aim of this dissertation, where we explore cytoskeletal crosstalk mechanisms in cancer cell invasion. In **Chapter 4** we review how cytoskeletal crosstalk mediates key processes involved in migration; including deformability, contractility, polarization, adhesion, and plasticity. By integrating findings from both live-cell (top-down) and cell-free (bottom-up) approaches, we illustrate how combining these perspectives advances our understanding of cytoskeletal contributions to cell migration.

Having discussed the current knowledge around cytoskeletal crosstalk in cell migration and the open questions in this field, we continue with research on septin-mediated crosstalk in **Chapter 5**. We focus on the role of septins in cancer cell invasion by performing migration assays on septin 7 knockout cancer cells. We show that septin expression supports single-cell and 3D spheroid invasion. Additionally, we discovered that septins regulate cell shape during confined migration by facilitating actin-rich protrusions that navigate matrix pores.

In **Chapter 6** we summarize the main findings of this thesis and propose future research paths. Preliminary experiments investigate the role of plectin in cancer invasion. Given plectin's known dual role in promoting and inhibiting invasion, we propose novel experimental designs using engineered plectin constructs to uncover the mechanisms behind this functional duality.

SAMENVATTING

Celmigratie is een proces waarbij cellen in ons lichaam zich verplaatsen van de ene locatie naar de andere. Dit proces is essentieel voor het aansturen van immuuncellen naar schadelijke indringers ter bescherming, het sluiten van wonden om infecties te voorkomen en weefselstructuren te herstellen, en voor een gezonde embryonale ontwikkeling. In kwaadaardige tumoren gebruiken tumorcellen – die van oorsprong niet beweeglijk zijn – celmigratie om het tumorgebied te verlaten en omliggende weefsels binnen te dringen. Het vermogen van tumorcellen om zich op deze manier te verspreiden is een belangrijke factor die bepaalt hoe dodelijk verschillende soorten kanker zijn. Invasieve tumorcellen ontsnappen aan de behandeling van de primaire tumor en vormen nieuwe uitzaaiingen (metastasen) in andere organen. Deze metastasen verstoren uiteindelijk de weefselstructuur en tasten de orgaanfunctie aan op meerdere plekken in het lichaam, wat resulteert in een slechte overlevingsprognose. Omdat celmigratie het onderliggende proces is in de ontwikkeling van kanker, kan inzicht in hoe tumorcellen precies migreren bijdragen aan het vinden van nieuwe aangrijpingspunten voor behandeling en hopelijk zelfs preventie.

De samenstelling van het omliggende weefsel rond een tumor, de zogenoemde tumor micro-omgeving (TMO), is een belangrijke factor in kankercelinvasie. De TMO bestaat voornamelijk uit verschillende celtypen (zoals specifieke weefselcellen en immuuncellen) en de extracellulaire matrix (ECM); een netwerk van macromoleculen en mineralen die door cellen worden geproduceerd en de intercellulaire ruimtes opvullen. Cellen kunnen met de ECM interacteren door zich te hechten aan matrixeiwitten, nieuwe matrix componenten aan te maken of enzymen uit te scheiden die matrixeiwitten afbreken. Deze interacties kunnen leiden tot veranderingen in de uitlijning, porositeit en stijfheid van de ECM, wat zowel invasie kan belemmeren als bevorderen. Cellen kunnen deze matrixeigenschappen waarnemen en hun interne processen daarop aanpassen, waaronder de strategieën die kankercellen inzetten voor invasie.

De interne cellulaire processen die deze invasiestrategieën bepalen, worden grotendeels gereguleerd door het cytoskelet: het skelet van de cel, opgebouwd uit netwerken van eiwitfilamenten. De belangrijkste componenten zijn actine, microtubuli, intermediaire filamenten en septines. Deze netwerken bepalen de celvorm, stijfheid en het vermogen tot contractie; allemaal cruciaal voor celmigratie. Het cytoskelet bindt tevens aan cel-matrixverbindingen, ook wel focale adhesies genoemd, die de koppeling tussen ECM en het cytoskelet mogelijk maken. Via deze adhesies kan het cytoskelet externe prikkels waarnemen en doorgeven aan de binnenkant van de cel, waar ze worden omgezet in biochemische signalen die cellulaire aanpassingen aansturen, zoals herstructurering van het cytoskelet. Dit proces, bekend als mechanotransductie, bepaalt hoe cellen reageren op hun omgeving, inclusief de migratiestrategieën die ze inzetten. Bovendien worden de verschillende migratiemechanismen vaak verfijnd door onderlinge afstemming, ofwel ’crosstalk’, tussen de cytoskeletnetwerken. Deze crosstalk wordt doorgaans gereguleerd door zogenoemde ‘cytolinkers’ die meerdere componenten met elkaar kunnen verbinden.

Samengevat weten we dus dat zowel cel-matrixinteracties als cytoskelet crosstalk kankercelinvasie beïnvloeden, maar de complexiteit en dynamiek van deze processen maken ze moeilijk te bestuderen en begrijpen. Daarom worden deze processen vaak onderzocht met vereenvoudigde modellen in het lab, zogenaamde *in vitro* live-cell experimenten (buiten het lichaam), waarin kankercelinvasie wordt nagebootst met kankercellijnen in kunstmatige omgevingen die elementen van de TMO nabootsen. In dit proefschrift voeren we verschillende *in vitro* experimenten uit waarin we direct kunnen bestuderen hoe cel-matrixinteracties en cytoskelet crosstalk invloed hebben op invasiestrategieën van kankercellen. We gebruiken microfluïdische chips, hydrogelen en 3D spheroid-invasie. Microfluïdische chips bevatten ontwerpen op microschaal waarmee we de geometrie van matrix poriën kunnen nabootsen, om te bestuderen hoe kankercellen daarop reageren. Hydrogelen bestaan uit netwerken van polymeren die veel water opnemen en lijken sterk op elementen van de tumor micro-omgeving. Spheroids zijn bolvormige structuren van samengeklonterde tumorcellen, en worden gebruikt als miniatuurmodellen van tumoren om 3D en collectieve migratie te onderzoeken.

In dit proefschrift bespreken we in **Hoofdstuk 1** eerst de verschillende migratietypes van kankercelinvasie en hoe deze worden beïnvloed door cel-matrixinteracties en cytoskelet crosstalk. We introduceren de complexe wisselwerking tussen cellen en ECM en gaan in op verschillende mechanismen van ECM remodellering. We bespreken de huidige inzichten in cytoskelet crosstalk die migratie mogelijk maken, en introduceren belangrijke ‘cytolinkers’ zoals septine en plectine. **Hoofdstuk 1** sluit af met een overzicht van de *in vitro* live-cell experimenten die in dit proefschrift worden gebruikt, en geeft een samenvatting van het centrale doel en de structuur van het werk.

Het eerste onderzoeksdoel richt zich op de rol van cel-ECM interacties in **Hoofdstuk 2** en **3**. In **Hoofdstuk 2** onderzoeken we het verband tussen de vervormbaarheid van kankercellen en migratie door nauwe ruimtes met behulp van microfluïdische apparaten. We meten de vervormbaarheid van verschillende kankercellijnen met een microfluïdische aspiratie test en vinden een duidelijke correlatie met de migratie-efficiëntie van deze cellen. Deze resultaten tonen aan dat cel mechanica invasief gedrag in kleine poriën direct kan beïnvloeden.

Om te onderzoeken hoe ECM-remodellering invasie beïnvloedt, analyseren we in **Hoofdstuk 3** de 3D spheroid-invasie in hydrogelen die gebaseerd zijn op het matrixeiwit collageen. We gebruiken kankercellijnen met verschillende EMT-statussen (wat beschrijft in hoeverre de cel is veranderd van een onbeweeglijke type naar een beweeglijke type) en onderzoeken hun invasie in hydrogelen met variërende stijfheid en porositeit. We ontdekken dat matrixporositeit en vimentine-expressie het begin van de invasie reguleren, terwijl de invasiesnelheid wordt beïnvloed door porositeit en de expressie van matrix-afbrekende enzymen. Deze bevindingen laten zien hoe wederzijdse cel-ECM interacties zorgen voor een koppeling tussen EMT en unjamming-gebaseerde invasie.

Daarna verschuift de focus naar het tweede doel van dit proefschrift: de rol van cytoskelet crosstalk in kankercelinvasie. In **Hoofdstuk 4** bespreken we hoe cytoskelet crosstalk verschillende migratieprocessen reguleert, waaronder vervormbaarheid, contractiliteit, polarisatie, adhesie en plasticiteit. Door bevindingen uit zowel live-cell (top-down) als celvrije (bottom-up) benaderingen te integreren, tonen we aan dat deze perspectieven elkaar aanvullen en ons begrip van cytoskelet mechanismen tijdens celmigratie versterken.

Na het bespreken van de huidige kennis en open vragen omtrent cytoskelet crosstalk, richten we ons in **Hoofdstuk 5** op septine-gemedieerde interacties. We voeren migratie testen uit met septin 7 knock-out kankercellen en laten zien dat septine-expressie zowel individuele als 3D spheroid invasiestrategieën ondersteunt. Bovendien ontdekten we dat septines de celvorm tijdens migratie reguleren door actine-rijke uitsteeksels te bevorderen waarmee cellen matrixporiën kunnen navigeren.

In **Hoofdstuk 6** vatten we de belangrijkste bevindingen van dit proefschrift samen en stellen we toekomstige onderzoekslijnen voor. We laten eerste experimenten zien waarin we de rol van plectine in kankercelinvasie onderzoeken. Gezien plectine's dubbelzinnige rol in het bevorderen en remmen van invasie, stellen we nieuwe experimentele benaderingen voor met behulp van genetisch gemodificeerde plectine constructen om de onderliggende mechanismen van deze dualiteit te ontrafelen.

1

INTRODUCTION

Cell migration plays a vital role in development, immune defense, and tissue repair. In cancer, however, it enables tumor cells to invade surrounding tissues and spread throughout the body. This invasive behavior is influenced by the tumor microenvironment, particularly the extracellular matrix (ECM), and by the cytoskeletal organization inside the cells. Both ECM properties and cytoskeletal crosstalk guide how cancer cells adapt their migration strategies. Due to the complexity of these processes, we use in vitro live-cell models such as microfluidic chips, hydrogels, and 3D spheroids to study how cell-matrix interactions and the cytoskeleton determine cancer cell invasion strategies.[1]

---

[1] The figures in this chapter were made with BioRender.

1.1. TUMOR FORMATION

TUMORS start to form when changes in cell DNA cause it to grow and divide in an uncontrolled way. This can lead to an accumulation of abnormal cells exhibiting atypical behavior, which can progress into tumor formation. Benign tumors can disturb the local tissue structure but they are self-contained and can therefore usually be removed without recurrence to prevent further harm to the patient. In contrast, malignant tumors progress into cancer once tumor cells gain the ability to **invade** surrounding tissues, by breaking through dense tissues such as basement membranes (Fig. 1.1). During the progression of cancer, invading tumor cells intravasate the blood or lymph circulation and extravasate at distant body sites to grow into new metastatic colonies. These secondary tumors will disrupt tissue organization and impair vital functionalities of organs that keep us alive, thus **operating an attack on our tissues** [1, 2] (Fig. 1.1). Therefore, cancerous tumors cannot be removed without recurrence risks and progression into metastasis lowers the survival rates of all cancer patients [3], highlighting the significance of understanding, preventing and treating cancer invasion and metastasis.

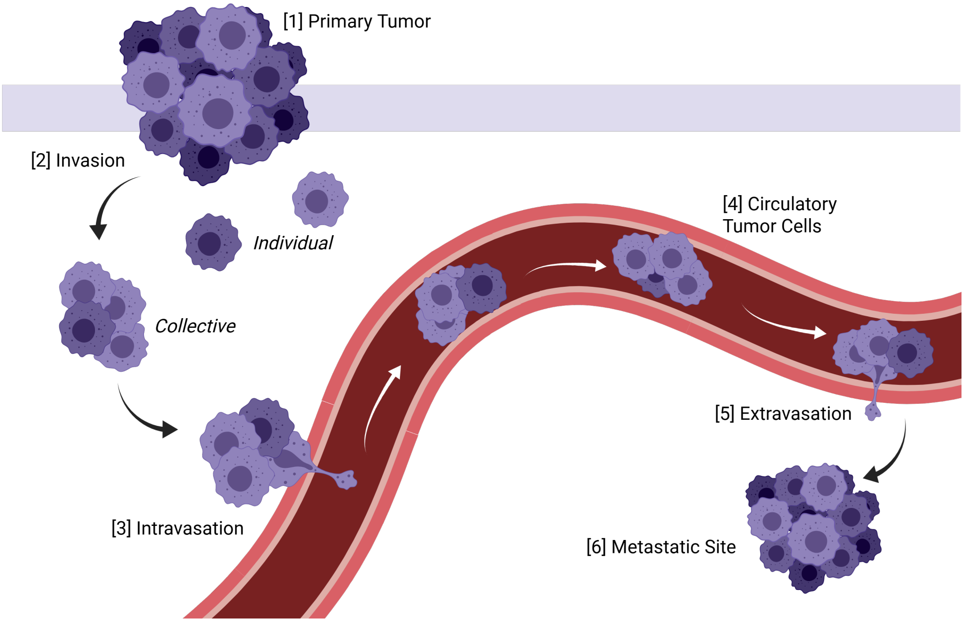

Figure 1.1: Schematic showing the different steps of cancer progression into metastasis. [1] Formation of a primary tumor from which [2] motile tumor cells can break through basement membranes and invade surrounding tissues, either as individual cells or in collective clusters. [3] Cancerous cells intravasate into the blood (or lymph) circulatory system and become [4] circulatory tumor cells that can eventually [5] extravasate across blood (or lymph) vessel walls into distant tissues to form [6] a new metastatic site.

1.2. CELL-MATRIX INTERACTIONS CONTROL CANCER CELL INVASION STRATEGIES

Metastasis is initiated when tumor cells start to invade surrounding healthy tissue. Invasion critically relies on cell migration: a directed movement of cells in response to environmental cues. During **mesenchymal migration**, a classical motility mode for many cell types, cells change shape and organize their contents to construct a front and rear. The process of front-rear polarity establishment happens through processes of molecular signalling and cytoskeletal rearrangements. The front, or leading edge, will form cell protrusions that have increased proteolytic activity and microenvironment adhesions, which the cell uses to sense the local environment and to pull itself forward. In addition, the rear end of the cell will retract via actomyosin contraction to complete the movement [4, 5]. Besides mesenchymal migration, numerous other cell migration modes exist that are controlled by intrinsic properties of the cell but also features of the extracellular matrix (ECM). For instance, cell type determines cell motility through influencing important migration characteristics such as contractility, integrin expression and cell morphology. Many factors that influence migration have been extensively studied in two-dimensional (2D) cell cultures, but most cells in our body perform three-dimensional (3D) migration, which is far more complex and less understood.

Compared to 2D cell migration, cells migrating in 3D dimensions exhibit greater extents of **plasticity**. Especially cancer cells are agile at undergoing fast transitions between different modes of migration in response to environmental factors [6, 7, 8]. The distinct modes of 3D cell migration can be categorized by their dependency on actomyosin contractility and adhesions to the microenvironment (Fig. 1.2). **Mesenchymal migration** is found in fibrous and intermediate adhesive environments, and is dependent on both contractility and matrix adhesions, required for the cells to pull themselves forward on matrix fibers. **Amoeboid migration** is found in low fiber density environments, in which the cells display low adhesive interactions, rounded morphology and extensive deformations with actin protrusions or blebs to swim forward. Furthermore, **lobopodial migration** is a hybrid between amoeboid and mesenchymal migration that occurs in highly cross-linked and confining matrices, in which the cells have bleb-like protrusions called lobopodia. These lobopodia are high in cell adhesions and exert pulling forces on the ECM, while the nucleus moves forward in a piston-like manner. Besides characterizing 3D cell migration with these three motility modes, migration can also be distinguished based on whether cells move singly or together in clusters [9]. This **collective migration** mode is linked to higher directional efficiencies, therapy resistance and more metastatic site formations [8, 10, 11, 12, 13].

All of these 3D migration modes are greatly influenced by ECM features such as topology, molecular compositions and concentrations, crosslinking, stiffness and pore sizes [9]. Moreover, mechanical cues such as interstitial fluid pressures and compressive stresses also influence the migratory mode [9]. Therefore, cells migrating in 3D tissues probe different regions of the local ECM before deciding on a certain migration mode and di-

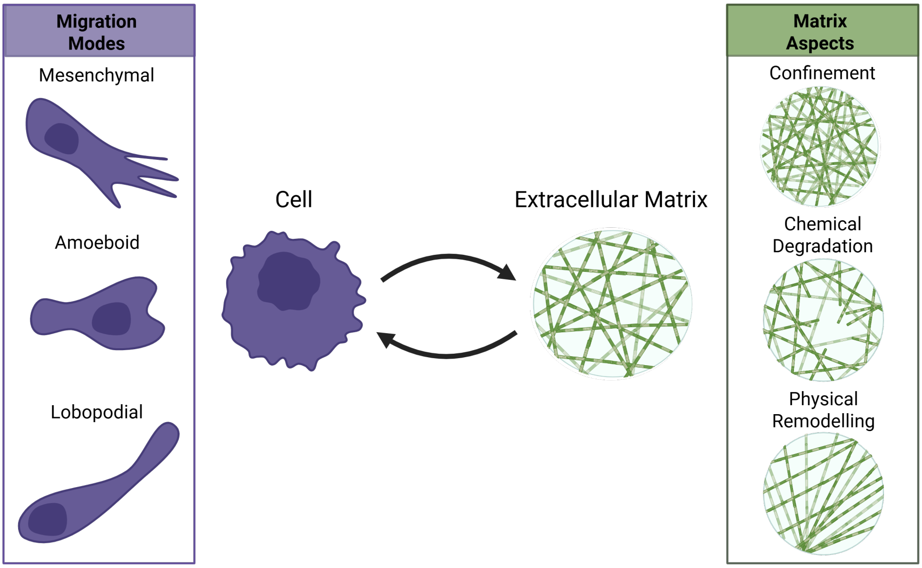

Figure 1.2: Schematic illustrating the effects cells have on extracellular matrix composition and architecture, and *vice versa*. Cells can manipulate the matrix through (1) increasing confinement and stiffness via crosslinking enzymes, (2) decreasing confinement and stiffness by biochemical degradation of matrix proteins, and (3) physical remodelling by pulling and pushing on matrix fibers. Conversely, the matrix composition influences the migration modes of cells by inducing (1) mesenchymal migration in fibrous matrices, (2) amoeboid migration in low-density environments, and (3) lobopodial migration in very dense and crosslinked matrices.

rection [6]. In addition, cells can actively remodel the ECM by increasing the confinement through ECM deposition and secretion of crosslinking enzymes, decreasing confinement via chemical degradation of ECM, and physical remodelling of the network via force transitions through ECM adhesions [14, 11, 15]. All of these cell-matrix interactions play a role during cancer cell invasion and form a complex and dynamic interplay (Fig. 1.2). Because of this complexity, the exact mechanisms of cell-matrix interplay that play a role in determining the **invasion strategies of cancer cells** are not well understood. Therefore, the first focus of this dissertation is to research how different aspects of cell-matrix interplay impact cancer cell invasion.

1.3. CYTOSKELETAL CROSSTALK FINE-TUNES MIGRATION MECHANISMS

The cytoskeleton of cells is a dynamic intracellular network composed of four distinct filamentous proteins: actin, microtubules, intermediate filaments and septins (Fig. 1.3).

The cytoskeleton has a major role in driving all the different migration mechanisms, regulating the matrix-dependent switches between them, and regulating cell deformability - a key factor in confined migration. Actin networks have a central role in coordinating cell polarity, mechanotransduction, contractility, and leader-follower dynamics in collectively invading cells [16, 17, 18]. Microtubules are important for motility-associated protrusions such as pseudopods, invapodia and podosomes [19, 20, 21, 22], and inhibition of microtubule networks decreased the average migration speed of cell clusters [23]. Intermediate filaments are known to impact migration by constructing a perinuclear cage that mechanically protects the nucleus and thus prevents nuclear rupture and DNA damage in cells that experience large strains as they migrate through confining spaces [24, 25, 26]. Therefore, loss of intermediate filaments is often associated with enhanced motility under confinement. In contrast, many studies also report specific intermediate filament proteins as markers and inducers of migration [27, 28]. Vimentin is for instance associated with a switch from an epithelial-to-mesenchymal phenotype (the EMT transition) that makes cells more invasive.

While these studies suggest that cytoskeletal networks have separate effects in determining 3D migration and associated motility modes, the networks also engage in **cytoskeletal crosstalk**. Crosstalk between cytoskeletal networks is crucial for effective migration, because it ensures cooperation between networks and thus fine-tuning of essential migration mechanisms such as focal adhesion turnover and contractility. Cytoskeletal crosstalk can occur through direct interactions between the different cytoskeletal filaments or indirect interactions mediated by cytolinkers such as **plectin**. Additionally, signalling pathways can also ensure indirect crosstalk through the initiation and coordination of polarization of different cytoskeletal networks simultaneously [6, 29]. Crosstalk between cytoskeletal networks during migration has been studied predominantly for actin and microtubules. Microtubules were shown to impact actin polymerization by nucleating actin filaments from their tips and by releasing signalling factors, while actin stabilizes and guides microtubule organization [6, 30, 31, 32, 33, 34]. Furthermore, a few studies describe the crosstalk between intermediate filaments and actin or microtubules during migration [6, 35, 36, 37, 38], but the mechanisms behind cytoskeletal crosstalk involving intermediate filaments are not well studied. Moreover, the role of the relatively newly identified fourth cytoskeletal component **septin** in cytoskeletal crosstalk is largely unknown, although this protein is already implicated in cytoskeletal crosstalk and cancer [39, 40, 41, 42, 43]. In summary, cytoskeletal crosstalk during 3D migration and its role in migration mode switching is understudied, while it is expected to contribute to cancer dissemination by regulating effective invasion of cancer cell clusters. Therefore, the second aim of this dissertation is to understand how cells use cytoskeletal crosstalk during 3D migration and how this is related to the effective invasion of cancer cells in confining matrices.

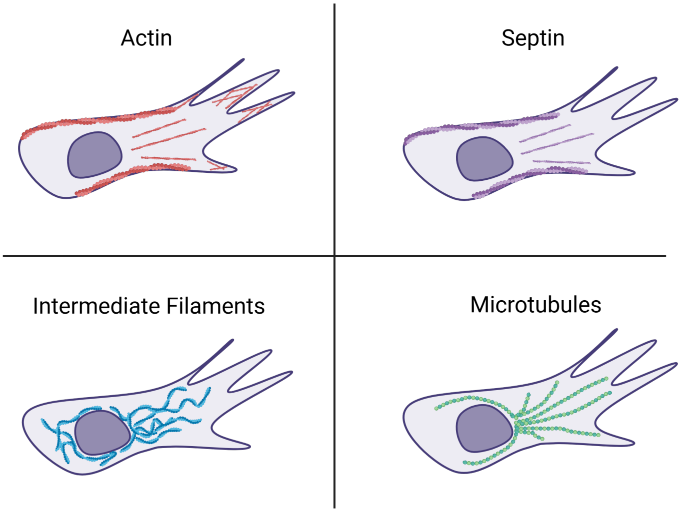

Figure 1.3: The cytoskeleton of mammalian cells consists of four major components: Actin networks (red) are present along the cell cortex, in protrusions and can form thicker stress fibers. Septin networks (purple) are mainly found along actin fibers in the cortex and along actin stress fibers. Intermediate filament networks (blue) form elaborate structures, often with an enrichment in a perinuclear cage surrounding the nucleus but reaching all the way to the plasma membrane. Microtubule networks (green) in many cells extend from the microtubule-organizing center near the nucleus into the cytoplasm towards the plasma membrane (but note that there are also non-centrosomal networks [44]).

1.4. OUTLINE OF THIS THESIS

To study the diverse biophysical processes involved in cancer cell invasion, we use various biomimetic *in vitro* models of the tumor microenvironment in combination with different cancer cell lines in which we manipulate the EMT status or cytoskeleton (Fig. 1.4). In **microfluidic chips**, we use constriction designs with different geometries and pore sizes to study the direct effect of confinement on cell migration strategies. Furthermore, cells are subjected to bifurcation designs in the chips to analyse how cells make decisions when confronted with a choice between channels with different pore sizes. In addition to this, we perform more physiologically relevant single-cell **hydrogel invasion** assays in which we allow cells to invade into a hydrogel that is placed on top of them. Here, cells have to navigate a 3D fibrous environment and can actively remodel physical parameters from the environment, such as pore size. In addition, we research multicellular 3D migration in **spheroid invasion** assays. We create cell spheroids that mimic tumors from cancer cell lines and place them inside collagen-based hydrogels with various physical properties. These assays allow us to study the complex interaction of multicellular systems migrating into ECM-like networks.

In the first part of this thesis we investigate how different aspects of cell-matrix interplay regulate cancer cell invasion strategies. In **Chapter 2** we investigate the direct relation between cancer cell deformability and constricted migration in microfluidic devices. In a microfluidic aspiration device we measure cell deformability of different cancer cell lines, and find a correlation with confined migration efficacy in microfluidic migration devices. These findings show how cell mechanics can directly determine cell invasion strategies through small pores. To also examine how ECM remodelling impacts invasion strategies, we study 3D spheroid invasion into collagen-based hydrogels in **Chapter 3**. Cancer cell lines with different EMT-status are used for spheroid invasion into hydrogels with a range of physical parameters. We measure the influence of EMT-status of the cells on the one hand and the pore size and stiffness of the ECM on the other hand on cell invasion, quantified in terms of the onset time, invasion rate and invasion strategies. We find that matrix porosity and expression of the EMT marker vimentin regulate the onset of spheroid invasion, while matrix porosity and the expression of matrix-degrading enzymes determine the rate of spheroid invasion. We conclude that reciprocal cell-ECM interactions in 3D spheroid invasions link the two main mechanisms that have previously been proposed to initiate invasion: EMT as a more cell-centered biological mechanism and unjamming as a more generalized physics-based mechanism. For the second part of this dissertation, we research the contribution of cytoskeletal crosstalk to cancer cell invasion strategies. In **Chapter 4** we first review how cytoskeletal crosstalk regulates the cellular mechanisms that together determine migration: cell deformability, contractility, polarization, adhesions and plasticity. We summarize the main findings from live-cell (top-down) and cell-free (bottom-up) experimental approaches, and we discuss how bridging these perspectives can help us understand the contribution of cytoskeletal crosstalk in cell migration. To investigate the role of septin-mediated crosstalk, in **Chapter 5** we perform several migration assays with septin 7 knockout cancer cells. We find that septin expression promotes both single-cell and 3D spheroid invasion strategies. We also show that septin regulates cancer cell shape during constricted migration by promoting the formation of actin-based protrusions that enable cells to navigate porous ECM networks. Finally, in **Chapter 6** we summarize the main findings of this thesis and propose new research directions. We show first experiments aimed at uncovering the role of cytoskeletal crosstalk mediated by the actin-intermediate filament crosslinker plectin in cancer invasion. Plectin is known to have a dual role in cancer invasion, with evidence supporting both invasion promoting and inhibiting functions, and we propose new experimental pathways via novel engineered plectin constructs to understand the mechanisms behind this duality.

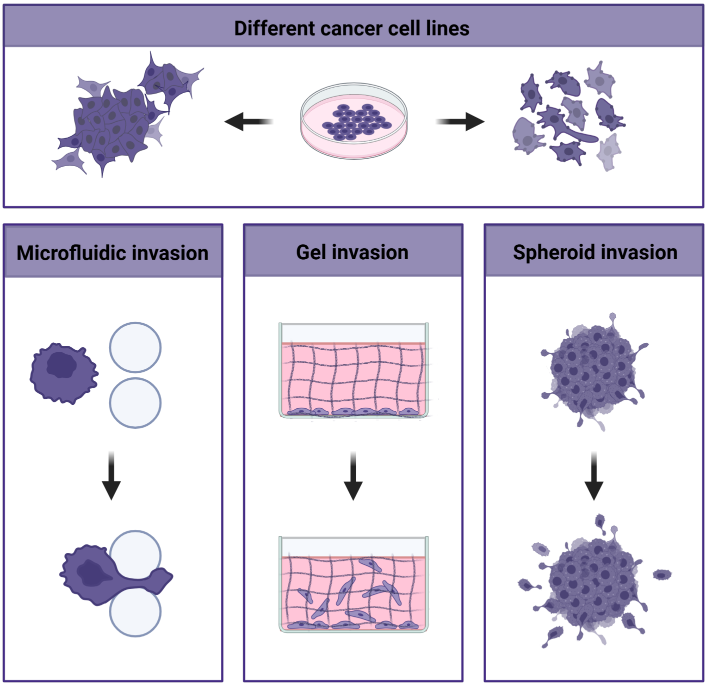

Figure 1.4: *In vitro* models for studying cancer cell invasion used throughout this dissertation. Schematic of the *in vitro* invasion models, which includes microfluidic migration set-ups with different constriction sizes and geometries and hydrogel assays for single-cell invasion and spheroid invasion. We combine these models with cancer cell lines with different EMT status or cytoskeletal manipulations, to dissect the interplay between intrinsic cell characteristics and the physical properties of the tumor microenvironment.

2

CELL DEFORMABILITY CORRELATES TO CONFINED MIGRATION

Cancer cells can utilize different invasion strategies to overcome physical arrest during confined migration through tissues with small pores. Cancer cell plasticity allows switches between different migration modes and transitions between single-cell and collective migration. The biophysical parameters that guide these decisions are poorly understood. In this work we investigated the link between cell deformability and migration efficacy in constrictions of two mesenchymal cancer cell types with similar invasion strategies: HT1080 fibrosarcoma cells and MV3 melanoma cells. To this end, we designed microfluidic platforms for (1) high-throughput cell deformability measurements and (2) migration through a variety of confining geometries. We measured different deformabilities for HT1080 and MV3 cells and correlated this to their migration efficacy through confinements. However, higher deformability and improved squeezing ability did not impact path selection at junctions of channels of different widths. Our findings show that cell deformability correlates with better squeezing abilities through confinements, but does not impact confinement directionality. [1]

---

[1] This chapter is co-authored with Ruben C. Boot, Imke van Dijk, James P. Conboy, Pouyan E. Boukany and Gijsje H. Koenderink and is the basis for a manuscript in progress. Preprint is available in BioRxiv (2025) [45].

2.1. INTRODUCTION

INVASION of tumor cells from a primary tumor site into the surrounding tissue is the first step of metastasis. Next, invasive tumor cells can intravasate into blood or lymph vessels, where they can travel to other organs and proliferate into new tumors. As metastasis accounts for over 90% of the mortality rates from cancer, understanding how cancer cells successfully invade local tissue with complex compositions is crucial to develop effective therapies [1, 2, 3]. Interestingly, despite being so lethal, tissue invasion is a highly inefficient process where most cells die from mechanical or oxidative stress or from successful attacks by our immune system [46, 47]. Mechanical stress arises from cells invading into dense tissues, where small pore sizes force cells to deform and 'squeeze'. During squeezing, contractile actin bundles confine the nucleus, which can lead to ruptures of highly deformed regions of the nuclear envelope and eventually loss of nuclear compartmentalization and DNA damage [48, 49, 50]. Therefore, single cell migration is limited by extracellular matrix (ECM) density and nuclear deformability, which can lead to physical arrest of cancer invasion when the pore size is smaller than 10% of the nuclear diameter [51]. However, cancer cells are highly adaptive and have different strategies to avoid physical arrest. One strategy is to deploy proteolytic enzymes such as matrix metalloproteases in order to degrade the matrix and create a migration path [51, 52]. Another strategy is to switch to alternative motility mechanisms to better propel the nucleus through confinements, for instance switching to amoeboid or nuclear piston mechanisms [51, 53, 24, 7]. Alternatively, mesenchymal cells can switch to collective migration in response to confinement [11, 54] to circumvent physical arrest in narrow pores [55]. Although single cells migrate faster, migrating cell clusters have more directional efficiency and result in more metastatic site formations [12, 10].

Although there is abundant evidence for cancer cell plasticity in response to confinement, it remains unclear how cells select between different invasion strategies to avoid physical arrest. While it is well established that both chemical and mechanical cues guide cell migration directionality, the extent to which cell deformability contributes to this process under conditions of physical arrest remains unclear. An interesting side-by-side comparison was made in a study of Haeger et al. [55], which compared the ability of human melanoma cells (MV3) and fibrosarcoma cells (HT1080), two mesenchymal cancer cell lines, to invade 3D collagen networks with pore sizes ranging from 35 μm^2 to 3.5 μm^2. Both cell types underwent a similar single-to-collective transition when the pore size was smaller than a threshold value around 16 μm^2, a pore size in which cells have to start to deform to 'squeeze' through. Although HT1080 and MV3 cells deployed a similar strategy in response to physical confinement, HT1080 cell invasion was less dependent on matrix degradation and higher numbers of single HT1080 cells could still invade for every pore size that was tested. HT1080 invasion into small pores was hence less dependent on the individual-to-collective transition and on proteolytic strategies [55].

We hypothesize that HT1080 cells are less dependent on the migration mode transitions in dense networks because of a higher ability to squeeze through narrow confinements compared to MV3 cells, and that this stems from a difference in cell deformability between the two cell types. Prior studies already found a correlation between cancer cell deformability and invasion [56, 57, 58, 59], but relied on indirect measurements of metastatic potential from separate *in vivo* studies [56, 57] or focused on a specific context of breast cancer [58, 59]. To test our hypothesis, we studied how HT1080 and MV3 cell deformability is related to migration efficacy under confinement. In addition, we tested the relation of cell deformability to confinement directionality when cells face a choice between channels of different widths. This was motivated by a recent study showing that cells migrate in the direction of least confinement to minimize energetic costs directed by force generation necessary to migrate through confining channels [60]. Although collagen-based hydrogels are a convenient reductionist model system to mimic the confinement imposed by the tumor microenvironment, their heterogeneous structure and wide distribution of pore spaces and connectivities make it challenging to interpret the exact effects of confinement on invasion strategies. In contrast, environments with standardized pore geometry allow us to isolate mechanical effects from variability in pore size, shape and distribution [61]. Therefore, in this work we used microfluidic devices with standardized well-controlled pore spaces to analyze the effects of constriction. Another important benefit of this model is that the pore spaces are fixed, whereas cancer cells actively remodel collagen networks by mechanical forces and proteolytic degradation.

Here, we correlated measurements of cell deformability and confined migration for HT1080 and MV3 cells. We first designed a cell deformability microfluidic device to perform high-throughput cell deformability measurements, combining the capillary constriction design by Au et al. [62], combined with the T-junction design from [63]. We could thus investigate how the deformability differs between the HT1080 and MV3 cell types when forced through vessel-sized constrictions by a flow. We subsequently studied the migration efficacy and path selection of the same cells in different confining geometries by introducing custom-made microfluidic migration devices, inspired by Davidson et al. [64]. Using the cell deformability device, we discovered that the HT1080 cells were more deformable than MV3 cells, especially for larger cell sizes (> 20 µm), where deformability was consistently larger than for smaller cells. Using the microfluidic migration devices, we found that HT1080 cells were better at crossing constrictions compared to MV3 cells, with a larger fraction of cells crossing (78% vs. 52%, respectively) and also crossing faster. Despite these differences in deformability and squeezing ability, path selection in narrow bifurcations was similar for HT1080 and MV3 cells. Both cell types showed a preference for wider constrictions, however, this preference was considerably reduced in narrower bifurcations. These results show that cell deformability correlates with better squeezing abilities through confinements, but does not impact path selection.

2.2. METHODS

CELL CULTURE

Human fibrosarcoma HT1080 cells (ATCC, CCL-121) and human melanoma MV3 cells were gifted by Peter Friedl (RadboudUMC, the Netherlands). The HT1080 cells are human male fibrosarcoma cells derived from biopsy, as described in ref. [65]. The MV3 cells are human male melanoma cells that were three times xenografted in nude mice and selected for highly metastatic behavior as described in ref. [66]. HT1080 cells were cultured in High Glucose Dulbecco's Modified Eagle's Medium (DMEM, #11574486, Thermo Fisher) and MV3 cells were cultured in DMEM/F12 1:1 medium (#11520396, Thermo Fisher), both supplemented with 10% Fetal Bovine Serum (FBS, Gibco) and 1% penicillin-streptomycin (Sigma-Aldrich). Cells were incubated at 37 ° C and 5% CO_2 and subcultured at 80-90% confluency, with regular tests for mycoplasma infections. Cell counting and cell size measurements were performed using a Countess 3 FL Automated Cell Counter (Thermo Scientific).

ACTIN POLYMERIZATION INHIBITION

Cells were incubated for a minimum of 30 minutes with culture media supplemented with 50 µM Cytochalasin D (Merck Sigma, #C2618) or 0.025 µL/mL DMSO (Bioke, #12611P) as a control. Previous research has shown that incubation of fibroblasts with this concentration of CD reduced the cell stiffness as measured by uniaxial stress-strain testing by 50 % [67].

CELL DEFORMABILITY DEVICE FABRICATION

Cell deformations were tested in a custom-designed microfluidic device that was inspired by devices reported by Au et al. [62] and by Davidson et al. [63]. The design is available in DWG format at https://github.com/RubenBoot/CellandClusterDeformation. By fusing the parallel microchannel array from [62] with the T-junction design from [63], which incorporates a main channel that leads past the array, the overall volumetric flow rate through the device was greatly increased compared to the original design by Au et al. [62] thus improving the throughput of cells reaching the microchannel array and traveling through the constrictions. The microchannels had dimensions of 10x10x280 μm^3 (width by height by length), while the main serpentine channel was 100 µm wide and high. This multi-layered design was created using standard soft lithography at the Kavli Nanolab Delft, with a µMLA laserwriter (Heidelberg Instruments). For the first layer containing the microchannel array, SU-8 2010 photoresist (Kayaku Advanced Materials) was spun on a clean 4-inch silicon wafer to a height of 10 µm. The coated wafer was then baked at 95 °C for 3 minutes, after which the first layer was written and post-baked at 95 °C for 4 minutes. After development with SU-8 developer (Propylene glycol monomethyl ether acetate (PGMEA), Sigma-Aldrich), a second layer was spun to a height of 100 µm using SU-8 2050 (Kayaku Advanced Materials). It was now baked at 65 °C for 5 minutes followed by 95 °C for 15 minutes, written, post-baked at 65 °C for

3 minutes followed by 95 °C for 10 minutes and developed again. The heights of the SU-8 features were determined to be within ± 10% of the desired heights using a Dektak Stylus Profiler (Bruker). Lastly, the master wafer was coated with trichloro(1H,1H,2H,2H-perfluorooctyl)silane (Sigma- Aldrich) to allow for easy demolding. The devices were made by pouring PDMS (Sylgard 184, Dow Corning) and curing agent at a mixing ratio of 10:1 (w/w) onto this master mold. The PDMS was degassed and cured at 65 °C for 3 hours. After curing, the PDMS was peeled off, 2 mm inlets and outlets were punched using a revolving punch plier (Knipex), and the devices alongside glass coverslips were plasma cleaned (Harrick Plasma) at 30 W for 2.5 minutes. The devices were kept in the oven at 65 °C to bond overnight.

CELL DEFORMABILITY ASSAYS

The connective ports of the cell deformability device served for cell entry (P_1), inlet of perfusion buffer (P_2) and an outlet (P_3) (Fig. 2.1A). The long serpentine main channel served to minimize the pressure drop over the parallel constriction channels at the center of the design. The devices were first filled and incubated for 45 minutes with 1% Pluronic F127 (Sigma) in phosphate buffered saline (PBS, Sigma), to decrease cell adhesion to the PDMS. PTFE 008T16-030-200 tubing (Diba Industries, inner diameter 0.3 mm, outer diameter 1.6 mm) was cut into three pieces with an identical length of 50 cm (to prevent the influence of different pressure drops over tubing of differing lengths) and then flushed with the perfusion media using an MCFS-EZ pressure controller (Fluigent). After connecting each tubing piece to one of the connective ports, the Pluronic solution, PDMS debris particles and possible air bubbles were flushed out with cell culture medium by inducing a flow from P_2 and P_3 towards P_1, with $P1$ connected to a waste tube. Once the main serpentine channel was free of obstacles, the tubing of P_1 was connected to the cell suspension while a minor flow was still present from P_2 to P_1, to prevent air from entering the tubing when connecting the cell suspension. A cell suspension of 1 mL (with cell concentrations ranging between 0.5–3.5 × 10^6 cells/mL depending on the experiment) was used. After reversing the flow direction, cells were subsequently flown through the main channel using a pressure gradient of 10 mbar (P_1 at 40 mbar, P_2 at 30 mbar). Outlet P_3 was kept at atmospheric pressure, such that the cells felt the pressure difference near the center of the design and were forced into the constriction channels (Fig. 2.1B). To compare the deformability of MV3 cells and HT1080 cells, we performed experiments sequentially on the same deformability device. After collecting data for one cell type, the main channel was flushed with medium by connecting a tube of medium after reversing the flow from P_2 to P_1 to prevent air from entering the tubing at P_1. Next, a suspension with the other cell type was connected to the device for further measurements.

Brightfield images of the deforming cells were captured using an inverted fluorescence microscope (Zeiss Axio Observer) with a 10x/NA 0.45 air objective and ORCA Flash 4.0 V2 (Hamamatsu) digital camera with a resolution of 2048x2048 pixels. We recorded time lapse image series of 30 seconds long, using an interval of 25 ms, with 13 constrictions fitting the field of view. Multiple sets were recorded per chip to capture data for a large number of cells, and the device was always discarded at the end of the experimental day. For all experiments, the cell suspension was kept at 37 °C using a Compact Dry Bath incubator (S 200-240V, Thermo Fisher Scientific) and time lapse image series were only recorded during the first hour after connecting the cell suspension to the chip, eliminating the need for CO_2 injection.

PASSIVE TRANSIT IMAGE ANALYSIS

Analysis of the deformation of cells in the constrictions was conducted using Fiji[68]. For each time lapse image series, multiple cells squeezed through the parallel constriction channels. Only the cells for which both the original diameter D_0 in front of the constriction (Fig. 2.1C, left panel) and the deformed length D once fully entered in the constriction (Fig. 2.1C, right panel) were clearly visible were included in the analysis. As the cells were not always perfectly round at the inlet, D_0 was determined by taking the average of the long and short diameters of the cell. Using Fiji, D_0 and the deformed length D for each cell were measured manually. Next we determined the strain S (dimensionless cell deformation) by taking the following ratio:

$$S = \frac{D - D_0}{D_0} \tag{2.1}$$

The theoretical strain S_*, being the strain expected in case of cell volume conservation, was calculated based on the cell volume estimated from the measurement of the cell size before it entered the constrictions. Assuming the cell in the inlet to be an approximate cylinder with a diameter D_0 and a height H of 10 µm (Supplementary Fig. S2.1A), we know the volume V_1 of a cell in the inlet to be:

$$V_1 = \frac{H\pi D_0^2}{4} \tag{2.2}$$

Once the cell enters the constriction channel, we approximate it as a beam of length L with a hemisphere on each end, having a radius R equal to half the width W and height H of the constriction (here, $R = 5$ µm) (Supplementary Fig. S2.1B). From this, the volume of the cell V_2 in the constriction is found as:

$$V_2 = c(WHL) + V_{side} \tag{2.3}$$

Here $V_{side} = \frac{4}{3}\pi R^3$ represents the combined volume of the two half-spheres. Assuming volume conservation ($V_1 = V2$), the length of the beam L is found by equating Eq. (2) and Eq. (3):

$$L = AD_0^2 - B, \tag{2.4}$$

with $A = \pi/4W$ and $B = V_{side}/WH$. Inserting Eq. (4) into Eq. (1), we finally find the theoretical strain S_* as:

$$S_* = \frac{(L + 2R) - D_0}{D_0} \tag{2.5}$$

MODELING OF PRESSURE DISTRIBUTION IN THE CELL DEFORMABILITY DEVICE

Due to the T-junction design of the cell deformability device, a pressure gradient exists both horizontally and vertically along the constriction channel array. To determine the size of these gradients, we computationally modeled the pressure distribution inside the device using the finite element modeling software COMSOL Multiphysics 5.6. We considered the fluid flow in the 3D-model to be laminar and following the Navier-Stokes equation. The pressure gradient was examined for two extreme cases: (1) all constrictions are open, and (2) the flow through all constrictions is blocked (this occurs when all channels are clogged by traversing cells). The pressure drop over a tubular channel with laminar flow scales with the length of the channel and the inverse of the channel radius to the fourth power. As the tubing used in our experiments had a long length of 50 cm and a cross-sectional area with the same order of magnitude as the main channel, the pressure drop over the tubing was non-negligible. For this reason, the tubing was modeled by including 50 cm long rectangular channels with a $300 \times 300\,\mu\text{m}^2$ cross-section connected to all three ports. We used boundary conditions of 4 kPa at the far edge of the channel connecting to the cell entry port P_1, 3 kPa at the edge of the channel connected to the perfusion port P_2, and 0 kPa at the edge of the channel connected to the outlet port P_3, similar to the pressures used in the experiments.

MICROINDENTATIONS

The effective Young's modulus of the cells was measured using a Chiaro Nanoindenter (Optics11 Life), using an optical fiber probe with a stiffness of 0.027 N/m and a spherical tip with a radius of 3 µm. Measurements were performed on 14 cells per condition, attached to the glass bottom of a 35 mm dish (#81218-200, Ibidi) in CO_2 independent medium (#11580536, Thermo Fisher). Cells were seeded at least 24 hours before experiments in order to adhere to the bottom. Indentations were made above the cell center with a loading rate of 2 µm/s. The modulus was calculated using the Hertzian contact model from the Optics 11 Life data viewer software (version 2) [69]. Measurements without a distinct contact point or with an otherwise unreliable model fit ($< 0.9R^2$) were regarded as outliers and discarded from further analysis.

MICROFLUIDIC MIGRATION DEVICE FABRICATION

We designed a microfluidic device tailored for observing cell deformation during migration through different custom-designed constriction areas inspired by Ref. [64]. The multi-layered master mold was created using standard soft lithography at the Kavli Nanolab Delft, with a µMLA laserwriter (Heidelberg Instruments). Similar to Ref. [64], the design consists of a 5 µm-tall and 440 µm-wide constriction area aligned with an adjacent 50 µm-tall perfusion channel for cell loading, chambers that end at the constriction area, and a bypass channel to equilibrate the fluid levels between the reservoirs positioned at the outer sides of the chamber.

The first layer of the design consisted of 5 µm SU-8 2005 photoresist (Kayaku Advanced Materials) and was spun on a 4-inch silicon wafer that was soft baked and post-baked at 95 °C for 2 minutes. The second layer consisted of 45 µm SU-8 3050 (Kayaku Advanced Materials) and was soft baked at 95 °C for 15 minutes, post-baked for 1 minute at 65 °C and 5 minutes at 95 °C, and developed with a SU-8 developer (Sigma Aldrich). After developing, trichloro(1H,1H,2H,2H-perfluoroctyl)silane (Sigma Aldrich) was coated on the master mold. Microfluidic chips were made from PDMS (Sylgard 184, Dow Corning), prepared with a curing agent with a 10:1 (w/w) ratio. The PDMS was poured on the silicon mold, degassed and cured at 65 °C for 3 hours. Reservoirs and cell-loading ports were punched with a revolving punch plier (Knipex) and a 0.75 mm diameter punch (Rapidcore, Welltech), respectively. PDMS chips and glass coverslips were plasma cleaned (Harrick Plasma) at 30 W for 150 seconds and bonded overnight at 65 °C.

MICROFLUIDIC MIGRATION ASSAYS

For live-cell experiments, microfluidic chips were sterilized with 70% ethanol and subsequently washed three times with MQ and once with PBS. Chips were coated with collagen by adding 100 µL 100 µg/mL PureCol type 1 bovine collagen (Advanced Biomatrix) in PBS through the cell-loading ports and incubating for 2 hours at room temperature. Chips were washed thrice with PBS and once with cell culture medium. Next, 6 µL containing a total of 30,000 cells was added to each chip via the cell-loading ports. The reservoirs were filled with cell culture media and the chips were incubated overnight at 37°C and 5% CO_2 in a 10 cm culture dish, together with a 15 mL falcon tube cap filled with MQ next to the device to prevent evaporation. One hour before imaging, cell culture medium was removed from the reservoirs and replaced with cell culture medium containing live-cell dyes: Hoechst 33342 (Thermo Fisher, 1:10,000 dilution) for staining cell nuclei and Cytotracker Orange (Thermo Fisher, 1:1000 dilution) for staining the cell cytoplasm. After one hour incubation at 37 °, the device was sealed with a glass coverslip.

Live-cell imaging of cell migration through the constrictions was imaged on a Stellaris 8 confocal microscope (Leica), equipped with a supercontinuum white light laser, 405 nm laser and three hybrid detectors. Imaging was performed with the 405 laser, a 488 nm laser line and a 20x/0.75 air objective. Time-lapse image series were acquires with time intervals of 15 minutes over a total period of 13-14 hours. Environmental control with an box incubator (Okolab, #158206046) regulated the temperature at a constant 37 °C and 5% CO_2. To analyze migration from the time-lapse series, we drew regions of interest as rectangles in between the diameters of two adjacent pillars (circles). First, the number of cells within these regions was counted. We identified cells as 'squeezing' if the cell entered and left the constriction region within the observation time and squeezed through the constrictions. We identified cells as 'stuck' when cells spent > 10 frames (≥ 150 minutes) in a constriction region without squeezing to the other side and did not squeeze through any constriction during the observation time. In addition, for squeezing cells we counted the number of frames the Cytotracker or Hoechst signal was within the constriction region, to determine the amount of time cells and nuclei spent within the constriction during squeezing. Counting of the number of frames with signal were done by three independent reviewers, which were averaged. Single scorings were excluded when >50% different from the other two scores and cells were removed from scoring when all three measurements were >50% apart or there was >200% difference. To analyze the path selection of the cells migrating through the bifurcating constrictions, three independent observers manually scored the number of cells migrating into the channels to minimize bias.

WESTERN BLOT ANALYSIS OF VIMENTIN EXPRESSION

MV3 cells and HT1080 cells were both seeded in 6-well plates (Thermo Fisher) with 300,000 cells/well and incubated overnight to ensure cell attachment. In the morning, cells were washed with PBS and lysed with 100 µL cold radioimmunoprecipitation buffer (RIPA, Thermo Fisher). Lysed samples were agitated at 4° C for 30 minutes and stored at -20 °C. Loading samples were made by adding Laemmli buffer (2x, Bio-rad) and 4% β-mercaptoethanol (Sigma Aldrich) to the lysed samples. Next, they were incubated at 95°C for 5 minutes. Sodium dodecyl sulfate-polyacrylamide gel electrophoresis (SDS-PAGE) was performed with Mini-PROTEAN TGX gels (Bio-rad) using 100 V for approximately 1.5 hours. Western Blotting was executed with a Trans-Blot Turbo Transfer System (Bio-rad) and Trans-Blot Turbo Mini 0.2 µm PVDF Transfer Packs (Bio-rad). The membranes were blocked in 5% Bovine Serum Albumin (BSA, Thermo Fisher) in phosphate buffered saline (PBS, company) overnight on a shaker at 4 °C. Membranes were stained with primary antibodies (mouse anti-vimentin (1:2000, #ab8978, Abcam) and rabbit anti-GAPDH (#CST2118S, Bioke)) in 5% BSA overnight on a shaker at 4°C. Membranes were washed thrice with 0.1% Tween (Sigma Aldrich) in PBS (PBS-T) on a shaker, and incubated for 3-5 hours with secondary antibodies: rabbit anti-mouse HRP (#ab97051, Abcam) and goat anti-rabbit HRP (#ab6728, Abcam), 1:5000 in PBS-T. Afterwards, membranes were washed thrice with PBS-T and imaged with an enhanced luminol-based chemiluminescent substrate kit (Thermo Fisher) on a gel imager (Bio-rad).

STATISTICAL ANALYSIS

Statistical analysis was performed using Microsoft Excel and Python. Two-tailed Student's t-tests were performed using the TTEST function in Excel on normally distributed data. Binomial tests were performed with the Python function binomtest. Statistical details of experiments are found in the figure legends and method details. P-value results from t-tests are indicated by: (ns) = $p \geq 0.05$, (*) = $p < 0.05$, (**) = $p < 0.01$, (***) = $p < 0.001$. Error bars represent the standard error of the mean.

2.3. RESULTS

HT1080 CELLS ARE MORE DEFORMABLE THAN MV3 CELLS

Microfluidic devices mimicking capillaries from the blood vascular network were developed to assess cell deformability, consisting of 18 parallel microchannels narrowing

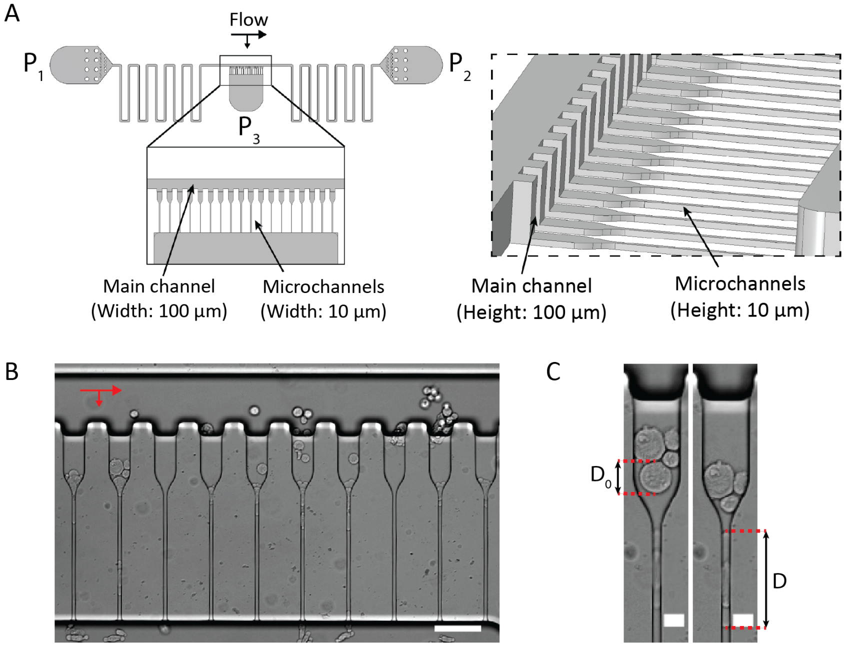

Figure 2.1: Overview of the microfluidic cell deformability device. (A) Schematic showing (left) the top view of the design together with a close-up view of the main channel and the parallel constriction microchannels, and (right) a tilted side view showing the differing heights for the main channel and the microchannels. (B) Bright-field top view image of the parallel microchannels with HT1080 cells flowing freely through the main channel and being squeezed through the microchannels due to a pressure gradient from top to bottom. Red arrows indicate the flow directions. Scale bar is 100 µm. (C) Bright-field images of a HT1080 cell entering a constriction inlet with a diameter D_0 (left panel) and subsequently stretching in the microchannel to a length D. Scale bars are 20 µm.

into $10\times10\,\mu\text{m}^2$ constrictions (see schematic in Fig. 2.1A). Cells first flow through a large $100\times100\,\mu\text{m}^2$ main channel due to a pressure difference of 1 kPa between the cell entry port P_1 and the perfusion port P_2. They are then directed towards the constriction microchannels by a pressure gradient between the main channel and the outlet port P_3, which is at atmospheric pressure. The two pressure inlets P_1 and P_2 allow precise control of the flow velocity of the cells through the main channel and the pressure forcing the cells into the microchannels. 3D COMSOL simulations of the device showed that the horizontal pressure gradient across the parallel microchannel array is negligible (~30 Pa, Fig. S2.2). They furthermore showed that the pressure that cells experience when entering the constrictions depends on whether the other channels are clogged by traversing cells. The pressure changed by ~20% between the case of all channels being open (2.9 kPa) versus closed (3.5 kPa, Supplemental Fig. 9B). While this pressure change is expected to influence the entry and traversal time of cells crossing the constrictions [62], it does not influence the cell deformability we focus on in this work.

At the inlet of the 50 µm-wide microchannels, cells are only confined in height, to a

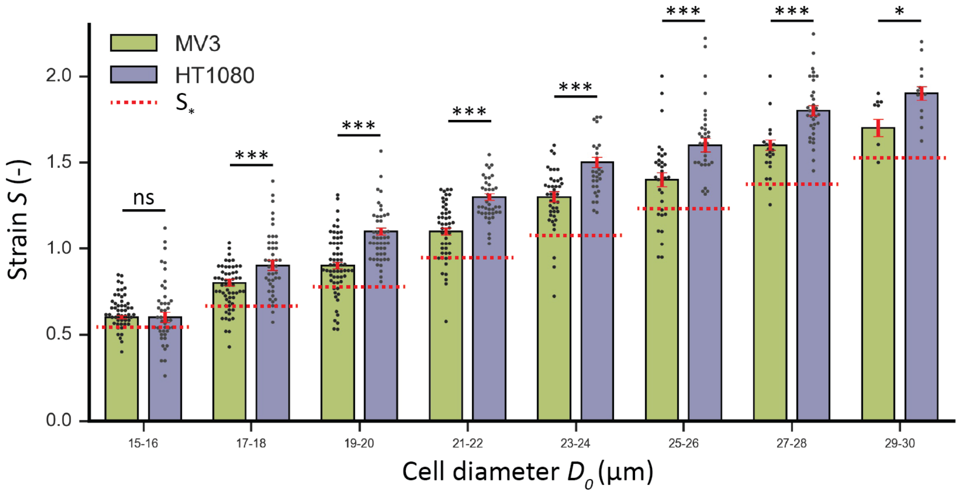

Figure 2.2: Histograms comparing the strain S for MV3 and HT1080 cells measured using the microfluidic cell deformability device. Cell diameters D_0 were binned for MV3 (green) and HT1080 (purple) cells. Red dotted lines depict the theoretical strain S_* in the limit of volume conservation, calculated using Eq. (5) and inserting the largest D_0 for each bin (e.g. $D_0 = 16\,\mu m$ for the 15-16 bin). (*) = $p < 0.05$, (***) = $p < 0.001$. (n.s.) = nonsignificant. Error bars are SEM. N = 300 cells per condition.

diameter D_0. When the cells enter the 10 µm-wide constrictions, they are also confined in width, leading to a deformation length D (Fig. 2.1B-C). We determined the dimensionless cell strain from D_0 and D using Eq. (1). As shown in Fig. 2.2, the strain increased with cell size (D_0) for both HT1080 and MV3 cells (see S2.10 regression analyses). The larger the cell, the more it has to stretch in the channel due to the confinement. We therefore binned the cells by sequential pairs of D_0 (e.g. cells with $D_0 = 15\,\mu m$ and $16\,\mu m$ were combined in one bin), and compared S between the respective bins for each cell type. This analysis revealed that the HT1080 cells consistently deformed more than the MV3 cells for the same cell size (note that the two cell types had similar size distributions, Fig. S2.8). These findings suggest that cell volume is not conserved, as cells with the same original volume in the constriction inlet display different deformations. Using Eq. (5), we determine a theoretical strain S_* in case of volume conservation, which is indicated in Fig. 2.2 by the red dotted lines. Comparing this theoretical limit to the data, we find that both the MV3 and HT1080 cells increased in volume in the constrictions. Possible mechanisms for these volume changes under confinement could be activation of stretch-sensitive ion channels and subsequent osmotic swelling [70], or temporary changes of actomyosin contractility [71].

MICROFLUIDIC CELL MIGRATION DEVICE DESIGN

To test whether the difference in HT1080 versus MV3 cell deformability affects their ability to migrate through narrow constrictions, we made three different microfluidic designs based on previous work by Davidson et al. [64]. All three designs have two media

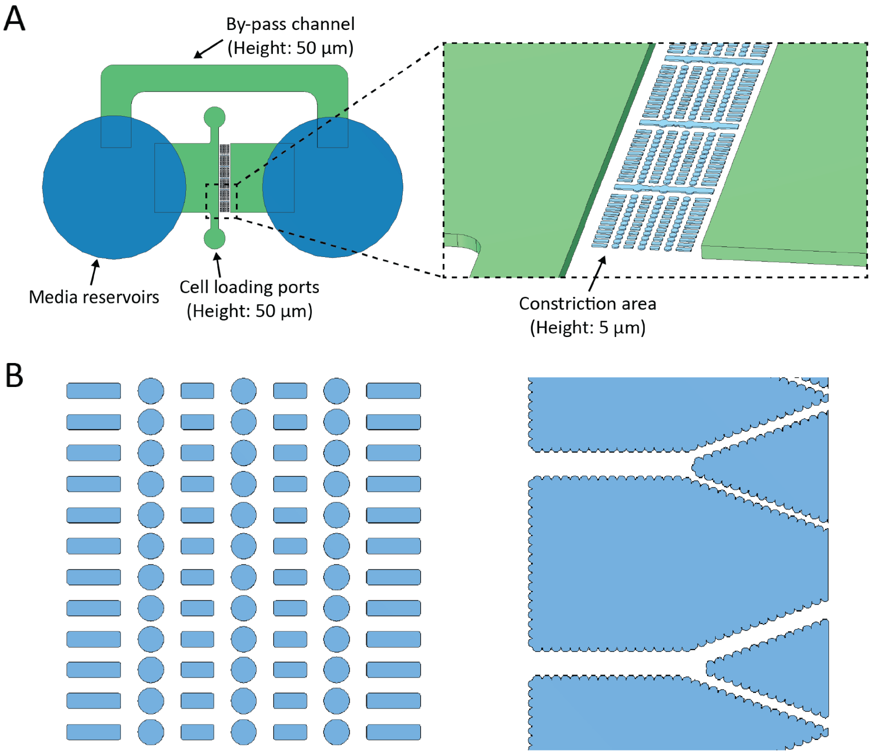

Figure 2.3: Overview of the microfluidic cell migration device. (A) Left: Schematic showing the top view of the design. The media reservoirs are punched (dark blue) to connect the by-pass channel and cell loading ports (green). Right: a tilted side view showing the constriction area between two non-constricted chambers. (B) The two different designs for the constriction areas: (left) rows with identical constrictions of 5 µm in width between the circular pillars, and (right) Y-junctions with a 30 µm wide channel, lined with inverted catenaries, splitting with a 40° angle into either a 10 µm and 5 µm wide channel (above), or into a 20 µm and 10 µm wide channel (below). Note that the pillars and the walls made of interconnected arcs mimic the discontinuous spatial environment that cells encounter when invading interstitial matrices.

reservoirs on both sides of the device, connected with a wide bypass channel to enable fast equilibration of fluid height between both reservoirs (Fig. 2.3A). Furthermore, they all have a constriction area with parallel migration channels that were functionalized with type I collagen to promote cell adhesion and crawling. Instead of long, straight channels, we designed pillars or walls made of interconnected arcs, to mimic the discontinuous spatial environment found in the interstitial matrix of connective tissues (Fig. 2.3B). Moreover, we chose constriction widths in the range of 5 µm to 30 µm, to mimic the range of pore sizes found in tumor microenvironments [72]. The first design had an array of parallel channels with sequential constrictions of 5 µm. The second design had Y-junctions that start as 30 µm wide channels and then split into either a 20 µm and 10 µm wide channel, or into a 10 µm and 5 µm channel. This design allowed us to investigate how cell deformability influences the migration path when cells face a choice between different constrictions.

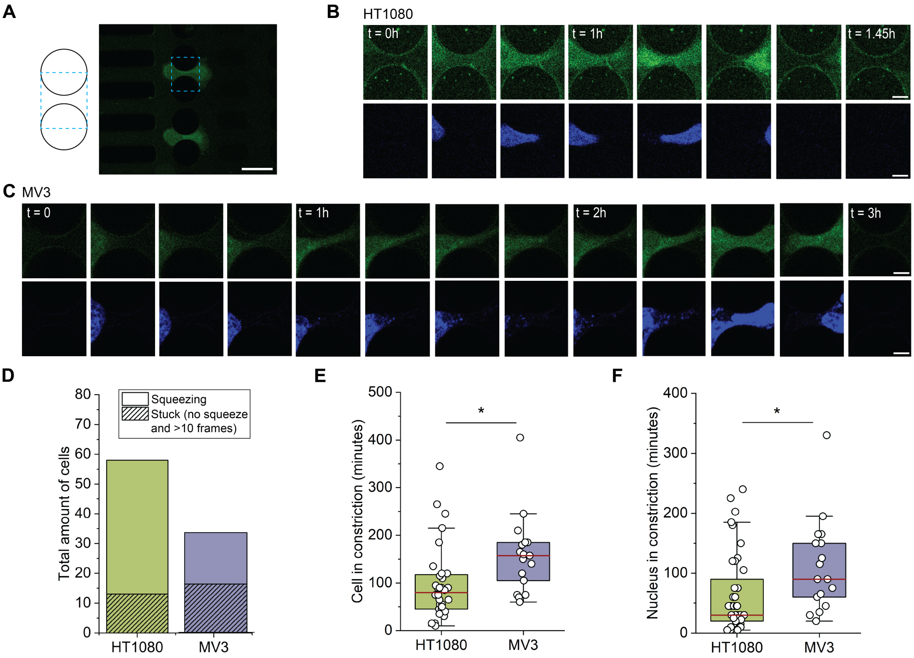

Figure 2.4: Analysis of confined cell migration efficacy in arrays of pillars. (A) Schematic and example fluorescence image showing how the constriction region was defined as the rectangular area (dashed box) formed by connecting the diameters of two adjacent pillars (circles). Scale bar is 15 µm. (B,C) Time lapse fluorescence image series showing HT1080 cells (B) and MV3 cells (C) squeezing through constrictions. The images are cropped to show the constriction region and show the cell cytoplasm labeled with Cytotracker Orange in green and the nucleus labeled with Hoechst 33342 in blue. Scale bars are 5 µm. (D) Stacked bar graph showing the total number of cells in constriction regions for HT1080 (green) and MV3 (purple) cells, separated between cells that actively squeezed through the constrictions (smooth) and cells that never squeezed through the area over an observation time of 13-14 hours and spent > 10 frames in a constriction (striped). (E,F) Boxplots for the amount of time (in minutes) that cells and nuclei were detected in the constriction areas, derived from the number of frames with 15 minutes time intervals. (*) = $p < 0.05$.

HT1080 SQUEEZE FASTER THROUGH CONSTRICTIONS THAN MV3 CELLS

To determine if higher deformability is associated with faster migration of cells through narrow constrictions, we performed migration experiments for HT1080 and MV3 cells in the microfluidic migration device with identical constrictions of 5 µm. From the time-lapse image series, we identified all squeezing cells and measured the time duration spent by cells and their nuclei in the constriction areas, defined as the rectangle between the diameter of two adjacent pillars (Fig. 2.4A-C, see S2.3 for videos). Migrating cells were defined as cells that entered a constriction area during imaging and exited the constriction area on the opposite side during imaging. Cells were classified as stuck when they spent > 10 frames (≥ 150 minutes) in the same constriction area without ex-

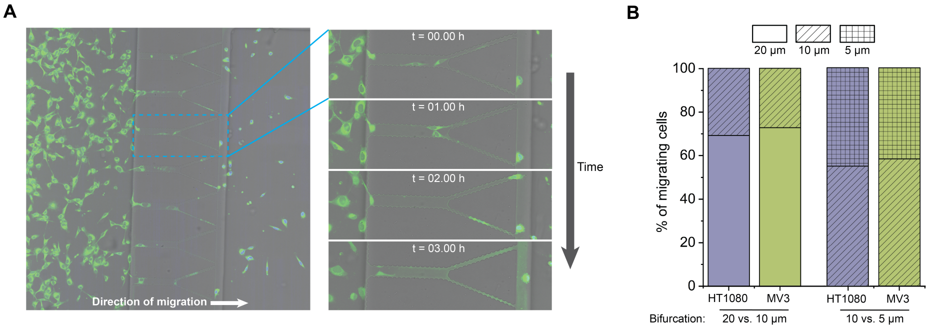

Figure 2.5: Bifurcation microfluidics to test decision making of migrating cells. (A) Overview of microfluidic chip in which cells (green) migrate through 30 µm channels with a bifurcation of 5 & 10 µm. Blue square indicates zoomed-in area at 4 different time points, showing two cells migrating. (B) Stacked bar graph showing the path selection of cells at the bifurcations, analyzed by visual inspection and converted to percentages, for bifurcations of 20 µm (smooth) versus 10 µm channels (striped) and of 10 µm versus 5 µm (cross-hatched). For each of the four conditions, 7 different bifurcation areas were analyzed resulting in $N = 11\text{-}19$. For 10 & 20 µm, corresponding p-values for choice significance are $p = 0.13$ (HT1080) and $p = 0.25$ (MV3). For 5 & 10 µm, corresponding p-values for choice significance are $p = 0.41$ (HT1080) and 0.39 (MV3).

iting during imaging. We found that with the same seeding densities, HT1080 cells had a larger number of cells squeezing through the constrictions compared to MV3 cells, while they had a similar amount of cells stuck in a constriction (Fig. 2.4D). In addition, HT1080 cells more often squeezed multiple times (2 or 3 times) during the time frame of imaging (around 16 hours) compared to MV3 cells, which on average only migrated through one constriction during imaging. To determine the amount of time it takes for cells (Fig. 2.4E) and their nuclei (Fig. 2.4F) to squeeze through a constriction, we measured the number of frames with a Cytotracker (cytoplasm) or Hoechst (nucleus) signal. For both cells and nuclei, HT1080 cells were significantly faster at squeezing compared to MV3 cells. After squeezing through a constriction, cells often showed nuclear deformations and/or ruptures, often also leading to migration inhibition and/or cell death. These deformations were more prominent in MV3 cells than in HT1080 cells (Fig. S2.4) and could indicate compromised nuclear integrity, that can lead to DNA damage and subsequently genomic instability, senescence or apoptosis as shown in previous studies [73, 49, 74]. Altogether, these results show that HT1080 cells, with a higher deformability, are indeed more efficient at squeezing through narrow pores as compared to MV3 cells.

HT1080 AND MV3 CELLS MAKE SIMILAR PATH SELECTIONS IN NARROW BIFURCATIONS

To understand if the higher deformability and squeezing efficiency of HT1080 cells compared to MV3 cells also impact confinement directionality at junctions between channels of different widths, we next performed migration experiments in the microfluidic migration chips with bifurcation designs. In these chips, both cell types were subjected to constriction designs of 30 µm wide channels splitting into either 20 µm- and 10 µm-wide channels, or into 10 µm- and 5 µm-wide channels. To analyze path selection by cells, we performed live-cell imaging of the constrictions to visualize the migrating cells (Fig. 2.5A). We then analyzed which size channel the cells migrated into from the wider channel (Fig. 2.5B). For the 20 µm vs. 10 µm bifurcation, both cells had a comparable preference for the wider (20 µm) channel, with 69.2% (HT1080) and 72.7% (MV3). Interestingly, when presented with smaller constrictions of 10 µm vs. 5 µm, both cell types lose their clear preference for the larger constriction, with 52.6% (HT1080) and 58.3% (MV3) of cells migrating into 10 µm channels. These results show that HT1080 and MV3 have very similar path selections when presented with confinements of different sizes.

2.4. DISCUSSION

The goal of this work was to test whether the different strategies of HT1080 and MV3 cells to perform confined migration correlate with their deformabilities. Our work was inspired by a study by Haeger et al. (2014), which showed that, even though both cells have similar mesenchymal features, HT1080 cells are able to squeeze through smaller pores than MV3 cells without resorting to MMP-mediated matrix degradation or switching to collective invasion [55]. To compare the mechanical properties of the two cell types, we first designed a microfluidic device with parallel constriction channels for high-throughput cell deformability measurements. Using this device, we found that HT1080 cells deformed more in the channels than MV3 cells when comparing cells of similar sizes. However, the channels in the deformability device often clogged with cells, which could potentially pre-select specific cell subpopulations for deformability measurements [74]. This could mean that the deformability measurements are only selective representations of certain pre-existing subpopulations. It would be interesting in future to test for this possibility using new “mechano-transcriptomics” approaches that correlate single-cell mechanical and transcriptomic measurements [58, 75, 76, 59]. We also found that both cell types exhibit a change in volume when forced into the narrow constrictions. A recent study reporting high-speed morphological measurements on cells migrating into narrow constrictions also showed changes in cell volume [77]. However, the exact process behind this dynamic volume change is not clear. Likely, plasma membrane channels and transporters, which transport intracellular osmolytes (inorganic ions and small organic compounds) in and out of the cell [78, 79], are involved. These transport processes generate osmotic gradients, which drive water across the cell membrane through aquaporin water channels [80]. Directed water permeation has indeed been implicated in confined cell migration, where polarized distributions of Na^+/H^+ transporters and aquaporins facilitate volume changes [81]. To further test this mechanism, we performed microfluidic confined cell migration experiments on MV3 cells treated with aquaporin-1 inhibitor Acetazolamide. Acetazolamide treatment strongly impaired MV3 confined cell migration and remaining migrating cells migrated with an altered elongated phenotype compared to untreated MV3 cells (Fig. S2.13). The squeezing also often resulted in cell rupture, indicating that aquaporin-dependent volume changes are an important mechanism during confined migration of the MV3 cells. To further investigate the exact volume changes that occur during cell squeezing in follow-up studies, it will be interesting to monitor cell volume during squeezing with high-resolution live-cell imaging, and to measure the change in cell deformability in presence of inhibitors of membrane transporters and aquaporins to manipulate or block water exchange [82].

To test whether the cytoskeleton plays any role in confinement-induced cell deformability, we treated MV3 cells with cytochalasin D to depolymerize actin and measured their deformability in the constrictions. Microindentation experiments showed an average ~5-fold decrease of the effective Young's modulus of the cells (Fig. S2.5), confirming successful inhibition of actin polymerization [83]. By contrast, the deformability of the MV3 cells in the microfluidic constrictions was completely unaffected by the CD treatment (Fig. S2.6). This suggests that, at least for these cells, the actin cytoskeleton does not affect cell deformability. Interestingly, although depolymerization of actin did not result in any measurable change in cell deformability in our assay, previous studies reported an increase in deformability upon actin depolymerization [84, 83, 85, 57, 86, 87]. This apparent discrepancy may reflect cell-type–specific responses, which could depend on the relative contributions of the actin versus intermediate filament cytoskeletal networks, or on compensatory mechanisms such as alterations in cellular volume. We also note that previous work comparing MCF7 and MCF10 breast cancer cells did suggest a correlation between cell deformability in constrictions and cellular elasticity [88]. Therefore, we suggest that follow-up research should validate our results with other actin polymerization drugs, such as latrunculin A, which has similar effects on Effective Young's moduli of MV3 cells (Fig. S2.14). It will also be interesting to test the role of actin in cell deformability further, together with the role of other cytoskeletal components, especially the vimentin cytoskeleton. Actin and vimentin form interpenetrating networks and jointly determine cell deformation under compressive and tensile loading [89, 90]. Western Blot analysis shows that the HT1080 cells express higher levels of vimentin than the MV3 cells (Fig. S2.7), which could potentially enable them to deform more without damage [91, 92, 24]. However, this does not provide functional proof, and immunocytochemistry of vimentin on HT1080 and MV3 cells does not indicate clear differences (Fig. S2.11). Therefore, future experiments with vimentin knockdown in HT1080 and MV3 cells should be performed to provide insight in the contribution of vimentin to cancer cell deformability. Other intermediate filaments of interest are nuclear lamins, which govern nuclear deformability and thereby impact confined migration [51, 93]. Nuclear stiffness is mainly dependent on the levels of lamin A/C [94], and recent work by Amiri et al. [95] demonstrates that nuclear lamins respond similarly to deformations during both aspiration and active cell migration. Immunocytochemistry of lamin A/C suggests higher fluorescent signals in HT1080 than MV3 cells, potentially indicating higher lamin A/C levels and thus an interesting distinction between the cell types (Fig. S2.12) and, interestingly, in contrast to previous findings [96]. Since the nucleus is the limiting factor in cell passage through constrictions, it will be interesting to further quantify the lamin A/C expression levels of the HT1080 and MV3 cells as well as the size and stiffness of their nuclei. In addition, lamin knockdowns or overexpression could further expand the mechanistic framework.

To couple the deformability of the cells to their ability to migrate through constrictions that are narrow enough to cause physical arrest, we next designed a second microfluidic device that allows for live-cell imaging of migration through a 3D environment of narrow constrictions with varying sizes. Although this set-up provides a controlled environment to isolate mechanical effects on confined migration, it does not fully capture the complexity of cancer invasion *in vivo*, such as influences of matrix remodeling, integrin-mediated signaling or mechanical memory. Here, we found that HT1080 could migrate faster through small constrictions compared to MV3 cells, with fewer cells getting stuck. Physical arrest of cell invasion is known to be controlled by cellular deformability and extracellular confinement [51]. However, studies on cancer cell invasion in different confining microenvironments, including extracellular matrix gels and microfluidic constrictions, have shown that cancer cell plasticity can prevent physical arrest and enhance the invasion potential. Cancer cells can adopt different strategies including migration mode switching [51, 53, 24, 7], proteolysis of the extracellular matrix [51, 52], and individual-to-collective migration transitions [11, 54, 55]. However, the decision-making process behind these choices is not well understood. There is evidence that selection between different strategies are interdependent; both mesenchymal-amoeboid migration mode switching and individual-to-collective transitions in response to confinement depend on proteolytic activity [97, 98, 55]. Additionally, collective invasion can also directly transition to single-cell amoeboid migration in response to hypoxia [99]. A side-by-side comparison between HT1080 and MV3 cells by Haeger et al. [55] showed that these cell types have similar invasion strategies but with subtle differences: HT1080 cells were less dependent on matrix proteolysis to squeeze through collagen gels with narrow pores. Our comparison of the single-cell migration speeds of these cells through microfluidic constrictions confirmed that HT1080 cells can squeeze faster through narrow pores and get less easily stuck. Moreover, we showed that this difference correlates with higher cell deformability. This correlation is consistent with earlier findings, where cell deformability was coupled to the metastatic potential of cancer cells [57, 56, 100]. Several recent studies [58, 101, 102, 103, 73, 59] suggested that migration through constricting channels can cause long-lived changes in 3D genome architecture and gene expression that may facilitate metastasis. Indeed we also observed that cells often showed nuclear deformations or even rupture after squeezing through constrictions, indicating significant deformation of the nuclear envelope which could activate histone modifying enzymes through different pathways. It will be interesting to test whether the HT1080 and MV3 cells undergo similar changes by imaging heterochromatin formation in migrating cells and collecting cells for transcriptomic analysis after constricted migration.

Finally, to understand how cell deformability and migration efficacy impact path selection in dense environments, we performed migration assays using bifurcation designs in the same migration microfluidic set-up. While these junctions provide insights into path selection in confined environments, the used Y-shaped junctions represent an oversimplification of the complex path choices encountered within the ECM and therefore allow limited conclusions about the actual path selection processes. We found that path selection was similar for HT1080 and MV3 cells and thus not influenced by their deformabilities nor migration efficacies. Cells showed a preference for larger constrictions when presented with a path selection between 20 µm and 10 µm constrictions, but this preference was lost when presented with narrower constrictions of 10 µm and 5 µm. Similar experiments with constriction bifurcations by Zanotelli et al. [60] described path selection to be mainly determined by cell stiffness (Young's modulus). This finding suggests that HT1080 and MV3 cells have a comparable Young's modulus. Indeed microindentation experiments confirmed that the cells had a comparable effective Young's modulus of ~500 Pa (Fig. S2.5). Although migrating cells generally prefer wider constrictions to reduce energetic costs [60, 104], both HT1080 and MV3 cells lost their clear preference for wider constrictions in the bifurcations of 10 µm versus 5 µm. Because the bifurcations designs in Zanotelli et al. [60] had similar constriction sizes (12 µm versus 7 µm) and they did not report any loss of preference, we hypothesize that energy costs might plateau under a certain constriction size. This size might potentially depend on cell and nucleus size; for our cells, it is around ~10 µm. This hypothesis should be further tested in future experimental studies using a wider range of channel widths, complemented by computational modelling for validation, similar to the approach used by Zanotelli et al., 2019[60].

In this work, we provide evidence that actin-independent cell deformability regulates the efficiency of cancer cell migration under confinement, while having only minor effects on migration directionality. Gaining a deeper understanding of how the physical parameters of cancer cells relate to migration efficacy, invasion strategies and therapy resistance can be of great value for clinical applications. For example, computational modeling based on spheroid-collagen invasion assays showed that tumor invasiveness is maximized by heterogeneity in cell deformability and cell size [105]. Furthermore, deformability heterogeneity could potentially also promote collective invasion strategies by enabling cells to dynamically adjust their position within the cluster [105]. As recent work also revealed that collective invasion *in vivo* can create radiation-resistant niches [13], it is important to further study how cell mechanics contribute to this invasive strategy. Moreover, recent studies prove the predictive power of deformability phenotyping, for example of patient-specific leukemia cells in response to treatment efficiency [106, 83] and of circulating tumor cells for patient prognosis [107], indicating the potential for the development of new prognostic tools.

2.5. ACKNOWLEDGEMENTS

I would like to thank Ruben Boot for this collaboration and sharing his expertise on microfluidics and cell mechanics. I also want to thank Ruben Boot and Imke van Dijk for the cell deformability measurements, and Imke van Dijk as well for her work on the optimization of the migration device. Additionally, thanks to James Conboy for the nanoindentation measurements and Jan Lammerding for helpful discussions.

2.6. SUPPLEMENTARY INFORMATION

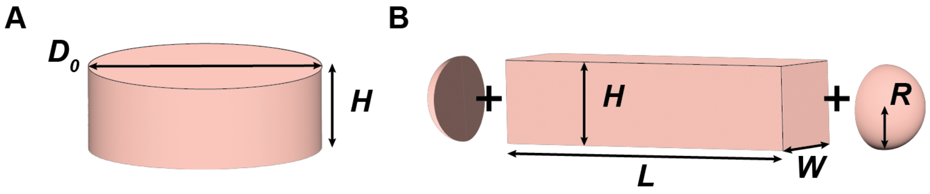

Figure S2.1: Geometrical assumptions made to derive the theoretical strain S_* in case of cell volume conservation when transiting through a narrow constriction with a square cross-section. (A) The cell being geometrically confined into a cylindrical shape at the inlet, with diameter D_0 and height H. (B) The cell being geometrically confined inside the constriction channel: the volume of the cell was determined as the sum of a beam of length L with width W and height H and two hemispheres with a radius R (= $\frac{1}{2}W = \frac{1}{2}H$).

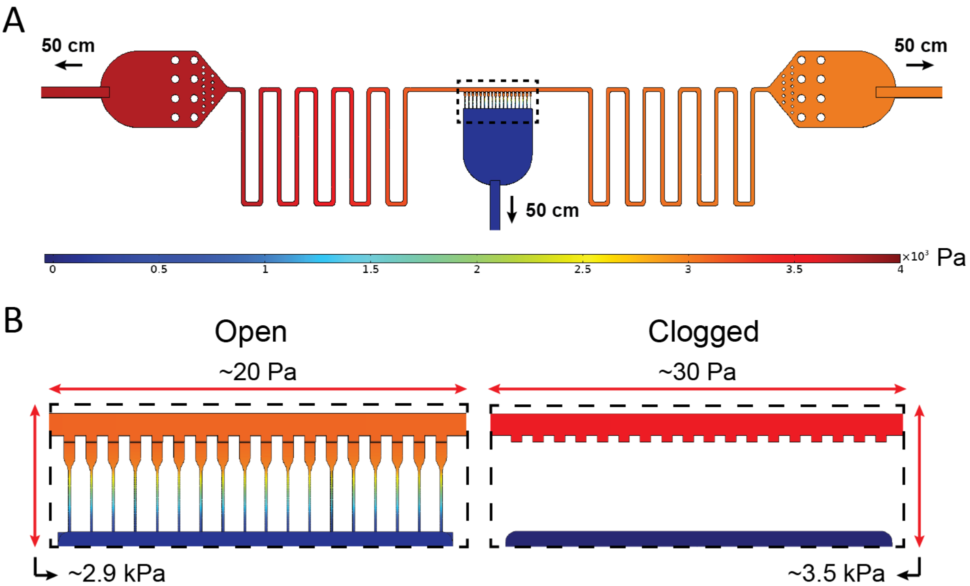

Figure S2.2: Simulation of pressure distribution across the microfluidic cell deformability device. (A) 3D numerical simulation of the pressure distribution assuming the three ports are connected to 50 cm long rectangular channels mimicking the experimental tubing. A pressure gradient of 1 kPa is simulated between the far end of the tube connected to the cell entry port P_1 (4 kPa) and the tube connected to the perfusion port P_2 (3 kPa), while the far end of the tube connected to the outlet port P_3 is kept at atmospheric pressure (0 kPa). (B) Zoomed-in image showing a simulation of the horizontal and vertical pressure gradients across the microchannel array, demonstrated by the dashed rectangle in (A), for two different configurations: all microchannels are open (left) and all microchannels are clogged (right).

MV3 - Cell

HT1080 - Cell

MV3 - Nucleus

HT1080 - Nucleus

Figure S2.3: QR codes for cell squeezing videos HT1080 and MV3.

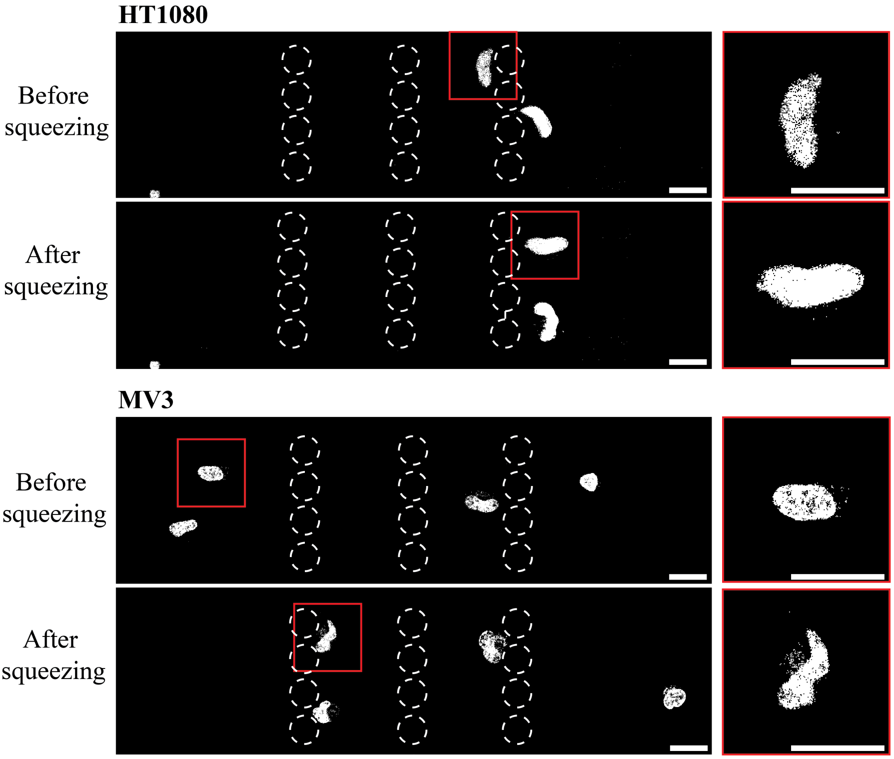

Figure S2.4: Fluorescence images showing nuclear shapes of HT1080 and MV3 cells stained with Hoechst, before and after migrating through a constriction region. Pillars with constriction regions are indicated with white dashed circles. Zoomed-in views of nuclei indicated with red rectangles on the left are shown on the right. Scale bars are 25 µm.

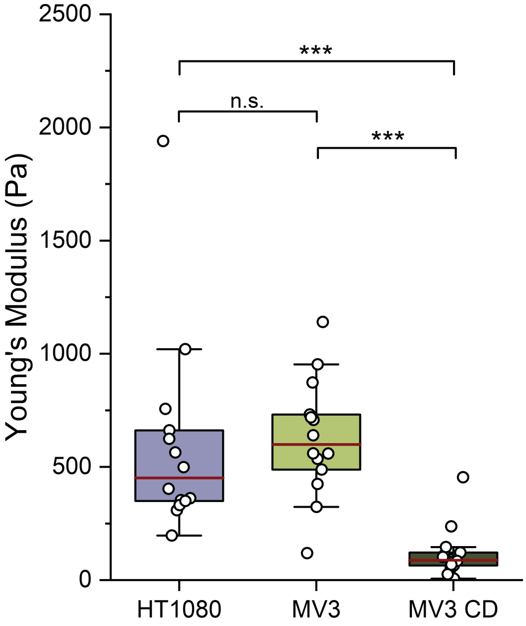

Figure S2.5: Distribution of Effective Young's moduli of adherent HT1080 cells, MV3 cells, and MV3 cells treated with cytochalasin D on glass, measured by microindentation using a probe with a spherical tip of radius 3 µm. Data are represented as box plots. The red lines represent the median values. (***) = $p < 0.001$ and (n.s.) = nonsignificant. n=23-31 for all conditions.

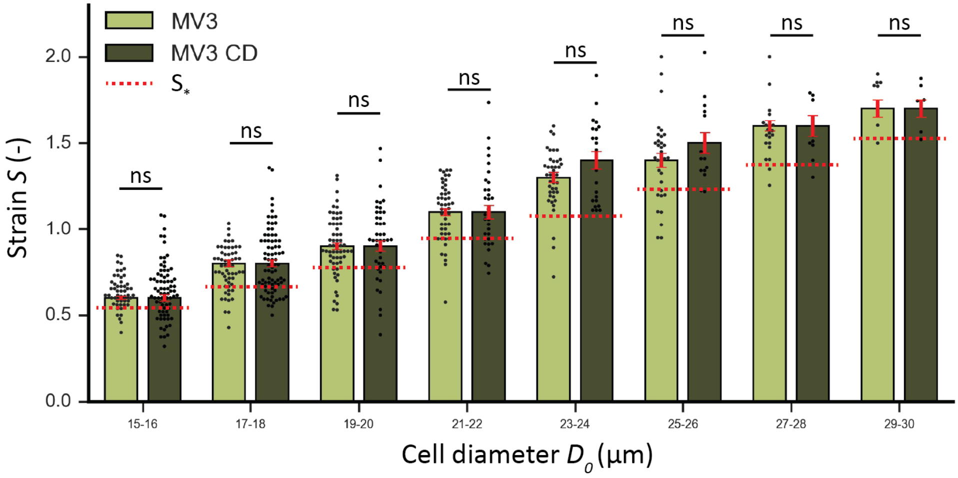

Figure S2.6: Strain measurements for MV3 cells in response to Cytochalasin D treatment using the microfluidic cell deformability device. Histograms comparing the strain S for control MV3 cells (light green) and MV3 cells treated with cytochalasin D (dark green), binned for cell diameter D_0. Red dotted lines depict the theoretical strain S_* in the limit of volume conservation, calculated using Eq. (5) and inserting the largest D_0 for each bin (eg. $D_0 = 16\,\mu$m for 15-16 bin. (ns) = nonsignificant. Error bars are SEM.

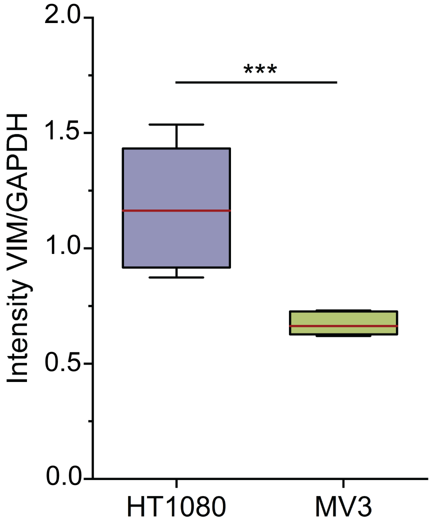

Figure S2.7: Vimentin expression levels in HT1080 and MV3 cells. Boxplot showing intensities of the vimentin bands in a Western Blot for HT1080 (purple) and MV3 (green) cells, relative to GAPDH. The red lines indicate the median. (***) = p < 0.001. For each condition, n = two biological replicates, each subtracted from three different background spots, resulting in n = 6. Full blots are provided in S2.9.

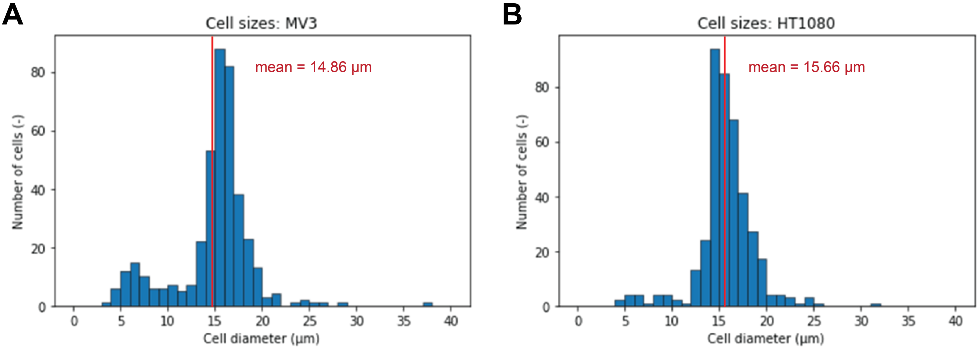

Figure S2.8: Cell size distributions measured by an automated cell counter. Binned cell sizes for MV3 cells (A) and HT1080 cells (B). Bin size = 1 µm, n = 408 cells per cell line.

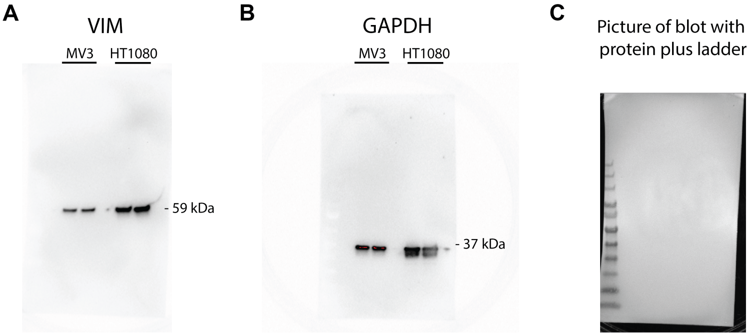

Figure S2.9: Full size Western Blots for probing vimentin expression levels in HT1080 and MV3 cells. Immunostained bands for (A) vimentin and (B) GAPDH, (C) and a picture of the blot showing the protein plus ladder.

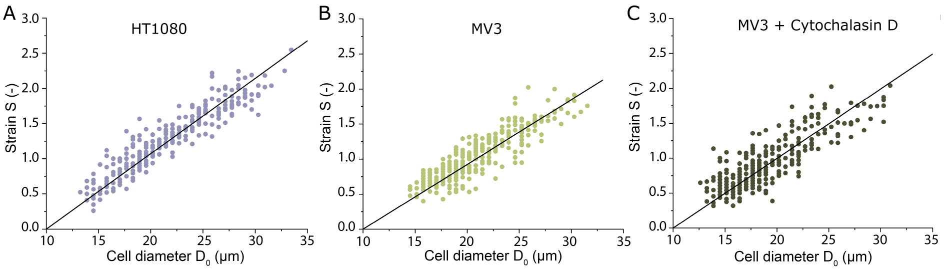

Figure S2.10: Regression graphs with linear fits for strain vs. size for (A) HT1080 with a linear fit of $y = 0.10718x$ with $R^2 = 0.98$, (B) MV3 with a linear fit of $y = 0.0924x$ with $R^2 = 1$ and (C) MV3 cells with Cytochalasin D treatment with a linear fit of $y = 0.09963x$ with $R^2 = 0.95$

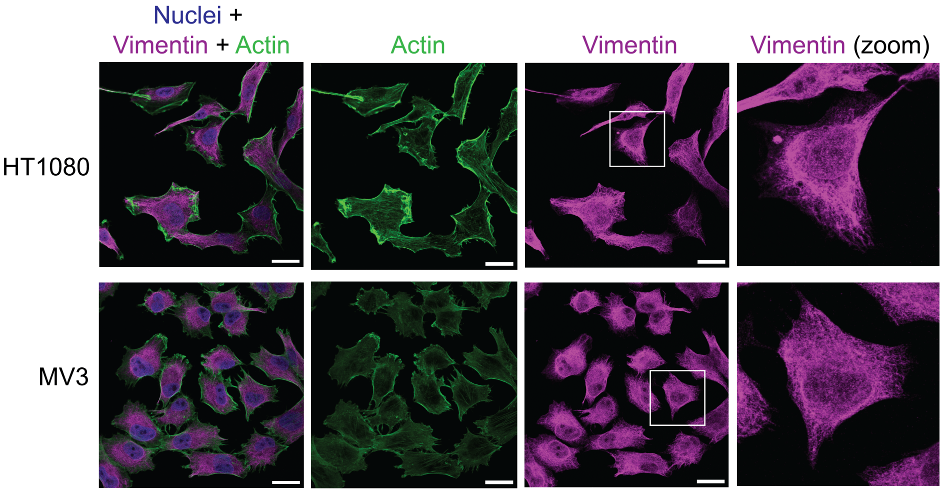

Figure S2.11: Immunocytochemistry on HT1080 (top row) and MV3 (bottom row) cells for actin (green, second column), vimentin (magenta, third and fourth column) and merged with nuclear staining (blue, first column). Scalebars are 25 micrometer. White boxes indicate areas used for zoom images.

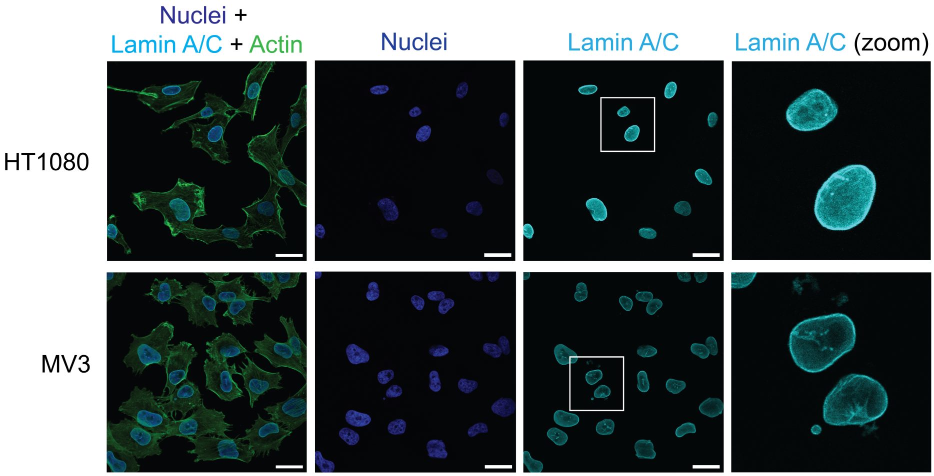

Figure S2.12: Immunocytochemistry on HT1080 (top row) and MV3 (bottom row) cells for nuclei (blue, second column), lamin A/C (cyan, third and fourth column) and merged with actin staining (green, first column). Scalebars are 25 micrometer. White boxes indicate areas used for zoom images.

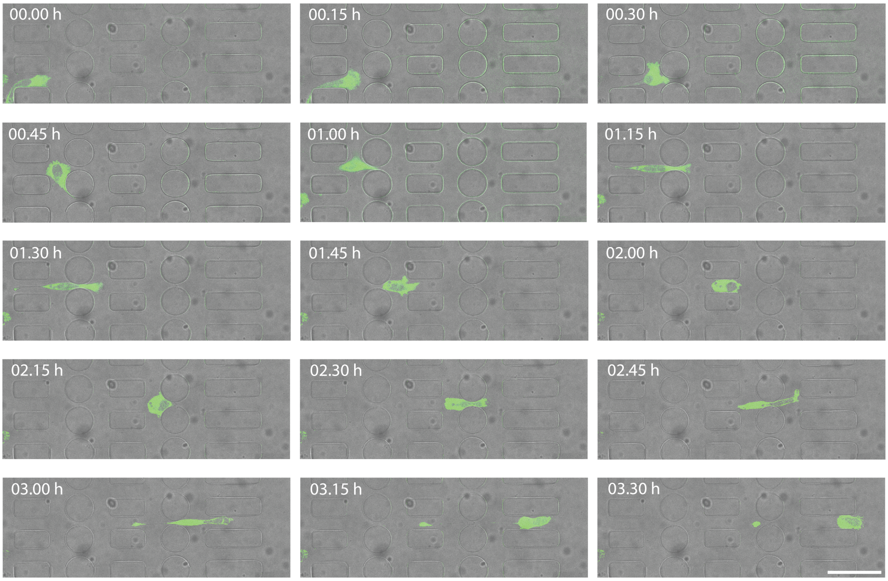

Figure S2.13: Confined cell migration microfluidic experiment in arrays of pillars, with MV3 cells treated with 10 10 micromolar Acetazolamide. Time-lapse images show merge between bright-field channel (gray) and fluorescent channel for cytoplasm (green). Top left corners show corresponding time-stamps.

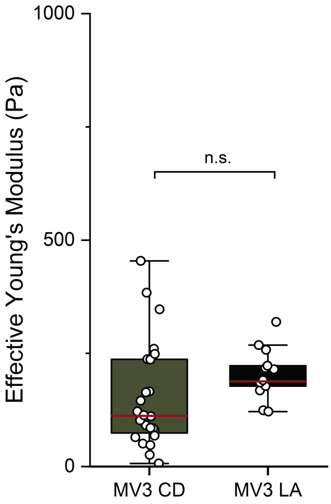

Figure S2.14: Distribution of Effective Young's moduli of adherent MV3 cells treated with cytochalasin D (CD) and Latrunculin A (LA) on glass, measured by microindentation using a probe with a spherical tip of radius 3 µm. Data are represented as box plots. The red lines represent the median values. (n.s.) = nonsignificant. n=24 for MV3 CD and n=14 for MV3 LA.

3

EMT-RELATED CELL-MATRIX INTERACTIONS ARE LINKED TO CELL UNJAMMING

Epithelial-to-mesenchymal transitions (EMT) and unjamming transitions provide two distinct pathways for cancer cells to become invasive, but it is still unclear to what extent these pathways are connected. Here we addressed this question by performing 3D spheroid invasion assays on epithelial-like (A549) and mesenchymal-like (MV3) cancer cell lines in collagen-based hydrogels, where we varied both the invasive character of the cells and the matrix porosity. We found that the onset time of invasion was correlated with the matrix porosity and vimentin levels, while the spheroid expansion rate correlated with MMP1 levels. Spheroids displayed solid-like (non-invasive) states in small-pore hydrogels and fluid-like (strand-based) or gas-like (disseminating cells) states in large-pore hydrogels and for mesenchymal-like cells. Our findings are consistent with different unjamming states as a function of cell motility and matrix confinement predicted in recent models for cancer invasion, but show that cell motility and matrix confinement are coupled via EMT-related matrix degradation. [1]

---

[1] This chapter is co-authored with Zaid Rahman, Ankur D. Bordoloi, Iain Muntz, Peter ten Dijke, Pouyan E. Boukany, and Gijsje H. Koenderink and was published in iScience (2024).

3.1. INTRODUCTION

DISSOCIATION of cancer cells from the primary tumor followed by invasion through the local tumor microenvironment (TME) is a crucial first step during metastasis of solid tumors. These first stages of invasion are often achieved through epithelial-to-mesenchymal transitions (EMT) that promote cell motility [108] and they are influenced by the composition of the TME. The TME has distinctive cellular components, including cancer-associated fibroblasts (CAFs) and immune cells, as well as non-cellular components, including cytokines, growth factors, and a unique organization of extracellular matrix (ECM) [109]. Tumor cells and CAFs remodel the ECM in the TME, generally turning the fibrous networks from healthy tissues into denser and stiffer matrices with smaller pores [110]. The resulting dysregulated ECM poses physical challenges for the invading tumor cells, as the cells have to tightly squeeze their nuclei while preventing excessive DNA damage [25, 111].

To deal with a wide variety of dysregulated tissue organizations in the TME, tumor cells are known to adapt their phenotype and associated migration strategy in response to their local environments. Tumor cells that migrate individually can adopt three main modes of migration, which can be categorized by their dependency on cell-matrix adhesions and actomyosin contractility. Cancer cells performing mesenchymal migration pull themselves forward on matrix fibers relying on matrix adhesions and cell contractility. In low-adhesion or high-density tissues, cancer cells can migrate through either amoeboid or lobopodial migration and increase their deformability [111]. Next to these individual cell motility modes, cancer cells can also switch to multicellular migration modes. This collective migration strategy is linked to increased survival in the bloodstream and higher metastatic potential [10]. The phenotypic plasticity of cancer cells enables switches between these different migration strategies in response to changes in ECM confinement and stiffness [112, 113], oxygen and energy deprivation [114] and cytokines [115].

While the role of intracellular signaling pathways (such as responses to TGF-β, epidermal growth factor, or cytokines released from CAFs) and the expression of EMT markers [116, 117] in cancer cell invasion are relatively well studied, the molecular mechanisms behind migration mode switches in response to different TMEs remain poorly understood [118]. The increasing attention for the biophysical aspects of tumor invasion in recent years has revealed that matrix confinement, determined by ECM protein density and porosity, is an important regulator of cell migration mode switches [112, 7, 119]. Mechanistically, the link between ECM confinement and cancer cell invasion has been explained by describing tumors as active liquid crystalline materials that undergo solid-to-liquid-like transitions during jamming conversions [120, 111] that are determined by cell-cell adhesions and ECM confinement [121]. Lattice-gas cellular automaton simulations suggested a theoretical jamming phase diagram that describes how variations in both cell-cell adhesions and ECM density (and hence confinement) determine unjamming transitions from a state where no invasion occurs (solid-like phase) towards collective cell invasion (liquid-like phase) or individual cell invasion (gas-like phase) [121]. Later agent-based simulations predicted a non-equilibrium phase diagram that describes these unjamming transitions in terms of 'cell motility' and 'matrix density' [122].

While this conceptual framework is appealing, it is complicated by the fact that these two variables, cell motility and ECM confinement, are not independent. They are coupled since cancer cells can actively modify the ECM composition and architecture, while conversely the ECM can induce changes in cell motility [123]. Cancer cells adhere to the ECM via integrin receptors, activating intracellular signalling pathways that trigger cellular responses such as ECM deposition and the release of matrix metalloproteases (MMPs) [14, 121]. MMPs are proteolytic enzymes secreted by cancer cells to break down ECM proteins such as collagen, forming proteolytic tracks that facilitate cancer cell invasion [15]. In addition, upregulation of collagen deposition by tumor cells (and CAFs) can also promote cell invasion with the formation of specialized anisotropic migration tracks [124, 125]. These complex events together contribute to an abnormal ECM composition, structure and stiffness, which in turn influences cell invasion [126, 109]. In addition, these changes in the ECM alter other cellular characteristics such as cell proliferation, differentiation and cell mechanics, all of which also impact cancer initiation and progression [127, 128, 129, 130]. Changes in ECM stiffness and porosity can affect the mode of migration of cancer cells [15, 131] and their invasion capacity [132, 133, 129, 134, 135]. Moreover, the ECM can also affect cell migration through the storage and release of growth factors [136], such as the latent form of transforming growth factor-β (TGF-β) [137, 138, 139]. TGF-β is a well-known cytokine found in the TME that triggers the up-regulation of proteins associated with a mesenchymal state such as vimentin, and the down-regulation of epithelial protein markers such as E-cadherin, promoting cell motility and invasion through EMT [140, 141]. Furthermore, TGF-β also stimulates the release of MMPs from cancer cells, promoting the formation of proteolytic tracks that promote invasion [15]. The role of TGF-β in tumor invasion is a clear example of the dynamic reciprocity of cell-ECM interactions during invasion.

Although much work has been done on elucidating the different matrix properties that influence cancer cell invasion, the reported correlations can be inconsistent. For example, increased matrix stiffness correlates with enhanced invasion in 3D *in vitro* models of epithelial cancers in 64% of the studies, but it is also negatively correlated in 36% of the studies [142]. This variability is probably due to the diversity in experimental setups. Especially the time scale over which invasion is monitored is likely important, since invasion is a highly dynamic process. Because of these inconsistencies, there are still many open questions about the roles of matrix properties in invasion, especially in combination with reciprocal cell-ECM interactions, where cell motility and matrix properties change in concert. To gain a better understanding of how cell-matrix interactions control cell invasion, we need cellular *in vitro* model systems that decouple interconnected matrix properties such as stiffness and porosity [143], differentiate between different stages of invasion, and analyse how matrix remodelling and cell signalling impact unjamming phase transitions during invasion.

In this study, we aimed to understand the effect of mechanochemical coupling between matrix confinement and cell motility on tumor invasion. For this, we analysed the invasion efficiencies and migration modes of melanoma and lung cancer cells in 3D spheroid-hydrogel assays. We related these phenotypic characteristics to protein levels of EMT markers (vimentin and E-cadherin) and MMPs and to the different states of unjamming that describe invasion behaviour [122]. To tune matrix confinement over a wide range, we used two types of hydrogels, natural collagen (bovine type I) and semi-synthetic gelatin methacrylate (GelMA), at different concentrations. GelMA matrices contain pore sizes that are substantially smaller ($\simeq$ 10 nm range) than average cell bodies ($\simeq$ 10 µm range) so cell motility requires matrix degradation [144, 145]. By contrast, the pore sizes of collagen type I matrices ($\simeq$ micrometric) allow for cell motility through a combination of cell squeezing and matrix degradation. We systematically compared the invasive capacity of epithelial-like cancer cells (A549, lung adenocarcinoma) and mesenchymal-like, highly metastatic cells (MV3 melanoma). Furthermore, we explored how cell-mediated matrix degradation influences invasion trends, by studying cancer cell invasion upon TGF-β or MMP inhibitor treatments. We used a broad spectrum MMP-inhibitor (Batimastat, BB-94), which binds to various metalloproteases including collagenases (MMP-1) and gelatinases (MMP-2, MMP-9), to inhibit cleavage of collagen type I and GelMA hydrogels used in this study [146]. Using a new image analysis method to analyze the spatiotemporal characteristic of spheroid invasion, we demonstrate that the onset of spheroid invasion is regulated by initial matrix confinement and vimentin, while the rate of invasion and unjamming state correspond with MMP1 levels. Our findings reveal that EMT-regulated cell-ECM mechanochemical interactions play an important role in 3D spheroid unjamming transitions.

3.2. METHODS

CELL CULTURE

MV3 human male melanoma cells which were three times xenografted in nude mice and selected for highly-metastatic behaviour [66] (a kind gift from Peter Friedl, Radboud University Nijmegen), were cultured in DMEM-F12 (Dulbecco's Modified Eagle Medium, Thermo Scientific) supplemented with 10% Fetal Bovine Serum (FBS, Thermo Fisher) and 1% penicillin/streptomycin (Thermo Fisher). A549 human male lung adenocarcinoma cells (CCL_185, ATCC) were cultured in DMEM (Gibco, #41965039), and supplemented with 10% FBS (Gibco) and 1% Antibiotic-Antimycotic solution (Gibco). All cells were incubated at 37°C and 5% CO_2, passaged at 80-90% confluency, and sub-cultured 2-3 times per week.

SPHEROID FORMATION

Spheroids were grown in a commercially available Corning^{TM} Elplasia^{TM} 96-well plate for high-throughput spheroid production. These well plates are round-bottom with an Ultra-Low Attachment (ULA) surface that prevents cell-surface attachment and promotes cell-cell adhesion. We used an initial seeding density of 40 × 10^3 cells (500 cells per micro-well) for each well to produce 79 spheroids. Spheroids were ready to use after 4 days of culture in the wells and had an average diameter of approximately 200 ±30 µm for both cell lines (Fig. S3.25). We restricted the spheroid diameter to less than 250 µm to avoid a necrotic core.

HYDROGEL PREPARATION

Bovine hide collagen type I (purity ≥ 99.9%, Advanced Biomatrix) stock solutions (3 mg/mL and 10 mg/mL in 0.01 N HCL) were used to prepare 2.4 mg/mL and 8 mg/mL collagen gels, respectively. The collagen was made isotonic by adding 12.5 v/v% of 10x Phosphate Buffered Saline (PBS, Thermo Fisher) to collagen. In addition, 0.1 M sodium hydroxide was added to bring the pH to 7.4. All solutions were kept on ice. Pre-cooled Milli-Q (MQ) was added to bring the final collagen concentration to either 2.4 or 8 mg/mL. Final collagen dilutions were vortexed for 30 seconds and polymerized at 37° C in an μ-slide 8-well (Ibidi) for at least 45 minutes. Gelatin methacryloyl (GelMA) was purchased from Sigma Aldrich (300g bloom, 60% degree substitution). GelMA retains the thermo-reversibility of gelatin [147], but the methacrylic anhydride groups can undergo covalent cross-linking under UV light (365 nm) in the presence of a photoinitiator. We used 3 and 5 wt% GelMA with a 1:16 mass ratio of photoiniator (Lithium phenyl-2,4,6- trimethylbenzoylphosphinate, LAP; Sigma Aldrich). LAP and GelMA were dissolved together in Dulbecco's Phosphate Buffered Saline (DPBS; Gibco) at 37° C in a water bath for about 2 hours. The hydrogel was crosslinked using a UV-lamp (Spectroline, Serial no. 1832066) at a wavelength of 365 nm for 45 s.

3D SPHEROID INVASION ASSAYS

Spheroids were embedded in collagen gels by a sandwich protocol adapted from [148]. First, collagen gel layers of 80 µL were polymerized in μ-Slide 8 well chambers (ibidi) for 45 minutes at 37° C. Next, spheroids were transferred from the culture plate onto the collagen layers by carefully pipetting them (to avoid spheroid disruption) in culture medium. Spheroids were incubated on the collagen gel for 30 minutes to ensure attachment. Next, culture medium was pipetted out of the chambers and collagen layers of 100 µL were added on top of the spheroids and polymerized for 45 minutes at 37° C. After polymerization, 200 µL of cell culture medium was added to the spheroid-collagen gels, which were then incubated at 37° C and 5% CO_2. For spheroids embedded in GelMA, we pipetted 125 µL of GelMA/spheroid suspension in a well of the μ-Slide 8-well chambers (ibidi). We then exposed the μ-Slide to 45 s of UV-light (365 nm) using a lamp, followed by addition of 200 µL culture medium.

Recombinant TGF-β (stock concentration 5 µg/mL was diluted in culture medium to a final concentration of 10 ng/mL, selected based on previous work [149, 150]. Batimastat (BB-94) broad spectrum MMP-inhibitor (stock concentration 1 mM) from Abcam was diluted to 30 µM in culture medium. This concentration has also been used in prior work [151, 152] and we verified by live-dead staining that this dose showed no cytotoxic effects on A549 spheroids after 24 hours of incubation. The supplemented media were added to the respective ibidi wells with spheroids embedded in hydrogels before incubation and imaging. Any cancer spheroids that made contact with the glass substrate or the side walls of the μ-Slide (ibidi) were excluded from analysis. Spheroid invasion was monitored using a Colibri Axio Observer 7 inverted microscope under bright-field settings with a 5x/NA 0.16 air objective for time-lapse imaging (multiple positions) at a time interval of 1 hr. MV3 spheroid invasion imaging was restricted to 24 hrs, while A549 spheroid invasion - which was slower - was imaged until 72 hrs. All experiments were conducted at 37° C, 90% humidity and 5% CO_2 using a stage top incubator (ibidi).

RHEOLOGY

Shear rheology of hydrogels was performed on a Kinexus pro+ rheometer (Malvern, UK), using a 20 mm stainless steel parallel plate and 0.5 mm gap. The collagen samples were pipetted on the bottom plate, which was held at 4° C using a Peltier system, the top plate was immediately lowered, and the temperature was set at 37° C to induce collagen polymerization. The GelMA samples were pipetted on the bottom plate at 37° C and were crosslinked using a UV lamp (Spectroline, Serial no. 1832066) for 45 seconds at 365 nm wavelength at a fixed distance of 2 cm from the sample. Immediately after crosslinking, the top plate was lowered. Mineral oil was added around the sample edge to prevent solvent evaporation. During and after polymerization, small amplitude oscillatory shear was applied to the hydrogels with a constant strain amplitude (0.5%) and frequency (1 Hz) to measure the storage shear modulus (G') and loss shear modulus (G"), which correspond to the elastic and viscous components of the complex shear modulus, respectively.

IMAGE AND DATA ANALYSIS FOR 3D SPHEROID INVASION ASSAYS

We developed a custom-made MATLAB script to detect the spheroid boundary and disseminated single cells in bright-field time-lapse image series of invading spheroids. We first adjusted the image brightness and contrast using the MATLAB command 'imsharpen'. We then created a binary gradient mask by adjusting the image segmentation threshold to detect discontinuities in brightness using the derivative of a Gaussian filter. This threshold value was optimized for each set of bright-field images. The binary gradient mask outlined the identified object, which was then post-processed to smoothen and dilate using the MATLAB command 'imdilate'. This dilated gradient mask finally underwent the 'fill hole' process using the MATLAB command 'imfill'. The spheroid boundary (outlined in red in Fig. S3.9) was detected by MATLAB command 'bwboundaries' that identifies exterior boundaries. From the boundary, we calculated the spheroid area and effective circular radius. To account for variations in initial spheroid size, we normalized the effective circular radius by its initial value at $t = 0$. Single dissociated cells were identified with the same threshold parameters (highlighted in green, see Fig. S3.9). In case individual cells were already present at $t = 0$, we subtracted these from the cell count at the end of the assay (24 hrs for MV3, 72 hrs for A549). Note that the cell counts likely underestimate the actual cell number since the limited contrast of the images made it difficult to distinguish whether cells close to the spheroid boundary had dissociated.
To identify multicellular protrusions of MV3 and A549 spheroids and determine their lengths, we developed another MATLAB script. First we converted 2D bright-field im-

ages from the Cartesian coordinate system (x, y) to a polar coordinate system (θ, r). Next we detect protrusions as peaks relative to the average spheroid radius (highlighted in cyan, see Fig. S3.9C, D). The protrusion length analysis was performed on images obtained at the end time point of each experiment ($t = 24$ hrs for MV3, $t = 72$ hrs for A549). The average protrusion length was used as a criterion to distinguish between a solid-like phase (length below 25 µm) versus a liquid-like state (length above 25 µm).

WESTERN BLOT ANALYSIS

For '2D Western Blot' analysis (i.e., Western Blots for cells in 2D cell culture), bovine type I collagen (Procol, Advanced Biomatrix, 3 mg/mL) was diluted 1:100 with MilliQ water and pipetted into six-well plates (Thermo Fisher) to cover the surface and left to incubate for 2 hours at room temperature. The collagen coatings were washed twice with PBS. Next, MV3 cells (300,000/well) and A549 cells (400,000/well) were seeded in the coated plates in culture medium under control conditions 2 µL/mL DMSO) or with recombinant TGF-β at 10 ng/mL (stock concentration 5 ng/μL) or Batimastat at 30 μM (stock concentration 1 mM, BB-94/Abcam). After 48 hrs (or 1 hour for SMAD activity tests), cells were washed with PBS, lysed with cold radioimmunoprecipitation buffer (RIPA, 100 µL/well, Thermo Fisher) and transferred to Eppendorf tubes. Lysed samples were agitated at 4° C for 30 minutes and stored at -20° C. For 3D spheroid invasion Western Blot analysis, 3D invasion assays were made as described above with n=4 and incubated for 72 hrs at 37° C and 5% CO_2. After 72 hrs, collagen gels were removed from the wells with a spatula and collected in pairs in 15 mL tubes with 450 μL of PBS. For each tube, 150 μL of 80 mg/mL collagenase (C0130, Sigma Aldrich) was added and the tubes were incubated and agitated at 37°C for 3 minutes to degrade the collagen. Next, each tube was filled with 8400 μL of PBS and centrifuged for 5 minutes at 250 rcf at 4° C. Next, supernatant was removed and cell pellets were lysed in 100 μL RIPA buffer.

Laemmli buffer (2x, Bio-rad) and 4% β-mercaptoethanol (Sigma Aldrich) were added to the lysed samples, which were incubated at 95° C for 5 minutes. Sodium dodecyl sulfate-polyacrylamide gel electrophoresis (SDS-PAGE) was performed with Mini PROTEAN TGX gels (Bio-rad) using 100 V for 1.5 hours. Western Blotting was executed with a Trans-Blot Turbo Transfer System (Bio-rad) and Trans-Blot Turbo Mini 0.2 µm PVDF Transfer Packs (Bio-rad). The membranes were blocked in 5% Bovine Serum Albumin (BSA, Thermo Fisher) in phosphate buffered saline (PBS, company) overnight. Membranes were stained with primary antibodies: rabbit anti-SMAD2 (1:1000, #5339, Cell signaling), rabbit anti-pSMAD2 (1:1000, kind gift from Peter ten Dijke [153]), rabbit anti-MMP1 (1:1000, #54376, Bioke), mouse anti-MMP2 (1:1000, #436000, Thermo Fisher), rabbit anti-E-cadherin (1:1000, #ab40772, Abcam), mouse anti-vimentin (1:2000, #ab8978, Abcam), rabbit anti-SNAIL (1:1000, #3879T, Bioke), rabbit anti-ZEB1 (1:1000, #3396T, Bioke) and rabbit anti-GAPDH (#CST2118S, Bioke) in 5% BSA overnight on a shaker at 4° C. Membranes were washed thrice with 0.1% Tween (Sigma Aldrich) in PBS (PBS-T) on a shaker, and incubated for 3-5 hours with secondary antibodies: rabbit anti-mouse HRP (#ab97051, Abcam) and goat anti-rabbit HRP (#ab6728, Abcam), 1:5000 in PBS-T. Afterwards, membranes were washed thrice with PBS-T and imaged with an enhanced luminol-based chemiluminescent substrate kit (Thermo Fisher) on a gel imager (Bio-rad).

IMMUNOCYTOCHEMISTRY

Spheroid invasion assays were fixated with 4% formaldehyde (Thermo Fisher) in PBS for 15 minutes, washed three times with PBS and permeabilized with 0.5% Triton-x 100 (Sigma Aldrich) in PBS for 3 minutes. Spheroids were first blocked in 3% BSA at 4° C overnight and subsequently incubated in 1.5% BSA/PBST with chicken anti-vimentin (ab24525, Abcam) 1:200 at 4° C overnight. After primary incubation, spheroids were washed three times with PBST and incubated with goat anti-chicken 488 (ab150169, Abcam) 1:1000 and Hoechst 33342 (Thermo Fisher) 1:1000 in PBST for 6 hours at room temperature. Spheroids were washed three times with PBST before imaging. The spheroids were imaged on a Stellaris 8 confocal microscope (Leica), equipped with a supercontinuum white light laser, 405 nm laser and three hybrid detectors. Imaging was performed with the 405 laser, a 488 nm laser line and a 20x/0.75 air objective.

PORE SIZE AND VOID FRACTION ANALYSIS OF HYDROGELS

Collagen and GelMA hydrogels were prepared in μ-Slide 8 well chambers and were imaged by confocal reflectance on a Stellaris 8 confocal microscope (Leica), equipped with a white light laser and a hybrid detector (HyDS), using a 488 nm laser line and a 63x magnification objective (1.3 NA, glycerol immersion) at room temperature. We recorded Z-stacks starting at 100 µm above the glass surface over a total depth of 30 µm with a 2 µm step size. For the collagen networks, we used a custom-made python script [154, 155], which implements the bubble method to measure the sizes of the pores in between collagen fibers (see Fig. S3.2). Confocal images were denoised using the total variation minimization method [156] on a slice-by-slice basis. A local threshold was then applied to obtain a binary confocal stack. The Euclidean distance map was determined, representing the distance to the nearest fiber at each point in the image, and a Gaussian filter was applied with a standard deviation of 5 pixels to the Euclidean distance map. Finally, the local maxima of the Euclidean distance map were determined, which represent the furthest distance from a fiber in the image. We selected these distances as half of the pore size. The average pore size was calculated of three replicates for each concentration (n=3). The GelMA hydrogels with their nanometric pores were too dense to be able to directly measure the pore size distribution. Instead, we performed a void fraction analysis on maximum intensity projections of confocal reflectance microscopy Z-stacks of GelMA and collagen hydrogels made in Fiji [157]. The images were adjusted for brightness and contrast by maximum intensity projection. The adjusted images were then converted to a binary image using the 'Make Binary' function in Fiji with white (1) pixels corresponding to hydrogel fibers and black (0) pixels corresponding to the voids. We determined the void fraction as the ratio of black pixels to white pixels.

GELMA HYDROGEL PERMEABILITY ANALYSIS

Permeability analysis was performed on GelMA hydrogels (30 mg/mL and 50 mg/mL) to estimate their pore size. The permeability, K, of a hydrogel can be obtained from Darcy's

Law by estimating the flow velocity of tracer particles through the material. To measure the flow velocity, we used a microfluidic platform equipped with three channels, where the middle channel was filled with GelMA hydrogel and crosslinked by a UV-light source (365 nm)[150]. The top and bottom channels were operated using a pressure pump device to create a pressure gradient that drives the flow through the hydrogel channel at room temperature. The microfluidic chip was mounted on a Zeiss Axio Observer 7 microscope equipped with an ORCA Flash 4.0 V2 (Hamamatsu) digital camera with a resolution of 2048 × 2048 pixels. We used Rhodamine B dye (Merck Sigma) (1% v/v solution in 1X Dulbecco's Phoshate Buffer Solution from Sigma Aldrich) as a tracer particle. After applying a pressure gradient $\Delta P = 20$ mbar, the displacement of the dye front was tracked by time-lapse imaging with a time interval of 30 seconds. Imaging was performed using 543 nm LED (excitation/emission: 543 nm/568 nm) at 30% intensity and 1.58 s exposure time, and a 5x (NA 0.16/Air) objective. The images were then converted into 8-bit color images using ImageJ [157]. A line was drawn in the direction of the flow to obtain a histogram of the fluorescence intensity as a function of distance. The fluorescence intensity is tracked by identifying the distance (pixel value × pixel length (0.62 μm) value at which the mean intensity of fluorescence is zero. This position was recorded for the next 10 consecutive images at 30 second intervals. The difference between two consecutive images is divided by the time interval between images to obtain the flow velocity. Averaging for each pair of consecutive images thus gives the average flow velocity. From the measured velocity, we computed the hydraulic permeability of the GelMA hydrogels using the Darcy equation:

$$v = (\Delta P \times K)/(L \times \mu), \tag{3.1}$$

where μ is the fluid velocity across the hydrogel (m/s), ΔP is the pressure gradient across the hydrogel (Pa), L is the length of the hydrogel channel in the direction of the flow (m), K is the hydraulic permeability (m^2), and μ is the fluid dynamic viscosity (10^{-3} Pa.s). We recovered an average permeability of 2.36×10^{-16} m^2 for 30 mg/mL GelMA and 1.29×10^{-16} m^2 for 50 mg/mL GelMA. The corresponding pore sizes, calculated as the square root of the permeability, were 1.54 nm for 30 mg/mL GelMA and 1.14 nm for 50 mg/mL GelMA (for a detailed summary see Table 3.1).

STATISTICAL ANALYSIS

Statistical analysis was performed with Origin. Statistical details of experiments are found in the figure legends and method details. P-value results from t-tests are indicated by: (ns) = $p \geq 0.05$, (*) = $p < 0.05$, (**) = $p < 0.01$, (***) = $p < 0.001$.

3.3. RESULTS

DESIGN AND CHARACTERIZATION OF THE 3D SPHEROID INVASION MODEL

To identify the impact of ECM confinement on the invasion of cancer cells with different metastatic potentials, we performed 3D spheroid invasion assays using two different human cancer cell lines and two different types of hydrogels. MV3 (melanoma) cells were

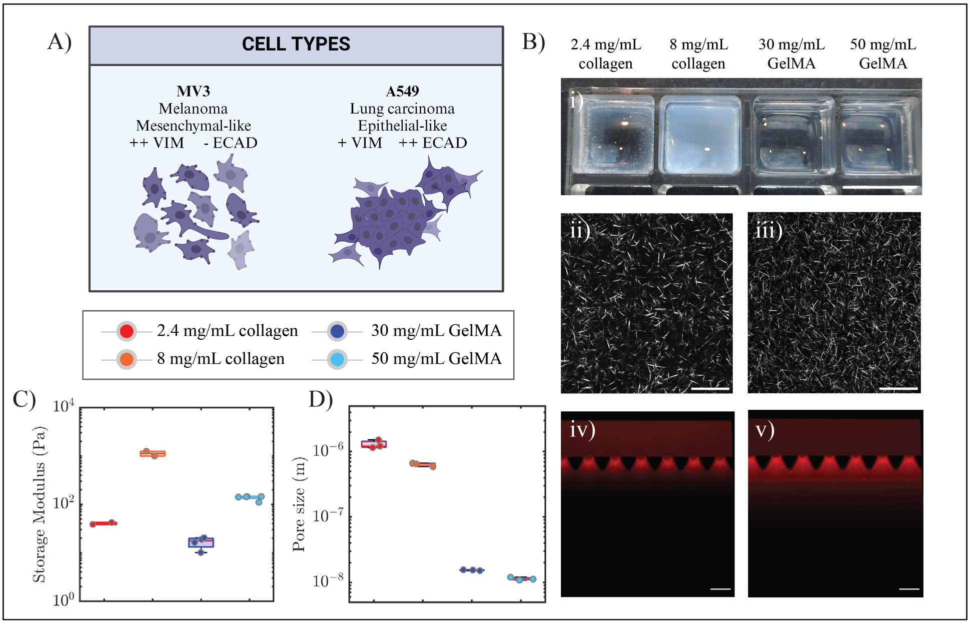

Figure 3.1: Characterization of the 3D spheroid invasion model. A) Schematic showing the distinctive features of MV3 melanoma cells and A549 lung adenocarcinoma cells. MV3 cells are mesenchymal-like, with high vimentin expression (++VIM) and low E-cadherin expression (-ECAD), whereas A549 cells are epithelial-like, with lower vimentin (+VIM) and high E-cadherin (++ECAD) expression and more cell-cell interactions. B) Structural characterization of the ECM-mimicking hydrogels. (i) Photograph of the four hydrogels in an ibidi 8-well slide (without spheroids), scale bar is 10 mm. The collagen hydrogels are more turbid than the GelMA hydrogels because of the larger width of collagen fibers as compared to GelMA strands. Confocal reflection images of collagen at concentrations of (ii) 2.4 mg/mL and (iii) 8 mg/ml. Scale bars are 25 µm. Permeability analysis of GelMA (30 mg/mL) based on fluorescence images of Rhodamine B dye (red) at (iv) $t = 0$ and (v) $t = 10$ min, performed in a microfluidic chip, scale bar is 200 µm. We inferred the hydraulic permeability from the distance travelled by the dye under a pressure gradient of 20 mbar (top to bottom) using Darcy's law. C) Storage shear moduli (G') of collagen and GelMA hydrogels obtained by rheology measurements. D) Pore sizes of collagen and GelMA hydrogels, obtained by image analysis and permeability analysis, respectively.

chosen as they are highly metastatic and mesenchymal-like, in contrast to the epithelial-like character of A549 (lung carcinoma) cells (see schematic in Fig. 3.1A). We confirmed the mesenchymal and epithelial features of the two cell lines by bright-field imaging of the cell morphology (see Fig. S3.1A) and Western blot analysis of the protein levels of E-cadherin and vimentin (see Fig. S3.1B,C). For hydrogel systems, we chose collagen type I and GelMA hydrogels, because of their contrasting fibrous open-mesh network structure versus dense confining microenvironment, respectively (Fig. 3.1Bi). Two different concentrations for each type of hydrogel were characterized for stiffness and for the pore size and corresponding fiber density. Measurements of the storage modulus (G') from small amplitude oscillatory shear rheology showed that the hydrogels covered a wide range of storage moduli from 10^1 Pa to 10^3 Pa (see Fig. 3.1C). Note that these values correspond to Young's moduli $E = 2G(1+\nu)$, which are approximately three times larger in magnitude. Pore size measurements were conducted through analysis of confocal microscopy reflection images for collagen networks (Fig. 3.1Bii,iii and Fig. S3.2) and through permeability measurements for GelMA hydrogels (Fig. 3.1Biv,v and Table 3.1). The GelMA hydrogels had pore sizes in the $\simeq 10$ nanometer range, two orders of magnitude smaller than the micrometric pores of collagen hydrogels (Fig. 3.1D). Furthermore, for both hydrogel types, the pore size decreased with increasing biopolymer concentration (30 mg/mL versus 50 mg/mL for GelMA; 2.4 mg/mL versus 8 mg/ml for collagen). As an independent test of matrix porosity, we also compared the fiber densities of the four hydrogels by measuring the void fraction in confocal reflection microscopy images. These estimations showed that the hydrogels with the smaller pores indeed had the highest matrix fiber densities (see Fig. S3.3). These results demonstrate that the ECM-mimicking hydrogels in this study offer a wide range of levels of cell confinement, from full confinement of cells in GelMA hydrogels to partial confinement of cells in the collagen hydrogels.

SPHEROID INVASION DEPENDS ON MATRIX CONFINEMENT AND ON CELL TYPE

To understand the impact of matrix confinement (i.e., pore size) on the ability of the cells to invade, we performed invasion assays by bright-field imaging of 200 µm diameter cancer spheroids embedded in hydrogels at the spheroid equator. For MV3 spheroids in low density (2.4 mg/ml) collagen, we observed substantial cell invasion already by $t = 8$ hours (hrs), and even more invasion after 24 hrs (Fig. 3.2A). After 24 hrs, the spheroid was partially disintegrated, leaving an intact spheroid core surrounded by many disseminated individual cells. Therefore, we limited the MV3 invasion assay to 24 hrs. In a denser (8 mg/ml) collagen hydrogel, the MV3 spheroids showed a similar invasion pattern (Fig. S3.4A). In 30 mg/mL GelMA hydrogels, the MV3 spheroids also showed an isotropic invasion pattern, but invasion was delayed and the cells reached less far into the gel (Fig. 3.2B). In 50 mg/mL GelMA gels, we could not observe any signs of invasion on a 24 hrs time scale (Fig. S3.4B).

The A549 spheroids showed a very different invasion behavior as compared to MV3 spheroids. Even in the least confining hydrogel (2.4 mg/mL collagen), the A549 spheroids remained compact and developed only a small number of multicellular protrusions from sites that were non-uniformly distributed around the spheroid periphery. Also, there were much fewer disseminated cells (Fig.3.2C). The A549 spheroids furthermore showed a much longer onset time for invasion ($t \approx 24$ hrs) compared to the MV3 spheroids ($t \approx 8$ hrs) in the same matrix. To allow sufficient time for cell invasion, we therefore performed 72 hrs of time-series imaging for A549 spheroids. In denser collagen hydrogels (8 mg/mL) and GelMA hydrogels (30 mg/mL and 50 mg/mL), A549 spheroids showed hardly any protrusions nor disseminated cells even after 72 hrs (Fig.3.2D for 30 mg/mL GelMA and Fig. S3.5 for 8 mg/mL collagen and 50 mg/mL GelMA). These findings demonstrate that the mesenchymal-like MV3 cells are more invasive than the epithelial-like A549 cells and that matrix density impacts invasion in both cases.

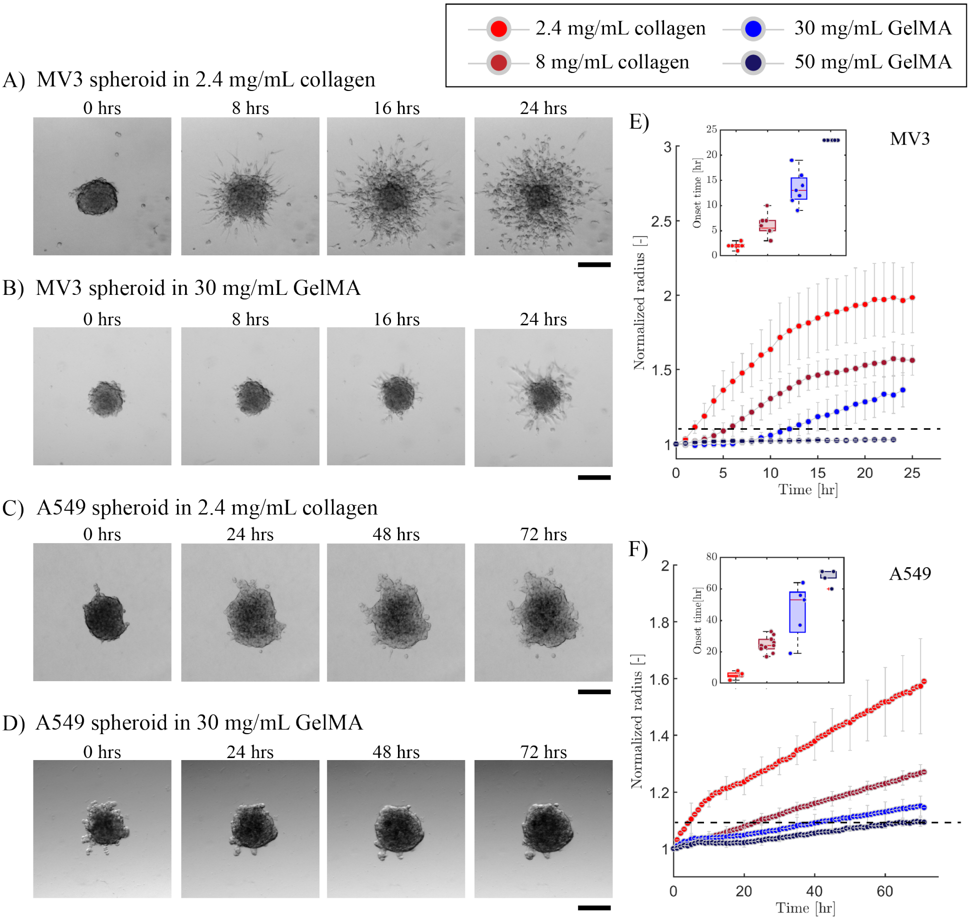

Figure 3.2: MV3 and A549 spheroid invasion in collagen and GelMA matrices. Bright-field microscopy images of spheroids at different time intervals for 24 hrs invasion of a MV3 spheroid in A) collagen (2.4 mg/mL) and B) GelMA (30 mg/mL), and for 72 hrs invasion of an A549 spheroid in C) collagen (2.4 mg/mL) and D) GelMA (30 mg/mL). Scale bars are 200 µm. Time evolution of the normalized effective circular radius of E) MV3 and F) A549 spheroids, for different matrix compositions (see legend on top). Horizontal black dashed lines indicate the onset time for invasion, defined as the time where the normalized radius reaches a value of 1.1. Data are averages with standard deviations of N = 4-10 spheroids (from n = 2 independent experiments). Insets in E) and F) show the onset time (t_{ons}) of invasion in the different matrices (same color code as main plots).

To quantify the effects of cell type and matrix density on spheroid invasion, we tracked the spheroid periphery for each time point through automated image analysis of the bright-field time-lapse images. To account for varying spheroid shapes and initial sizes, we computed the effective circular radius normalized by its initial value at t = 0 hr. For the MV3 spheroids, we found a clear trend of decreasing cell invasion with decreasing matrix pore size, going from 2.4 mg/mL collagen to 8 mg/mL collagen and to 30 mg/mL GelMA and finally to 50 mg/mL (Fig. 3.2E). In the densest hydrogel (50 mg/mL GelMA), no appreciable invasion took place. The A549 spheroids showed the same trend as MV3 spheroids as a function of matrix pore size and likewise showed complete inhibition of invasion in 50 mg/mL GelMA (Fig. 3.2F). These invasion trends strongly suggest that the matrix pore size is an important determinant of the spheroid invasion capacity. Compared to pore size, the matrix storage modulus appeared to have less predictive value of the amount of invasion, as a higher storage modulus (30 mg/mL GelMA < 2.4 mg/mL collagen < 50 mg/mL GelMA < 8 mg/mL collagen) did not correlate with invasion capacity for either cell line. It is also interesting to note that the GelMA (50 mg/mL) gel had a rather low storage modulus of just $G' = 200Pa$, yet showed complete inhibition of invasion for both cancer cell types.

INCREASED MATRIX CONFINEMENT DELAYS THE ONSET OF CELL INVASION

The invasion time curves clearly showed a delay time before measurable spheroid invasion occurred, followed by a steady increase of normalized spheroid radius (Fig. S3.6). To quantify this delay, we defined the onset time for invasion (t_{ons}) as the time point at which spheroids achieved a 10% increase in normalized radius, shown by the horizontal dashed lines in Fig. 3.2E,F. For MV3 spheroids in collagen, the delay time was shortest (t_{ons} = 3 hrs) in 2.4 mg/mL collagen, somewhat longer (t_{ons} = 5 hrs) in 8 mg/mL collagen, and even longer (t_{ons} = 11.5 hrs) in 30 mg/mL GelMA (inset of Fig.3.2E). For A549 spheroids, the onset times were always longer than for MV3 spheroids, but there was a similar trend of increasing onset time with decreasing pore size, from t_{ons} = 15 hrs for 2.4 mg/mL collagen, to t_{ons} = 24 hrs for 8 mg/mL collagen, and t_{ons} = 57 hrs for 30 mg/mL GelMA (inset of Fig.3.2F). In 50 mg/mL GelMA, neither the MV3 nor the A549 spheroids ever reached the threshold of a 10% increase in normalized spheroid radius. Based on these results, we conclude that the matrix porosity affects the invasion capacity of the spheroids by controlling the onset time of invasion.

MMP-MEDIATED MATRIX DEGRADATION PROMOTES SPHEROID INVASION

Since matrix porosity strongly impacted the invasion capacity of the spheroids, we hypothesized that MMP secretion might be an important determinant of the invasion capacity. To test this hypothesis, we decided to tune the ability of the cells to degrade the matrix by using treatments with TGF-β to promote MMP secretion [158, 159]. Bright field imaging showed that TGF-β strongly promoted invasion of MV3 spheroids in 8 mg/mL collagen (Fig. 3.3A, left). After 24 hrs, the spheroid was disintegrated, with a partially diminished spheroid core. We observed an even more drastic effect for MV3 spheroids in 2.4 mg/mL collagen, where TGF-β treatment resulted in spheroid disintegration already after 10 hrs and caused the spheroid core to sink to the bottom of the well (Fig. S3.7A). For MV3 spheroids in GelMA (30 mg/mL), we observed a less drastic effect of TGF-β addition (Fig. 3.3A, right). After 24 hrs, the spheroid core did not disintegrate, but we did observe invasion and the presence of individual disseminated cells. For A549 spheroids, we observed qualitatively similar effects of TGF-β treatment. In 2.4 mg/mL collagen, spheroid invasion now was already substantial after 24 hrs, with a completely disintegrated spheroid core that sunk to the bottom of the well (Fig. S3.7B). In denser (8 mg/mL) collagen and in GelMA (30 mg/mL), the A549 spheroids displayed protrusions into the matrix but without any individual cell dissemination (Fig.3.3B). For both cell

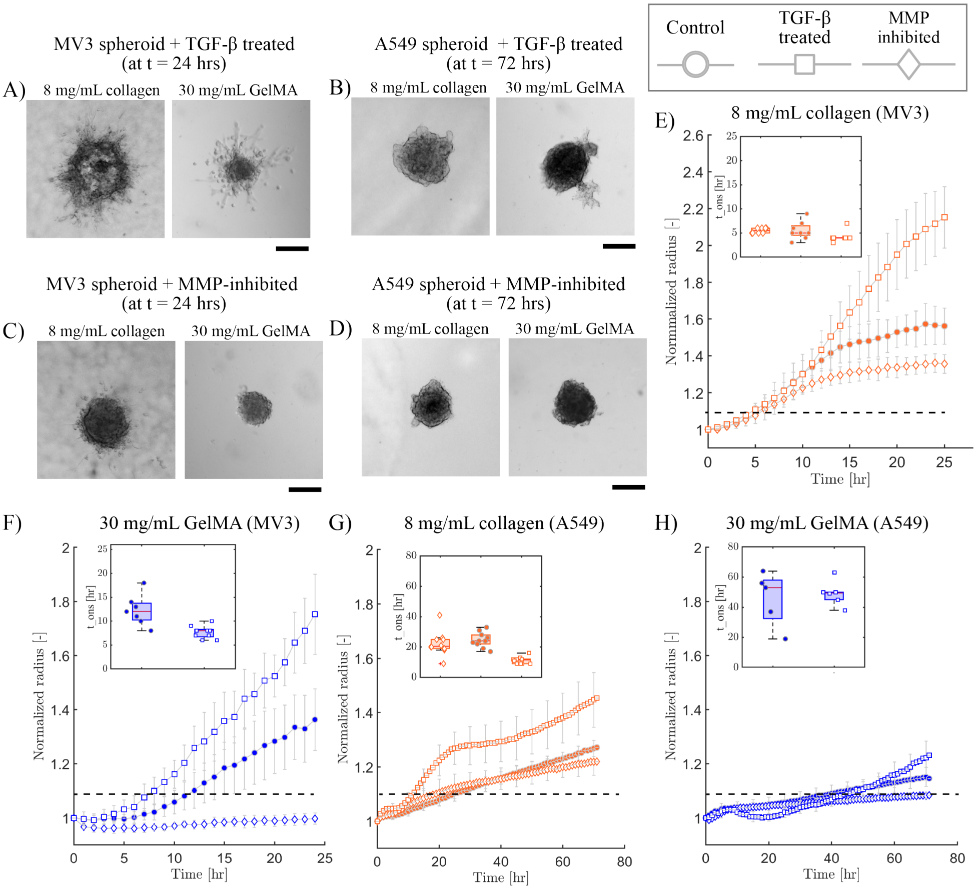

Figure 3.3: Spheroid invasion in different matrices in the presence of either TGF-β or the broad-spectrum MMP-inhibitor Batimastat. Bright field images of spheroids after invasion (24 hrs for MV3 spheroids, 72 hrs for A549 spheroids) for TGF-β-treated A) MV3 spheroids and B) A549 spheroids, and Batimastat-treated C) MV3 spheroids and D) A549 spheroids. In all cases, data are shown for spheroids in 8 mg/mL collagen (left) and in 30 mg/mL GelMA (right). Scale bars are 200 µm. Time evolution of normalized effective circular radius of the spheroids for E) MV3 spheroids in collagen (8 mg/mL), F) MV3 spheroids in GelMA (30 mg/mL), G) A549 spheroids in collagen (8 mg/mL) and H) A549 spheroids in GelMA (30 mg/mL). Horizontal black dashed lines indicate the onset time for invasion, defined as the time where the normalized radius reaches a value of 1.1. Data are averages with standard deviations of $N = 5-10$ spheroids in 2 independent experiments. Insets: invasion onset times (t_{ons}).

types, TGF-β treatment was ineffective to produce invasion in 50 mg/mL GelMA hydrogels (Fig. S3.8). These findings are consistent with our hypothesis that MMP-mediated degradation can promote spheroid invasion in dense matrices, but only up to a point.

Conversely, to test the effect of reduced MMP-mediated matrix remodelling, we repeated the spheroid invasion assays in the presence of the broad-spectrum MMP-inhibitor Batimastat [160, 161]. Bright field imaging showed a subtle effect on MV3 spheroids in

8 mg/mL collagen, where MMP-inhibitor treatment resulted in shorter cellular protrusions and fewer disseminated individual cells as compared to control conditions (Fig. 3.3C left). A similar behavior was seen for MV3 spheroids in 2.4 mg/mL collagen (see Fig. S3.7A). The effect of the MMP-inhibitor was more pronounced for MV3 spheroids in GelMA (30 mg/ml), where invasion was completely inhibited over the 24 hrs time window of observation (Fig. 3.3C right). For the A549 spheroids, MMP-inhibitor treatment completely suppressed spheroid protrusions and cell dissemination, both in collagen hydrogels (Fig. 3.3D left and Fig. S3.7B) and in GelMA hydrogels (Fig. 3.3D right).

To quantify the observed effects of TGF-β and MMP-inhibitor treatments on invasion, we again measured the normalized spheroid radii as a function of time. Compared to control conditions, TGF-β treatment increased invasion of MV3 spheroids, as quantified by the final spheroid size, by 38% in collagen (8 mg/mL) and by 29% in GelMA (30 mg/mL) (Fig. 3.3E). In 2.4 mg/mL collagen, we observed a 20% increase in final spheroid size compared to control conditions, but we note that in this case we only quantified invasion up to 14 hrs since the TGF-β treatment caused spheroid disintegration and sedimentation (Fig. S3.7C). By contrast, MMP-inhibition reduced invasion of MV3 spheroids as quantified by the final spheroid size, by 15% in 8 mg/mL collagen, 36% in 30 mg/mL GelMA, and 34% in 2.4 mg/mL collagen (Fig. S3.7C). The effects of the drugs were similar for A549 spheroids. TGF-β treatment increased invasion (after 72 hrs) by 14% in 8 mg/mL collagen (Fig. 3.3G) and by 10% in 30 mg/mL GelMA (Fig. 3.3H) compared to control conditions. By contrast, MMP-inhibition reduced invasion by 4% in 8 mg/mL collagen, 7% in 30 mg/mL GelMA (Fig. 3.3G, H), and 38% in 2.4 mg/mL collagen (Fig. S3.7D). These findings show that MMP-mediated degradation promotes spheroid invasion in dense matrices (for both cell types) and that it is absolutely required for invasion in dense GelMA gels that present pores smaller than the cell size.

MMP ACTIVITY AFFECTS THE INVASION ONSET TIME MORE STRONGLY IN GELMA THAN IN COLLAGEN

Since we found that confinement influences invasion by delaying the onset time, we tested whether the TGF-β and MMP-inhibitor treatments change t_{ons}. For MV3 spheroids in 8 mg/mL collagen, we observed a trend of reduced onset time with TGF-β treatment (t_{ons} = 4 hrs) and increased onset time with MMP inhibition (t_{ons} = 5.5 hrs) compared to the control condition (t_{ons} = 5 hrs), but the differences were not statistically significant (inset of Fig. 3.3E). For MV3 spheroids in 2.4 mg/mL collagen, we similarly observed a slight increase in onset time (t_{ons} = 3 hrs) with MMP inhibition compared to control and TGF-β treated spheroids (both t_{ons} = 2 hrs) (insets of Fig. S3.7C, D). For MV3 spheroids in 30 mg/mL GelMA, TGF-β treatment significantly reduced the onset time (t_{ons} = 8 hrs) compared to control conditions (t_{ons} = 11.5 hrs), while MMP-inhibition resulted in complete inhibition of invasion (inset of Fig. 3.3F). Thus, MV3 spheroid invasion into this dense matrix was dependent upon MMP-mediated degradation. In 50 mg/mL GelMA the MV3 spheroids never invaded, even when TGF-β was added to upregulate MMP expression (Fig. S3.8C).

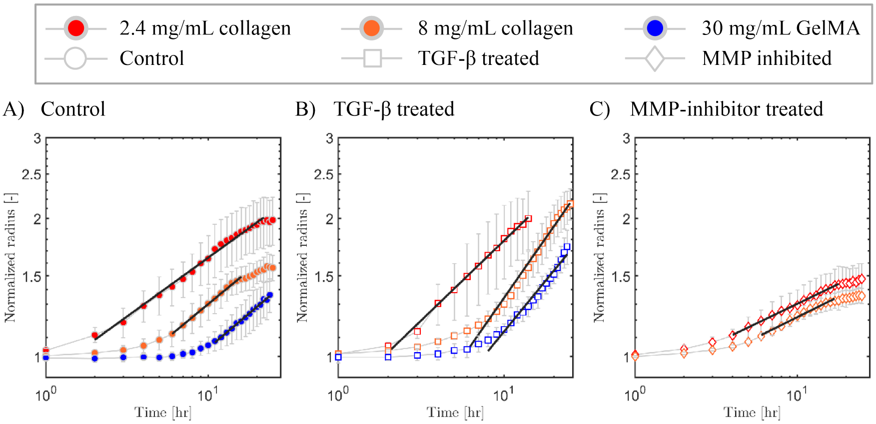

Figure 3.4: Expansion rates of MV3 spheroids. We determined the expansion rates by fitting the increase in normalized spheroid radius with time (symbols) to a power law (black lines) over the indicated temporal range. We compare MV3 spheroid invasion behavior under A) control conditions with B) TGF-β treatment and C) MMP-inhibitor treatment. In each case, data are shown for different matrix compositions (see legend on top). Note that in panel C, we did not include MV3 spheroids in 30 mg/mL GelMA since there was no measurable invasion. Data are averages with standard deviation of $N = 4-10$ spheroids for each condition performed in 2 independent experiments.

For A549 spheroids in 8 mg/mL collagen, we observed a stronger effect of TGF-β treatment on the invasion onset time ($t_{ons} = 11.5$ hrs) compared to control conditions ($t_{ons} = 24$ hrs) than for MV3 spheroids (inset of Fig. 3.3G). However, MMP-inhibition did not significantly change the onset time ($t_{ons} = 21$ hrs). In 2.4 mg/mL collagen, MMP-inhibition did have a major influence on the onset time, increasing it from $t_{ons} = 5$ hrs to $t_{ons} = 30$ hrs (Fig. S3.7D). For A549 spheroids in 30 mg/mL GelMA, we did not see a significant difference between the onset time with TGF-β ($t_{ons} = 53$ hrs) versus control conditions ($t_{ons} = 47$ hrs), but MMP-inhibition completely suppressed invasion (inset of Fig. 3.3H). This finding again shows that invasion into the dense GelMA networks requires MMP-mediated remodelling. In 50 mg/mL GelMA, TGF-β-treatment caused a slight (2%) increase in final normalized spheroid radius compared to control and MMP-inhibited spheroids (Fig. S3.8D) and a small reduction of the onset time ($t_{ons} = 57$ hrs) compared to control and MMP-inhibited conditions ($t_{ons} = 67.5$ hrs and 68 hrs, respectively, inset of Fig. S3.8D).

MMP-MEDIATED REMODELLING IMPACTS SPHEROID EXPANSION RATES

The TGF-β and MMP-inhibitor treatments strongly affected the final spheroid radii yet only minimally affected the invasion onset time, particularly in collagen. To understand this discrepancy, we analyzed the rate of expansion of the spheroids after the onset of invasion. We determined the expansion rates as the power-law slopes of the normalized radius versus time curves. Note that we did not perform any expansion rate analysis for MV3 and A549 spheroids in 50 mg/mL GelMA, since invasion was negligible under these conditions. For MV3 spheroids in collagen, the spheroid radius reached a plateau value around t = 20 hrs (Fig. 3.4), likely due to dissociation of cells from the spheroid that are not included in the normalized spheroid radius (Fig. S3.9). We therefore determined the expansion rate over an intermediate time range between the onset time and the time where the normalized radius saturated (Fig. S3.6). For A549 spheroids, the equivalent circular radius showed a steady increase until 72 hrs since there was little to no dissociation of cells, so we calculated the expansion rate from the onset of invasion till the end time-point (Fig. S3.10). The spheroid expansion rates measured under all the different conditions are summarized in Table 3.1.

The expansion rate of the MV3 spheroids was enhanced by TGF-β treatment (Fig. 3.4B) and reduced by MMP-inhibition (Fig. 3.4C) as compared to control conditions (Fig. 3.4A). The expansion rate of the A549 spheroids was similarly impacted by TGF-β and MMP-inhibitor treatments. Strikingly, for both cell types, the spheroid expansion rate in control conditions was independent of matrix composition, showing comparable values in collagen (2.4 mg/mL and 8 mg/mL) and in GelMA (30 mg/mL). The expansion rate for MV3 spheroids was about two-fold higher than for A549 spheroids, as expected based on their more mesenchymal-like character. Upon TGF-β treatment, the spheroid expansion rates significantly increased for both cell types, by about 1.5-fold for MV3 spheroids and 2-fold for A549 spheroids. The relative increase for MV3 spheroids was highest in 8 mg/mL collagen, while for A549 spheroids it was highest in 2.4 mg/mL collagen, showing a cell type-dependent factor. By contrast, MMP-inhibition caused a 1.7-fold reduction of the spheroid expansion rates for both A549 and MV3 spheroids in both collagen matrices (2.4 mg/mL and 8 mg/mL). In GelMA (30 mg/mL), there was no detectable invasion at all in MMP-inhibited conditions. Altogether, this analysis demonstrates that the expansion rate of the spheroids is strongly dependent on MMP-mediated matrix remodelling for both cell types. In collagen hydrogels, MMP-mediated matrix remodeling speeds up invasion but is not a prerequisite. However, in GelMA hydrogels, MMP-mediated matrix degradation is a prerequisite for invasion.

TGF-β AND MMP INHIBITOR TREATMENTS AFFECT EXPRESSION OF EMT MARKERS

The MV3 and A549 spheroids showed a similar sensitivity to MMP inhibitors, but a slightly different sensitivity to TGF-β treatment. The response to TGF-β likely is a combined effect from multiple upregulated cellular processes besides enhanced MMP expression. To test the effects of the TGF-β as well as MMP inhibitor treatments on these phenotypic changes, we used Western blot analysis to measure the levels of MMPs and EMT marker proteins, specifically vimentin as a mesenchymal marker and E-cadherin as an epithelial marker. For both cell lines, TGF-β treatment resulted in significantly upregulated levels of MMP1 (Fig. 3.5A, fold changes ~3) and MMP2 (Fig. 3.5B, fold changes ~4 and ~3) compared to the control samples. The TGF-β increased MMP2 much more than MMP1, which is consistent with a recent study showing that in mouse models of melanoma and lung cancer, TGF-β-induced Smad3 upregulation acts as a transcriptional activator for MMP2[162]. At the same time, TGF-β treatment increased vimentin expression (Fig. 3.5C, fold change of ~1.3) and reduced E-cadherin expression (Fig. 3.5D, fold change

MV3 spheroid expansion rates			
	2.4 mg/mL collagen	**8 mg/mL collagen**	**30 mg/mL GelMA**
Control	0.26 [0.24 – 0.27]	0.29 [0.28 – 0.31]	0.29 [0.28 – 0.31]
TGF-β treated	0.34 [0.33 – 0.36]	0.51 [0.49 – 0.55]	0.44 [0.40 – 0.48]
MMP-inhibited	0.17 [0.16 – 0.18]	0.17 [0.16 – 0.19]	NA
A549 spheroid expansion rates			
Control	0.15 [0.14 – 0.16]	0.14 [0.13 – 0.14]	0.1 [0.1 – 0.2]
TGF-β treated	0.37 [0.35 – 0.39]	0.19 [0.19 – 0.2]	0.23 [0.21 – 0.25]
MMP-inhibited	0.07 [0.07 – 0.08]	0.08 [0.07 – 0.08]	NA

Table 3.1: Expansion rates quantified as power law slope values (unit: hrs^{-1}) obtained from normalized spheroid radius [-] versus time (hrs) curves for control, TGF-β-treated and MMP-inhibited MV3 and A549 spheroids in different hydrogel compositions. The table represents the average slope value for spheroids in collagen (2.4 and 8 mg/mL) and GelMA (30 mg/mL) with upper and lower limit of error (in square brackets). NA (not applicable) means no slope analysis was performed since no invasion was observed (MMP-inhibited MV3 and A549 spheroids in 30 mg/mL GelMA).

of ~0.4) in A549 cells, confirming that TGF-β treatment induces an EMT switch in these epithelial-like cells. For MV3 cells, TGF-β treatment did not affect vimentin expression (Fig. 3.5C) nor E-cadherin expression (Fig. 3.5D), confirming that these cells are intrinsically already mesenchymal-like and therefore less affected by TGF-β treatment than the A549 cells. The mechanism of action of TGF-β is through activation of the SMAD pathway [139]. To test activation of this pathway and its intrinsic activity in the two cell lines, we analyzed phosphorylated SMAD2 (pSMAD2) levels in response to 1 hr TGF-β treatment by Western blot analysis. We observed a clear upregulation of pSMAD2 in response to TGF-β treatment in both cell lines, while the SMAD2 level remained constant (see Fig. S3.13). This confirms that TGF-β treatment activated the SMAD pathway and that the intrinsic activity of the SMAD pathway in both cell lines was at a similar level that could be upregulated by TGF-β.

Interestingly, the MMP-inhibitor also caused changes in protein expression in both cell lines. MMP inhibition reduced the expression levels of MMP1 and MMP2 (Fig. 3.5A,B) and decreased vimentin expression levels (Fig. 3.5C) in A549 cells compared to control conditions. However, MMP-inhibited MV3 cells showed no significant change in MMP2 and vimentin protein expression and only showed significant difference in MMP1 protein expression. MMP inhibition also reduced E-cadherin expression for A549 cells (Fig. 3.5D), with a fold change of ~0.3 compared to control. Consistent with the reduction in E-cadherin levels in A549 cells by MMP inhibitor and TGF-β treatment, bright-field imaging showed that the drug-treated cells were more individual with less contact with neighboring cells compared to control conditions (see Fig. S3.14). In addition, we confirmed that these effects were related to EMT by testing for the expression levels of EMT

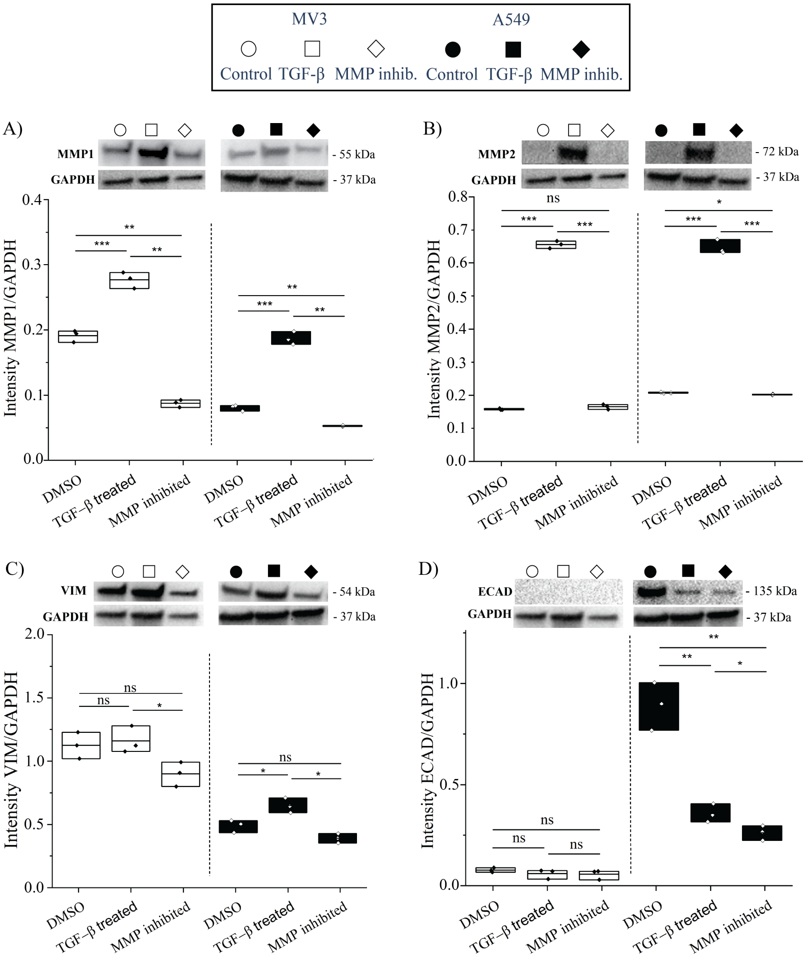

Figure 3.5: Western blot analysis of EMT marker protein expression in MV3 and A549 cells, showing the impact of TGF-β stimulation and MMP inhibition. Protein levels normalized by the GAPDH levels for MV3 cells (white, left side) and A549 cells (black, right side) treated with DMSO (control conditions), TGF-β, or the broad spectrum MMP inhibitor Batimastat, for A) MMP1, B) MMP2, C), vimentin (VIM), and D) E-cadherin (ECAD). P-value results from t-tests are indicated by: (ns) = p≥0.05, (*) = p<0.05, (**) = p<0.01, (***) = p<0.001. Each condition depicts one biological sample (*n* = 1) with three data points based on different background subtractions. The other three biological replicates (total of *n* = 4) showed similar trends (Fig. S3.11A and Fig. S3.12A,B). We emphasize that the compared band intensities are always from the same blots, which are shown in their entirety in Fig. S3.11C,D and Fig. S3.12B.

transcription factors SNAIL and ZEB1 in response to TGF-β and MMP inhibition (Fig. S3.15). In summary, the Western blot data confirm that TGF-β and MMP-inhibitor treatments alter MMP-levels in opposite directions and show that both treatments also impact EMT processes, especially in A549 cells.

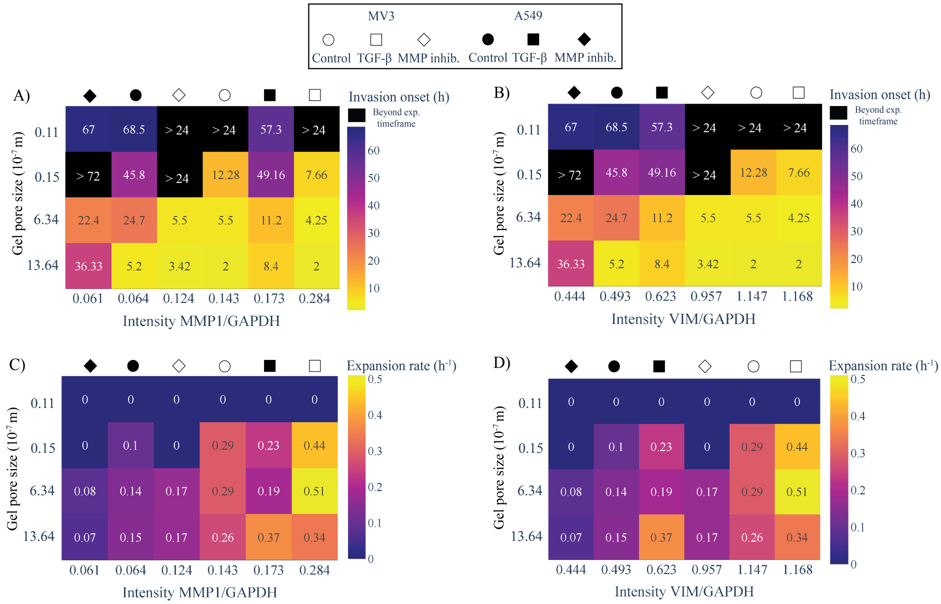

A) Invasion onset (h)

Gel pore size (10^{-7} m)	0.061 ◆	0.064 ●	0.124 ◇	0.143 ○	0.173 ■	0.284 □
0.11	67	68.5	> 24	> 24	57.3	> 24
0.15	> 72	45.8	> 24	12.28	49.16	7.66
6.34	22.4	24.7	5.5	5.5	11.2	4.25
13.64	36.33	5.2	3.42	2	8.4	2

B) Invasion onset (h)

Gel pore size (10^{-7} m)	0.444 ◆	0.493 ●	0.623 ■	0.957 ◇	1.147 ○	1.168 □
0.11	67	68.5	57.3	> 24	> 24	> 24
0.15	> 72	45.8	49.16	> 24	12.28	7.66
6.34	22.4	24.7	11.2	5.5	5.5	4.25
13.64	36.33	5.2	8.4	3.42	2	2

C) Expansion rate (h^{-1})

Gel pore size (10^{-7} m)	0.061 ◆	0.064 ●	0.124 ◇	0.143 ○	0.173 ■	0.284 □
0.11	0	0	0	0	0	0
0.15	0	0.1	0	0.29	0.23	0.44
6.34	0.08	0.14	0.17	0.29	0.19	0.51
13.64	0.07	0.15	0.17	0.26	0.37	0.34

D) Expansion rate (h^{-1})

Gel pore size (10^{-7} m)	0.444 ◆	0.493 ●	0.623 ■	0.957 ◇	1.147 ○	1.168 □
0.11	0	0	0	0	0	0
0.15	0	0.1	0.23	0	0.29	0.44
6.34	0.08	0.14	0.19	0.17	0.29	0.51
13.64	0.07	0.15	0.37	0.17	0.26	0.34

Figure 3.6: Heat map representations showing the correlation of invasion onset times and spheroid expansion rates with MMP1 and vimentin protein expression levels for MV3 and A549 spheroids. A) Dependence of the invasion onset time (indicated by the number (in units of hrs) in each square and the color code, see color bar on the right) on hydrogel pore size (y-axis) and expression level of MMP1 (x-axis). B) Corresponding heat map with the expression level of vimentin (x-axis). Note that spheroids that did not invade during the time frame of the assay are shown in black. C) Dependence of the spheroid expansion rate (indicated by the number (in units of hrs^{-1}) in each square and the color code, see color bar on the right) on hydrogel pore size (y-axis) and expression level of MMP1 (x-axis). D) Corresponding heat map with the expression level of vimentin on the x-axis. Data for MV3 spheroids (white) symbols above the heat maps) and A549 spheroids (black symbols) and for different treatment conditions (see symbol shapes) were pooled. Protein expression levels were normalized by the GAPDH levels.

INVASION ONSET AND SPHEROID EXPANSION RATE ARE CORRELATED WITH MATRIX POROSITY AND LEVELS OF EMT MARKERS

The quantitative analysis of spheroid invasion showed that matrix porosity is a major determinant of the onset of cancer cell invasion. At the same time, the Western blot analysis suggests that the EMT status and MMP expression levels of the cells are also major determinants of invasion. MV3 cells were consistently more invasive than A549 cells, consistent with their higher basal levels of MMPs and the mesenchymal marker protein vimentin. TGF-β treatment made both MV3 and A549 cells more invasive, by upregulating MMP and vimentin expression while downregulating E-cadherin expression. Conversely, MMP inhibition made the cells less invasive by blocking MMP activity while also changing EMT marker expression. To study the interplay between matrix porosity and cell invasiveness, we prepared heat map representations to correlate the invasion onset times and the spheroid expansion rates with the cellular levels of EMT markers (x-axis) and with the hydrogel pore size (y-axis). Because the heat maps combine data retrieved from the 3D spheroid invasion assays (invasion onset times, spheroid expansion rates and hydrogel pore size) with Western Blot measurements from 2D cell cultures, we checked that the treatments had a consistent effect on the cellular levels of EMT-markers in the 3D spheroid invasion assays. We validated that the treatments indeed had similar effects on E-cadherin (Fig. S3.16) and vimentin (Fig. S3.17) expression levels. The color code in the heat maps encodes the invasion onset time (Fig. 3.6A,B) and the spheroid expansion rate (Fig. 3.6C,D). Note that we combined the data for A549 and MV3 cells (distinguishable by symbol color) and for DMSO (control), TGF-β and MMP inhibitor treatments (distinguishable by symbol shape).

The heat maps reveal that the invasion onset time is mainly determined by matrix confinement, with a progressively longer delay as the pore size becomes smaller (Fig. 3.6A,B). In the densest 50 mg/mL GelMA hydrogels, spheroid invasion is even fully blocked under most conditions (black squares). Higher vimentin levels were correlated with shorter invasion onset times (Fig. 3.6B). By contrast, we did not observe any clear correlation with invasion onset time for the other tested EMT markers, MMP1 (Fig. 3.6A), MMP2 (Fig. S3.18A) and E-cadherin (Fig. S3.18B).

The heat maps further reveal that the spheroid expansion rate was rather insensitive to matrix confinement, except at the smallest pore sizes (50 mg/mL GelMA), where spheroid expansion was blocked (Fig. 3.6C,D). By contrast, the spheroid expansion rate strongly increased with increasing expression levels of MMP1 enzymes (Fig. 3.6C). The expansion rates did not show any clear correlation with the levels of vimentin (Fig. 3.6D), MMP2 (Fig. S3.18C) or E-cadherin (Fig. S3.18D). Altogether, the heat maps therefore reveal an intriguing interplay of cellular properties and matrix porosity in determining the onset of invasion and the spheroid expansion rate.

3.4. DISCUSSION

Here we studied how matrix porosity and cell motility parameters, specifically EMT status, together determine tumor invasion by quantitative analysis of 3D spheroid invasion in collagen-based hydrogels. We found that matrix confinement and cell motility have distinct effects on the initiation of invasion and the subsequent rate of spheroid expansion. Matrix confinement and the vimentin expression level of the cells were the main determinants of the onset time of invasion. Larger pores and higher vimentin expression levels promoted the onset of spheroid invasion. By contrast, the spheroid expansion rates were rather insensitive to changes in matrix confinement except in dense GelMA gels, which completely blocked invasion. The insensitivity of the expansion rate to pore size could potentially be due to cell-mediated matrix remodeling, which may facilitate cell invasion by providing empty space or guiding collagen bundles. The spheroid expansion rate did depend on the MMP1 expression level, suggesting that MMP-mediated matrix degradation aids cell migration and/or cell survival into the matrix. Recent studies have explored the role of other tumor microenvironment components, for instance showing how fibroblasts in a 3D bio-printed breast cancer model upregulate proteolytic degradation by tumor cells [163]. Additionally, signaling pathways originating from mechanotransduction events revealed a distinct 3D EMT gene signature characterized by extracellular matrix remodelling in 3D culture using collagen- and GelMA-based hydrogels [164]. It will be interesting in future studies to analyse the roles of different matrix remodelling mechanisms, including matrix degradation, matrix deposition, matrix crosslinking, and active remodeling by actomyosin-based traction forces. Although matrix stiffness is often described as a factor that influences cell invasion [142, 165], the invasion measurements in our assays did not demonstrate any clear dependence on the elastic shear modulus of the hydrogels. However, in this work we did not research stiffness as an independent variable, which limits our understanding of its role. Therefore, follow-up research is needed that also examines local mechanics, as spheroids and invading single cells are known to generate traction forces onto matrices that induce stiffening, while degradation can soften the ECM [166]. Viscoelasticity of matrices is also known to affect collective strand formation and EMT processes [167]. In our hydrogel characterization, measurements of the viscoelasticity of the matrices showed predominantly solid-like behavior ($G' > G''$) of our hydrogels.

Previous studies of spheroid invasion for MCF-10A and MDA-MB-231 breast cancer cells showed that spheroids show different states of unjamming that depend on cell motility and matrix density [112, 122]. Jammed spheroids do not invade and are considered to be in a solid-like state. Spheroids can unjam to a fluid-like state characterized by collectively invading cell strands or to a gas-like state characterized by dissociation of cells that then migrate individually [121]. In addition to these clearly distinct phases, spheroids can also exist in transitional or in-between phases [168, 122]. To test whether this unjamming framework also applies to MV3 and A549 spheroids, we classified the spheroids as solid-like, fluid-like or gas-like based on the morphological appearance of the spheroids at the end point of the experiments ($t = 24$ hrs for MV3 spheroids, $t = 72$ hrs for A549 spheroids). Since fluid-like spheroid states are characterized by multicellular strands protruding into the matrix, we developed an image analysis method to detect multicellular protrusions and measure their length (Fig. S3.19). We classified spheroids as fluid-like when the average protrusion length was above 25 µm. We chose this cut-off value since spheroids in their initial state at $t = 0$ occasionally showed apparent protrusions up to this length. Since gas-like spheroid states are characterized by dissociated individually migrating cells, we furthermore measured the number of dissociated cells for all spheroids. We classified spheroids as gas-like when the individual cell count was above 10. Spheroids with protrusion lengths below 25 µm and no disseminated cells were classified as solid-like. We found that MV3 spheroids sometimes showed co-existence between a liquid-like phase (with long multicellular protrusions) and a gas-like phase (with many dissociated cells), especially in collagen (8 mg/mL) and in GelMA (30 mg/mL) (Fig. S3.20) in control condition. However, when MV3 spheroids were treated with MMP-inhibitor in collagen (8 mg/mL) and GelMA (30 mg/mL), spheroids only existed in a liquid-like phase (cell count below 10) (Fig. S3.21). Similar analysis was performed for A549 spheroids in control and treated (TGF-β and MMP-inhibitor) conditions to determine the different unjamming states in collagen and GelMA hydrogels (Fig. S3.22). For future research, it would be interesting to complement this analysis with high-resolution 3D imaging of the shapes of the cells (and cell nuclei) within the spheroids, since these have been shown to correlate with (un)jamming [169].

We then constructed a phase diagram of the 3D spheroid invasion states in terms of the degree of matrix confinement (pore size) and the MMP1 expression level of the cells (Fig. 3.7). Spheroids in matrices with high confinement (small pores) and low cellular MMP1 levels showed solid-like behaviour (blue squares). With increasing MMP1 expression levels, spheroids in collagen (2.4 mg/mL and 8 mg/mL) and GelMA (30 mg/mL) unjammed, initially to a liquid-like state (red squares), and eventually to a gas-like state (yellow squares). Spheroids in GelMA (50 mg/mL) remained solid-like irrespective of the MMP1 expression level. The unjamming phase diagram is qualitatively very similar to earlier unjamming phase diagrams reported for breast cancer cells [112, 122]. However, instead of the 'cell motility' parameter used in earlier studies, we find that the MMP1 expression level is an important determinant of spheroid invasion. The MMP1 expression level depends on cell type (being higher in the mesenchymal-like MV3 cells than in the epithelial-like A549 cells). Additionally, it can be tuned in both cell types through TGF-β and MMP-inhibitor treatments, which change the levels of MMP1 and other EMT-markers (vimentin and E-cadherin). Because unjamming transitions and EMT both describe the behaviour of immotile multicellular structures that gain motility, the question has been raised in what way these two processes are related [170]. In epithelial monolayers, it was shown that unjamming transitions can operate without EMT [171]. Our findings suggest that in 3D tumoroid invasion, EMT is coupled to unjamming, because the transition to a more mesenchymal state enables cells to proteolytically degrade the matrix and thus reduce confinement. Compared to previous experimental studies of spheroid unjamming [112, 172], which used only collagen gels, we achieved stronger confinement by additionally using GelMA gels with nanometric pores. This allowed us to identify a new regime in the phase diagram, where cells that are in principle highly motile (with high MMP1 and vimentin levels) undergo a jamming transition and turn solid-like again. Moreover, MV3 cells under control and TGF-β-treated conditions in 30 mg/mL GelMA often showed amoeboid-like behaviour, characterized by cells migrating with a round morphology and blebbing (see Fig. 3.7, orange square). This behavior suggests the presence of a fourth (or transitional) spheroid phase, in which high matrix confinement pushes highly motile cells towards an amoeboid migration mode before jamming. This behaviour is consistent with described mesenchymal-to-amoeboid transitions of (cancer) cells in response to narrow microchannels [173, 174] and confining micropatterns [7]. Moreover, a recent study reported that human melanoma cells in dense microenvironments migrate via bleb-driven degradation of extracellular matrix components rather than by the conventional proteolytic degradation[175]. It will be interesting to further explore this tentative amoeboid-like migration phase for high confinement and high cell motility in more detail with high-resolution microscopy and carefully tuned GelMA concentrations just below and above 30 mg/mL.

Our data are suggestive that TGF-β stimulation may drive spheroid unjamming by upregulating the expression level of MMP1. However, we acknowledge that the TGF-β pathway has pleiotropic effects and controls many other cellular characteristics [176]. For in-

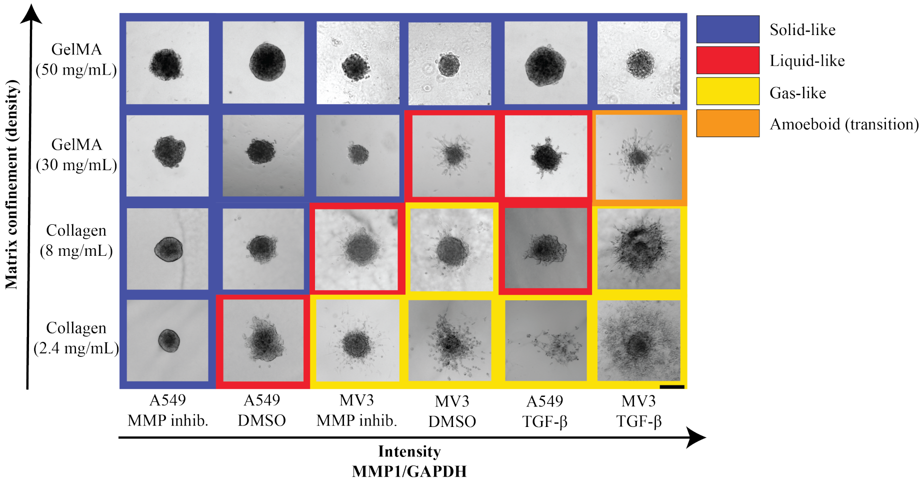

Figure 3.7: Phase diagram describing (un)jamming states of MV3 and A549 cell spheroids in terms of the degree of matrix confinement (which depends on matrix type and concentration) and MMP1 expression level (which depends on cell type and treatment condition). Images were ranked along the x-axis by the MMP1 expression level, as quantified by Western blot analysis. Spheroids were classified as gas-like (yellow squares) when more than 10 cells dissociated from the spheroid during the experimental time window, liquid-like (red squares) when the spheroids developed protrusions longer than 25 µm, and solid-like (blue squares) otherwise. Amoeboid behavior (transitional phase) is shown in orange square for MV3 spheroids in GelMA (30 mg/mL). Images are bright-field images taken at $t = 72$ hrs (A549) and $t = 24$ hrs (MV3). Scale bar is 200 µm

stance, TGF-β has been reported to affect cell-matrix adhesions by downregulating integrins [177] and enhance cellular traction forces during cell invasion [178, 179]. Confocal reflection microscopy images of MV3 spheroids in collagen (2.4 mg/mL) at the endpoint of invasion experiments ($t = 24$ hrs) indeed indicated that TGF-β treatment not only enhanced matrix degradation, but also activated cellular traction forces, as evidenced by densified and aligned collagen fibers (Fig. S3.23). We note that the collagen images also revealed that the MV3 spheroids exerted larger traction forces on the matrix than A549 spheroids, as indicated by radially oriented collagen fibers around the MV3 spheroids as opposed to more uniform collagen networks around A549 spheroids [180]. These differences in the mechanical cell-matrix interplay could also have impacted spheroid invasion, as tensile forces on collagen are known to influence the onset of invasion [181]. To test whether the effects of TGF-β treatments in our invasion assays were indeed driven by changes in MMPs, we performed invasion experiments with A549 spheroids embedded in GelMA (30 mg/mL) that were pretreated with Batimastat and subsequently treated with TGF-β (Fig. S3.24). Pretreatment with MMP-inhibition blocked invasion, which further supports our proposal that TGF-β upregulates invasion mainly through MMP upregulation. These findings are also consistent with other studies that have shown that MMP-inhibitor pretreatment leads to blockage of the TGF-β -induced invasion potential in breast cancer cells [159]. To our surprise, MMP inhibition in the epithelial-like A549 cells resulted in reduced E-cadherin levels compared to control conditions. Because E-cadherin levels can also be affected by compressive forces in 2D [182], we validated that the effects of the TGF-β and Batimastat treatments on E-cadherin levels were similar in the 3D spheroid invasion assays by analysing E-cadherin levels of 3D spheroid invasion assays with Western Blot (Fig. S3.16). The E-cadherin levels responded similarly to the treatments in 2D and 3D, showing that the observed effects were not due to compressive forces and/or cell-matrix interactions. MMPs, including MMP1 and MMP2, have been shown to induce EMT by regulating E-cadherin levels [183, 184, 185]. Several MMPs are associated with E-cadherin cleavage and the soluble E-cadherin extracellular domain that results from cleavage was found to promote cancer invasion by in turn increasing MMP production [184, 186]. MMP-mediated E-cadherin cleavage is also found downstream of TGF-β activation, providing a pathway for reduced E-cadherin levels in TGF-β-treated A549. However, the downregulation of E-cadherin levels in response to MMP inhibition was unexpected, and to the best of our knowledge not previously reported. We propose this effect could be an interesting direction for future research to further elucidate the mechanisms behind MMP inhibitors, which so far failed in the clinic for cancer treatments [184].

In this work, we did not distinguish between invasion by cell migration versus cell proliferation. Proliferation could play a role in setting the onset time for invasion, as it can increase spheroid packing densities and increase the active forces of cells that regulate solid-to-liquid transitions [187]. Furthermore, the initiation of invasion has been linked to solid tumor growth [188]. Tumor proliferation and invasion are interconnected processes and changes in proliferation could have impacted the normalized spheroid radius over time [189]. To improve our understanding of the contribution of proliferation in invasion, follow-up studies could measure proliferation rates or proliferation could be blocked by adding chemical agents or cell synchronization [190], although these agents might cause undesired effects on the cells such as replication stress or increased cell death [191].

While jamming-unjamming transitions have become a well-established framework to explain cancer invasion, the underlying biological mechanisms are poorly understood. Recent studies have revealed possible mechanisms that impact plasticity pathways. For instance, the ERK1/2 pathway triggers cell motility and results in invasive strands of collectively invading cells [120]. Also mechanosensitive pathway was identified whereby cellular confinement directly causes deformations of the cell nuclei accompanied by chromatin remodelling [192]. Here we showed evidence that EMT is also a mechanism involved in 3D unjamming transitions by regulating cell-matrix interplay. This is in line with earlier findings that reported EMT-independent unjamming transitions in 2D monolayers [171]. Our findings demonstrate that the vimentin expression level impacts the onset time of spheroid unjamming, while the MMP1 expression level impacts the subsequent spheroid expansion rate and associated unjamming transitions. Understanding the biological mechanisms behind unjamming transitions is beneficial for cancer patients, as unjamming is considered a predictor for distant metastasis [193].

3.5. ACKNOWLEDGEMENTS

I would like to thank Zaid Rahman for this collaboration, in particular performing together the great set of spheroid invasion assays in this project. Also thanks to Zaid Rahman and Ankur Bordoloi for the image analysis. I also want to thank Iain Muntz for his help on hydrogel rheology and the pore size measurements. Thanks to Peter ten Dijke for his expertise on Western Blotting and MMPs, and the shared reagents.

3.6. SUPPLEMENTARY INFORMATION

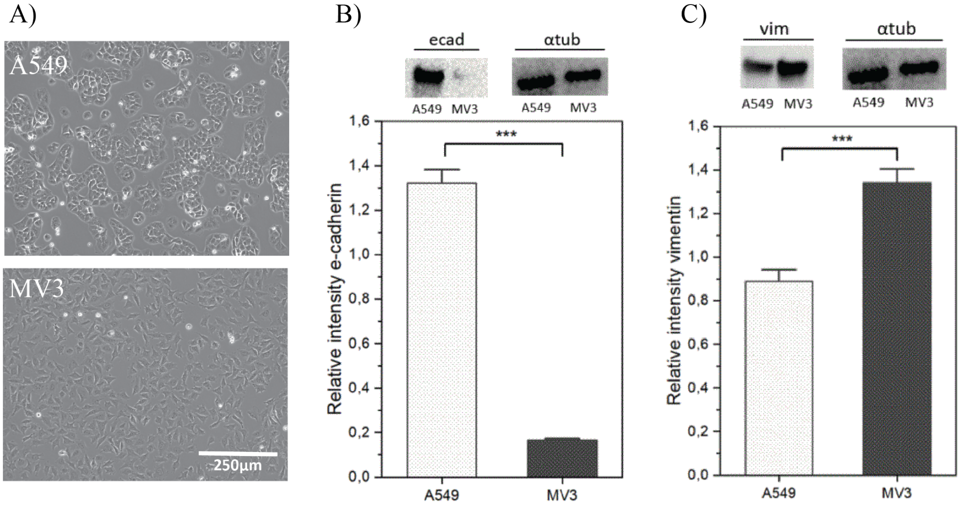

Figure S3.1: Cell morphology and Western Blot analysis for A549 and MV3 cancer cells. A) Bright-field images of the cells cultured on collagen-coated 6-well dishes. A549 cells (top panel) show clustering, which is a characteristic of cells expressing high levels of E-cadherin (epithelial marker). MV3 cells (bottom panel) show individual spindle-shaped cells with mesenchymal-like features. Scale bar is 250 µm. B) Western Blot analysis of A549 and MV3 cells for E-cadherin (ecad) expression levels, normalized to α-tubulin expression, showing that A549 cells are more epithelial-like than MV3 cells. C) Corresponding Western Blot analysis for vimentin expression levels, showing that MV3 cells express significantly more vimentin than A549 cells.P-value results from t-tests are indicated by: (ns) = p≥0.05, (*) = p<0.05, (**) = p<0.01, (***) = p<0.001.

Repeat	Average velocity	Hydraulic permeability (m^2)	Pore size (nm)
GelMA (30 mg/mL)			
1.	0.54	2.43×10^{-16}	15.58
2.	0.51	2.29×10^{-16}	15.13
3.	0.53	2.38×10^{-16}	15.42
GelMA (50 mg/mL)			
1.	0.28	1.26×10^{-16}	11.22
2.	0.32	1.44×10^{-16}	12.00
3.	0.26	1.17×10^{-16}	10.81

Table 3.1: Average pore size estimated from hydraulic permeability measurements for GelMA hydrogels with concentrations of 30 mg/mL (15.3 ± 0.18 nm) and 50 mg/mL (11.3 ± 0.5 nm). The permeability was determined from the average flow velocity of Rhodamine B dye measured in permeation experiments performed in a microfluidic chip at a pressure gradient of 20 mbar.

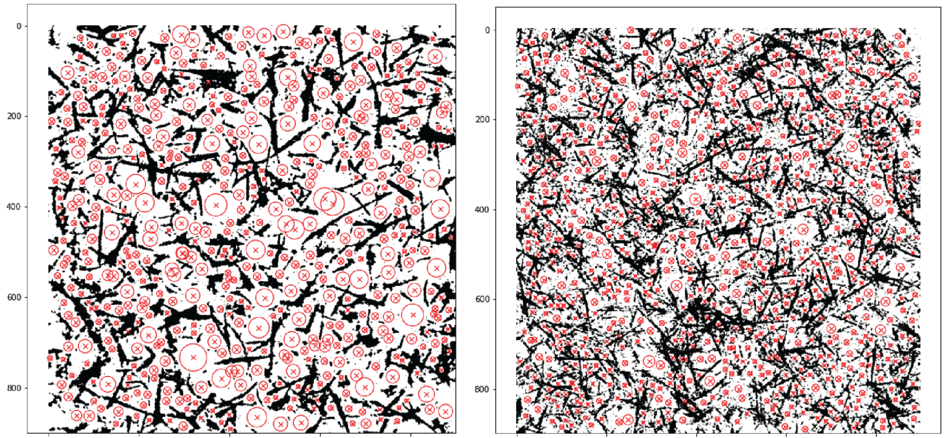

Collagen (2.4 mg/mL) Collagen (8 mg/mL)

Figure S3.2: Binarized confocal microscopy reflection images of collagen networks with concentrations of 2.4 mg/mL (left) and 8 mg/mL (right) with fitted bubbles (red circles), to determine the pore size distribution. The x- and y-axes indicate the length scale in pixels.

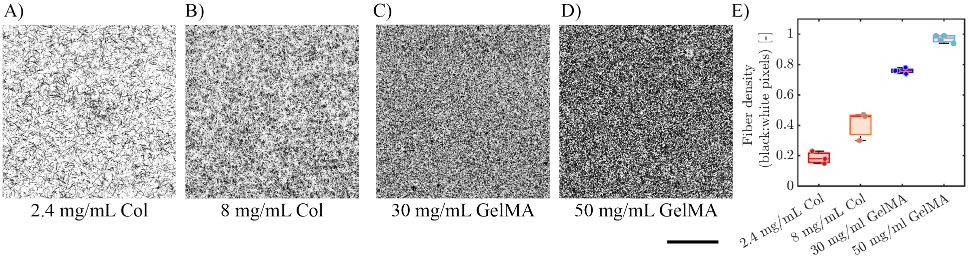

2.4 mg/mL Col 8 mg/mL Col 30 mg/mL GelMA 50 mg/mL GelMA

Figure S3.3: Hydrogel fiber density measurements based on confocal reflectance images. Binarized maximum intensity projections of confocal Z-stacks composed of 16 slices at 2 µm intervals for hydrogels of A) collagen (2.4 mg/mL), B) collagen (8 mg/mL), C) GelMA (30 mg/mL) and D) GelMA (50 mg/mL). E) Fiber density (black to white pixel ratio) measurements for hydrogels. Data are averages with standard deviations for 3 repeats. Scale bar is 25 µm.

A) MV3 spheroid in 8 mg/mL collagen

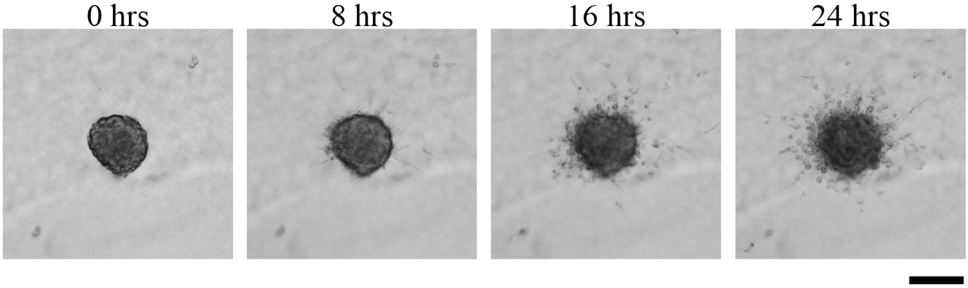

B) MV3 spheroid in 50 mg/mL GelMA

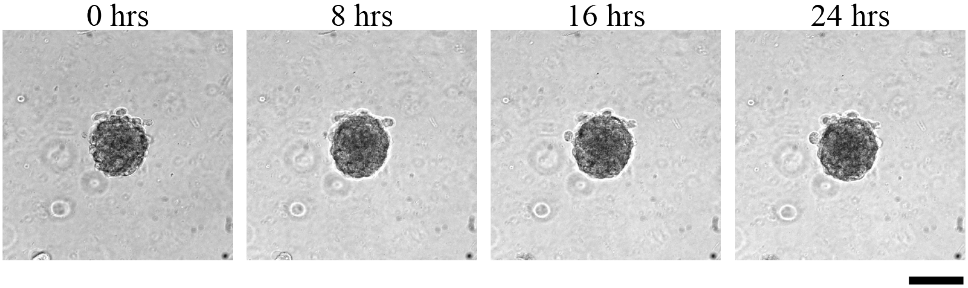

Figure S3.4: MV3 spheroid invasion in collagen and GelMA matrices. Bright-field images of MV3 spheroids at 8 hr time intervals in A) 8 mg/mL collagen and B) 50 mg/mL GelMA at t = 0, 8, 16 and 24 hrs. Scale bars are 200 µm. MV3 spheroids invaded into the collagen network, as seen from the spheroid protrusions and presence of disseminated single cells, but did not invade in the GelMA hydrogel.

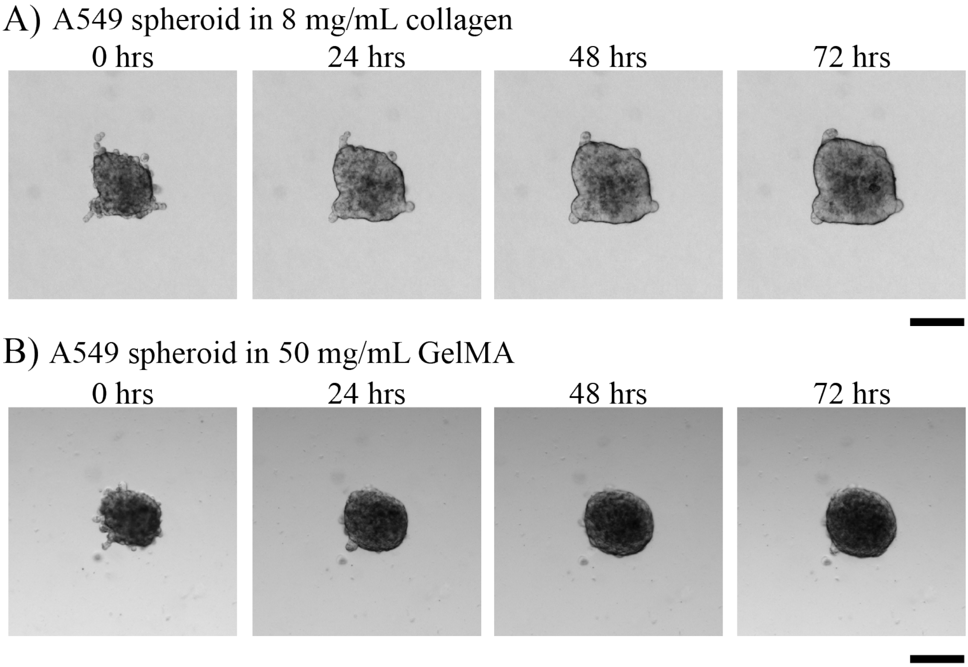

Figure S3.5: A549 spheroid invasion in collagen and GelMA matrices. Bright-field images of A549 spheroids at 24 hr time intervals in A) 8 mg/mL collagen and B) 50 mg/mL GelMA. Scale bars are 200 µm. The A549 spheroids had an irregular shape with occasional protrusions. Over time, the spheroid boundary remained rather smooth and the spheroids uniformly expanded in size without the formation of protrusions or dissociation of single cells.

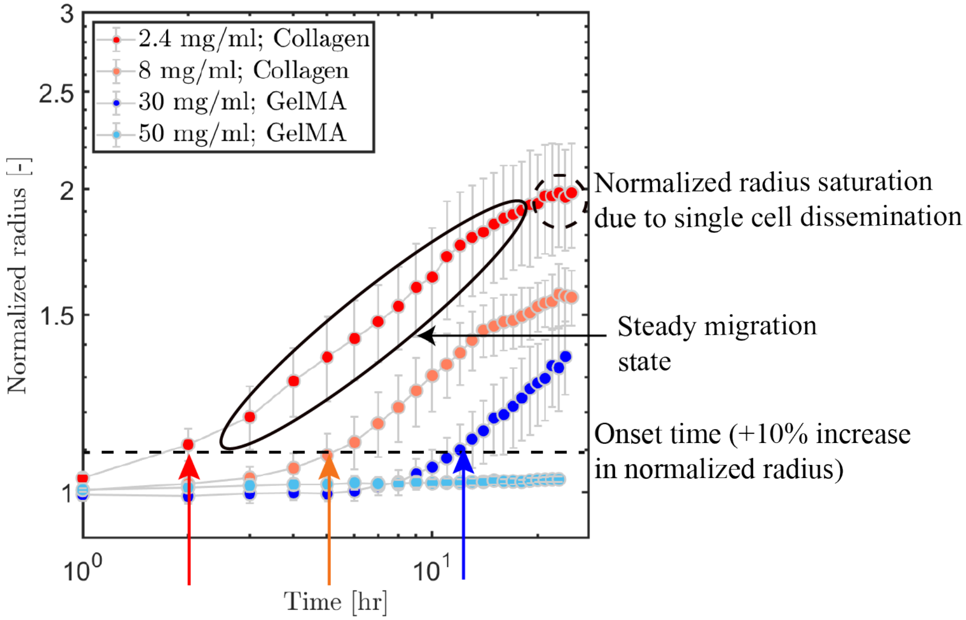

Figure S3.6: Definition of invasion onset time and spheroid expansion, illustrated for MV3 spheroids. The effective circular radius of MV3 spheroids normalized by its initial value is tracked as a function of time for spheroids in collagen and GelMA hydrogels (see legend). The invasion onset time is defined as the time point where the normalized radius reaches a value of 1.1 (indicated by the arrows and the horizontal dashed line). The expansion rate was defined as the power-law slope of the spheroid growth curves after the onset of invasion. Since the growth curves plateaued at long time due to the dissociation of cells from the spheroid (dashed circle), the curves were fitted within the time range enclosed within the solid ellipse. The maximum time for the fit range was taken as the time point where the difference in normalized spheroid radius became less than 0.01 between two successive time points.

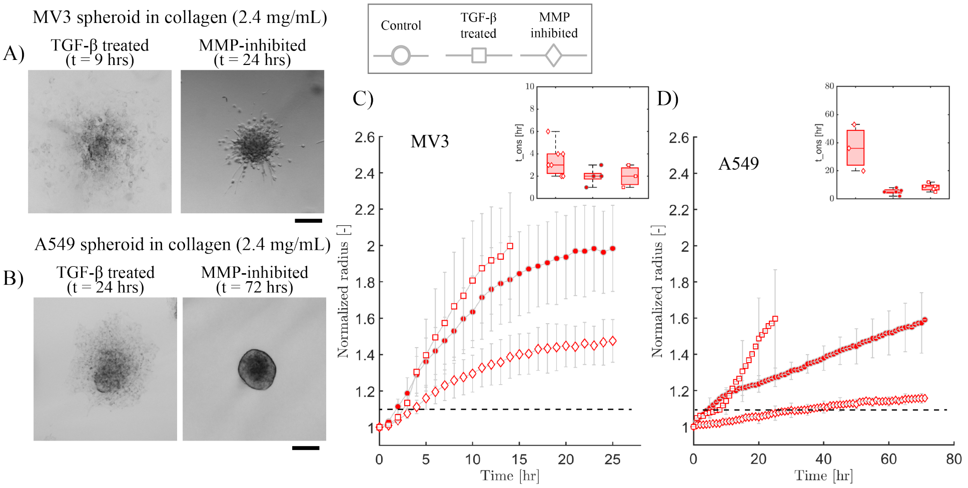

Figure S3.7: Effect of TGF-β and MMP-inhibitor treatments on spheroid invasion in collagen (2.4 mg/mL). A) Bright field images of MV3 spheroids treated with TGF-β (left, t = 9 hrs) and with MMP-inhibitor (right, t = 24 hrs). B) Bright field images of A549 spheroids treated with TGF-β (left, t = 24 hrs) and MMP-inhibitor (right, t = 72 hrs). Scale bars in A,B are 200 µm. C) Increase in spheroid radius with time for MV3 spheroids under control, TGF-β, and MMP inhibition conditions (see legend). D) Corresponding data for A549 spheroids. Horizontal dashed lines in C,D denote the threshold value for the normalized radius of 1.1 defined as the onset of invasion. Insets show the invasion onset times in control and treated conditions. Neither treatment affected the onset time of invasion much, except for MMP-inhibited A549 spheroids, where invasion was drastically delayed. Note that upon TGF-β treatment, the spheroid cores eventually disintegrated and sedimented to the bottom glass surface. In this condition we therefore only tracked invasion up to t = 14 hrs for MV3 spheroids and up to t = 24 hrs for A549 spheroids.

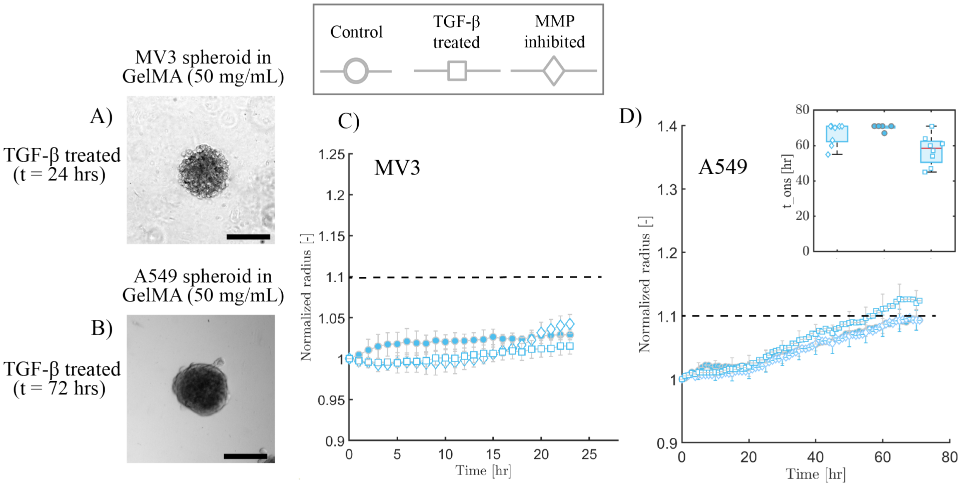

Figure S3.8: Effect of TGF-β and MMP-inhibitor treatments on spheroid invasion in GelMA (50 mg/mL). A) Bright field image of a MV3 spheroid treated with TGF-β at $t = 24$ hrs. B) Bright field image of an A549 spheroid treated with TGF-β at $t = 72$ hrs. Neither the MV3 nor the A549 spheroids showed protrusions or single cell dissemination, despite the TGF-β treatment. Scale bars in A, B are 200 µm. Increase in spheroid radius with time in control, TGF-β treated and MMP-inhibited conditions (see legend on top) for C) MV3 spheroids and D) A549 spheroids. Horizontal dashed lines in (C,D) denote the threshold value for the normalized radius of 1.1 defined as the onset of invasion. Inset in D): onset time of invasion for A549 spheroids. TGF-β treated A549 spheroids had a slightly lower onset time (at $t = 57$ hrs) compared to control and MMP-inhibited conditions (at $t = 68$ hrs). Note that we could not determine the onset of invasion for the MV3 spheroids over the 24 hrs experimental time frame.

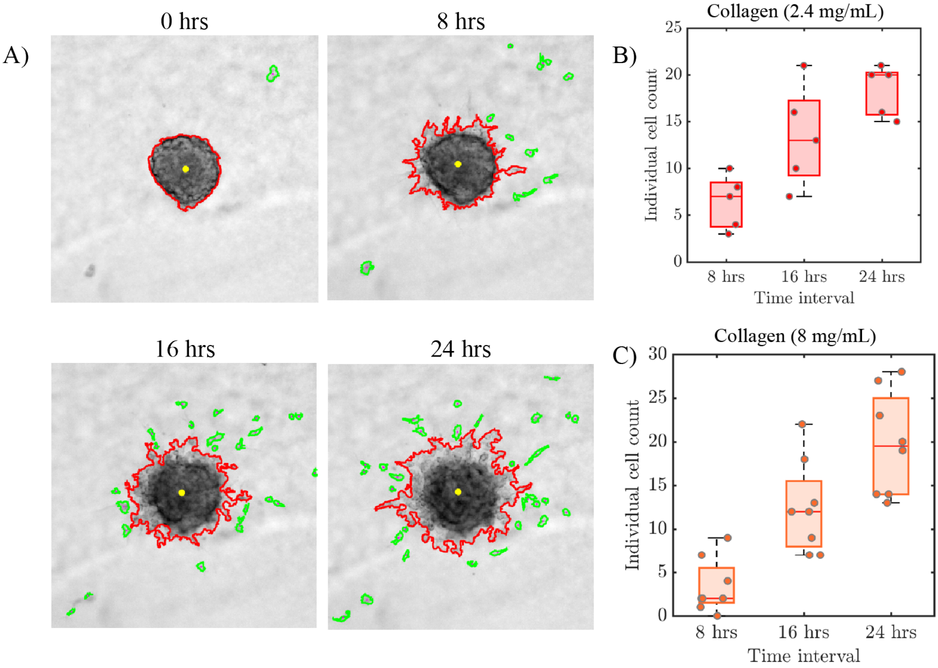

Figure S3.9: Quantification of cell dissociation from MV3 spheroids in collagen matrices. A) Bright-field images of MV3 spheroids in collagen (8 mg/mL) at 8 hr time intervals. The spheroid border is outlined in red while dissociated cells are outlined in green. B) Number of individual cells disseminated in 2.4 mg/mL collagen at time intervals of $t = 8$, 16 and 24 hrs. C) Corresponding data for MV3 spheroids in 8 mg/mL collagen.

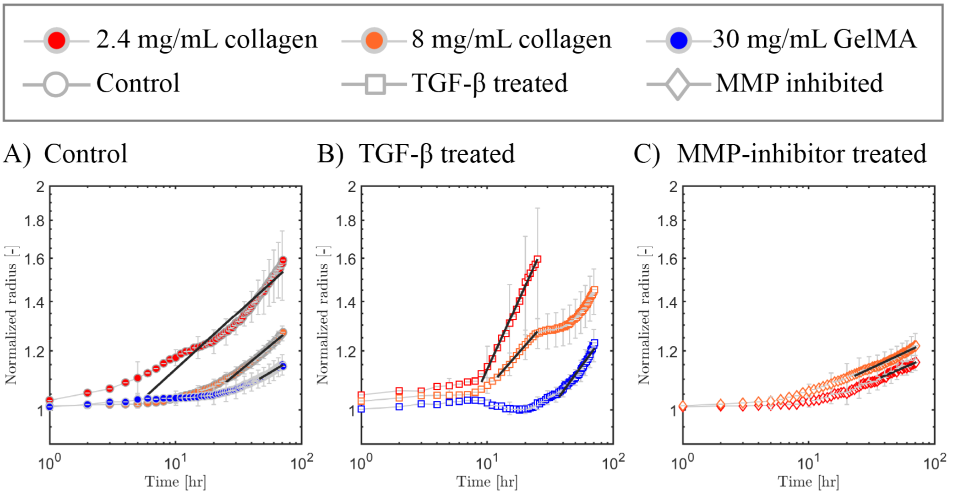

Figure S3.10: Effect of TGF-β and MMP-inhibitor treatments on expansion rates of A549 spheroids. Quantification of the increase in spheroid radius with time for A549 spheroids in collagen (2.4 mg/mL and 8 mg/mL) and GelMA (30 mg/mL) under A) control conditions, B) with TGF-β treatment, and C) with MMP-inhibitor treatment. The expansion rates were determined as the power law slope of the curves after the onset of invasion. The solid black lines indicate the fits together with the temporal range.

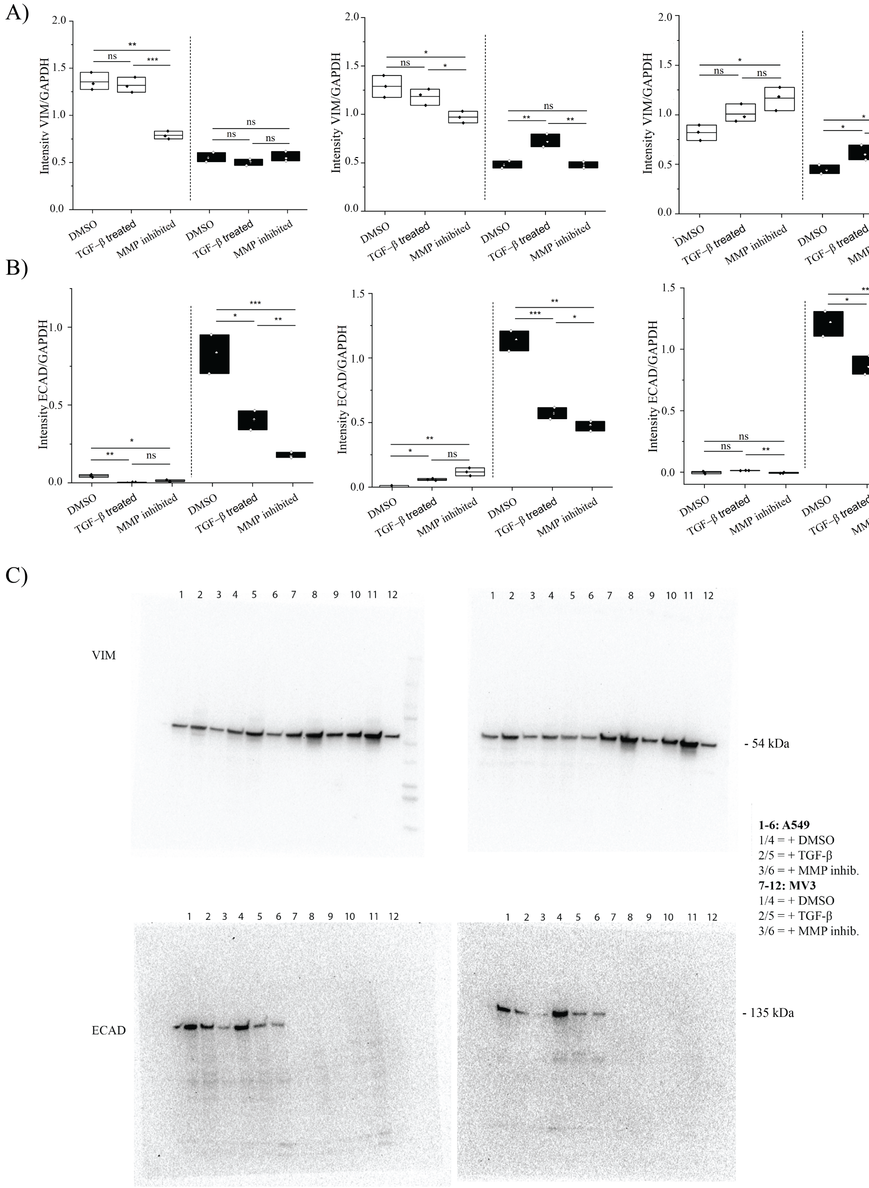

Figure S3.11: Western Blot analysis for vimentin and E-cadherin protein expression levels in A549 and MV3 cells cultured in 2D on collagen-coated 6-well plates. We performed a total of n = 4 biological replicates for each condition (DMSO (control), TGF-β, and MMP-inhibitor treatments). One replicate of each is shown in the main text. Additional replicates are shown here. A) Three replicates showing vimentin expression levels normalized by GAPDH. B) Three replicates showing E-cadherin expression levels normalized by GAPDH. P-value results from t-tests are indicated by: (ns) = $p \geq 0.05$, (*) = $p < 0.05$, (**) = $p < 0.01$, (***) = $p < 0.001$. Western Blot images are shown for C) E-cadherin and D) vimentin. The legend on the right shows the content of each lane (indicated by numbers above the gels).

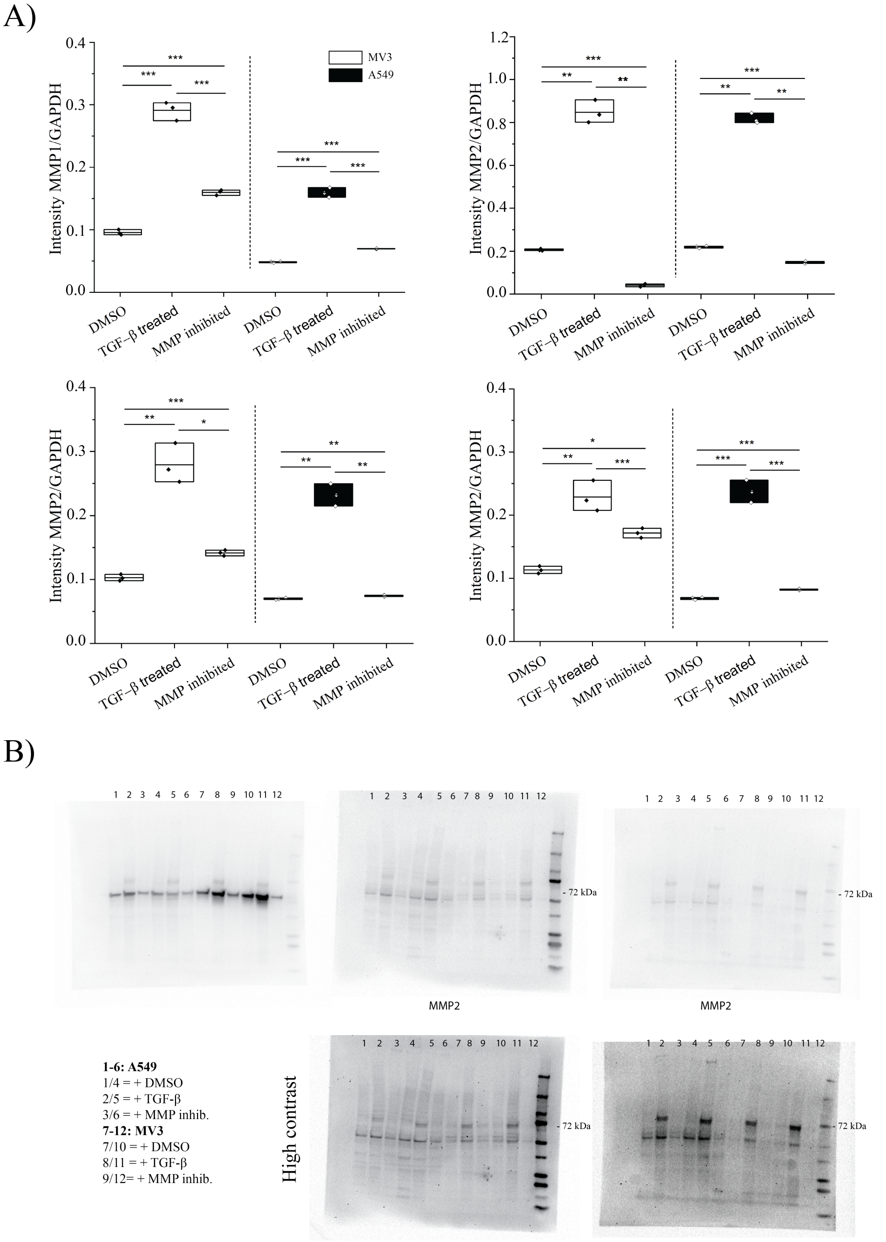

Figure S3.12: Western Blot analysis for MMP1 and MMP2 protein expression levels in A549 and MV3 cells cultured in 2D on collagen-coated 6-well plates. We performed a total of n = 2 biological replicates for the MMP1 quantification and n = 4 for the MMP2 quantification, for different conditions: DMSO (control), TGF-β, and MMP-inhibitor treatments. One replicate of each is shown in the main text. Additional replicates are shown here. A) One replicate showing MMP1 expression levels normalized by GAPDH and three replicates showing MMP2 expression levels normalized by GAPDH. P-value results from t-tests are indicated by: (ns) = $p \geq 0.05$, (*) = $p<0.05$, (**) = $p<0.01$, (***) = $p<0.001$. B) Three Western Blot images are shown for MMP1 (left) and MMP2 (middle and right). The legend shows the content of each lane (indicated by numbers above the gels).

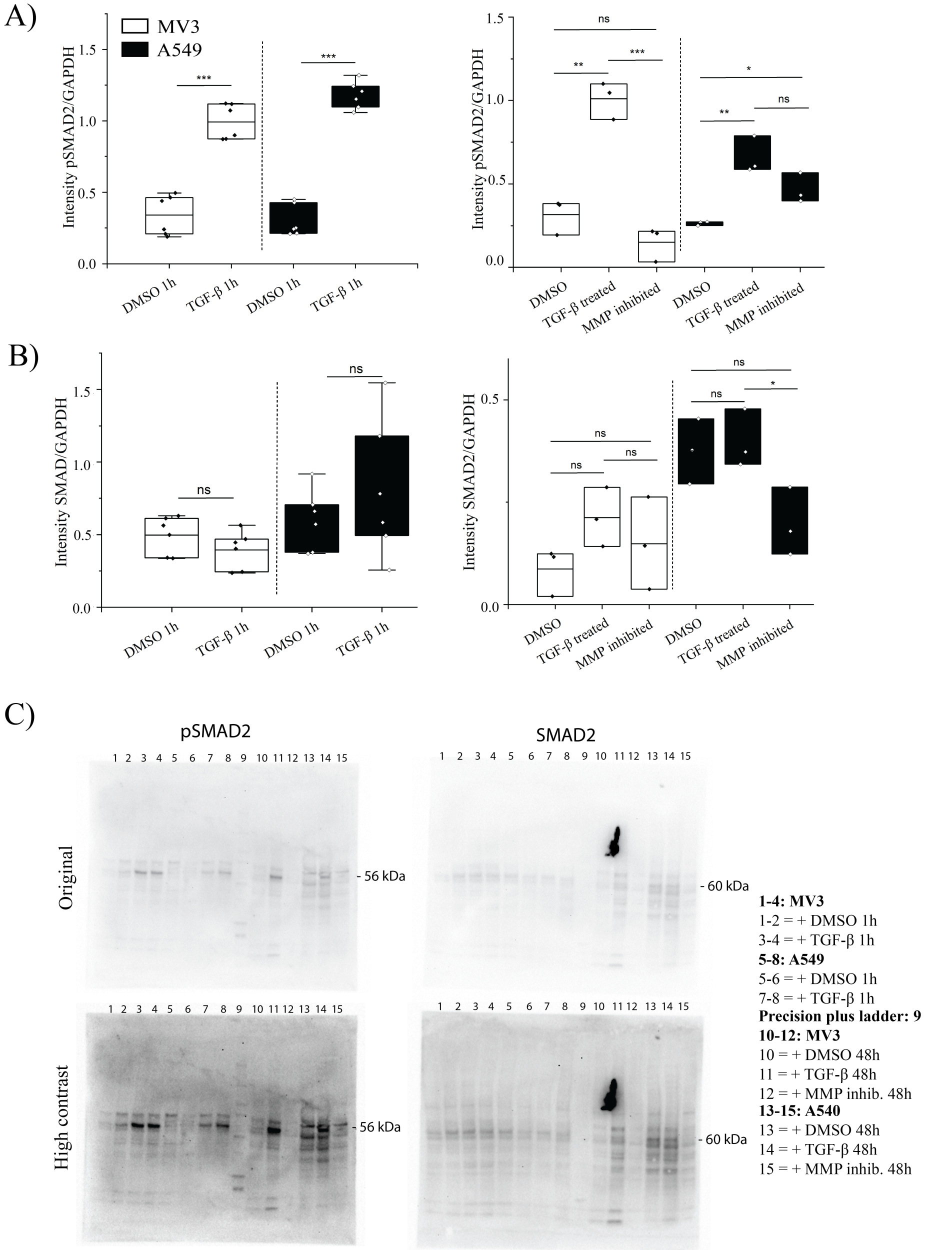

Figure S3.13: Western Blot analysis for SMAD2 and pSMAD2 expression of MV3 and A549 cells cultured in 2D on collagen coated 6-well plates. A) Protein expression of pSMAD2 after 1h (left) and 48h (right) of TGF-β treatment in A549 and MV3 cells. B) Protein expression of SMAD after 1h (left) and 48h (right) of TGF-β. P-value results from t-tests are indicated by: (ns) = p≥0.05, (*) = p<0.05, (**) = p<0.01, (***) = p<0.001. C) Western blot images of pSMAD2 (left) and SMAD2 (right). The legend shows the content of each lane (numbered on top of the gels). For 1h treatments: (n=2). For 48h treatments: (n=1).

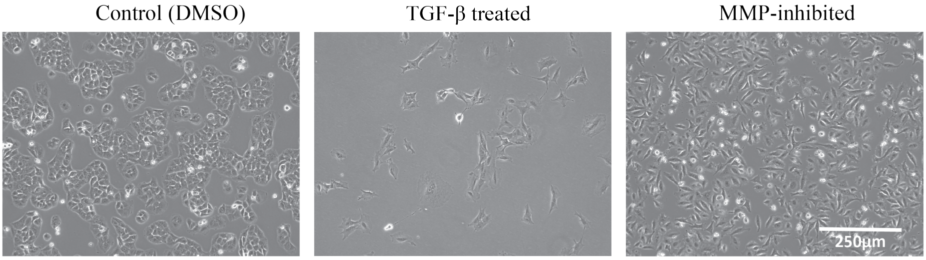

Figure S3.14: A549 cell morphology in 2D cell culture under control (DMSO), TGF-β treated and MMP-inhibited conditions. Bright field images were taken 2 days after seeding on collagen coated 6-well plates. Scale bar is 250 µm.

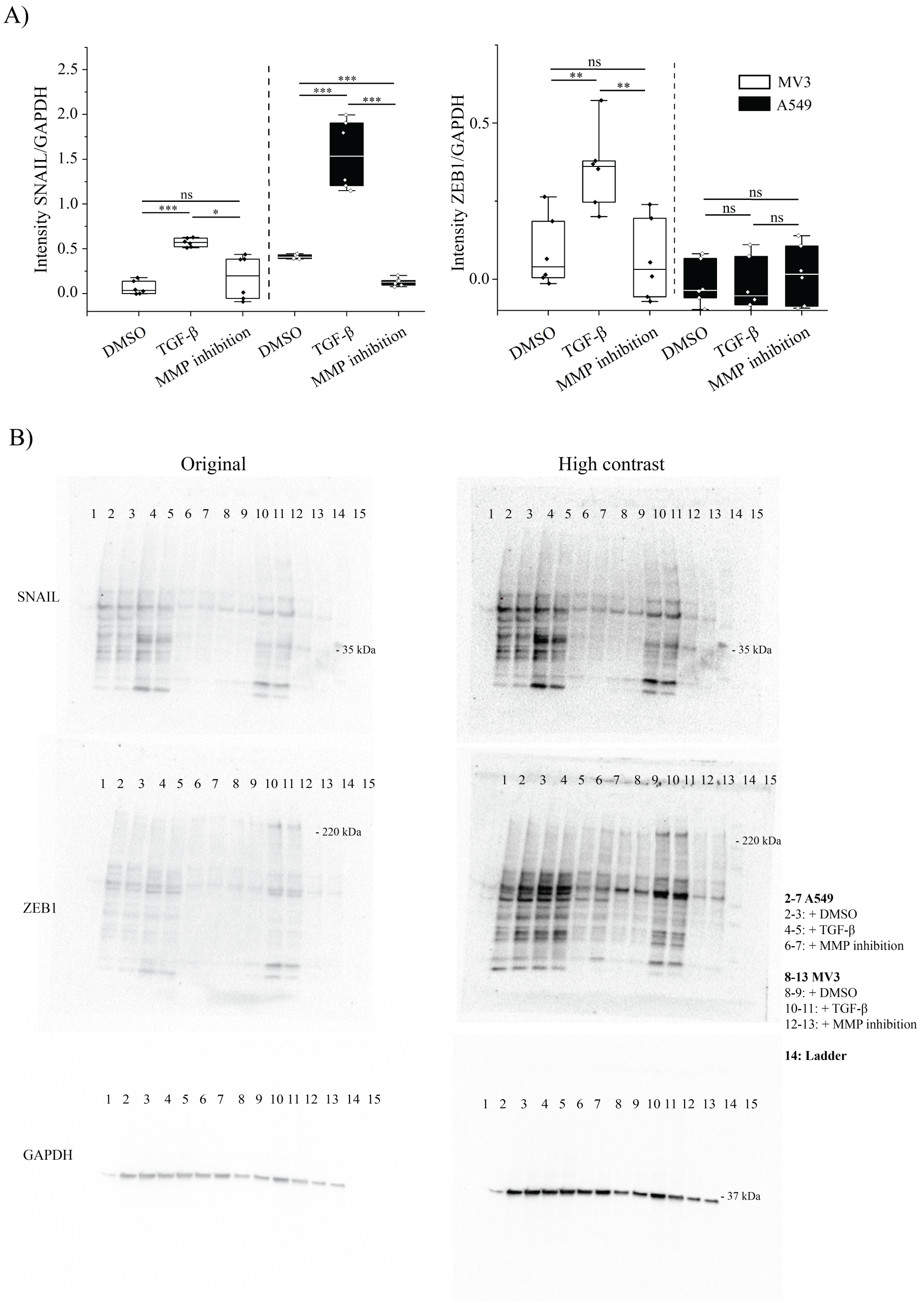

Figure S3.15: Western Blot analysis for SNAIL and ZEB1 expression of MV3 and A549 cells treated with DMSO, TGF-β and MMP inhibitor Batimastat. A) Protein expression of SNAIL and ZEB1 relative to GAPDH. P-value results from t-tests are indicated by: (ns) = $p \geq 0.05$, (*) = $p < 0.05$, (**) = $p < 0.01$, (***) = $p < 0.001$. Each condition depicts two biological samples (n=2) with three data points based on different background subtractions. B) Western blot images of SNAIL, ZEB1 and GAPDH. For SNAIL blots the correct band height was chosen based on earlier reports for this antibody [Fan et al; The EMBO Journal, 2023 & Fan et al, Science Signaling, 2023]. The legend shows the content of each lane (numbered on top of the blots).

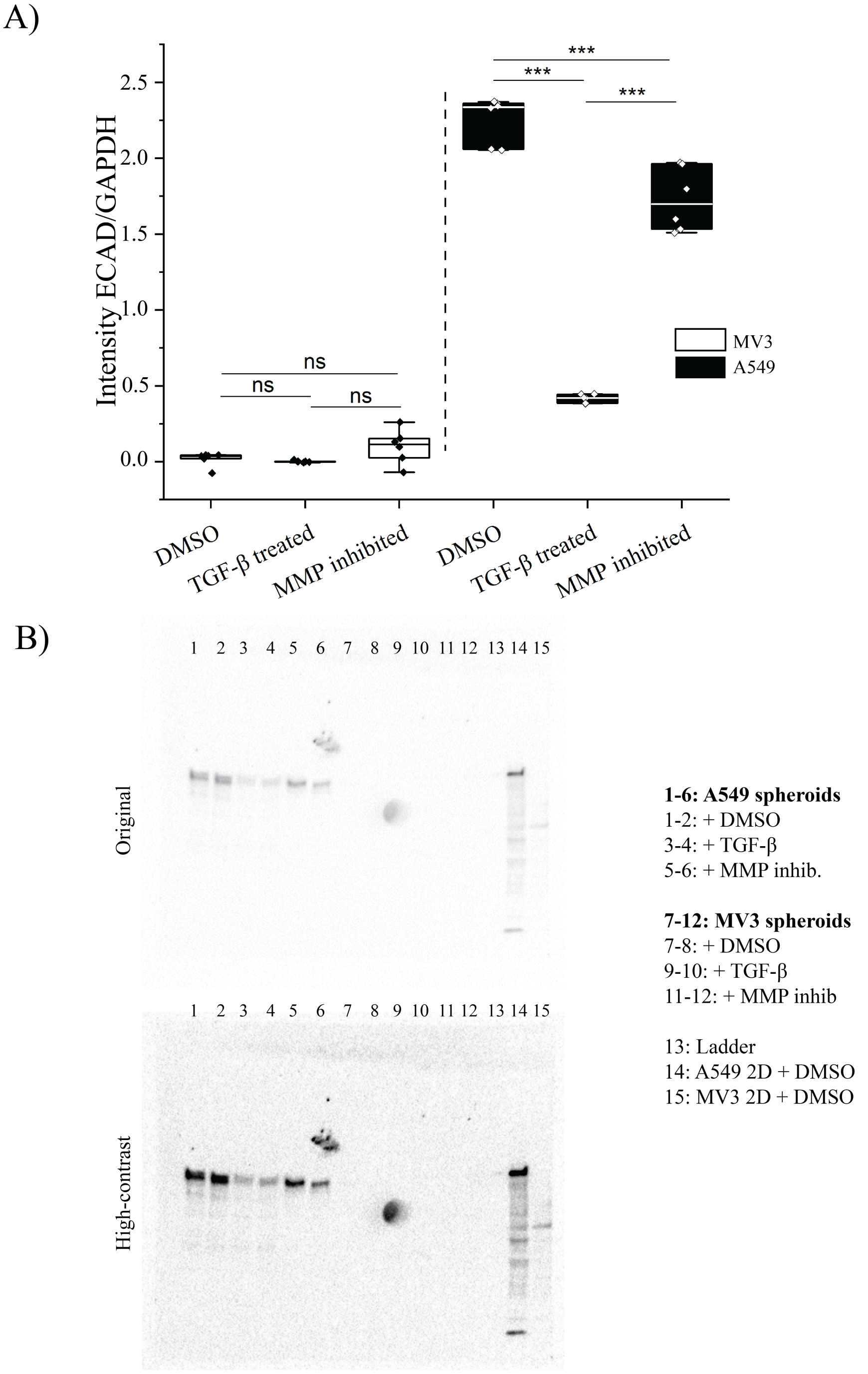

Figure S3.16: Western Blot analysis for E-cadherin expression of 3D spheroid invasion assays in 2.4 mg/mL collagen. A) Protein expression of E-cadherin after 72h of invasion with DMSO, TGF-β and Batimastat treatments in A549 and MV3 spheroids. P-value results from t-tests are indicated by: (ns) = p≥0.05, (*) = p<0.05, (**) = p<0.01, (***) = p<0.001. B) Western blot images of E-cadherin. The legend shows the content of each lane (numbered on top of the blot).

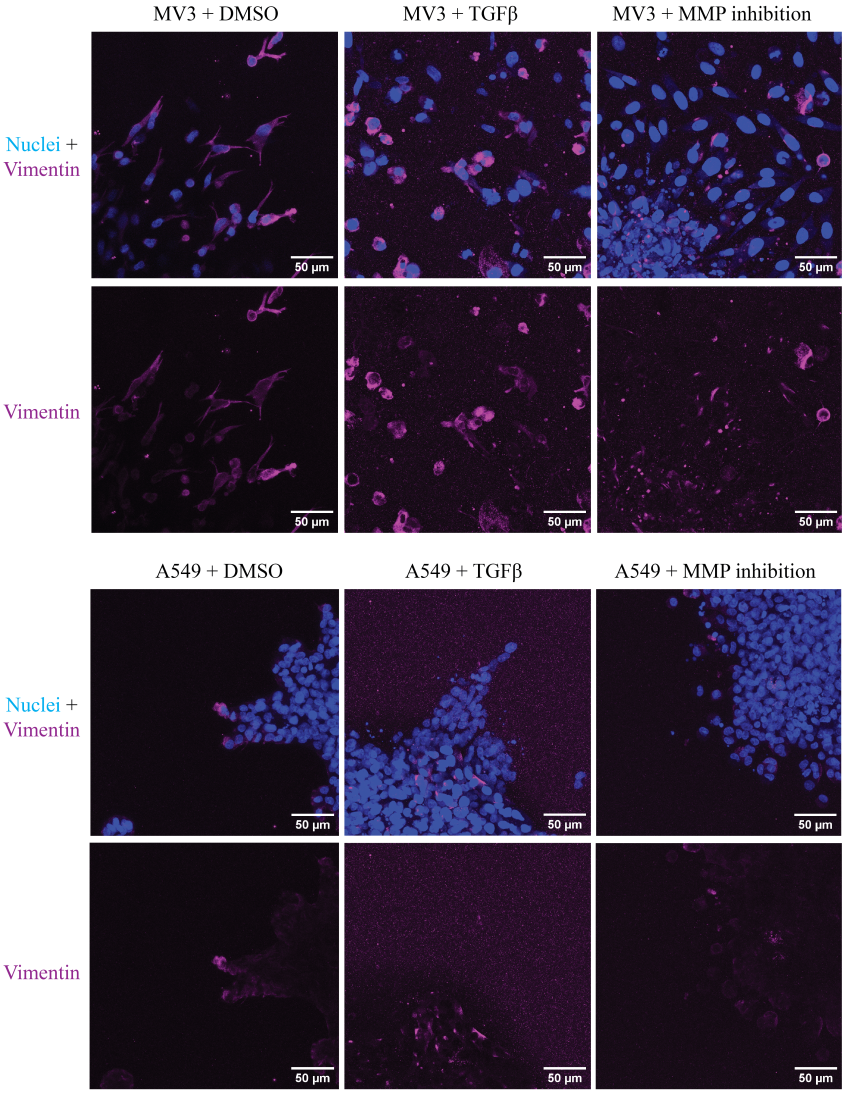

Figure S3.17: Immunocytochemistry for vimentin (magenta) and cell nuclei (blue) in MV3 and A549 spheroid invasion assays in 2.4 mg/mL collagen hydrogels, treated with DMSO, TGF-β and MMP inhibitor Batimastat. Images were taken at the periphery of the invaded spheroids. Maximum intensity projections of Z-stacks over a Z-range of 100 µm recorded with a step size of 5 µm. Images are representative for a set of n=3 experiments.

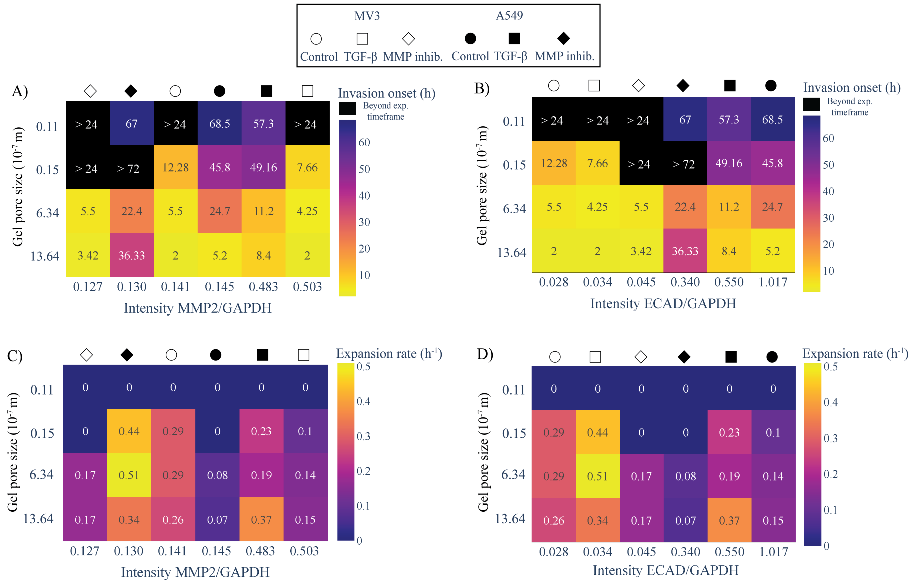

Figure S3.18: Correlation of the invasion onset times and spheroid expansion rates with MMP2 and E-cadherin protein expression levels for MV3 and A549 spheroids. A) Heat map showing the dependence of the invasion onset time (indicated by the number (in units of hrs) in each square and the color code, see color bar on the right) on hydrogel pore size (y-axis) and expression level of MMP2 (x-axis). B) Corresponding heat map showing the dependence of the invasion onset time on hydrogel pore size (y-axis) and expression level of E-cadherin (x-axis). Note that spheroids that did not invade during the time frame of the assay are shown in black. C) Heat map showing the dependence of the spheroid expansion rate (number (in units of hr^{-1}) in each square and color code, see color bar on the right) on hydrogel pore size (y-axis) and expression level of MMP2 (x-axis). D) Corresponding heat map showing the dependence of the spheroid expansion rate on hydrogel pore size (y-axis) and expression level of E-cadherin (x-axis). In all cases, data for MV3 and A549 spheroids were pooled and protein expression levels were normalized by GAPDH.

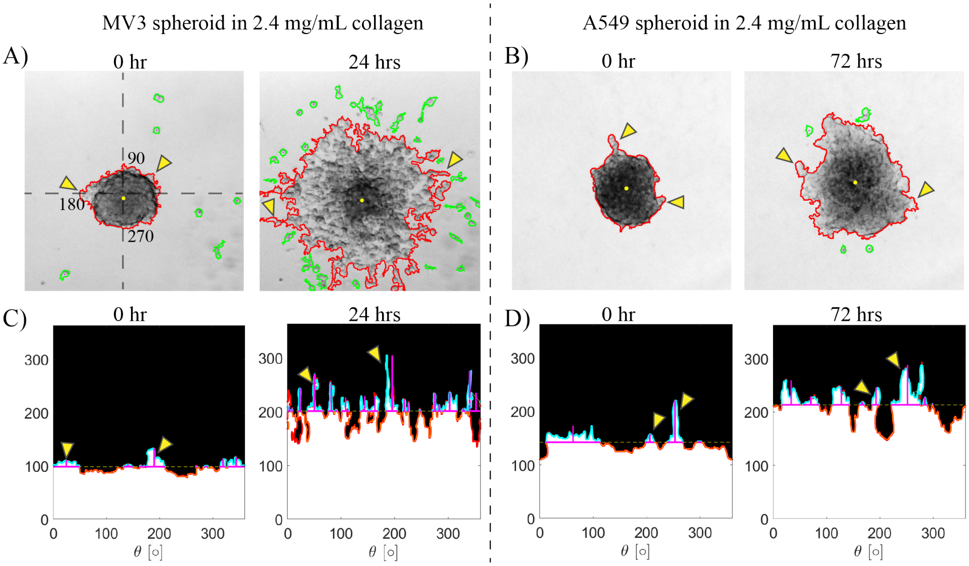

Figure S3.19: Analysis of spheroid protrusions and single cell dissemination aimed at classifying the state (gas, fluid, liquid) of spheroids under different conditions. A) Bright field images of a MV3 spheroid in 2.4 mg/mL collagen at $t = 0$ (initial state) and $t = 24$ hrs (final state). B) Bright field images of an A549 spheroids in 2.4 mg/mL collagen at $t = 0$ hr (initial state) and $t = 72$ hrs (final state). Spheroid boundaries are outlined in red while disseminated cells are outlined in green. The yellow arrowheads highlight examples of multicellular protrusions that grow over time. Note that both MV3 and A549 cells already showed some protrusions at $t = 0$ hr. Additionally, the images often revealed some disseminated cells at $t = 0$ hr. Therefore, in all cell count quantification, we subtracted the cells present at $t = 0$ hr. C) Polar plots determined from the MV3 spheroid images in A, based on the assumption of radial symmetry. D) Corresponding polar plots for the A549 spheroid images in B. In both cases, multicellular protrusions are seen as peaks (yellow arrowheads highlight examples). The polar plots were used as a basis to detect each peak (i.e., multicellular protrusion) and quantify its maximum height relative to the average spheroid radius (horizontal red lines). Spheroids with average protrusion lengths greater than 25 µm were considered to be in a liquid-like (unjammed) state.

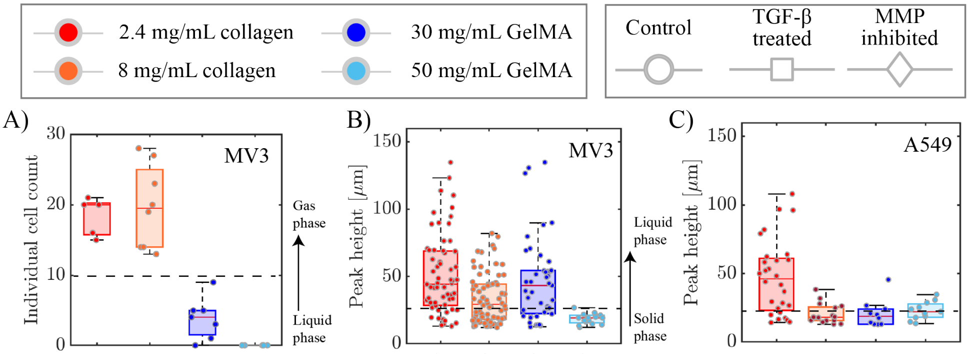

Figure S3.20: Analysis of spheroid protrusions and single cell dissemination aimed at classifying the state (gas, fluid, liquid) of MV3 and A549 spheroids in control conditions. A) Individual cell count analysis of MV3 spheroids in collagen (2.4 and 8 mg/mL) and in GelMA (30 and 50 mg/mL) matrices. Spheroids are considered to be in a gas-like state when the cell count is above 10 (above the horizontal dashed line) and solid-like or liquid-like when the cell count is below 10. MV3 spheroids were gas-like in collagen (2.4 and 8 mg/mL) and solid-like in GelMA (30 and 50 mg/mL GelMA). B) Protrusion lengths for MV3 spheroids. C) Protrusion lengths for A549 spheroids. Spheroids are considered liquid-like when the protrusion lengths are above 25 μm (above the dashed lines) and solid-like when the protrusion lengths are below 25 μm. MV3 spheroids were gas-like in collagen (2.4 and 8 mg/mL) and 30 mg/mL GelMA hydrogels and solid-like in 50 mg/mL GelMA. A549 spheroids were liquid-like only in 2.4 mg/mL collagen and solid-like otherwise.

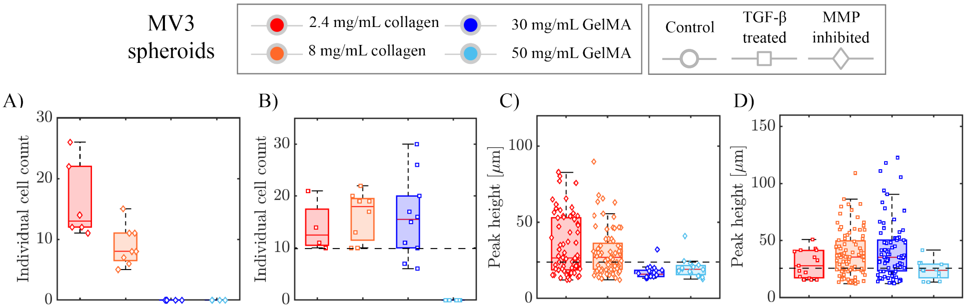

Figure S3.21: Quantification of disseminated cells and protrusion lengths for MV3 spheroids in order to classify the state (gas, fluid, solid) of the spheroid. A) Individual cell count analysis for MV3 spheroids treated with MMP-inhibitor in different collagen and GelMA gels (see legend on top). MMP-inhibitor treatment caused a strong (40-50%) drop in the cell count in collagen (2.4 mg/mL and 8 mg/mL) gels and blocked cell dissociation in 30 GelMA hydrogels. B) Corresponding data for MV3 cells treated with TGF-β. The dashed lines indicate the transition between a liquid/solid state (cell count below 10) and a gas state (cell count above 10). TGF-β treatment caused a large (73%) increase in cell count in 30 mg/mL GelMA compared to control conditions but did not result in any individual cell dissemination in 50 mg/mL GelMA. C) Protrusion lengths for MV3 spheroids treated with MMP-inhibitor in different collagen and GelMA gels. D) Corresponding data for MV3 spheroids treated with TGF-β. The dashed lines indicate the transition between a solid state (maximum protrusion length below 25 μm) and a liquid state (average protrusion length above 25 μm). Box plots show N = 5-10 spheroids per condition performed in 2 independent experiments.

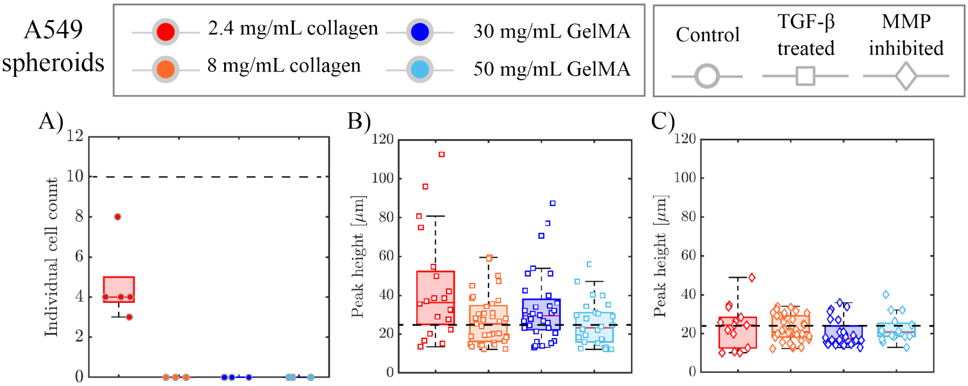

Figure S3.22: Quantification of disseminated cells and protrusion lengths for A549 spheroids in order to classify the state (gas, fluid, solid) of the spheroid. A) Individual cell count analysis for A549 spheroids embedded in collagen and GelMA matrices (see legend on top) in control conditions. The dashed line indicate the transition between a liquid/solid state (cell count below 10) and a gas state (cell count above 10). Under control conditions, the A549 spheroids only disseminated individual cells in 2.4 mg/mL collagen. Note that A549 spheroids embedded in 2.4 mg/mL collagen treated with TGF-β disintegrated and sedimented to the bottom, so we were unable to count the disseminated cells. At early times, however, we could observe cell dissociation, so we classify this condition as a gas-like phase. B) Protrusion lengths of A549 spheroids treated with TGF-β. A549 spheroids formed protrusions characteristic of a liquid-like state in 8 mg/mL collagen and in 30 mg/mL GelMA upon TGF-β treatment, whereas they were solid-like in control conditions. In 8 mg/mL collagen, the TGF-β-treated spheroids made shorter protrusions with an average length of 26 µm. No protrusions were observed for spheroids embedded in 50 mg/mL GelMA. C) Protrusion lengths of A549 spheroids treated with MMP-inhibitor. Upon MMP inhibition, A549 spheroids were liquid-like only in 2.4 mg/mL collagen. The dashed lines in B and C indicate the transition between a solid state (average protrusion length below 25 µm) and a liquid state (average protrusion length above 25 µm). Box plots show N = 5-10 spheroids per condition.

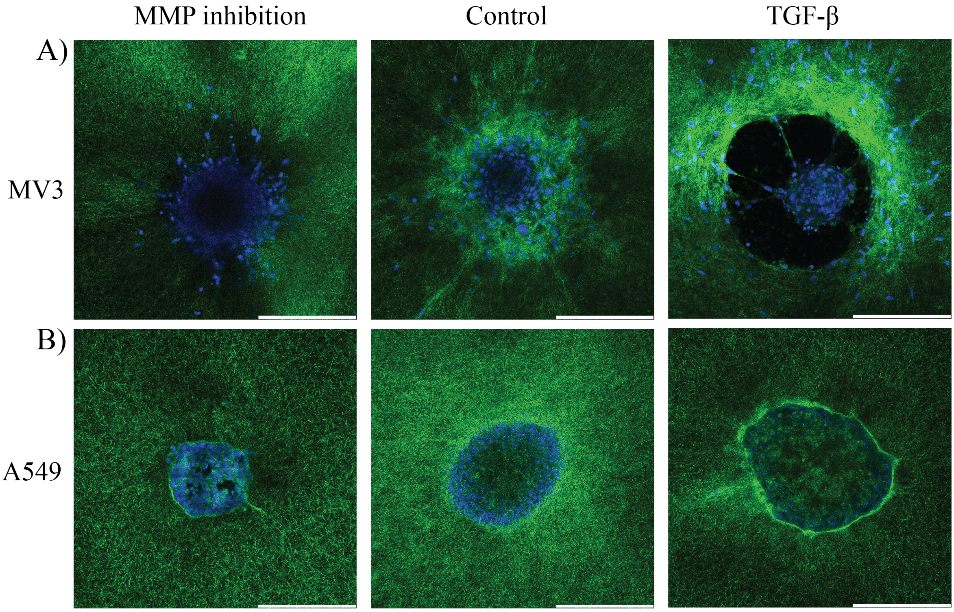

Figure S3.23: Visualization of cell-mediated extracellular matrix remodelling for spheroids embedded in collagen (2.4 mg/mL). Confocal images of A) MV3 and B) A549 spheroids in control conditions (middle) and with MMP-inhibition (left) or TGF-β treatment (right) around spheroid equator. Collagen fibers were imaged by reflection and are shown in green. Nuclei stained with Hoechst were imaged by fluorescence and are shown in blue. Scale bars are 250 250 µm. Compared to control conditions, TGF-β stimulation causes more matrix remodeling whereas MMP inhibition diminishes matrix remodeling. MV3 spheroids appear to exert higher traction forces on the collagen than A549 spheroids, as shown by radially oriented fibers around the spheroid under MMP inhibition and control conditions and extensive collagen accumulation upon TGF-β stimulation. Furthermore, the black void around the MV3 spheroid upon TGF-β stimulation is indicative of MMP-mediated matrix degradation.

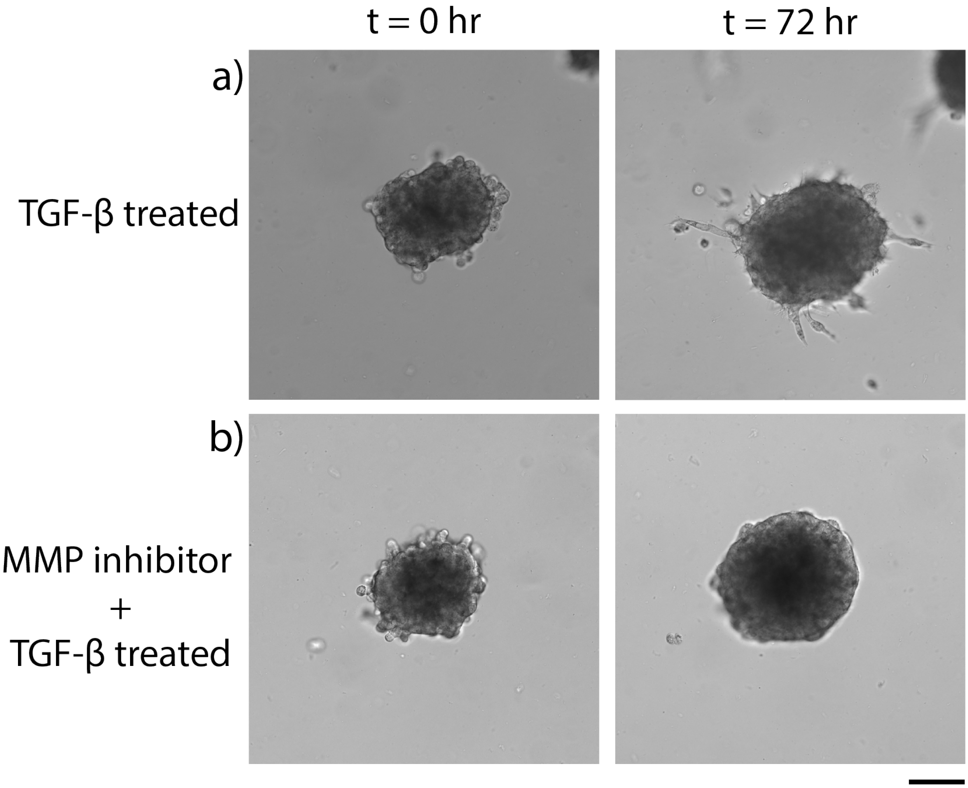

Figure S3.24: A549 spheroid invasion in GelMA (30 mg/mL) at t = 0 and t = 72 hr. A549 spheroid treated with TGF-β (10 ng/mL) A) without MMP-inhibitor pretreatment and B) with MMP-inhibitor (30 µM) pretreatment. Scale bar is 100 µm.

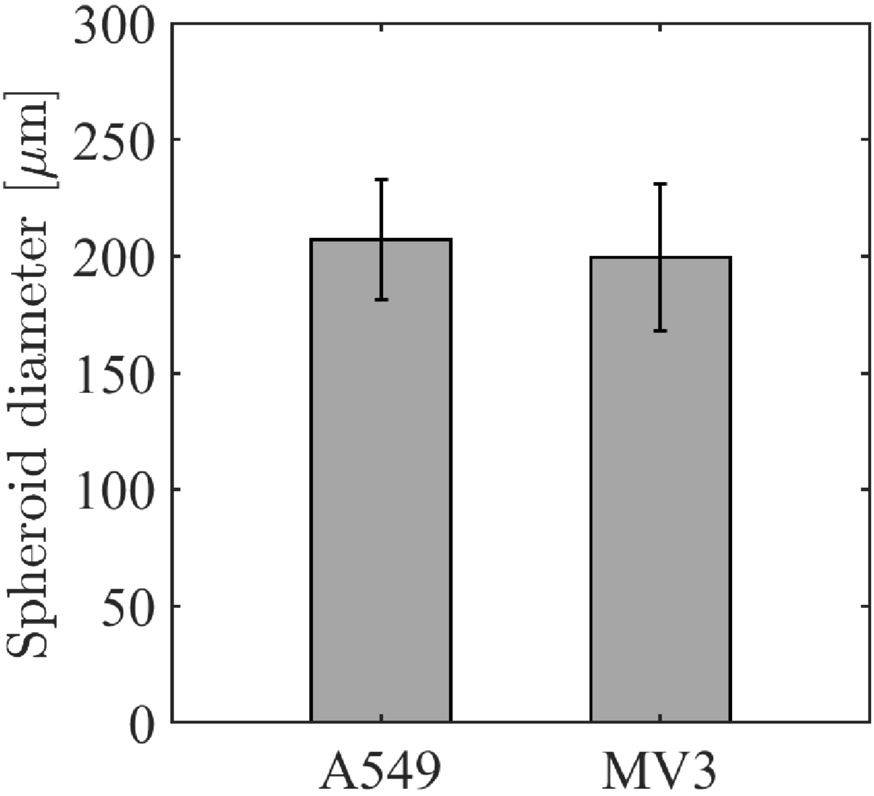

Figure S3.25: Average diameter of MV3 (N = 80) and A549 (N = 85) spheroids at t = 0 hr determined from bright field images. The spheroids had comparable average diameters of 200±30 µm (MV3) and 207±26 µm (A549).

4

HOW CYTOSKELETAL CROSSTALK MAKES CELLS MOVE

Cell migration is a fundamental process for life and is highly dependent on the dynamical and mechanical properties of the cytoskeleton. Intensive physical and biochemical crosstalk between actin, microtubules, and intermediate filaments ensures their coordination to facilitate and enable migration. In this chapter we review the different mechanical aspects that govern cell migration and provide, for each mechanical aspect, a novel perspective by juxtaposing two complementary approaches to the biophysical study of cytoskeletal crosstalk: live-cell studies (often referred to as top-down studies) and cell-free studies (often referred to as bottom-up studies). We summarize the main findings from both experimental approaches and end with our perspective on bridging the two perspectives to address the open questions of how cytoskeletal crosstalk governs cell migration and makes cells move. [1]

---

[1] This chapter is co-authored with James P. Conboy, Irene Istúrez-Petitjean and Gijsje H. Koenderink and was published in Biophysics Reviews (2024).

4.1. INTRODUCTION

CELL migration is a process that is fundamental for life. It is a major contributor to tissue morphogenesis in developing embryos [194] and drives angiogenesis [195], bone formation [196], tissue repair [197] and immune surveillance [198]. On the flip side, however, cell migration is also responsible for pathological cell migration during chronic inflammation [199] and cancer metastasis [200]. Cell migration depends on the mechanical and dynamical properties of the *cytoskeleton*, a network of dynamic biopolymers that self-assemble from small protein building blocks. There are three main cytoskeletal biopolymers: actin filaments, microtubules, and intermediate filaments (Figure 4.1A). They have markedly different structural, mechanical and dynamical properties. In addition, septins are identified as the fourth cytoskeletal component [39] (see Chapter 5 of this dissertation).

Actin filaments are double helices with a diameter of ~ 7 nm, made of two strands of globular monomers [201]. The filaments are semiflexible since their thermal persistence length $l_p = \kappa / k_B T$ (where κ is the bending rigidity and $k_B T$ thermal energy) is ~ 10μm, of the same order as the filament contour length [202]. Actin filaments have an intrinsic structural polarity with a “barbed end” and a “pointed end”. Polymerization-linked ATP hydrolysis causes treadmilling, where the filaments grow at the barbed end and disassemble from the pointed end [203]. Filaments reconstituted from purified actin turn over slowly (one subunit every 3–4 s), but actin turnover in the cell is catalyzed by actin-binding proteins. Typical actin network turnover times are of order seconds in the leading edge of motile cells [204] to minutes in the actin cortex [205]. Together with myosin motor proteins, actin filaments form networks and bundles that generate contractile forces [206]. *Microtubules* form hollow tubes of 13 protofilaments that are much wider (~ 25 nm)[207] and hence substantially stiffer (l_p ~ 1 mm)[208] than actin filaments. Like actin filaments, microtubules have an intrinsic structural polarity with distinct plus and minus ends. GTP hydrolysis results in dynamic instability, characterized by alternating phases of microtubule growth and shrinkage [209]. In the cell, this process is tightly regulated by accessory proteins that bind at the microtubule tip or lattice. *Intermediate filaments* are homo-/heteropolymers made of rod-shaped proteins that are encoded by more than 70 genes in humans [210]. Intermediate filament proteins are expressed in a cell-type-specific manner. Mesenchymal cells for instance express vimentin, whereas epithelial cells express keratins. The intermediate filament proteins share a common secondary structure consisting of an alpha-helical rod domain flanked by intrinsically disordered head and tail domains. Intermediate filaments are somewhat thicker (~ 10 nm) [211] than actin filaments, but their rope-like structure nevertheless makes them more flexible (l_p ~ 0.5 - 2 μm, depending on intermediate filament composition and ionic strength [212, 213, 214, 215, 216]). Intermediate filaments are much more stable than actin filaments and microtubules, with slow subunit exchange along their length and annealing and fragmentation on hour time scales in reconstituted systems [217, 218] and in cells [219, 220].

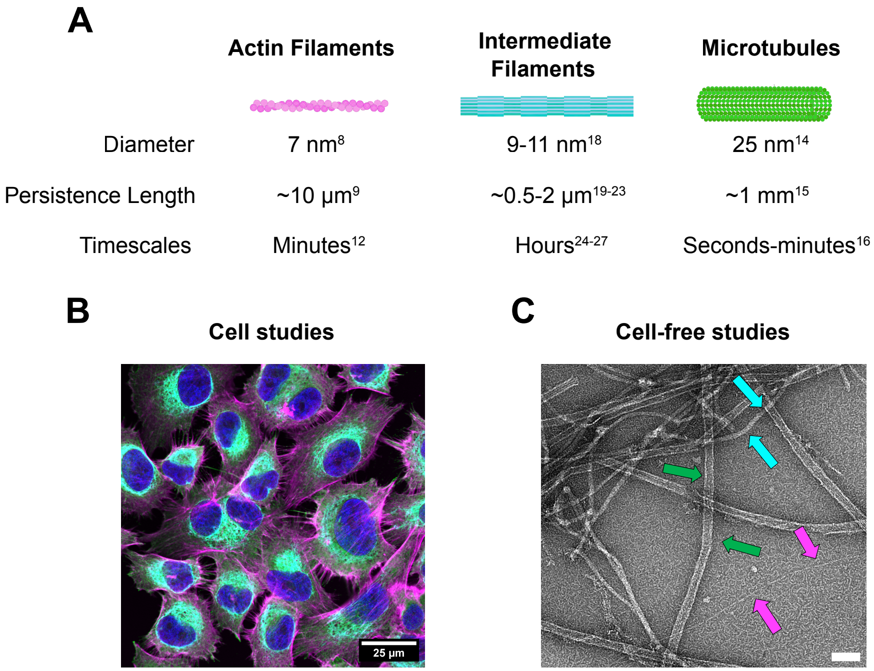

Figure 4.1: (a) Schematic of the three major cytoskeletal filament types and their distinctive physical properties. (b) Fluorescent confocal microscopy image of human melanoma (MV3) cells stained for α-tubulin (green), F-actin (magenta), and vimentin (cyan). The cell nuclei are shown in blue. (c) An electron microscopy image of an *in vitro* reconstituted three-component cytoskeletal network showing F-actin (magenta arrows), microtubules (green arrows) and vimentin (cyan arrows). Filaments were pre-polymerized separately at 1 μM. Actin and microtubules were polymerized in MRB0 buffer (80 mM PIPES pH 6.8, 1 mM EGTA and 4 mM $MgCl_2$) with 50 mM KCl, 1 mM DTT and 0.5 mM ATP, while vimentin was polymerized in V-buffer (40 mM PIPES pH 7, 1 mM EGTA and 4 mM $MgCl_2$, 100 mM KCl, 1 mM DTT). The filaments were combined in MRB80 buffer (with 50 mM KCl, 1 mM DTT and 0.5 mM ATP). Scale bar is 100 nm.

The physical properties of the cytoskeletal filaments are directly connected to their functions in cell migration. Actin, with its ability to generate protrusive and contractile forces, provides the main driving forces for polymerization-driven *mesenchymal migration* and bleb-based *amoeboid migration* [221, 222]. Meanwhile microtubules play a key role in establishing front-rear polarity and promoting persistent migration, aided by their large persistence length that is much longer than the size of the cell [223]. Finally, intermediate filaments, with their mechanical resilience, protect the migrating cell and its nucleus from mechanical damage, which is especially important when cells squeeze through confined environments [224, 225].

There is growing evidence that cell migration requires a dynamic interplay between the three cytoskeletal filament systems that depends on mechanical and signaling crosstalk. In mesenchymal migration, coupling of actin to microtubules and intermediate fila-

Modality	Cytoskeletal element #1	Cytoskeletal element #2	Mediator(s)	Function of the crosstalk
Direct interaction	Microtubules	Vimentin	Excluded volume	Promoted strain-stiffening[136, 137]
	Actin	Vimentin	Excluded volume	Mechanical synergy[133]
Crosslinker	Actin	Vimentin	Plectin	Force transmission to nucleus[147]
	Microtubule	Actin	ACF7/MACF	Guided filament growth[141, 193]
Molecular signalling	Actin	Microtubules	GEF-H1/RhoA	Detachment of leader cells[232]
	Actin	Vimentin	RhoGTPases	Inhibition of stress fiber assembly[156]
Steric interaction	Actin	Microtubules	Electrostatic interactions	Promoting filament alignment[141]

Table 4.1: Table highlighting the different cytoskeletal crosstalk modalities that are discussed in this chapter, each with an example from the text.

ments is for instance essential to polarize the actin cytoskeleton and control force generation [6]. In Figure 4.2 we highlight examples of the different cytoskeletal crosstalk modalities. Here we review recent insights in the role of cytoskeletal crosstalk in cell migration, with a focus on mechanical aspects. For more detailed cell biological insights, we refer the reader to several excellent reviews [226, 6, 227, 228, 229]. We take a mainly experimental perspective and refer the reader to other reviews for more theoretically oriented perspectives [230, 231]. Throughout this review, we confront two opposite experimental approaches to studying the biophysics of cytoskeletal crosstalk: *live cell (top-down)* studies (Figure 4.1B) versus *cell-free (bottom-up)* studies of simplified model systems reconstituted from component parts (Figure 4.1C). Live-cell studies have the benefit of physiological relevance, but mechanistic dissection is challenging because of the cell's compositional complexity. Each cytoskeletal system exhibits enormous compositional diversity with different isoforms and posttranslational modifications [232]. Moreover, cytoskeletal coupling is mechanosensitive as a consequence of mechanosensory signalling loops and transcriptional regulation [233]. Cell-free studies provide a powerful approach to complement live-cell studies because they allow for highly controlled experiments from the level of single protein, to filaments, to networks.

Cytoskeletal crosstalk contributes to every aspect of cell migration (Figure 4.2). We structure this chapter according to these aspects, from cell deformability, to front-back polarity, contractility, adhesion control in collective cell migration, and finally plasticity, which refers to the ability of cells to adapt their mode of migration to their environment [234]. We end with a perspective on how connections can be made between cell-free and live-cell studies to address the many open questions on the role of cytoskeletal crosstalk in cell migration.

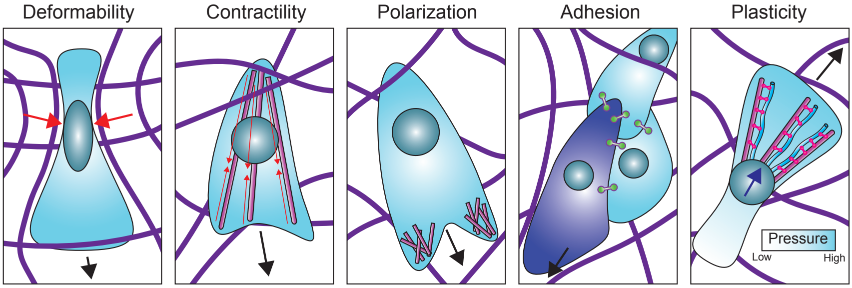

Figure 4.2: Cytoskeletal crosstalk contributes to every aspect of cell migration including: (1) Cell deformability that governs the ability of cells to migrate through confining environments. Red arrows show deformation caused by the cell migrating through the extracellular matrix. (2) Contractility as a major driver of cell motility. Red arrows show actin-myosin contraction. (3) Front-rear polarity for directional migration. (4) Cell-cell adhesions to coordinate collective migration. The leader cell is shown in dark blue. (5) Plasticity, the ability of cells to interconvert between different migration strategies in response to their environment, for example between mesenchymal and nuclear piston modes. Here the nucleus is pulled forwards (dark blue arrow). Black arrows show the direction of migration. Actin (magenta), vimentin (cyan), nucleus (teal), intercellular adhesions (green linkers), plectin (pink linkers) and extracellular matrix fibers (purple).

4.2. CELL DEFORMABILITY

4.2.1. LIVE-CELL STUDIES

MECHANICAL CHALLENGES IN CELL MIGRATION

Migrating cells must deform their nucleus and cytoskeleton, especially when they move through interstitial tissues that impose significant confinement. Depending on tissue type, cells encounter extracellular matrix (ECM) and interstices between tissues with sizes ranging between 2 and 30 μm, comparable to their own body and sometimes even nuclear size [235]. Metastasizing cancer cells have to overcome even more severe physical barriers as they intravasate across the endothelium into blood vessels or across epithelial tissues into lymphatic vessels. Cell deformability is therefore an important determinant of cell migration [236]. For many cancer cells, for instance, lower stiffness correlates with higher motility [237]. In Chapter 2 of this dissertation, we also provide a similar finding that migration of cancer cells through constrictions correlates with cellular deformability.

Migrating cells experience a complex combination of tensile, compressive and shear deformations of varying amplitude and rate. The effect of these mechanical parameters on cell deformability has been extensively characterized using quantitative biophysical techniques. To study the viscoelastic properties of cells without the impact of cell adhesion, cells can be detached from their substrate and measured in suspension by micropipette aspiration [238], optical stretching [239], parallel-plates rheometers [240], or high-throughput microfluidic methods [241]. These measurements are mostly relevant for amoeboid migration where cells exhibit only weak adhesion to their environment. For mesenchymal migration, it is more relevant to study mechanics on adherent cells. Whole-cell measurements of adherent cells can be done by monolayer rheology or stretching [242, 243, 244] or by single-cell atomic force microscopy [245, 246]. Localized measurements to resolve the mechanics of specific subcellular regions can be done by magnetic twisting cytometry [247], atomic force microscopy [248], optical or magnetic tweezers [249, 250], or particle tracking microrheology [251]. Some of these methods allow for *in situ* measurements in migrating cells [252, 253].

The nucleus is the stiffest and largest organelle with a stiffness ranging from 0.1 to 10 kPa, dependent on cell type [254]. The main contributors to the rigidity of the nucleus are heterochromatin and the nuclear lamina (also termed the nucleoskeleton), which contains lamin intermediate filaments [94, 255, 256]. Intact nuclei *in situ* have a higher stiffness than isolated nuclei because the nucleus is coupled to the cytoskeleton through the LINC complex (composed of SUN-domain proteins and KASH-domain proteins, which physically connect the cytoskeleton to the nucleoskeleton) [257]. Since the nucleus is not only the stiffest but also the largest cellular organelle, it poses a major bottleneck for confined migration [25]. When cells are embedded in collagen networks or microfabricated microchannels, their migration velocity linearly decreases with decreasing pore size until migration is physically blocked when the pore size reaches 10% of the nuclear cross section [51]. Under highly confined conditions, cells can only move if they are able to remove blocking ECM fibers with proteolytic enzymes [51, 258].

REGULATION OF CELL DEFORMABILITY THROUGH CYTOSKELETAL CROSSTALK

The actin cytoskeleton is often considered the main determinant of cell mechanics. Drug-induced depolymerization of actin filaments indeed significantly softens cells both under non-adherent and adherent conditions [259, 260]. An important contribution of the actin cytoskeleton to cell stiffness comes from contractile forces generated by actin-myosin stress fibers [261] and by the actin cortex [262]. Intermediate filaments form dense networks that are mainly perinuclear, so they contribute little to cortical stiffness but strongly affect the cytoplasmic shear modulus [263] and the resistance of cells to compression [246]. For leukocytes and tumor cells performing 3D migration, the intermediate filament cytoskeleton is a major determinant of cell deformability. Intermediate filament protein deletion or network disruption causes significant cell softening while at the same time enhancing cell migration [264, 265, 26, 266]. Microtubules generally do not contribute much to cell stiffness, with drugs that interfere with microtubule polymerization having minor effects on cell mechanics [267]. Recently, though, microtubules were shown to exhibit interesting mechano-responsive properties. Cytoskeletal compression induced by cyclic cell stretching or by confined migration was shown to stabilize deformed microtubules by triggering recruitment of the microtubule-binding protein CLASP2 [268]. When cells are transferred from rigid 2D substrates to softer 3D hydrogels, the mechanical contribution of microtubules becomes more important because actin stress fibers become less prominent. In cells migrating through collagen gels, microtubules for instance play a crucial role in mechanical support of cellular protrusions [269].

It remains an open question how the interactions between the three cytoskeletal biopolymers influence the mechanics of the composite cytoskeleton. Theoretical models predict that composite networks composed of interpenetrating networks of a rigid and a flexible polymer are substantially stiffer than expected from the sum of the moduli of the separate networks [270]. Rigid fiber networks by themselves are expected to be soft at low deformation because they deform in a non-affine manner, where the elasticity is governed by fiber bending [271]. The presence of a background network of flexible polymer suppresses these non-affine bending deformations [270]. Unfortunately this prediction is difficult to directly test in live-cell experiments because it is very challenging to specifically remove one cytoskeletal network without also affecting the others. Microtubule depolymerization is for instance well-known to activate acto-myosin contraction by the release of the microtubule-associated guanine nucleotide exchange factor GEF-H1 [272]. At large strains, there is some evidence of mechanical synergy between the cytoskeletal networks. Epithelial cell layers are able to undergo extreme stretching under constant tension ('active superelasticity') by strain-softening of the actin cortex followed by re-stiffening thanks to the keratin intermediate filament network [273]. Physical crosslinking between actin and keratin is essential for the maintenance of epithelial stability [274]. The ability of flexible polymers to suppress bending deformations of rigid polymers has the interesting consequence that the rigid polymers are reinforced against compressive loads [275]. Under compressive loading, rigid polymers exhibit an Euler buckling instability at a critical compression force $f_c \sim 10\kappa/L^2$, where L is the polymer length. For microtubules, the critical compression force is only of order 1 pN [276]. In the cell, however, microtubules can bear 100-fold larger compression forces because the surrounding actin and intermediate filament cytoskeleton constrains microtubule buckling [277, 278]. This is consistent with the so-called tensegrity model, which states that cellular shape stability is achieved via a balance between actin filaments and intermediate filaments loaded under tension, and microtubules and thick actin bundles under compression [279].

4.2.2. CELL-FREE STUDIES

MECHANICAL PROPERTIES OF INDIVIDUAL CYTOSKELETAL COMPONENTS

Live-cell mechanical measurements can be difficult to interpret in quantitative terms because they are sensitive to the amplitude, type and rate of deformation, geometry of the mechanical probe, the probed location in the cell, and the cell's extracellular environment [280]. Cell-free studies provide a useful complement because they permit quantitative measurements of the mechanical properties of isolated cytoskeletal components, both at the single filament and at the network level.

At the single filament level, cytoskeletal biopolymers have been bent, stretched, compressed, and twisted using optical and magnetic tweezers [281, 282, 283, 284], atomic force microscopy [285, 286], and microfluidic devices [287]. Actin filaments and microtubules have a high bending and stretching rigidity, but they break at rather low tensile strains (~ 150% strains) [288, 289]. Moreover, actin filaments become more fragile under torsion [288] and microtubules soften upon repeated bending [287]. This fragility is likely related to the fact that actin filaments and microtubules are made of globular subunits. By contrast, intermediate filaments are made of fibrous subunits held together by extensive lateral interactions. Intermediate filaments easily stretch and bend due to their open structure and they can withstand tensile strains of more than 200% before rupture [285]. Similar to a car's safety belt, intermediate filaments are soft under small and slow deformations but stiff under large and fast deformations [281]. Recent evidence suggests that different intermediate filament proteins respond differently to tensile loads. When subjected to stretch-relax cycles, keratin filaments elongate with every cycle but keep the same stiffness, whereas vimentin filaments soften with every cycle but always return to the same initial length [290]. It appears that vimentin stretches by monomer unfolding [291], whereas keratin filaments stretch by viscous sliding of subunits [290]. It will be interesting to see what further diversity may be generated by co-polymerization of different intermediate filament proteins and by post-translational modifications.

On the network level, mechanical properties of cytoskeletal filaments are most conveniently probed by either bulk rheology or microrheology. In bulk rheology, cytoskeletal networks are sheared between the two parallel plates of a rheometer, providing a readout of the macroscopic viscoelastic response [292]. Microrheology instead probes the localized viscoelastic response of a material by tracking the motion of embedded probe particles, either in response to thermal fluctuations (passive microrheology [293]) or to a force applied by optical or magnetic tweezers (active microrheology [294]). The mechanical response of cytoskeletal networks is determined by an interplay of the stiffness of the filaments and their interactions.

EFFECTS OF CROSSLINKING ON THE MECHANICAL PROPERTIES OF CYTOSKELETAL NETWORKS

Actin filaments and microtubules form entangled networks that easily fluidize under shear due to filament disentanglement [295, 296, 297]. Filament crosslinking via crosslinker proteins prevents this fluidization and causes the networks to strain-stiffen. This strain-stiffening response is only moderate for microtubules because of their high rigidity and because shearing causes force-induced unbinding of crosslinks [295, 294]. Actin networks exhibit more pronounced strain-stiffening because their elasticity is affected by the entropic elastic response of the filaments to tensile loading [298]. Tensile loading reduces the conformational entropy of actin filaments, pulling out bending fluctuations, causing entropic strain-stiffening [299]. Increased crosslink densities shift the onset of strain-stiffening to smaller shear strains because less excess length is stored in bending fluctuations when the crosslinks are more closely spaced [298]. Some crosslinker proteins (most notably filamin) are so large that their compliance directly contributes to the network response. Crosslinker extensibility increases the rupture strain by postponing the point where the actin filaments experience tensile loading [300, 301]. Bundling of actin filaments, which is common at high concentrations of crosslinker proteins, suppresses entropic elasticity. Bundled actin networks still strain-stiffen [298], but by an enthalpic mechanism that involves a transition from soft bending modes at low strains to rigid stretching modes at high strain [302, 303]. Under compression, actin and microtubule networks soften due to filament buckling [246]. For branched actin networks, compressive softening has been shown to be reversible, likely because the buckled filaments are prevented from collapsing by their connections with the network [304].

The mechanical properties of intermediate filament networks differ in various respects from those of actin and microtubule networks. First, intermediate filaments form strain-stiffening networks even in absence of any crosslinker proteins, as demonstrated for vimentin, neurofilaments, desmin, and keratin [305, 306]. The filaments spontaneously form crosslinks mediated by electrostatic interactions between their disordered C-terminal tails. Upon tail truncation, the networks no longer strain-stiffen [307, 308, 309]. The effective crosslink density depends on the concentration of divalent cations such Mg^{2+}, Ca^{2+} or Zn^{2+} [307, 306, 310, 311] and is sensitive to the buffer ionic strength and pH [312]. For keratins, there are additional hydrophobic interactions between the central rod domains that stiffen the networks [214]. Second, intermediate filament networks have much larger rupture strains than actin and microtubule networks as a consequence of the larger single-filament extensibility. This is reflected in the dependence of the elastic modulus K on the applied shear stress σ. While actin networks only exhibit an entropic strain-stiffening regime where K increases as $\sigma^{\frac{3}{2}}$, intermediate filament networks exhibit an additional enthalpic regime where K increases more weakly, reflecting strain-induced filament alignment [305]. After yielding, intermediate filament networks can even recover their initial shear modulus, likely by the re-establishment of tail-tail crosslinks [313, 308].

MECHANICAL CHARACTERIZATIONS OF COMPOSITE CYTOSKELETAL NETWORKS

Recently there has been increasing attention for the mechanical properties of cytoskeletal composites. Reconstitution of composite networks requires careful tuning of the buffer conditions since the different cytoskeletal polymers are traditionally reconstituted in their own optimized buffer conditions. Intermediate filaments are especially sensitive to solution pH and ionic concentrations, forming filaments of different widths and protein mass-per-length ratios depending on the buffer [314]. Until now nearly all studies of composite networks have focused on two-component composites of cytoskeletal filaments co-polymerized in the absence of crosslinkers. At small strains, co-entangled composites (specifically combinations of actin/vimentin [315], actin/keratin [316, 317], actin/microtubules [318], and vimentin/microtubules [319]) have generally been shown to exhibit a simple additive viscoelastic response. However, there is evidence for direct interactions of vimentin filaments with actin filaments [320] as well as microtubules [321], which could potentially influence the network rheology. These interactions could potentially lead to cell-type specific cytoskeletal crosstalk, since they are mediated by the C-terminal tail of intermediate filaments that shows large length and sequence variations between different intermediate filament proteins. It was furthermore shown that vimentin can impose steric constraints that hamper actin network formation and thus cause network weakening [322]. At large strains, there is evidence of synergistic enhancement of the mechanical properties in certain cytoskeletal composites. For actin/keratin composites, the strong strain-stiffening response of the keratin network was found to dominate the high-strain response of the composites [317]. For actin/microtubule composites, microtubules were shown to promote strain-stiffening of the actin networks, even at low density [323, 324]. This effect was explained by the ability of rigid microtubules to suppress nonaffine bending fluctuations of actin filaments. It will be interesting to explore how these synergies are modified in the presence of crosslinkers. Recent work showed that when actin filaments and microtubules are crosslinked to each other by biotin-streptavidin, the composite is more elastic than when both filaments are independently crosslinked [325].

To the best of our knowledge, there has so far been only one study of three-component networks combining actin, vimentin and microtubules [326]. It was shown by microrheology that the linear elastic modulus of the composite is dominated by actin, with little contribution from either microtubules or vimentin. Yet vimentin was shown to significantly extend the elastic regime to longer timescales. The authors proposed that the vimentin network that fills in the pore spaces of the actin network [327] slows stress relaxation by constraining actin reptation. More work is needed to systematically study cytoskeletal composites and to explore the impact of crosslinking with cytolinker proteins such as plectin. Due to their high molecular weight these proteins are difficult to purify. To circumvent this problem, one can engineer proteins that contain only the cytoskeletal binding domains separated by a spacer [328]. Using this approach, our group recently found that crosslinking with a plectin-mimetic crosslinker causes synergistic stiffening of actin-vimentin composites [329].

4.3. CELL CONTRACTILITY

4.3.1. LIVE-CELL STUDIES

ACTO-MYOSIN CONTRACTION IS THE DRIVING FORCE BEHIND CELL MIGRATION

The actin cytoskeleton is the engine behind cell migration[330]. Depending on the extracellular environment, cells can switch between different mechanisms that use actin-based forces in different ways[331]. Fibroblasts and other adherent cells perform *mesenchymal migration*, which relies on integrin-based adhesion to the extracellular matrix (ECM). The process occurs via a four-step cycle. First, actin polymerization pushes against the membrane at the leading edge, producing lamellipodia in cells migrating on flat rigid surfaces or pseudopodia in cells migrating in 3D extracellular matrices. Next, the cell generates integrin-based adhesions with the substrate that connect to the contractile machinery of acto-myosin stress fibres. Through a combination of pulling from the front and squeezing from the rear, the cell body moves forward. Finally, old adhesions are detached from the substrate or dissolved at the trailing edge [332]. The contractile forces involved in cell migration have been measured through the traction forces exerted on the substrate. This is usually done by adhering cells to a hydrogel substrate with known mechanical properties, such as polyacrylamide. By measuring the displacements of fluorescent tracer particles incorporated in the gel with fluorescence microscopy, one can computationally infer the traction forces using continuum mechanics models [333]. Adherent cells that experience strong confinement utilize a *nuclear piston* mechanism where actin-myosin contraction in front of the nucleus pulls the nucleus forward. Since the nucleus divides the cell in forward and rearward compartments, it acts as a piston that pressurizes the forward compartment and drives forward a cylindrical lobopodial protrusion [334]. Weakly adherent cells such as leukocytes and physically confined fibroblasts and cancer cells perform *amoeboid migration*, characterized by spherical membrane blebs at the leading edge (reviewed in [335]). Blebs are created by myosin-driven contraction of the actin cortex underneath the cell membrane, which builds up hydrostatic pressure in the cytoplasm. Local rupture of the actin cortex or its attachment to the membrane causes local membrane delamination, pushing forward a membrane bleb. Over time the actin cortex regrows under the bleb membrane and myosin contraction drives bleb retraction. Confinement can also induce other migration modes that require little substrate adhesion. Cells can move via friction generated by actin flows within the cortex generated by myosin contraction and actin turnover [336], and some tumor cells can still migrate by using active transport of water from the front to the back of the cell to propel themselves forward (*osmotic engine* model [337]).

THE ROLE OF MICROTUBULES AND INTERMEDIATE FILAMENTS IN ACTO-MYOSIN MEDIATED CELL CONTRACTILITY

While not being components of the contractile machinery, both microtubules and intermediate filaments are important for regulating cell contraction. Microtubules negatively regulate the assembly and contractility of actin stress fibers by sequestering GEF-H1, an activator of the small GTPase Rho, in an autoinhibited state [338]. Microtubule depolymerization by nocodazole releases active GEF-H1, leading to a global increase of contractility as measured by traction force microscopy [339]. During both mesenchymal and amoeboid migration, microtubule depolymerization and consequent GEF-H1 is tightly regulated so that actin contractility can be precisely timed and localized in a mechanosensitive manner [340, 341, 342]. Besides biochemical regulation, it is likely that mechanical synergy is also involved in microtubule-based control of actin contractility, since microtubules are able to absorb some of the forces from the contractile actin cytoskeleton [279].

Intermediate filaments likewise regulate actin-based cell contraction by a combination of mechanical synergy and biochemical signaling. In cells migrating on flat surfaces, vimentin has been reported to inhibit stress fiber assembly and contractility through down-regulating GEF-H1 and RhoA [343]. Nevertheless, traction force measurements have shown that vimentin-null cells are less contractile than their wild-type counterparts [327]. Taken together with the observation that vimentin filaments orient traction stresses along the front-rear axis, this suggests a mechanical synergy where vimentin helps build up and transmit larger contractile forces [344]. Recently it was shown by structured illumination microscopy and electron microscopy that vimentin filaments are closely associated with actin stress fibers, forming meshworks that wrap around stress fibers or co-align with them [327, 233]. Physical coupling between the two systems is dependent on the cytolinker protein plectin [345] Interestingly, it was recently shown that plectin binds vimentin in response to acto-myosin pulling forces [346]. The mechanism for this mechanosensitivity is unknown but could involve catch bonding [347].

Plectin-mediated coupling of actin and vimentin was recently shown to be essential for cells migrating via the nuclear piston mechanism [346]. The vimentin network helps transmit acto-myosin pulling forces to the nucleus, thus enhancing the pressure in the front of the nucleus. It is not yet known whether intermediate filaments also influence cell migration modes driven by contractile activity of the actin cortex, but recent observations that vimentin and F-actin are associated within the cell cortex suggest this is likely [327].

4.3.2. CELL-FREE RECONSTITUTION STUDIES

There is an extensive body of work using cell-free reconstitution to elucidate the mechanisms by which myosin II motor proteins contract actin networks (reviewed in [206]). The contraction mechanism has been found to depend on the actin network connectivity, which is controlled by filament length and by crosslinking. Well-connected networks of long filaments contract because myosins generate compressive stress that causes the actin filaments to buckle and break [348]. By contrast, when the filaments are short, myosins contract the network by polarity sorting, transporting and clustering actin filament plus ends to form polar actin asters [349]. In both cases, the length scale of contraction is set by the network connectivity. Global network contraction requires the actin network to be crosslinked above a critical percolation threshold [350]. However, excessive crosslinking will prevent contraction by making the network too rigid [351]. As described above, several cell migration mechanisms rely on myosin-driven contraction of the actin cortex. Recently several groups have been able to reconstitute biomimetic actin cortices by co-encapsulating actin and myosin inside cell-sized lipid vesicles. For weak actin-membrane attachment, the network detaches from the membrane upon contraction [352]. In case of stronger attachment, myosin contraction can cause membrane blebbing [353]. Cortical flows that are important for driving amoeboid migration require not only myosin activity, but also network remodeling through actin depolymerization [354]. Under particular conditions, crosslinked actin-myosin cortical networks in emulsion droplets have been observed to exhibit cortical flows [355], likely because myosin can promote actin turnover [356]. Cell extracts, which contain additional proteins to promote actin turnover, also exhibit cortical flows when encapsulated in emulsion droplets [357, 358, 359]. When these droplets are confined, the myosin-driven cortical flows can propel the droplets forward due to friction with the channel walls, mimicking amoeboid migration of nonadhesive cells [360].

So far only few studies have looked at the effect of intermediate filaments or microtubules on contraction of actin-myosin networks. The addition of a vimentin network that interpenetrates an actin network has been shown to promote myosin-driven contraction by increasing the network connectivity [361]. Similarly, also the addition of microtubules has been shown to promote uniform macroscopic myosin-driven contraction [362].

4.4. FRONT-REAR POLARIZATION

4.4.1. LIVE-CELL STUDIES

CROSSTALK BETWEEN ACTIN AND MICROTUBULES GOVERNS CELL POLARIZATION IN MIGRATION

Directed cell migration requires the breaking of cell symmetry to generate a cell front and a cell rear along an axis aligned with the direction of locomotion. Until now, the role of cytoskeletal crosstalk in front-rear polarity has mostly been studied in the context of 2D mesenchymal cell migration [363]. It is long known that the microtubule cytoskeleton is essential for maintaining a polarized distribution of actin-based forces with actin polymerization in the front and myosin II-based contraction forces in the cell body and rear [364]. Microtubules align along the axis of cell movement with their plus ends oriented towards the leading edge. They appear to stimulate actin-driven cell protrusion by multiple mechanisms. They activate Rac1 and inhibit Rho, therefore promoting actin polymerization and preventing myosin-II-driven contractility at the leading edge. Moreover, actin filaments have been observed to grow directly from microtubule tips toward the leading edge in growth cones of neurons, with the help of protein complexes involving APC and CLIP-170 [365, 366]. There is an interesting actin/microtubule reciprocity, though, since the microtubules require guidance along actin stress fibers to reach the leading edge. This guidance requires actin-microtubule crosslinking, for instance by ACF7, Growth Arrest-Specific Proteins (Gas2L1), CLIP-associating proteins (CLASPs) or drebrins (reviewed in [226]). These proteins target growing microtubule plus ends by binding to EB (end-binding) proteins, and all of them except drebrin also possess a microtubule-lattice-binding domain. When these crosslinkers are depleted from cells, microtubules cease to grow along actin stress fibers and the microtubule array loses its front-rear polarity [367, 368]. Persistent cell migration is strongly hampered as a consequence, not only because actin-based protrusions are misregulated, but also because microtubules fail to reach cortical microtubule stabilizing complexes (CMSCs) that surround focal adhesions [369]. Microtubule dynamics have been shown to regulate amoeboid cell migration by locally promoting the retraction of protrusions. In migrating dendritic cells, microtubule depolymerization within protrusions distant from the microtubule organizing center triggers actomyosin contractility, which is controlled by RhoA and its corresponding exchange factor Lfc [342]. Tethering and stabilization of microtubule plus ends by CMSC binding is required for microtubule-dependent focal adhesion turnover, which is essential for migration (reviewed in [229]).

It is not yet clear how these crosstalk mechanisms are modified when cells perform 3D mesenchymal migration, but likely the core mechanisms are shared. One important new factor in 3D migration is that microtubules have a more important mechanical role and are needed to support pseudopodia [269]. A second important new factor is that the rigidity of the nucleus hampers migration through small pores. It was recently shown that microtubules anchored to the nucleus play an important role in active transport of MT1-MMP, which degrades the extracellular matrix, to the cell surface where it drives extracellular matrix proteolysis in front of the nucleus [370].

INTERMEDIATE FILAMENTS CONTRIBUTE TO CELL POLARIZATION VIA CROSSTALK WITH ACTIN AND MICROTUBULES

Although intermediate filaments lack intrinsic polarity, they do contribute to directed mesenchymal migration [227]. When the vimentin network is disassembled using peptides or when vimentin expression is knocked down, cells lose their polarity and lamellipodia appear all around the cell [371]. Vimentin forms closely associated parallel arrays with microtubules in migrating cells [372, 373]. Experiments conducted using vimentin-deficient mouse embryonic fibroblasts attached to polarized and non-polarized protein micropatterns demonstrated that the lack of vimentin alters microtubule organisation, disrupting cell polarity [374]. The two cytoskeletal networks organize in an interdependent manner. The vimentin distribution is polarized by a collaboration between active motor-driven transport along microtubules and actin-driven retrograde flow [375]. Conversely, since the vimentin network is about 10-fold more long-lived than the microtubule network, it can serve as a template for guiding microtubule growth along previous microtubule tracks [344]. This provides a feedback mechanism to sustain front-rear polarity. Moreover, the alignment of the vimentin network with the polarity axis mechanically integrates actin-based forces and orients them to promote directional migration [376]. This mechanical integration is probably aided by vimentin-microtubule crosslinker proteins such as plectin and APC [377]. In addition to this mechanical role, there is growing evidence for signalling functions of intermediate filaments in cell migration (reviewed in[6]). At the cell periphery, there is for instance Rac-mediated crosstalk between vimentin and actin, where Rac causes vimentin disassembly by controlling the phosphorylation of vimentin at Ser-38, a p21-activated kinase phosphorylation site, promoting actin-driven membrane protrusion [371]. Intermediate filaments also regulate focal adhesion clustering and turnover by binding integrins and via biochemical signalling [378].

4.4.2. CELL-FREE RECONSTITUTION STUDIES

POLARIZATION CROSSTALK STUDIES INVOLVING INTERMEDIATE FILAMENTS

Several studies have explored how interactions between two different cytoskeletal filament types may contribute to the front-rear polarity of migrating cells. These studies mostly used surface assays where one or both cytoskeletal filaments were surface-anchored to facilitate imaging and control the geometry of interaction. Here, we are able to probe the crosstalk involved in filament polymerization, an essential component of cell polarization. Just a few of these investigated the interplay of intermediate filaments with actin or microtubules. When surface-anchored microtubules are grown in the presence of an entangled vimentin network, they were found to be stabilized against depolymerization by direct interactions with vimentin filaments [321]. Vimentin attachment reduced the catastrophe frequency and induced rescue of depolymerizing microtubules. However, in the absence of crosslinker proteins, these interactions were found to be short and infrequent. It is likely that vimentin-microtubule crosslinkers such as APC and plectin create more drastic effects on vimentin and microtubule polymerization. Interestingly, the vimentin-binding region of APC by itself was shown to promote vimentin polymerization [377], which may perhaps promote vimentin polymerization along microtubules. It was recently shown that actin and vimentin filaments do not interact in the absence of crosslinkers, but when an engineered plectin-mimicking crosslinker was added, actin filaments polymerized along surface-anchored vimentin filaments [329].

MUTUAL REGULATION OF POLARIZATION BY ACTIN AND MICROTUBULES

A larger set of studies investigated the interplay of microtubules with different actin network structures designed to mimic structures found at front of crawling cells. Branched or densely entangled actin network that mimic the dense actin array in the lamellipodia were shown to act as a steric barrier for microtubule growth[379, 380, 381]. However, when microtubules were crosslinked to actin by Tau protein, they were able to generate sufficient polymerization force to penetrate dense actin barriers [381]. By contrast, when actin was arranged in stiff bundles that mimic actin stress fibers and bundles in filopodia, steric interactions were instead found to promote alignment and growth of microtubules along the actin bundles [379, 381]. Actin-microtubule crosslinking proteins such as ACF7, Gas2L1, or CLASP2 were shown to promote actin-guided microtubule growth by allowing growing microtubules to be captured by and zippered along the actin bundles [379, 381, 382, 383, 328, 384]. Conversely, microtubules can also influence actin polymerization. Microtubule-lattice binding crosslinkers can induce guided polymerization of actin filaments along microtubule [383, 385]. Microtubule-tip binding crosslinkers can induce active transport of actin filaments by the growing microtubule tip [328, 386]. Computer simulations and theoretical modeling showed that this transport is driven by the affinity of the cross-linker for the chemically distinct microtubule tip region [386]. These interactions may potentially enable growing microtubules to relocate newly nucleated actin filaments to the leading edge of the cell and thus boost migration. Altogether, these studies suggest that coupled polarization of the three cytoskeletal filament systems can at least partly be understood on the basis of a mechanical interplay.

4.5. COLLECTIVE MIGRATION & INTERCELLULAR ADHESIONS

4.5.1. LIVE-CELL STUDIES

INTERCELLULAR ADHESIONS ESTABLISH MECHANICAL COUPLING AMONG CELLS DURING COLLECTIVE MIGRATION

Many cell types have the ability to synchronize their movement and perform collective migration. Collective migration is important for organogenesis and wound healing but also contributes to cancer metastasis. Depending on cell type and tissue context, different modes of collective migration can emerge. Epithelial cells tend to move as sheets adhered to the extracellular matrix [387], while cancer cells often migrate as three-dimensional strands or clusters through tissues [388]. Remarkably, multi-cellular migrating structures behave similarly to liquid crystalline materials and undergo solid-to-liquid transitions in response to confinement. These jamming/unjamming transitions are linked to cell and nucleus shapes [169, 389] and are determined by molecular interactions that regulate cell-matrix and cell-cell adhesions [11, 390, 120]. Traction force measurements for epithelial and endothelial monolayers have shown that cells within the monolayer tend to migrate in the direction in which the normal stress is greatest and the shear stress least [391]. This mechanism of collective cell guidance called *plithotaxis* critically relies on mechanical coupling between the cells by cell-cell adhesions. Plithotaxis is regulated by the tumor suppressor protein merlin, which coordinates polarized Rac1 activation and lamellipodium formation at the multicellular scale [392]. We speculate that, since Rac1 is an important shared regulator of all three cytoskeletal systems, there could be crosstalk with intermediate filaments and microtubules in plithotaxis. At the same time, intercellular adhesions help collectively migrating cells to establish supracellular polarization with leader cells at the front and follower cells behind [393]. The leader cells explore the tissue environment using focal adhesions, find the path, and - if necessary - carve out a path by degrading the ECM. Cancer cells dynamically rearrange leader and follower positions during collective invasion to cope with the large energy usage of the leader cells [394].

Epithelial and endothelial cells interact through mechanosensitive *adherens junctions* based on classical cadherins and VE-cadherins, respectively, which connect to the actin cytoskeleton via α-catenin and vinculin[393, 395]. Endothelial cells are additionally connected by complexus adhaerentes junctions that connect to vimentin via VE-cadherin [396]. Epithelial cells are additionally connected by *desmosomes* based on desmosomal cadherins that connect to the keratin intermediate filament cytoskeleton via the adaptor proteins desmoplakin, plakophilin, and plakoglobin [397, 398, 395]. The desmosomal junctions are expendable under homeostatic conditions but strictly required for preserving cell-cell adhesion under mechanical stress [399]. As reviewed elsewhere [6, 400], there is growing evidence that cytoskeletal crosstalk is important for the organization, dynamics and mechanoresponsiveness of intercellular adhesions during multicellular migration, although the exact extent is not clear.

CYTOSKELETAL CROSSTALK MEDIATES INTERCELLULAR ADHESION DYNAMICS

Keratin intermediate filaments and actin jointly influence desmosomes and adherens junctions because they are crosslinked via plectin. In epithelia, plectin organizes keratin into a rim-and-spoke configuration where contractile forces generated by acto-myosin are balanced by compressive elements provided by the keratin network, thus balancing internal tension and stabilizing cell-cell contacts [274]. Deletion of plectin therefore causes perturbations of both desmosomes and adherens junctions. Although endothelial cells do not have desmosmes, also here plectin-mediated crosslinking between F-actin and vimentin intermediate filaments regulates adherens junction strength and tissue integrity [401]. Migrating epithelial cells need to dynamically rearrange their adhesive contacts. Desmosome remodeling is dependent on both actin and keratin. Assembly of desmosomes at the leading edge and subsequent transport to the lateral sides is mediated through extensive actin remodelling, while more matured desmosomes are guided via keratins to the cell center to eventually disassemble [402]. Intermediate filaments have an important mechanical role in distributing actin-myosin based forces, similar to their role in single-cell migration. Collective movement of both embryonic cells and astrocytes with proper leader-follower dynamics was shown to be highly dependent on this mechanical synergy of actin and intermediate filaments [403, 404]. 3D tumor cultures of *ex vivo* breast cancer demonstrated heterotypic keratin expression between leader and follower cells [27], which was speculated to be necessary to regulate individual cytoplasmic viscoelasticity and mechanical coupling through desmosome anchoring during collective invasion [405]. Invasion assays of epithelial cancers with manipulated keratin expressions also indicate that keratin expression can regulate migration mode; keratin-14-positive cells are leaders of migrating strands in organoid carcinoma assays, while keratin-8 and keratin-18 depletion can shift migration from individual to collective [27, 406]. Interestingly, keratins can also organize asymmetrically in migrating cells and localize in lamellipodia to support polarization and invasive phenotype, which is mediated by actin filaments [407].

There is ample evidence that microtubule-actin crosstalk affects adherens junctions via mechanisms similar to those observed for focal adhesions. Adherens junctions contain multiple proteins that bind microtubule plus ends, including APC, ACF7 and CLASP [408, 409]. This allows microtubules to promote myosin II activation and local concentration of cadherin molecules [410] and facilitates trafficking of junctional components to the cell surface [411, 412]. At the same time, microtubules promote junctional actin assembly by promoting liquid-liquid-phase separation of the actin nucleator cordon bleu (Cobl) [413]. During collective migration in vivo, it was found that cell-cell contacts differed in their requirement for dynamic microtubules along the leader-follower axis [414]. Cells of the leading domain remained cohesive in the absence of dynamic microtubules, whereas dynamic microtubules were essential for the conversion of leader cells to epithelial followers. Interestingly, it was recently shown that physical confinement of collectively migrating cancer cells can induce the dissociation of leader cells by actin-microtubule crosstalk [415]. Confinement-induced microtubule destabilization releases and activates GEF-H1, which promotes RhoA activation and results in leader cell detachment.

4.5.2. CELL-FREE RECONSTITUTION STUDIES

Interactions between cytoskeletal filaments and cell-cell adhesion complexes are relatively unexplored in reconstituted systems. Adherens junctions are based on transmembrane cadherin adhesion receptors. The extracellular domains of cadherins on adjacent cells form adhesions by homodimerization. The cytosolic domains of cadherins bind β-catenin, which in turn binds α-catenin [416]. Biochemical studies showed that actin filaments do not bind directly to cadherins, but are tethered indirectly via α-catenin [417, 418]. In solution, α-catenin does not interact with actin filaments and the cadherin-β-catenin complex simultaneously [419]. However, under tension α-catenin stably connects the cadherin-catenin complex to actin filaments via a directionally asymmetric catch bond [420, 421]. This mechanosensitivity implies directional regulation of cell-cell adhesion in response to tension, which may connect to cooperative phenomena such as (un)jamming and plithotaxis mentioned above. Biochemical studies have shown that α-catenin influences the organization of junctional actin both directly, by inhibiting barbed-end growth, and indirectly, by interactions with various actin-binding proteins including Arp2/3 [422]. With the complexity of cadherin-actin interactions starting to become uncovered, it will be interesting to study how crosstalk with microtubules may further regulate adherens junctions. Recently a first study in this direction was able to reconstitute the effect of microtubules on junctional actin nucleation, as was described above in live-cell studies [413]. When dynamic microtubules were incubated together with G-actin and Cobl, actin filaments were found to be nucleated via Cobl condensates from both the tips and lattice of microtubules.

Regarding desmosomes, so far there have been mainly biochemical and structural studies, but few cell-free biophysical studies. Biochemical studies of the desmosomal cadherins showed that they form cell-cell connections via heterodimerization of the extracellular domains of desmogleins and desmocollins [423]. Single-molecule force spectroscopy by AFM showed that the binding force is 30 to 40 pN [424]. The cytoplasmic domains of desmosomal cadherins bind plakoglobin and plakophilins, an interaction that has also been reconstituted [425]. Plakoglobin and plakophilins in turn bind to desmoplakin [426], which finally binds keratins. Biochemical and structural studies showed that desmoplakin interacts via its C-terminus to the rod domain of keratin [427, 428]. To the best of our knowledge, there are no cell-free studies addressing cytoskeletal crosstalk with desmosomes.

4.6. PLASTICITY OF CELL MIGRATION

4.6.1. LIVE-CELL STUDIES

CELLULAR PLASTICITY IS MEDIATED THROUGH FOCAL ADHESIONS

Most terminally differentiated cells such as epithelial and stromal cells migrate only during morphogenesis. However, tissue injury can induce cell plasticity. Mature cells can reenter the cell cycle and change their phenotype guided by paligenosis programs [429]. Unfortunately plasticity can also contribute to disease. For instance, malignant cancer cells are often hyperplastic, contributing to their invasiveness. A well-studied example of cell plasticity is epithelial-mesenchymal transition (EMT), a reversible process in which epithelial cells lose polarity through cytoskeletal remodelling, individualize and gain motility. EMT is a critical process in embryonic development and wound healing, but it also plays a key role in fibrosis and cancer invasion. EMT and the reverse mesenchymal-epithelial transition (MET) are influenced not only by biochemical cues, but also by mechanical properties of the ECM [430, 431].

Cells sense the mechanical properties of the ECM through their acto-myosin cytoskeleton at focal adhesions, mediating mechanotransduction and activating downstream plasticity mechanisms in response to environmental changes. Focal adhesions are based on integrin adhesion receptors that interact with the ECM through their extracellular domains and with the actin cytoskeleton through their cytoplasmic tails [432]. The actin-integrin connection is mediated through talin and kindlin (reviewed in [433]). Single integrins form small and transient junctions, but mechanical stimulation reinforces integrin adhesions by causing maturation into large focal adhesions. Upon mechanical stimulation, talin and kindlin undergo conformational changes that expose cryptic binding sites for additional cytoskeletal and signalling proteins [432]. Mechanical stimulation further reinforces focal adhesions by inducing actin polymerization [434]. Variations in the biochemical composition and physical properties of the ECM can elicit different 3D cell migration modes characterized by different amounts of cell-ECM adhesion [331, 435]. Highly crosslinked and dense matrices elicit lobopodial migration, characterized by a high number of focal adhesions and high actomyosin contractility. Less dense, fibrous environments elicit mesenchymal migration with a characteristic front-to-rear gradient of focal adhesions. In low-confining areas that lack adhesion sites, cells depend on bleb formation to drive themselves forward, a mechanism that does not require focal adhesions [331].

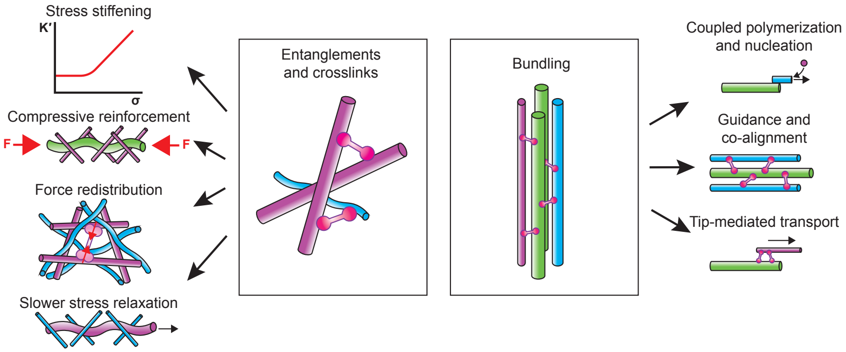

Figure 4.3: Schematic of the two general cytoskeletal crosstalk mechanisms and their effect on cytoskeletal biophysics. *Entanglements* and *crosslinks* regulate stress stiffening, compressive reinforcement, force distribution and slower stress relaxation. *Bundling* regulates coupled polymerization and nucleation, guidance and co-alignment, and tip-mediated transport of filaments. Actin (magenta), microtubules (green), intermediate filaments (cyan) and crosslinkers (pink).

Not much is known about the role of cytoskeletal crosstalk in migration plasticity. Microtubules are likely involved through their feedback interactions with actin near focal adhesions. It was recently shown that higher substrate rigidity promotes microtubule acetylation through the recruitment of α-tubulin acetyltransferase (α TAT) to focal adhesions by talin [233]. In turn, microtubule acetylation tunes the mechanosensitivity of focal adhesions by promoting the release of GEF-H1 from microtubules to activate RhoA and thereby promote actomyosin contractility [233]. In breast cancer cells, actin-microtubule crosstalk near focal adhesions via the scaffolding protein IQGAP1 was demonstrated to promote invasion in wound healing and transwell assays [436]. In fibrosarcoma cells, the microtubule-destabilizing protein stathmin was shown to influence migration mode switching [437]. Increased stathmin activity, and as a result less stable microtubule networks, promoted amoeboid-like migration, while phosphorylation of stathmin led to a more elongated migratory phenotype. Besides crosstalk near focal adhesions, microtubules can also influence migration mode switching through mechanical effects. In confined or compressed cells, microtubules are stabilized through CLASP2 localization to the lattice, providing a mechanosensitive pathways for cells to adapt to highly constricting environments [268].

CONTROL OF MIGRATION MODES BY CYTOSKELETAL CROSSTALK AT FOCAL ADHESIONS

The intermediate filament protein vimentin is considered a key cellular plasticity regulator and marker of tumor cell malignancy, especially based on its general upregulation in EMT and in motile cancer cells [438]. Carcinoma cells in addition express integrin $\alpha6\beta4$, which recruits vimentin to focal adhesions through its binding to plectin, promoting a 3D invasive phenotype switch [439]. Together with nuclear lamins, vimentin contributes to migration plasticity through regulation of nuclear deformation, for instance allowing for a transition towards amoeboid-like and faster migration in Hela cells and melanoma cells when encountering confinement [82, 225]. Moreover, cells migrating under high confinement use their nucleus as a piston to squeeze through small pores. This complicated pulling mechanism is regulated through crosstalk between the vimentin cage around the nucleus and actomyosin in front of the nucleus [334].

4.6.2. CELL-FREE RECONSTITUTION STUDIES

Understanding the molecular basis of migration plasticity is an enormous challenge since integrin-based matrix adhesions contain over 100 types of molecules that are potentially mechanosensitive [440]. One of the first mechanotransduction events during adhesion maturation is stretching of talin, followed by vinculin binding and activation. This core process was elegantly reconstituted by overlaying a network of actin-myosin bundles mimicking stress fibers on a talin-micropatterned surface [441]. It was shown that direct binding of the contractile actin-myosin network to talin was sufficient to stretch the protein and induce the association and activation of vinculin. Talin binding facilitates vinculin activation by allosterically weakening the head–tail interaction that keeps it in an auto-inhibited conformation [442]. Exposure of the actin-binding tail induces a positive feedback that reinforces the connection with actin [441]. Using the same assay, it was shown that activated vinculin can interact with Arp2/3 complex-mediated branched actin networks and modify their organization by crosslinking actin filaments into bundles [443]. This is likely an important step towards focal adhesion maturation. Single-molecule studies showed that vinculin forms a directionally asymmetric catch bond with F-actin [444]. In this way vinculin can organize the polarity of the actin cytoskeleton and contribute to front-rear asymmetry in migrating cells. Recently the interaction of integrins, talin and kindlin, another major focal adhesion regulator, was reconstituted on giant unilamellar vesicles [445]. It was shown that phosphoinositide-rich membranes recruit talin and kindlin, which then cause the formation of large integrin clusters that can recruit actin-myosin. Another study showed that membrane-bound talin can also activate vinculin and the two proteins together can link actin to the membrane [446].

Cell-free reconstitution studies suggest that the actin cytoskeleton itself also contains proteins that mediate mechanotransduction. An example is filamin A (FLNA), a large multi-domain scaffolding protein that cross-links actin filaments and binds numerous proteins via cryptic binding sites along its length. Using reconstituted actin networks crosslinked with FLNA, it was shown that mechanical strain on the FLNA crosslinks alters its binding affinity for its binding partners [447]. Both externally imposed bulk shear and contraction by myosin-II increased binding of the cytoplasmic tail of β-integrin while it weakened binding of FilGAP, a GTPase that inactivates Rac. Mechanical strain on FLNA can thus stabilize extracellular matrix binding and at the same time influence actin dynamics through Rac activity.

4.7. THE ROAD AHEAD

Cytoskeletal crosstalk is increasingly recognized as a major determinant of cell migration. Coupling between the actin, microtubule and intermediate filament cytoskeleton influences cell migration by regulating cell deformability, contractility, front-rear polarity and migration plasticity. Coupling of filaments through entanglements, crosslinking and bundling regulates a variety of mechanisms that mediate cellular mechanics and cytoskeletal dynamics involved in these migration strategies (Figure 4.3). To complicate matters, there is growing evidence that a fourth cytoskeletal protein family, the septins, also strongly impacts cell migration. Septins are well-equipped to mediate cytoskeletal crosstalk since they can bind to the cell membrane, actin and microtubules [448]. Recent research demonstrated roles of septins in mesenchymal and amoeboid single-cell migration [449, 450] and in the regulation of endothelial and epithelial cell-cell adhesion [451, 452]. In Chapter 5 of this dissertation, we further investigate the role of septins in cancer invasion through regulation of cell shape. Elucidating the biophysical mechanisms by which cytoskeletal crosstalk regulates cell migration is challenging due to the enormous molecular complexity of the cell and feedback between mechanical forces and biochemical signaling. Cell-free reconstitution provides a valuable complement to live-cell studies because it simplifies the challenge of separating biochemical and physical contributions to cytoskeletal crosstalk. We note that caution should be used when translating findings regarding cytoskeletal crosstalk from bottom-up studies to cells. Cell-free model systems present a highly simplified environment in terms of molecular complexity, crowding, ionic conditions, spatial heterogeneities, mechanical conditions, etcetera. Cytoskeletal interactions or mechanical effects observed in a cell-free system do not necessarily occur (in the same way) in the cellular environment. The power of cell-free studies is to develop and test hypotheses regarding possible interactions and their biophysical impact under well-controlled conditions. Using cell-based studies, one can then test how these findings carry over to the cellular environment. Clearly there still remains an enormous gap between the complexity of cells and the simplicity of reconstituted systems. How can this gap be bridged?

We propose different routes to bridge this gap (Figure 4.4). One obvious direction to bridge this gap is to enhance the complexity of cell-free assays. Simple assays combin-

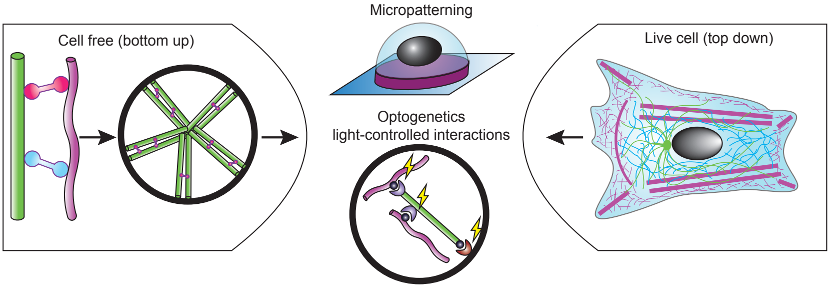

Figure 4.4: The proposed route to bridge the gap between live cell (top down) and cell free (bottom up) approaches in the research of cytoskeletal crosstalk in cell migration. *Micropatterning* and *optogenetic tools* can be used to manipulate cytoskeletal interactions and help to bridge the gap between the two research approaches. Actin (magenta), microtubules (green), intermediate filaments (cyan) and crosslinkers (pink).

ing cytoskeletal filaments without any accessory proteins showed that steric interactions alone suffice to give rise to nonlinear stiffening and enhanced compressive strength. There is some evidence that intermediate filaments directly interact with actin filaments and microtubules via electrostatic interactions [320, 321], but this could be an artefact of *in vitro* conditions. Single-molecule measurements of filament interactions within cells or cell lysates could shed light on this issue. An important next step to bridge the gap to the cell is to incorporate accessory proteins that mediate cytoskeletal coupling. Several studies have shown that crosslinking via cytolinkers is sufficient to give rise to cytoskeletal filament co-alignment and mechanical synergy (e.g. [328, 329]). More detailed investigations of the effects of cytolinkers, both *in vitro* and in cells, will be important to delineate their roles in cytoskeletal co-organization, mechanical synergy, and mechanotransduction. In the cell, cytoskeletal crosstalk is guided by geometrical constraints provided by the cell membrane. The membrane organizes the cytoskeleton through spatial confinement and by providing adhesion sites where cytoskeletal filaments are nucleated or anchored. Reconstitution experiments have begun to recapitulate these constraints by encapsulating cytoskeletal proteins inside cell-sized emulsion droplets or lipid vesicles, including actin/microtubule and actin/keratin composites [316, 453]. These model systems could form a basis for reconstituting synthetic cells capable of migration. Adhesion-independent migration is probably easiest to reconstitute. Flow-driven confined migration was recently reconstituted, although based on a cell extract, so the minimal set of ingredients is not yet known [360]. It will be interesting to incorporate microtubules and/or intermediate filaments in this assay to control cell polarity and mechanics. Mesenchymal migration is likely more challenging to reconstitute because it requires coordinated actin polymerization, contraction, and cell-matrix adhesion. Motility driven by actin polymerization has been successfully reconstituted on the outer surface of lipid vesicles (reviewed in [454]), but motility of vesicles with actin polymerization inside will require substrate adhesion. Surface micropatterning provides an interesting approach to impose polarized shapes to synthetic cells by forcing them to adapt to the pattern shape and size [455]. In addition, one can use light-induced dimerization to induce spatial patterning and symmetry breaking of cytoskeletal networks. Light-inducible dimers (LIDs) come from photoactivatable systems naturally occurring in plants and allow for reversible photoactivation [456]. Recently it was for instance shown that microtubule-interacting proteins fused to optochemical dimerization domains can be used to drive symmetry breaking of microtubule networks inside emulsion droplets [457].

The opposite direction to bridge the gap between live-cell and cell-free studies is to tame the complexity of living cells. Some of the same techniques that can provide more control over cell-free systems can also provide control over the behavior of living cells. Surface micropatterning for instance allows one to confine cells to adhesive islands with precisely controlled geometries, forcing the cells to adopt prescribed shape and corresponding cytoskeletal organizations (see Chapter 5 of this dissertation). Imaging many cells adhered on the same pattern greatly facilitates quantification of cytoskeletal crosstalk [374]. Moreover, micropatterning can be used to investigate how cytoskeletal interactions affect single-cell and collective cell migration dynamics [458]. Light-inducible dimerization can be used to manipulate cytoskeletal interactions with high spatial and temporal control. It was for instance recently shown that F-actin can be crosslinked to microtubule plus ends by transfecting cells with an iLID-tagged EB-binding SxIP peptide and SspB-tagged actin-binding domains [459]. This could be an interesting tool to systematically study the crosstalk of microtubules with actin and intermediate filaments that takes place near cell adhesions. Finally, molecular tension sensors provide a very interesting tool to selectively interrogate mechanical interactions between cytoskeletal networks. Tension sensors consist of two fluorescent proteins separated by a peptide with a calibrated mechanical compliance. Under strain, the fluorescent proteins are separated, decreasing fluorescence energy transfer (FRET) between them. By embedding a tension sensor in the actin crosslinker FLNA, it was recently shown that molecular tension can be measured within the actin cytoskeleton [460]. It will be interesting to use a similar approach to measure tension within the intermediate filament cytoskeleton and test force transmission between the actin and intermediate filament cytoskeleton.

4.8. ACKNOWLEDGEMENTS

I would like to thank Irene Istúriz Petitjean and James Conboy for their expertise on *in vitro* reconstitutions and cell mechanics, interesting discussions and for their contributions to our review work. I would like to thank Gijsje Koenderink for her helpful feedback and broad expertise that evolved this review into a valuable resource in the research field.

5

SEPTINS PROMOTE BREAST CANCER INVASION

Septins are cytoskeletal proteins that assemble into hetero-oligomers that form fibers and bundles in cells to act as scaffolds and diffusive barriers. Through interactions with the cell membrane and the cytoskeleton, septins are known to contribute to cell division, morphology, mechanotransduction and migration. High expression of septins is correlated to breast cancer malignancy by promoting invasion, but it is challenging to dissect the mechanisms by which septins impact cancer cell invasion. Here we created a CRISPR/Cas9 septin 7 knockout in the metastatic triple-negative breast cancer cell line Hs578T to examine the role of septin in breast cancer invasion. Invasion from 3D spheroid assays in collagen hydrogels was inhibited in response to septin 7 depletion. Additional single-cell migration studies with physical constriction mimicked by micropatterns, microchannels and 3D collagen gels showed that septin 7 expression regulates confined cell migration through control of cell shape and actin-based protrusions.

5.1. INTRODUCTION

SEPTINS belong to a family of proteins that is increasingly recognized as an essential component of the cytoskeleton in mammalian cells [461]. All septins are guanosine triphosphate (GTP)-binding proteins. Paralogous septins are categorized into four groups based on sequence homology, named SEPT2, SEPT6, SEPT7 and SEPT3 [462]. Humans possess 13 septin genes referred to as SEPT1-12 and SEPT14. Septins from each group assemble into palindromic hetero-oligomers in a defined linear sequence of subgroups [463]. In mammalian cells, both hexamers (with the general sequence SEPT2-6-7-7-6-2) and octamers (with the general sequence SEPT2-6-7-3-3-7-6-2) are found in cell-type-specific proportions [464]. Each septin subunit can be exchanged with another from the same group (Kinoshita Rule [465]) and certain septins, like SEPT9, have multiple splice variants. The large variety of ensuing septin combinations may contribute redundancy, but also cell-specific functions. Each septin has two interaction sites for binding adjacent septins: one formed by the GTP-binding domain (G-interface) and the other by N- and C-terminal extensions (NC-interface). This enables the complexes to assemble end-to-end via their SEPT2 subunits to form thin (4 nm) linear filaments that are nonpolar [466]. These filaments can laterally pair through interactions of the C-terminal coiled coil domains [467]. It is still poorly understood how cells regulate septin (de)polymerization and higher-order organization, although post-translational modifications of septins [468] and Borg family proteins [469, 470, 471, 472] are known to be important.

Septin filaments in mammalian cells are often found in association with the plasma membrane. Membrane-associated septin structures have been proposed to serve as scaffolds and diffusive barriers [473, 474]. Septins can directly bind lipid membranes through interactions with phosphoinositide lipids including phosphotidylinositol 4,5-bisphosphate (PIP2) [475, 476]. However, septins can also associate with the cell cortex through interactions with the actin cytoskeleton, either through direct actin binding or through indirect binding via nonmuscle myosin-2 and anillin [477, 465, 183]. Actin-associated septins have been found to regulate the structural stability and contractility of actin stress fibers in adherent cells [478, 479, 480], the actin cortex in immune cells [481], and the actin cortex in epithelial and endothelial tissues [482]. Septins may also bind to microtubules in certain cell types or physiological circumstances α-tubulin [483, 484] through a short amino-terminal repeat motif unique to the septin 9 splice isoform SEPT9-i1 [485, 486]. Through their interactions with cell membranes and the cytoskeleton, septins contribute to a wide range of cellular functions. They are essential for cell division and promote cell migration, cell and tissue shape regulation, immune responses, and mechanotransduction [487, 488, 489, 481, 490].

Septin dysfunctions are associated with a wide range of diseases including different forms of cancer [491]. Some septin family members function as suppressors of tumor cell invasion, which prevents cancer progression and metastasis. In glioma cells, for instance, high septin expression is linked to inhibition of cell invasion through downregulation of metalloproteases (MMPs) and integrins and through reorganization of the actin and microtubule networks [492, 493]. In contrast, septins function as tumor cell invasion promoters in breast cancer. For example, high expression of SEPT2 and SEPT7 in breast cancer is associated with more aggressive forms of the disease [494, 495]. In various breast cancer cell lines, inhibition of septin dynamics with forchlorfenuron was shown to lower cell proliferation and invasion rates, while septin over-expression had the opposite effect [494]. Of all septins, SEPT9 is most strongly linked to cancer, especially breast cancer [496]. High expression of SEPT9 has been associated with a high clinical stage, poor clinical outcomes and resistance to treatment. SEPT9 overexpression promotes metalloprotease-dependent invasion of breast cancer cells [497], which is also associated with adaptations of the cytoskeleton and focal adhesions [498]. Given the complexity of septins and their vast interactome, it is challenging to dissect the mechanisms by which septins impact cancer cell invasion.

Cancer cell invasion is a complex process that relies on all cytoskeletal networks jointly regulating cell deformability, cell contractility, integrin-mediated interactions with the tissue microenvironment, and formation of specialized membrane protrusions [499, 500, 501, 502]. Septins influence all of these functions. They influence cell deformability by enhancing the mechanical stability of the actin cortex [473]. They influence cell contractility by reinforcing actin stress fibers [503, 464]. Septins can both recruit and compete with myosin for actin binding, directly impacting actomyosin activity and thus cell contractility [479, 504, 505]. Septins influence focal adhesions through their stabilization of actin stress fibers [503, 464]. In migrating endothelial cells, they furthermore influence focal adhesion turnover through the guidance of growing microtubuli towards focal adhesions [506]. Finally septins influence the formation of various types of specialized membrane protrusions that contribute to cell migration. Protrusion types are associated with different migration modes, that are dependent on cell type and environmental factors. Mesenchymal migration is characterized by actin-rich lamellipodia and filopodia, while amoeboid migration uses actin-independent bleb formation [9]. Cancer cells often also contain podosomes and invapodia, which are specialized in matrix degradation to enhance invasion [507], and microtubule-enriched microtentacles of the cell membrane [508, 509]. In breast cancer cells, septins influence microtentacle formation by controlling actin-microtubuli crosstalk [501]. In T-cells, septins contribute to persistent amoeboid cell motility by preventing blebbing and promoting retraction of the cell's leading edge when cells change direction [489, 481]. It is still unknown how septins regulate membrane protrusion formation, but this may involve curvature-sensitive membrane binding [510, 511, 512].

Because septins play extensive roles in cytoskeletal reorganization and membrane dynamics, we hypothesized that septins govern breast cancer cell motility through affecting cell shape and specifically protrusion formation. To test this hypothesis, we produced an inducible CRISPR/Cas9 knockout of septin 7 in Hs578Ts, a metastatic triple negative human breast cancer cell line that is resistant to various therapeutic strategies [513]. Hs578T cells express septins 1/2/7/9/11, which co-localize with actin filaments and not with microtubules [501]. To knockdown septins, we decided to target septin 7, since this septin is the only member of its family and it plays a critical role in the stability of septin complexes within the cell [473, 514]. When septin 7 is absent, expression levels of other septins are often reduced as well and the remaining septins are unable to form stable oligomers or filaments. Furthermore, septin 7 expression has been implicated in breast cancer [494]. We first investigated how septin 7 depletion influences breast cancer cell invasion using 3D spheroid invasion assays in collagen hydrogels. To investigate the mechanism by which septins impact invasion, we then studied single cell invasion in different artificial environments (micropatterns, microchannels and 3D collagen gels) that mimic physical constriction. We found that septin 7 is a crucial regulator of confined cell migration. Without septin, confined cell shapes in 2D and 3D were more compact and less complex, indicating reduced contractility and protrusion formation.

5.2. METHODS

CELL CULTURE AND GENERATION OF KNOCKOUTS

Human breast cancer cells (Hs578T, #HTB-126, ATTC) were cultured in Dulbecco's Modified Eagle Medium (DMEM, Thermo Fisher, #11574486) supplemented with 5% Fetal Bovine Serum (Thermo Fisher Scientific, #11573397) and 1% penicillin-streptomycin (Thermo Fisher Scientific, #11528876). Cells were subcultured between 80-90% confluency and incubated at 37°C and 5% CO_2.

A doxycycline-inducible Hs578T Cas9 cell line was produced using Edit-R Inducible Lentiviral hEF1α-Blast-Cas9 Nuclease Plasmid DNA (Dharmacon, CAS11229, CO, USA). A subconfluent monolayer of Lenti-X 293T cells (Clontech, #632180, CA, USA) was adhered to a 10 cm dish overnight. A DNA mixture was prepared with third generation lentiviral helper vectors using 2.6 µg pMDLg-RRE, 1.4 µg pCMV-VSVG and 2.0 µg pRSV-Rev (all from Addgene, #12251, #8454, #12253, respectively, MA, USA, adjusted by the Netherlands Cancer Institute) and 4.0 µg of the Cas9 plasmid. Lenti-X 293 T cells were transfected with the DNA mixture and 0.05 mg Polyethylenimine (Polysciences, #23966-2, PA, USA) in 10 mL culture medium. After 24 hours the medium was refreshed, after 48 hours and 72 hours the medium was collected and filtered through a 0.45 µm filter. 50,000 Hs578T cells were adhered in a 6-wells plate (Greiner Bio-one, #657160, Austria) and virus-containing medium was added and supplemented with 5 µg/mL Polybrene (Sigma-Aldrich, MO, USA). After 24 hours the medium was changed and cells were selected using 2 µg/mL Blasticidin (Sigma-Aldrich, #203350, MO, USA). A single clone of Hs578T-Cas9 was isolated, expanded and tested for Cas9 expression upon Doxycycline (Selleckchem, #S5159, TX, USA) exposure. For sgRNA plasmids, the following guide RNA was added into U6-gRNA/PGK-Puro-2A-BFP vector (Addgene, #50946) by the LUMC: SEPT7: 'CCTGTTATCGACTACATTGATAG'; Additionally a non-targeting sgRNA was used as negative control. HEK293T cells were transfected with the pKLV-U6-gRNA/PGK-Puro-2A-BFP vectors cloned with sgSEPT7 or a non-targeting control sgRNA, with 2.5 mg/mL polyethylenimine (Polysciences, #23966-2) in phosphate-buffered saline (PBS). Lentivirus-containing medium was collected from the HEK293T cells for 2 days and used to transduce Hs578T-Cas9 cells. Selection of transduced cells was performed with 1 µL puromycin

(Thermo Fisher, #A1113803) for two days. For induction of the CRISPR-Cas9 knockout, media was supplemented with 1 µg/mL doxycycline (Bio-connect, S5159), creating Hs578T cells with a septin 7 knockout (Hs578T SEPT7 KO) and a non-targeting control (Hs578T NT CTRL). We found that a minimum of 7 days was needed for maximal septin 7 knockdown (Fig. S5.1 and S5.2). Knockout cultures were used for a maximum of three weeks.

ACTIN POLYMERIZATION INHIBITION

In experiments requiring actin depolymerization, we incubated the cells for a minimum of 30 minutes with culture media supplemented with 50 µM Cytochalasin D (Merck Sigma, #C2618) or with 0.025 µL/mL DMSO (Bioke, #12611P) as a control. Previous research has shown that incubation of fibroblasts with this concentration of CD reduced the cell stiffness as measured by uniaxial stress-strain testing by 50 % [67].

MICROFLUIDIC MIGRATION ASSAYS

We designed a microfluidic device tailored for observing cell deformation during migration through custom-designed constriction areas inspired by the work of Davidson et al. [64]. The multi-layered master mold was created using standard soft lithography at the Kavli Nanolab Delft, with a µMLA laserwriter (Heidelberg Instruments). The design consists of a 5 µm tall and 440 µm wide constriction area aligned with an adjacent 50 µm tall perfusion channel for cell loading, chambers that end at the constriction area, and a bypass channel to equilibrate the fluid levels between the reservoirs positioned at the outer sides of the chamber.

The first layer of the design consisted of 5 µm SU-8 2005 photoresist (Kayaku Advanced Materials) and was spun on a 4-inch silicon wafer that was soft-baked and post-baked at 95 °C for 2 minutes. The second layer consisted of 45 µm SU-8 3050 (Kayaku Advanced Materials) and was soft-baked at 95 °C for 15 minutes, post-baked for 1 minute at 65 °C and 5 minutes at 95 °C, and developed with a SU-8 developer (Sigma Aldrich). After developing, trichloro(1H,1H,2H,2H-perfluoroctyl)silane (Sigma Aldrich) was coated on the master mold. Microfluidic chips were made from PDMS (Sylgard 184, Dow Corning), prepared with a curing agent with a 10:1 (w/w) ratio. The PDMS was poured on the silicon mold, degassed and cured at 65 °C for 3 hours. Reservoirs and cell-loading ports were punched with a revolving punch plier (Knipex) and a 0.75 mm diameter punch (Rapidcore, Welltech), respectively. PDMS chips and glass coverslips were plasma cleaned (Harrick Plasma) at 30 W for 150 seconds and bonded overnight at 65 °C.

For live-cell experiments, microfluidic chips were sterilized with 70% ethanol and subsequently washed three times with MQ and once with PBS. Chips were coated with collagen by adding 100 µL 100 µg/mL PureCol type 1 bovine collagen (Advanced Biomatrix) in PBS through the cell-loading ports and incubating for 2 hours at room temperature. Chips were washed thrice with PBS and once with cell culture medium. Next, 6 µL containing 30,000 cells was added to each chip via the cell-loading ports. The reservoirs were filled with cell culture media and the chips were incubated overnight at 37°C and 5% CO_2, together with a 15 mL falcon tube cap filled with MQ to prevent evaporation. One hour before imaging, cell culture medium was removed from the reservoirs and replaced with cell culture medium containing live-cell dyes to stain the nucleus (Hoechst 33342, Thermo Fisher, 1:10,000 solution) and the cytoplasm (Cytotracker Orange, Thermo Fisher, 1:1,000 dilution). After one hour incubation, the device was sealed with a glass coverslip and imaged.

MICROPATTERNING

For micropattern fabrication, we adapted a deep UV printing protocol from Ref. [515]. Coverslips were first cleaned with isopropanol (VWR Chemicals, #20922.264) and Milli-Q (MQ) and sonicated for 5 minutes in an Ultrasonic Cleaner (Emerson, Brandson 2510), followed by 5 minutes in a UV plasma cleaner (BioForce Nanoscience, UV Ozone Pro-Cleaner Plus). PLL-PEG coatings were made using PLL-g-PEG (Susos AG) diluted 1:10 in 10 mM HEPES buffer, pH 7.4 (Thermo Fisher, #11560496) and pipetted in 50 µL droplets on parafilm. Cleaned coverslips were placed on top of the droplets and incubated at room temperature for 1-2 hours. Next, coated coverslips were washed 10x in MQ and dried using a nitrogen spray gun.

The photomask was fabricated by DeltaMask BV. The photomask was first cleaned with acetone and isopropanol and next plasma cleaned for 10 minutes in the UV plasma cleaner. To attach the coverslips to the photomask, 1.5 µL droplets were pipetted onto the patterns before adding the coverslips on top. The patterns were printed in the UV plasma cleaner for 10 minutes. Patterned coverslips were sterilized with 70% ethanol and washed twice with PBS. Patterned coverslips were incubated with 100 µL 10 µg/mL Rhodamine-labeled fibronectin (Universal Biologicals, #FNRO1-A) in PBS for 1 hour. Next, coverslips were washed with PBS and stored in PBS at 4 °C for a maximum of 1 week. To seed the cells on the patterns, patterned coverslips were placed in 6-well plates and seeded with a density of 50,000 cells/well for at least 24 hours to ensure attachment.

SPHEROID INVASION IN COLLAGEN GELS

Bovine hide collagen type I (purity ≥ 99.9%, Advanced Biomatrix) stock solution of 3 mg/ml collagen in 0.01 N HCL was used to prepare 2.4 mg/ml collagen gels. The gels were made isotonic by adding 12.5 v/v% of 10x Phosphate Buffered Saline (PBS, Thermo Fisher). Next, 0.1 M sodium hydroxide was added to bring the pH to 7.4. The solution was further diluted with pre-cooled MQ and vortexed for 30 seconds and polymerized at 37°C in an µ-slide 8-well (Ibidi) for 45 minutes.

For spheroid formation, cells were seeded in round-bottom and ultra-low attachment Elplasia^{TM} 96-well plates (Corning), with a seeding density of 40,000 cells/well to create spheroids with an average size of ~200 µm. Spheroids were incubated for 2-3 days for spheroid formation and compaction, with a moderately necrotic core, and pipetted out of the wells using a cut-open 200 µL pipet tip to prevent shearing the spheroids. Spheroids were pipetted on top of 80 µL polymerized collagen in each Ibidi well and incubated for 45 minutes. Medium was pipetted out of the well, and another 100 µL collagen was polymerized on top of the spheroids, creating a sandwich model, adapted from Ref. [148]. The collagen samples were supplemented with culture medium containing Hoechst 33342 and Cytotracker Orange.

IMMUNOCYTOCHEMISTRY

For fixation of samples, culture medium was removed and 4% para-formaldehyde (PFA, Tebu-Bio) in PBS was incubated for 10 minutes. PFA was removed and samples were washed three times with PBS. Next, cells were permeabilized with 0.5% Triton X-100 (Merck Sigma) in PBS for 3 minutes and washed three times with PBS supplemented with 0.1% Tween (PBS-T, Merck Sigma). The samples were blocked for 30 minutes with 3% Bovine Serum Albumin (BSA, Merck Sigma) in PBS.

Primary stainings were made in 1.5% BSA/PBS and incubated between 6-24 hours at 4 °C. Primary antibodies used were anti-α-tubulin (1:1000, Invitrogen, #32-2500), anti-gm130 mouse (1:500, BD Biosciences, #610823), anti-PIP2 mouse IgG2a (1:100, Sigma, #MABS2282), anti-septin 7 rabbit IgG (1:250, Thermo Fisher, #PA5-56181) and anti-septin 9 rabbit IgG (1:200, Proteintech, #10769-1-AP). After primary staining, samples were washed three times with PBS-T.

Secondary stainings were made in PBS-T and incubated between 1-6 hours at room temperature. Secondary antibodies and dyes used were anti-rabbit goat IgG 488 (1:1000 Thermo Fisher, #A11008), anti-mouse goat IgG 568 (1:1000, Thermo Fisher, #a11004), anti-rabbit goat IgG 647 (1:1000, Thermo Fisher, #a27040), Hoechst 33343 (1:1000) and Phalloidin 647 (1:250). After secondary staining, samples were washed three times with PBS-T and once with MQ. Coverslip samples were mounted on microscope slides (Thermo Fisher, #16309475) using ProLong Diamond mounting solution (Thermo Fisher, #15468070), air-dried and stored at 4 °C. Ibidi chamber slide samples were stored in PBS at 4 °C.

Spheroid-collagen samples were stained with the same protocol as described above, but with increased incubation times and without mounting the samples. Instead, the samples were stored in PBS at 4 °C. Incubation times were adapted for BSA blocking (overnight), primary staining (overnight), secondary staining (overnight) and wash steps (30 minutes).

MICROSCOPY IMAGING AND AUTOMATED IMAGE ANALYSIS

Confocal fluorescence and reflectance imaging was done on a Stellaris 8 confocal microscope (Leica), equipped with a supercontinuum white light laser, 405 nm laser and three hybrid detectors. Immunocytochemistry samples were imaged with 40x/1.25 or 63x/1.30 glycerol objectives, 405 nm laser, and 488/553/650 nm laser lines. Live-cell imaging of microfluidic chips and spheroid assay was performed with a 20x/0.75 air objective, 405 nm laser, 458 nm laser line and 488 laser line for confocal reflection. Time-lapse image series at multiple locations were acquired with time intervals of 15 minutes over a total period of 24-72 hours. Environmental control regulated the temperature at a constant 37 °C and 5% CO_2.

Automated image analysis to detect 2D cell shape parameters was done in in Fiji [68] in which we binarized Cytotracker Orange and actin signals from which we measured area, aspect ratio, circularity and solidity. To measure cell lengths we analyzed the skeleton with the 'skeletonize' plugin in Fiji and measured the longest path of the skeleton. In 3D samples, cells had a variety of orientations which was challenging to quantify. For 3D image analysis, we used the 'skeletonize' plugin of Fiji on binarized maximum projections of actin intensities. From the skeleton, we could count the number of junctions in the skeleton as a measure for protrusions, and extract the longest path in the skeleton to determine the cell length in XY. To also determine the length in Z, we counted the number of Z-stacks in which the cell was imaged. Cell elongation was defined as the combination of measured cell lengths in XY and in Z. Cells were selected when placed > 20 µm from the coverglass. Maximum time projections of time-lapse imaging series of 3D spheroid invasion were made by making inverted maximum projections of the timelapses.

WESTERN BLOT ANALYSIS

Hs578T NT CTRL and SEPT7 KO cells were seeded with a cell density of 300,000/well in 6-well culture plates. After a minimum of 24 hours, cells were washed with PBS and lysed in radioimmunoprecipitation buffer (RIPA, 100 µL/well, Thermo Fisher) and stored at -20°C. Loading samples were made with Laemmli buffer (2x, Bio-rad) and 4% β-mercaptoethanol (Sigma Aldrich) and were boiled at 95°C for 5 minutes. Mini-PROTEAN-TGX gels (Bio-rad) were used for sodium dodecyl sulfate-polyacrylamide gel electrophoresis (SDS-PAGE) at 100V for approximately 1.5 hours. Western Blotting of the gels was done on Trans-Blot Turbo Mini 0.2 µm PVDF Transfer Packs (Bio-rad) using a Trans-Blot Turbo Transfer System (Bio-rad). After blotting, membranes were blocked in 5% BSA/PBS overnight. Membranes were stained with primary antibodies: anti-GAPDH rabbit IgG (1:1000, #CST2118S, Bioke), anti-septin 2 rabbit IgG (1:1000, Sigma, #HPA018481), anti-septin 7 Rabbit IgG (1:1000, #18991, IBL-America) and anti-septin 9 rabbit IgG (1:10000, Proteintech, #10769-1-AP) in 5% BSA/PBS overnight, on a shaker at 4°C. After primary stainings, membranes were washed thrice with PBS-T. Secondary stainings were done with goat anti-rabbit HRP (#ab6728, Abcam), 1:5000 in PBS-T. Membranes were washed thrice with PBS-T. Imaging was executed with an enhanced luminol-based chemiluminescent substrate kit (Thermo Fisher) on a gel-imager (Bio-rad). Intensity bands were measured three times in Fiji [68] and subtracted from different background spots.

DYNAMIC COMPRESSION OF SPHEROIDS

To measure the viscoelastic properties of the NT CTRL and SEPT7 KO spheroids, dynamic compression was imposed on spheroids using a microfluidic constriction device with constriction size of 84 µm in width and 110 µm in length. The microfluidic chip design and experimental setup are described in Ref. [516]. For spheroid formation, NT CTRL and SEPT7 KO cells were seeded in round-bottom and ultra-low attachment Elplasia^{TM} 96-well plates, with a seeding density of 60,000 cells/well. Spheroids were incubated for 3 days and pipetted out of the wells using a cut-open 200 µL pipette tip to prevent shearing the spheroids. Spheroid compression was imaged on an inverted fluorescence microscope (Zeiss Axio-Observer) with camera streaming using a 5xNA 0.16 air objective and Zeiss Axio-Observer 0.63x digital camera. Experiments with more than one spheroid present during compressions were not considered in the analysis. Automated image analysis via a Matlab function detected spheroid boundary and centroid, to calculate velocity and axial strain. The viscoelastic properties were extracted from the axial strain evolution over time, which characterized the spheroid deformation, via the fitting of a Dynamic Modified Maxwell Model (DMMM). The DMMM was derived by defining applied stress σ in the Modified Maxwell Model by pressure differences across the channel, accounting for time-dependent pressure differences present in the system (mathematical derivations are found in Ref. [516]).

STATISTICAL ANALYSIS

Statistical analysis was performed using Microsoft Excel. Two-tailed Student's t-tests were performed using the TTEST function. Statistical details of experiments are found in the figure legends and method details. P-value results from t-tests are indicated by: (ns) = $p \geq 0.05$, (*) = $p < 0.05$, (**) = $p < 0.01$, (***) = $p < 0.001$. Error bars represent the standard error of the mean.

5.3. RESULTS

CHARACTERIZATION OF SEPTIN 7 DEPLETION IN HS578T CELLS

To test the impact of septins on cancer cell invasion, we decided to create an inducible CRISPR/Cas9 knockout of septin 7 in Hs578Ts, a metastatic triple negative human breast cancer cell line [513]. Hs578T cells transfected with lentivirus containing a CRISPR/Cas9 construct with sgSEPT7 were treated for several days with doxycyclin to activate the CRISPR/Cas9 and induce the septin 7 knockout (SEPT7 KO). Control (NT CTRL) cells were obtained by performing the same treatment but using non-targeting sgRNA. We checked the extent of septin knockdown by immunofluorescence microscopy (Fig. S5.1) and Wester Blot analysis (Fig. S5.2) after 2-day, 5-day, 6-day and 7-day induction. We found that 7-day treatment with doxycyclin significantly reduced septin levels. To characterize the efficiency of septin knockout we first took immunocytochemistry images of cells at day 0 and after 7 days of doxycyclin treatment, staining for septin 7 and F-actin (Fig. 5.1A). In control cells, septin 7 was clearly visible as linear signals co-localizing with actin stress fiber (Fig. 5.1A(i-iii)). After 7 days of doxycyclin treatment, 80-90% of the cell population lost visible septin expression (Fig. 5.1A(iv-vi)). Western Blot analysis confirmed that doxycyclin treatment reduced the expression level of septin 7 by 6-fold after 7 days (Fig. 5.1B(i)). As septin 7 plays a critical role in the stability of septin complexes within the cell [464, 463], we also expected a decrease in the levels of other septins. Western Blot analysis indeed showed markedly reduced expression levels of both septin 2 and 9 after doxycyclin treatment (Fig. 5.1B(ii-iii)). Immunocytochemistry images confirmed that cells depleted of septin 7 also had a markedly lower signal for septin 9 as compared to control cells (Fig. 5.1C(i-ii,iv-v)). We additionally found that cells depleted of septin 7 regularly contained disrupted Golgi apparatus (Fig. 5.1C(iii,vi)) and dysregulated microtubules with dense compact structures near the cell cortex (Fig. 5.1D). Both of these artifacts showed co-localization with residual septin 9 structures, indicating that these defects originate from aberrant localization of residual septin 9 in the septin 7-depleted cells.

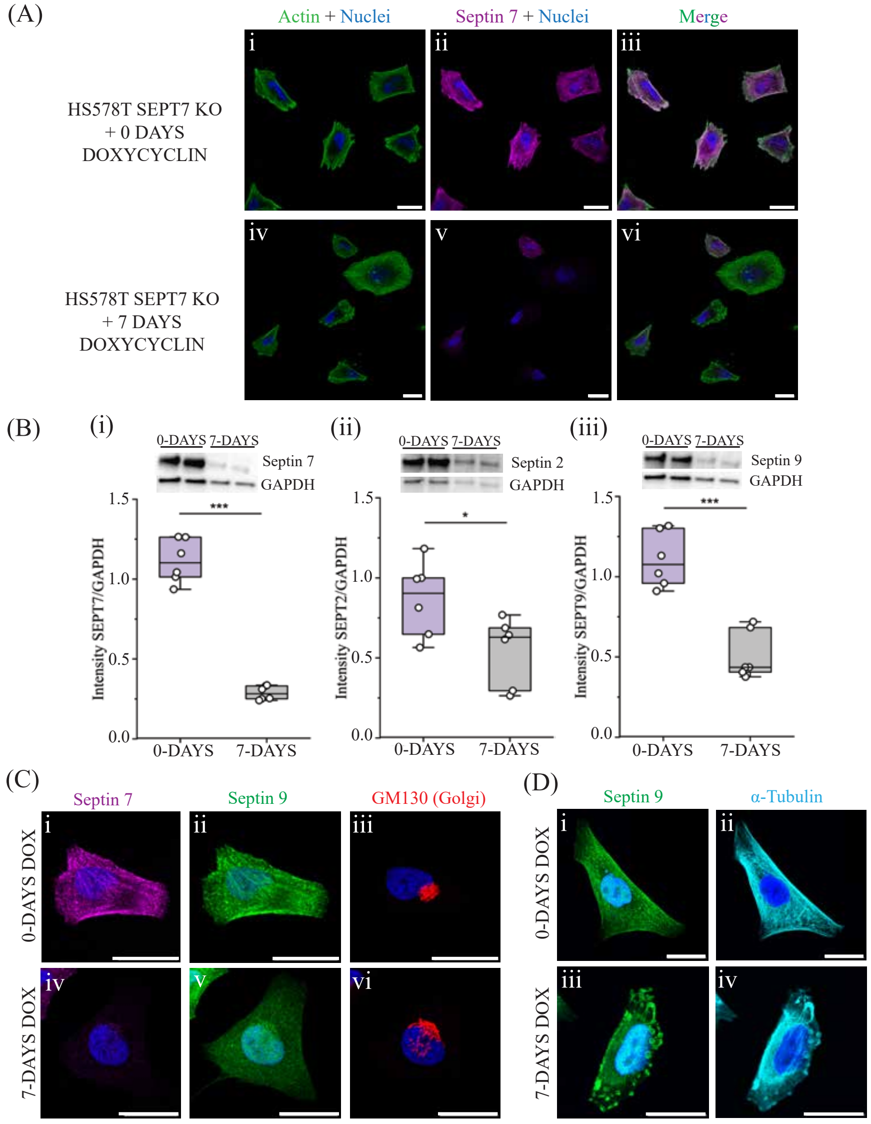

Figure 5.1: Characterization of septin 7 knockdown in Hs578T breast cancer cells. (A) Immunocytochemistry images and Western Blot quantification of Hs578T SEPT7 KO cells at day 0 and day 7 of doxycyclin treatment. Left: Cells are stained for F-actin (green), septin 7 (magenta) and nuclei (blue). Scale bars are 50 µm. (B) Western Blot (top) and corresponding boxplots quantifying Western Blot intensities relative to GAPDH (bottom) for septin 7, septin 2 and septin 9 before and after 7 days of doxycyclin treatment. (C) Immunocytochemistry images of cells before and after doxycyclin treatment for septin 7 (magenta), septin 9 (green), GM130/Golgi (red), α-tubulin (cyan) and nuclei (blue). Scale bars are 25 µm. In the boxplots, (*) = $p < 0.05$, (***) = $p < 0.001$.

SEPTINS MODULATE ACTIN ORGANIZATION AND CELL SHAPE ON MICROPATTERNS

In control cells, we observed that septins localize with actin stress fibers but not with microtubules, consistent with previous findings [501]. To investigate the interplay between the actin and septin cytoskeleton in Hs578T cells, we analyzed how each responded to depletion of the other. When we depleted actin fibers by cytochalasin D (CD) treatment, septins transformed from linear structures co-aligned with long stress fibers (Fig. 5.2A, top row; zoom-in areas indicated by white arrows) into smaller fibers, often crescent shapes and rings (Fig. 5.2A, middle row). Conversely, depletion of septin 7 from the cells resulted in minor actin reorganizations (Fig. 5.2A, bottom row). The most prominent change in the actin cytoskeleton was a clear loss of perinuclear fibers. In perinuclear areas of the cells (areas indicated by white squares in Fig. 5.2C, left, zoomed-in images in Fig. 5.2C, middle and right), stress fibers are visible in control cells but lost in septin 7 knockout cells. In addition, control cells had frequent linear actin-filled protrusions, likely non-motile cilia as they co-localized with microtubules, whereas septin 7-depleted cells showed much fewer such protrusions (Fig. 5.2D, zoom-in areas indicated by white squares). Analysis of the 2D cell areas showed that neither actin fiber inhibition nor septin 7 depletion significantly impacted the area on average (Fig. 5.2B). However, simultaneous depletion of F-actin and septin by CD treatment of SEPT7-KO cells caused a significant reduction in cell area (Fig. S5.3), indicating that the networks somehow jointly contribute to cell spreading on 2D substrates.

In the tissue microenvironment, breast cancer cells adhere to collagen fibers, which constrain adhesion from 2D to quasi-1D. To test how septin depletion affects cell spreading under quasi 1D-confinement conditions, we seeded cells on top of 15 μm-wide lined micropatterns coated with fibronectin. Control cells adapted to the pattern by forming rather regular elongated shapes with tapered ends (Fig. 5.2E, left). SEPT7 KO cells showed notably less well-defined shapes, suggesting a less contractile morphology (Fig. 5.2E, right). Quantification of the cell shapes showed that the SEPT7 KO cells indeed had significantly smaller aspect ratios than control cells (Fig. 5.2G) despite having similar cell areas (Fig. 5.2F). We conclude that in Hs578T cells, septin 7 interacts with F-actin and regulates perinuclear and cortical actin networks that are important for cell shape control under 1D and 2D adherent conditions.

SPHEROID INVASION IS REDUCED IN SEPT7 KO HS578T SPHEROIDS

The role of septin in breast cancer cell invasion was researched by generating Hs578T cell spheroids and performing spheroid invasion assays in 2.4 mg/mL collagen gels, providing confined conditions (average pore size ~1.3 μm [517]). We performed live-cell imaging on the spheroids to track the progression of cell invasion. At the start (defined as t = 0h, circa 2 hours after embedding the spheroid in collagen), we already observed distinct differences in the number of protrusions the spheroid displayed between control and septin knockout spheroids (Fig. 5.3A). NT CTRL spheroids show clear protrusive behavior into the collagen gel at various sites along their contour, while SEPT7 KO spheroids have a limited number of protrusions within the same incubation time. Imag-

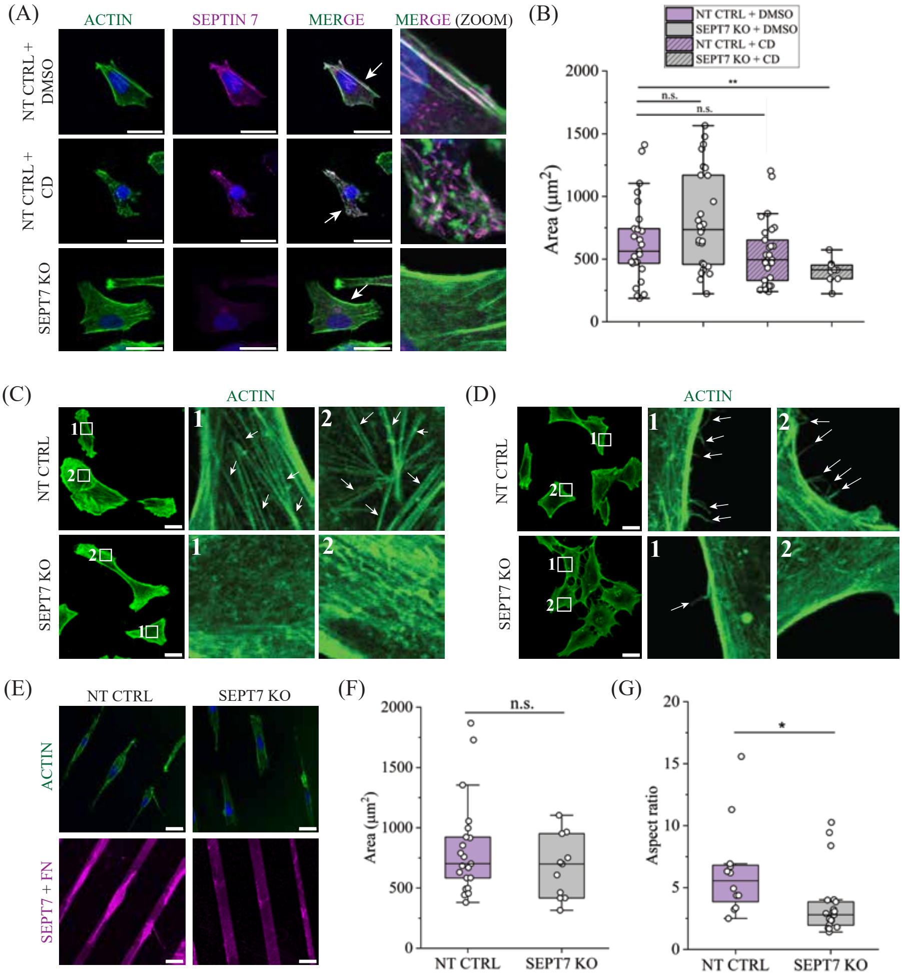

Figure 5.2: Interplay between septin and F-actin in Hs578T cells. (A) Immunocytochemistry of control Hs578T cells (NT CTRL) cells treated with cytochalasin D (CD) and control (DMSO) and images of septin 7 knockout cells (SEPT7 KO). The columns show fluorescence signals of F-actin (green), septin 7 (magenta) and nuclei (blue). White arrows in MERGE images indicate areas used for MERGE (ZOOM) images. (B) Boxplot indicating the cell areas of control Hs578T cells (NT CTRL + DMSO) and cells depleted of septin 7 (SEPT7 KO), actin fibers (NT CTRL + CD), or both (SEPT7 KO + CD). (C) Immunocytochemistry images of F-actin in NT CTRL cells (top) and SEPT7 KO cells (bottom). Numbered squares indicate zoomed-in areas for analysis of perinuclear areas. Stress fibers are indicated by white arrows. (D) Immunocytochemistry images of F-actin in NT CTRL cells (top) and SEPT7 KO cells (bottom). Numbered squares indicate zoomed-in areas for analysis of the cell cortex. Protrusions are indicated by white arrows.(E) NT CTRL and SEPT7 KO Hs578T on linear fibronectin-coated micropatterns with a width of 15 µm. Note that fibronectin is rhodamine-labeled and is therefore visible outside the cells in the SEPT7 channel. (F) Boxplot showing areas of micropatterned NT CTRL and SEPT7 KO cells. (G) Boxplot showing aspect ratios of micropatterned NT CTRL and SEPT7 KO cells. In boxplots, (*) = $p < 0.05$, (**) = $p < 0.005$, (ns) = non-significant. All scale bars are 25 µm.

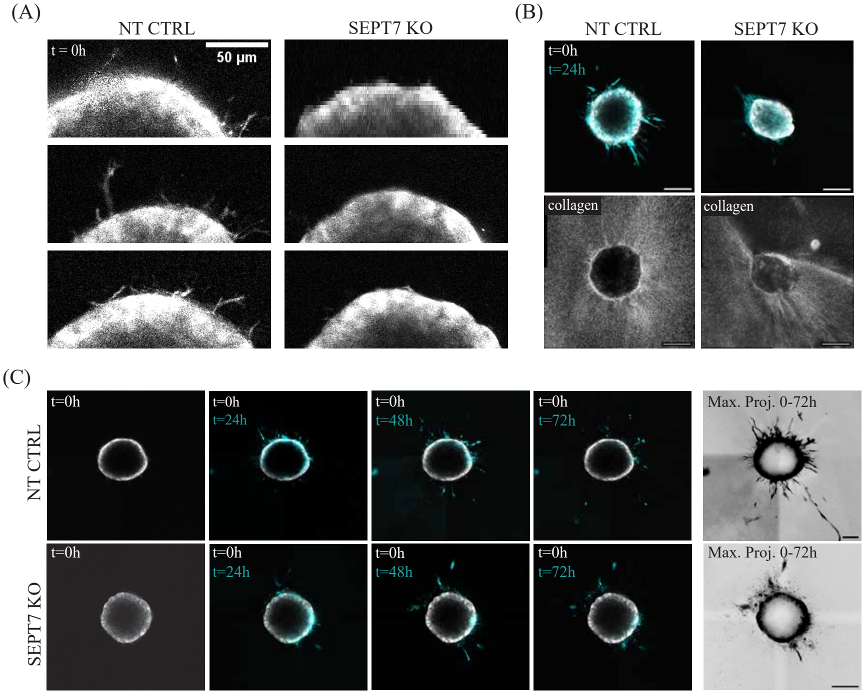

Figure 5.3: Impact of SEPT7 KO on Hs578T cell invasion in collagen type I networks measured by a 3D live-cell spheroid invasion assay. (A) Spheroid protrusions stained with cytotracker (gray) imaged at t = 0 h (~2 hours after placing spheroid in 2.4 mg/mL collagen) for NT CTRL and SEPT7 KO spheroids. (B) Correlation between cell invasion and collagen network remodeling. Top panels show an overlay of spheroid invasion for cytotracker signal at t = 0h (gray) and t = 24h (cyan), showing the amount of invasion for NT CTRL and SEPT7 KO spheroids. Bottom panels show the corresponding reflection images of the collagen network at t = 24h of invasion. (C) Time lapse image series of spheroid invasion. First four columns show overlays of spheroid invasion for cytotracker signal at t = 0h (gray) and t = 24h, t = 48h and t = 72h (cyan), indicating the progression of invasion. Far-right columns show maximum time projections of the spheroid invasion from 0 - 72h. Scale bars are 100 µm. N = 6-9 for 24h live-cell experiments and N = 3 for 72h live-cell experiments.

ing the invasion for 24 hours revealed that also at later times, 3D invasion was noticeably limited by septin depletion. NT CTRL spheroids consistently protruded in more areas and further away from the spheroids than SEPT7 KO spheroids, with mesenchymal-like invasion of single cells that detached from the spheroids (Fig. 5.3B). Interestingly, SEPT7 KO spheroids often invaded in a distinct way, where only cells on two opposite ends of the spheroid invaded in a collective-like manner, with little to no cell detachment (see Fig. 5.3B, top right panel). The resulting 'polarized' invasion shape also affected the collagen network surrounding the spheroids, with increased fiber bundling around SEPT7 KO spheroids compared to more homogeneous collagen networks surrounding NT CTRL spheroids. To test whether these differences persist on longer time scales, we also performed live-cell imaging of spheroid invasion for 72 hours (Fig. 5.3C). Consistent with the 24 hour invasion assays, septin 7 depletion again strongly restricted cell invasion, indicated by invasion in fewer areas and less far from the spheroid, with cells migrating > 500 µm in NT CTRL versus ~120 µm in SEPT7 KO invasions shown in Fig. 5.3C.

SEPTIN 7 IS NECESSARY FOR 3D SPHEROID INVASION

Septin 7 expression of the spheroid invasion assays was analyzed with immunocytochemistry to evaluate the residual septin 7 expression levels of cells that invaded the collagen. Invaded cells in the NT CTRL assays show consistent septin 7 expression (Fig. 5.4 left). Interestingly, the SEPT7 KO spheroids also showed some residual septin 7 expression but only in the few cells that protruded into the gel (Fig. 5.4 right). This indicates that these remaining cells with residual septin 7 expression are the ones that are responsible for the residual invasion in the SEPT7 KO assays. These results, together with the live-cell imaging of spheroid invasion, strongly indicate that septin expression is essential for 3D spheroid invasion in Hs578T cells.

SEPTINS GOVERN 3D INVASION POTENTIAL AND DIRECTIONAL PERSISTENCE OF HS578T CELLS

Time-lapse imaging of spheroid invasion showed that Hs578T cells confined in 2.4 mg/mL collagen exhibit a mesenchymal migration phenotype where cells invade singly. We therefore decided to quantify the invasion potential of individual control and septin knockout cells into collagen. To this end, we plated the cells on non-coated glass at sub-confluent density and tested what percentage of cells were able to migrate upwards into the 3D collagen network layered on top of them within a period of 3 days (Fig. 5.5A). To count the cells, we imaged the cell nuclei using Hoechst labeling in the first 250 µm of collagen. Side views (XZ-projections) of the invaded collagen gels indicate impaired invasion of septin 7 depleted cells (Fig. 5.5B). Image analysis of the XZ-projections allowed for quantification of the number of invaded cells, which we defined as the number of cell nuclei observed within the Z-range of 20 - 250 µm. Normalizing these numbers by the total cell count in these areas (over the entire Z-range of 0-250 µm), we measured a larger percentage of invaded cells for NT CTRL cells (8.2%) as compared to SEPT7 KO cells (4.7%) (Fig. 5.5C). Moreover, binning the distribution of invaded cells in 20 µm Z-steps showed that the SEPT7 KO cells invaded the collagen networks significantly less

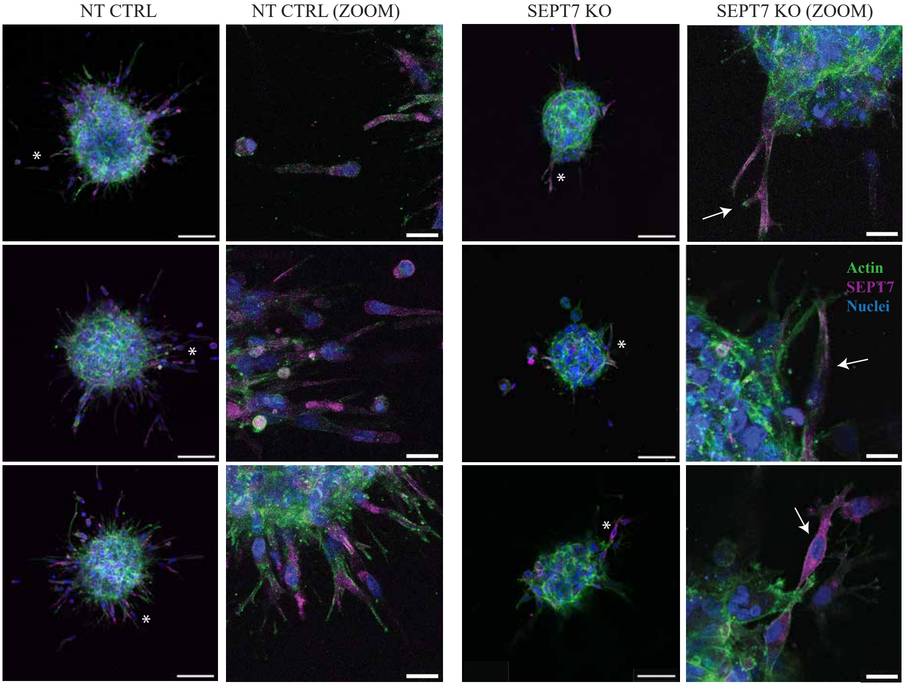

Figure 5.4: Immunocytochemistry of spheroid invasion shows that invading cells contain septin 7. NT CTRL spheroids (left) and SEPT7 KO spheroids (right) imaged after 24h of invasion in 2.4 mg/mL collagen gels, stained for actin (green), septin 7 (magenta) en nuclei (blue). Images are maximum projections of 70 µm Z-stacks with 10 µm Z-steps, with the spheroid equator positioned in the middle of the Z-stack. White asterisks on spheroid images indicate areas used for zoom-in images. White arrows in SEPT7 KO zoom-in images indicate invaded cells with residual septin 7 expression. Scale bars are 100 µm for whole-spheroid images and 25 µm for zoom-in images. N = 6-9 for each condition, consisting of three biological replicates with 2-3 spheroids.

far compared to the NT CTRL cells, with cells detected up to 200 µm versus 250 µm, respectively. These results demonstrate that septin 7 depletion reduces both the invasion potential and the directional persistence of breast cancer cells.

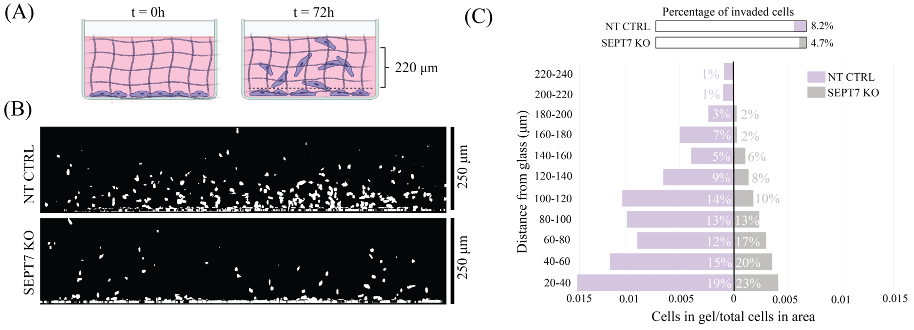

Figure 5.5: Quantitative analysis of the effect of septin knockdown on single-cell invasion into collagen. (A) Schematic of the assay. Hs578T NT CTRL cells or SEPT7 KO cells (in purple) are seeded on glass. At t=0 hr, they are overlaid with a 2.4 mg/mL collagen network. At t=72 hr, we image a confocal z-stack and count the cells remaining on the glass and those that invaded into the collagen gel. (B) Side views (XZ-projections) of 250 µm Z-stacks showing the nuclei (Hoechst label) of NT CTRL cells (top) and SEPT7 KO cells (bottom). Cells localized within 0-20 µm of the glass are classified as non-invaded. Cells localized between 20-240 µm (220 µm total) are counted as invaded. (C) Quantification of the percentage of invaded cells shown as a bar diagram (top) and as a population pyramid (bottom) demonstrates differences in the extent and range of invasion for NT CTRL (purple) and SEPT7 KO (gray). Percentages inside bars show the distribution of invaded cells, binned for 20 µm Z-steps. For both conditions, N = 9.

SEPTINS PROMOTE CELL PROTRUSIONS AND ELONGATION DURING CONFINED MIGRATION

Since 3D mesenchymal migration requires a distinct polarized cell shape with lamellipodial-like protrusions in front, we tested whether septin knockout affects the shape of individually migrating Hs578T cells in collagen networks. To this end, we seeded NT CTRL and SEPT7 KO cells in collagen networks (2.4 mg/mL) and immunostained the cells after 48 hours for nuclei, actin and septin 7. Confocal imaging revealed a striking difference in cell shape, with NT CTRL cells showing much more complex shapes than SEPT7 KO cells (Fig. 5.6A). Control Hs578T cells containing septin 7 showed a variety of shapes with numerous protrusions at the leading edge (see Fig. 5.6A, NT CTRL top). In addition, they often appeared in a 'crab' shape with the nucleus positioned in the middle, from which two equally sized 'arms' protrude forwards (see Fig. 5.6A, NT CTRL middle and bottom panels). Confocal reflection imaging revealed that the cells interacted with the collagen matrix, showing aligned collagen near protrusions. Septin depletion led to a marked change in cell shape, with fewer protrusions and more compact configurations (see Fig. 5.6A, SEPT7 KO). Confocal reflection imaging showed that the cells still interacted with collagen, but only at the cell poles where collagen alignment is visible.

To quantify the shape difference between the two cell types, we performed automated skeleton detection and counted the number of junctions in the skeletonized cells as an indicator for cell shape complexity/protrusions (Fig. 5.6B). As shown in Fig. 5.6C, septin 7 depletion significantly decreased the complexity of the 3D cell shapes as compared to control cells, meaning less (prominent) protrusions. The SEPT7 KO cells were also consistently less elongated in both the XY-plane and along the Z-axis compared to control cells, as shown by analyzing the cell lengths in all three dimensions (Fig. 5.6D). These results indicate that septin 7 contributes to cell shape regulation during confined 3D cell migration, promoting protrusion formation and elongation.

We hypothesized that the breast cancer cells need protrusions to navigate the complex confining pore space presented by the collagen gels and make directional decisions. To test this and examine the role of septin depletion, we seeded NT CTRL and SEPT7 KO cells in a microfluidic chip with constriction areas made from PDMS that mimic the interconnected narrow pores present in collagen (Fig. 5.5A(i-ii)). We imaged the cells in the constrictions to analyze the cell shapes during confined migration (Fig. 5.5A(iii)). Similar to cells in collagen gels, we found that SEPT7 KO cells had less complicated shapes compared to NT CTRL and more often migrated with rounder shapes (Fig. 5.5B). In contrast, NT CTRL cells more often showed protrusions into one or multiple constrictions, indicating a ’probing’ shape. These findings have a striking analogy to the 3D cell shapes presented in the collagen gels. We also further analyzed these shapes for cell area, length, circularity and solidity. We found that depletion of septin 7 did not affect average cell area, but decreased cell elongation, and increased circularity and solidity during squeezing (Fig. 5.5C(i-iv)). These quantifications further demonstrate the loss of complexity from the cell shapes upon septin depletion. We find that septins are necessary for cell protrusions and probing phenotypes during confined migration, both in systems with simple and complex irregular pore spaces.

5.4. DISCUSSION

Septins are cytoskeletal proteins that assemble into higher-order structures and interact with various key cellular components to support functions like cell polarity and cell shape control. High septin expression was previously correlated to metastatic breast cancers [494, 495, 496, 497, 498], but the exact mechanisms by which septins contribute to the enhanced invasion potential of breast cancer cells remain unknown. By using a gene-edited breast cancer model (based on the metastatic triple negative human breast cancer cell line Hs578T) together with a series of 2D and 3D microenvironments to mimic confinement imposed by the tumor microenvironment, we showed that septin expression regulates the invasion potential of Hs578T cells by allowing the formation of actin-based protrusions needed for navigating the collagen interstitial matrix.

Metastasis is driven by reorganization and crosstalk between cytoskeletal networks. Because septins are known to regulate cytoskeletal dynamics in various instances, we first characterized the effects of septin 7 depletion on the architecture of cytoskeleton

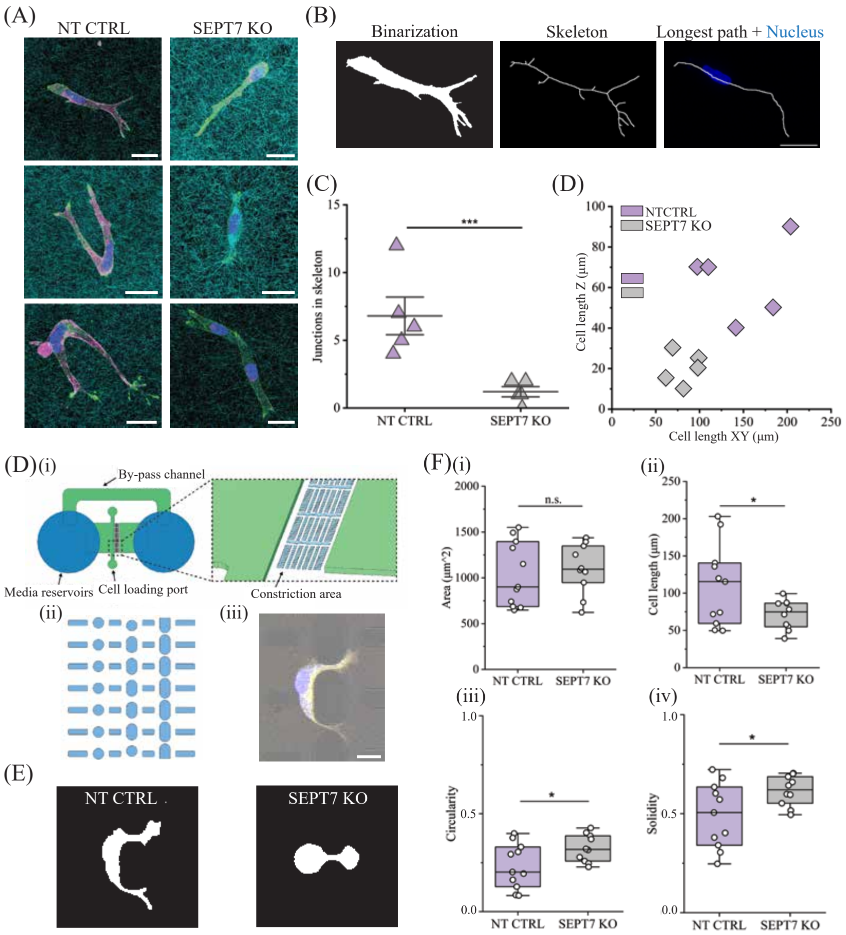

Figure 5.6: Impact of SEPT7 depletion on cell shape inside collagen matrices and in matrix-mimicking microfluidic constrictions. (A) Maximum intensity Z-projections of confocal images of NT CTRL and SEPT7 KO cells in a collagen gel after 48 hours. Cells were fluorescently stained for nuclei (blue), actin (green) and septin 7 (magenta), while collagen (blue) was imaged by reflection microscopy. Scalebars are 25 µm. Separate panels are shown in Fig. S5.4. (B) Image analysis pipeline for cell shape analysis. Maximum Z-projections were binarized and used for skeleton detection, from which we determined the cell length (longest path) and number of junctions. (C) Scatter interval plot of the number of junctions counted in each skeleton from 3D maximum Z-projections. (***) = p<0.001. (D) Scatter plot for the detected cell lengths in XY-plane and Z-axis in 3D stacks of NT CTRL (magenta) and SEPT7 KO (gray) cells. (D) (i) Schematic of the microfluidic set-up, zoomed in on the constriction areas. (ii) Design of the constriction area, with an array of pillars through which the cells migrate. (iii) Microscopy images of a Hs578T NT CTRL cell in the constriction area, constructed from bright-field (gray) and fluorescent channels for cytoplasm (yellow) and nuclei (blue). Scalebar is 25 µm. (E) Binarized images from cells in the constriction area, representative of NT CTRL and SEPT7 KO shapes during constriction. (F) Cell shape parameter boxplots, measured from NT CTRL and SEPT7 KO binary images, for (i) cell area, (ii) cell length, (iii) circularity and (iv) solidity. (*) = P<0.05, (n.s.) = non-significant.

in 2D-adherent cells. We found that septin 7 depletion also decreased septin 2 and septin 9 protein levels and often resulted in dysregulated Golgi and microtubule networks. Because both the Golgi apparatus and α-tubulin showed co-localization with residual septin 9, these defects likely arise from abnormal septin 9 localization, consistent with previous research showing that septin 9 interacts with Golgi-associated lipids and bundles microtubules [483]. In SEPT7 KO cell cultures we also noticed an increase in giant and multi-nucleated cells (Fig. S5.11), in line with previous reports of septin-depleted cells [494]. However, the percentage of these giant cells in the cultures was only 5 - 10 % and qualitatively it appeared that proliferation at a population level was not greatly affected. In many cell types septins have been shown to be necessary for cell division through their interactions with the contractile actomyosin ring and abscission machinery[518, 488, 519, 520, 521, 522, 523]. However, some cells such as hematopoietic cells can switch to septin-independent mechanisms of division [524]. Our observations suggest that the Hs578T cells also have ways to overcome septin-deficiency. Interestingly, we observed examples of cells that appeared to divide by crawling away from each other (Fig. S5.12). This mechanism of cytokinesis closely resembles wave-mediated cytofission observed in giant multinucleated amoebae, which is driven by cortical actin waves [525]. Because septins are known to interact with actin and co-localize with stress fibers[478, 479, 480], we additionally tested the interplay between septins and actin in Hs578T cells. Inhibition of actin polymerization with cytochalasin D (CD) altered septin architecture from fibers to rings, as was previously reported for other cell lines [478, 526]. Depletion of septin 7 resulted in loss of peri-nuclear stress fibers and small actin protrusions. The loss of peri-nuclear stress fibers could reflect destabilization due to the loss of septin structures. Alternatively, there could be a disturbed balance between septin 9 isoforms in response to the septin 7 knockout, as Sept9i2 expression is associated with a loss of perinuclear stress fibers [527]. The micron-sized actin protrusions that were lost in SEPT7 KO cells co-localized with microtubules (Fig. S5.10) suggesting they are primary cilia and/or tunneling nanotubes [528]. The loss of primary cilia in septin-depleted cells is consistent with prior evidence that septins contribute to the biogenesis and function of cilia [524]. The loss of septin-dependent cilia could contribute to the impact of septin depletion on impaired cell invasion, as Hs578T cells were previously reported to have a large primary cilium that promotes invasion [529]. We also noticed a decrease in intercellular actin protrusions in septin knockout Hs578T cells compared to control cells (Fig. S5.10A). Because these protrusions co-localize with microtubules (Fig. S5.10B), we identify them as tunneling nanotubes. These membranous protrusions provide intercellular transport and communication and are linked to tumor invasion, proliferation and therapy resistance [528, 530]. As we additionally found septin 7 co-localization with these protrusions in control cells (Fig. S5.10C), we hypothesize that septin 7 impacts tumor invasion strategies through regulating cell-cell communication.

To test the impact of the septin 7 knockout and associated loss of septin structures on Hs578T cell invasiveness, we performed 3D spheroid invasion assays in collagen gels. Upon septin knockdown, protrusive behavior by spheroids decreased and invasion within 24 hours and 72 hours time-frames was strongly inhibited. Immunocytochemistry additionally showed that residual invasion from SEPT7 KO spheroids came from the small fraction of septin 7 positive cells within the knockout culture. Moreover, septin knockout spheroids often collectively invaded into collagen, in contrast to the individual invasion in control spheroid assays. It would be interesting to further investigate why the migration mode was altered in these conditions as collective invasion is related to increased metastatic site formation *in vivo* [531]. We propose that the heterogeneity of the knockout spheroids, which consist of mainly immobile (SEPT7 KO) cells and a small fraction of motile cells (with residual septin 7), may impact the spheroid unjamming transition [532]. We noticed that the edges of SEPT7 KO spheroids before embedding in collagen appeared more rough than for control spheroids, which could indicate a smaller packing density and less cohesion of the spheroid (Fig. S5.5). To test this idea, we measured the viscoelastic properties of the spheroids in a microfluidic device designed for spheroid compression (Ref. [516]). We found that septin depletion significantly decreased spheroid elasticity, which could be the result from loss of stress fibers we observed in 2D adhered cells (Fig. S5.9). Furthermore, our measurements indicated a trend towards lower viscosity, which could be related to lower packing densities. Analysis of the effect of septin 7 knockout on cell-cell interactions and deposition of ECM proteins in the spheroids, for instance by Western Blot analysis, could further elucidate the role of septin in spheroid viscoelasticity, a factor that may impact the mode of invasion when the spheroids are embedded in collagen.

Since we observed mainly single-cell mesenchymal migration, we next used single-cell migration assays with physical constrictions that mimic the physical restrictions from the tumor microenvironment. This approach facilitates more high throughput and high-resolution analysis of cell shape and motility, and allows us to study the impact of septins on confined migration in absence of septin-dependent ECM remodeling [497, 533]. To this end, we used micropatterns, microfluidic constrictions and collagen hydrogels. We found that in minimal quasi-1D constriction conditions imposed by micropatterns, septin depletion led to reduced cell aspect ratios. In 3D single-cell invasion assays with collagen hydrogels, we confirmed that septin depletion impaired cell invasion and found that the septin knockout cells were less protrusive and less elongated than control cells. These shape indicators mainly describe the actin-based lamellipodia and filopodia protrusions, and indicate that the septin-depleted cells lose the ability to properly form these structures. These results suggest that septins stimulate lamellipodia and filopodia formation in breast cancer cells. A similar observation was previously made in MCF-7 breast cancer cells, where SEPT9 inhibited protrusion formation, while overexpression of the SEPT9i1 isoform promoted the formation of lamellipodia and filopodia [498]. Furthermore, the control cells adopted crab-like shapes, extending protrusions along different paths in the confining collagen gels and pillar arrays. Recent studies with micropatterned branched micropatterns show that cells extend these protrusions in a seesaw manner dependent on actin polymerization at the leading edge [534]. Hence our findings suggest that septins may regulate actin polymerization. Septins have been identified at the bases of actin-rich lamellipodia in endothelial cells and fibroblasts [535, 533]. Also, they were recently found to control lamellipodia formation through small Rho GTPase-mediated actin dynamics [536]. Since the bases of cell protrusions are defined by positive membrane curvature, we hypothesize that septins also contribute to stabilizing this curvature by sensing membrane geometry [512], a process potentially mediated by Borg proteins, which are known to crosslink actin and septins and promote actin filament polymerization along septin structures [535, 471]. Moreover, extensive elongation of protrusions found in NT CTRL cells, that we defined as long arms of so-called 'crab' shapes, were absent in SEPT7 KO cells. These long protrusions could also be indicators of the cells' ability to break through basement membranes, which contributes to invasiveness [537]. In microfluidic migration devices with constrictions that mimic ECM pores, the septin-depleted cells migrated through the constrictions with less complex and rounder cell shapes than the NT CTRL cells, resembling cell shapes in collagen. However, the overviews from microfluidic constriction areas do not show clear differences in the number of migrating cells (Fig. S5.7), indicating that the inhibitory effects of septin depletion on single-cell invasion may involve ECM remodeling besides protrusion regulation.

Besides actin-dependent effects on cell shape regulation, there could also be septin-mediated effects on the cell membrane, such as changes in membrane tension and sequestering of excess membrane [475]. Cell-free reconstitution studies have shown that septins interact with phosphoinositide lipids such as PIP2 and create membrane curvature [510]. Thus, direct septin-mediated membrane reshaping could contribute to cell shape and protrusion formation during confined migration. Preliminary immunofluorescence results indicate that the PIP2 levels are lower in cells depleted of septin 7 than in control cells (Fig. S5.6). Fluorescence lifetime imaging shows a lower fluorescent lifetime of the lipid-packing Flipper TR probe [538] in septin 7 knockout cells (Fig. S5.8), which could indicate changes in membrane tension and/or composition. However, more data is needed to interpret the origin of these changes, as the lifetime of Flipper TR and thus lipid packing in the cell membrane could be affected by various mechanisms. For example, septins can also change membrane trafficking through their interactions with Golgi-associated lipids and mediating microtubule-based vesicular transport [483, 539, 540].

Collectively, our findings show that septins regulate confined invasion by controlling cell shape and supporting protrusion formation to explore porous networks. The strong impact of septin on cell shape is interesting in light of evidence that cell shape indicators for complexity and protrusions correlate with triple negative breast cancer tumor growth and metastasis, tested in *in vivo* mouse models [541]. Although recent work proves the predictive power of cell shapes and protrusion analysis for cancer cell invasiveness [541, 542], we still understand little about the cellular processes that govern cancer cell shapes and protrusive behavior, and how these are impacted by the biophysical properties of the tumor microenvironments. In this research, we propose a role for a septin-mediated mechanism of cell shape and actin-based protrusion regulation that promotes 3D-tissue invasion.

5.5. ACKNOWLEDGEMENTS

I would like to thank Klara Beslmüller for creating the septin 7 knockout and control Hs578t cell lines. Thanks to Margherita Tavasso for the (fun) spheroid compression measurements. I also want to thank Ruben Boot for making the microfluidic devices, and Imke van Dijk for helping with the optimization of the microfluidic device. Thanks to Myrthe Beerens for her work on the characterization of the cells. Also thank to Manos Mavrakis for valuable discussions regarding the experimental design and interpretation of the data and Dimphna Meijers for sharing an aliquot of the anti-gm130 mouse IgG.

5.6. Supplementary Information

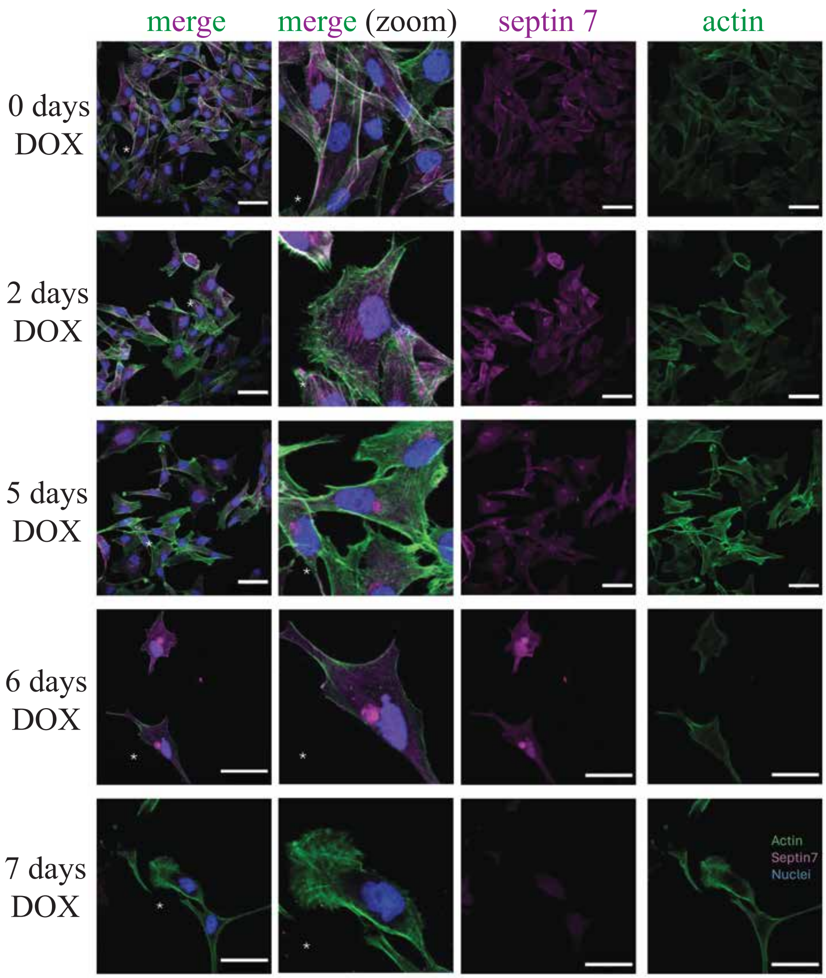

Figure S5.1: Immunocytochemistry analysis of the time dependence of doxycyclin induction of septin 7 knockout in Hs578T. Rows (from top to bottom): 0 days doxycyclin, 2 days doxycyclin, 5 days doxycyclin, 6 days doxycyclin and 7 days doxycyclin. Columns show stainings for actin (green), septin 7 (magenta), merge of actin and septin 7 and zoom-in of merge images at spots indicated with white asterisks. Scale bars are 50 µm.

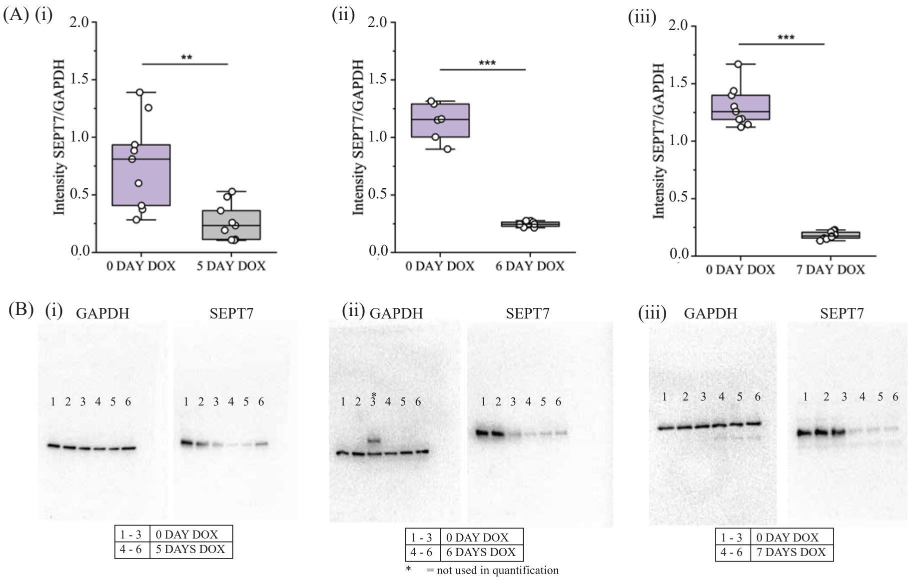

Figure S5.2: Western Blot analysis of the time dependence of doxycyclin induction of septin 7 knockout in Hs578T. (A) Quantification of septin 7 signal intensities normalized to GAPDH signal intensities for (i) 0 and 5 days doxycyclin treatment, (ii) 0 and 6 days doxycyclin treatment and (iii) 0 and 7 days doxycyclin treatment. (**) = $p < 0.005$, (***) = $p < 0.001$. (B) Western Blots showing GAPDH and septin 7 stainings for (i) 0 and 5 days doxycyclin treatment, (ii) 0 and 6 days doxycyclin treatment and (iii) 0 and 7 days doxycyclin treatment.

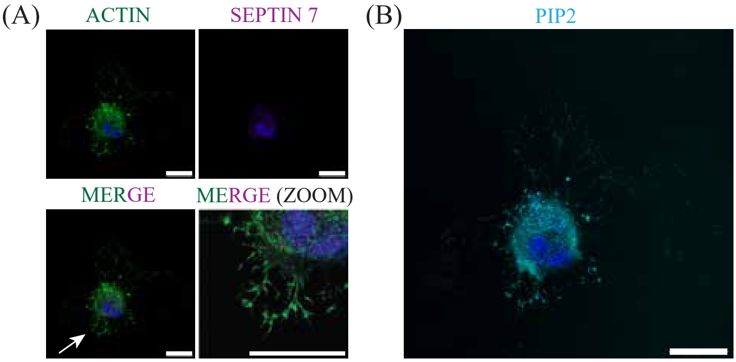

Figure S5.3: Cytochalasin D treatment of SEPT7 KO Hs578T cells adhered on glass results in small 2D-adhered cell size. Immunocytochemistry images of SEPT7 KO cells treated with cytochalasin D for (A) actin (green) and septin 7 (magenta), and (B) PIP2 - mouse anti-PIP2 (#MABS2283, Sigma-Aldrich), as an indicator for the cell membrane (cyan). Inhibition of actin polymerization with cytochalasin D combined with septin 7 depletion results in a small 2D-adhered cell size, as quantified in Fig. 5.2. White arrow in MERGE image indicates area used for MERGE (ZOOM) images. Scale bars are 25 µm.

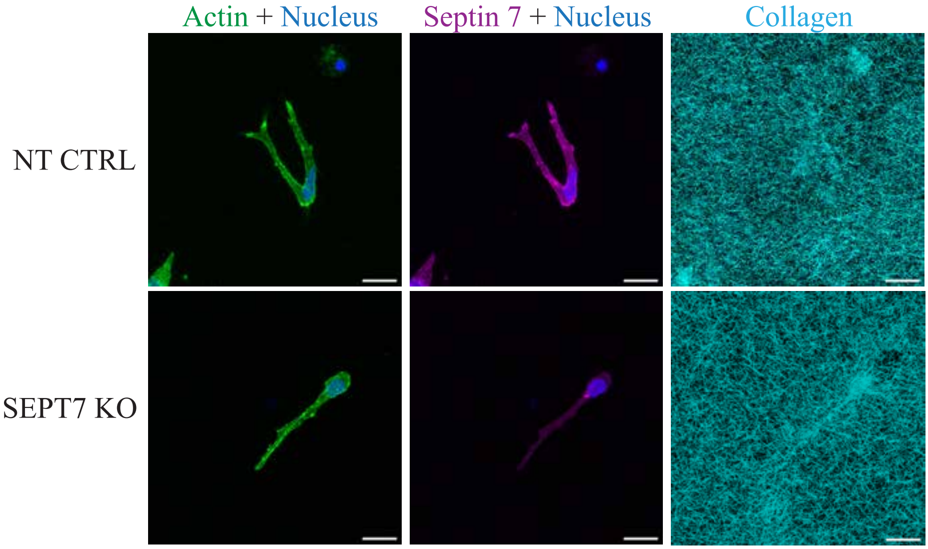

Figure S5.4: 3D-cell shapes of cells in collagen showing separate fluorescence and reflection panels. Maximum intensity Z-projections of confocal images of NT CTRL and SEPT7 KO cells in a 2.4 mg/mL collagen gel after 48 hours. Cells were stained for nuclei (blue), actin (green) and septin 7 (magenta). Collagen (blue) was imaged by reflection microscopy. Scale bars are 25 µm.

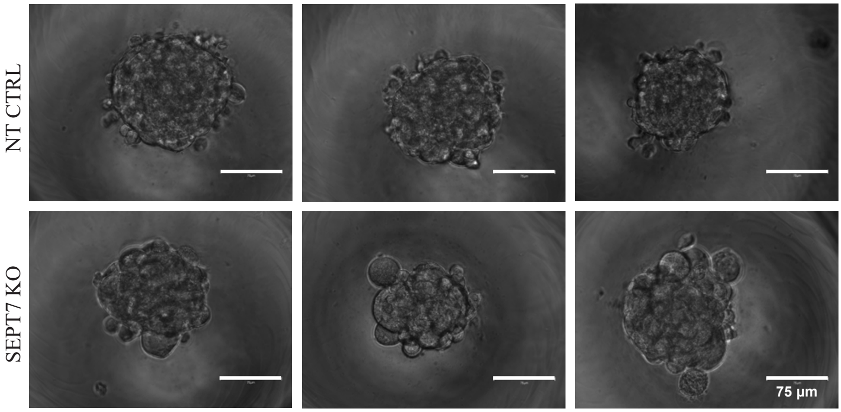

Figure S5.5: Morphological characterization of cell spheroids. Brightfield images of NT CTRL (top) and SEPT7 KO (bottom) Hs578T spheroids formed in round-bottom and ultra-low attachment Elplasia^{TM} 96-well plates after 48 hours of incubation. Note that the SEPT7 KO spheroids are less round and increased edge roughness compared to NT CTRL spheroids. Scale bars are 75 µm.

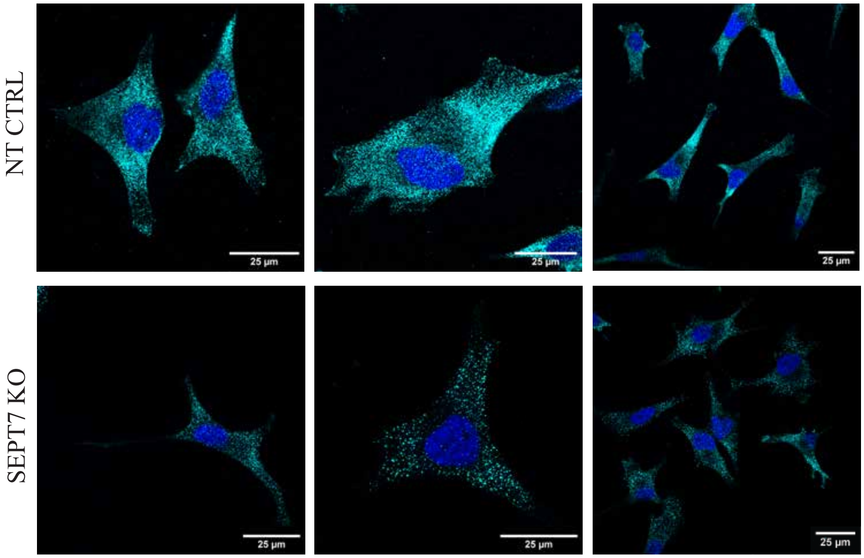

Figure S5.6: Immunocytochemistry indicates a difference in PIP2 content in the cell membrane of control and septin 7 knockout cells. Immunocytochemistry for NT CTRL (top row) and SEPT7 KO (bottom row) Hs578T cells for PIP2 (cyan) and nuclei (blue). Scale bars are 25 µm.

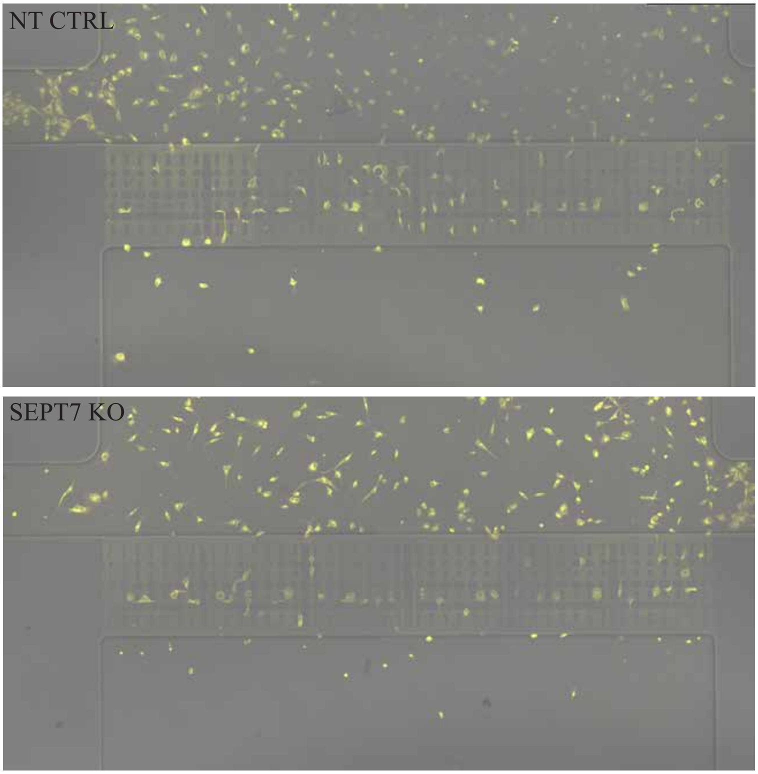

Figure S5.7: Overview images of cells in microfluidic migration chips. Brightfield images of microfluidic migration chips for NT CTRL (top) and SEPT7 KO (bottom) Hs578T cells after 24 hour incubation, merged with Cytotracker Orange (yellow) signals for cell labeling. Note that the number of cells within the constriction areas is comparable for NT CTRL and SEPT7 KO cells.

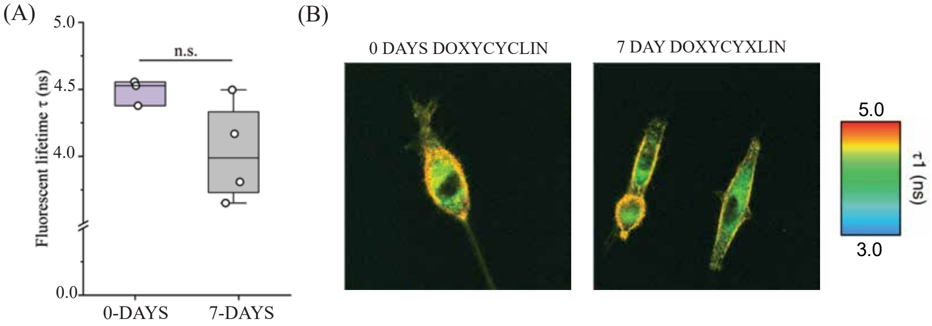

Figure S5.8: Measurements of lipid packing in control and septin 7 knockout cells. (A) Boxplot showing fluorescent lifetime τ measurements for SEPT7 KO Hs578T cells before septin 7 knockout (0-DAYS doxycyclin) and after septin 7 knockout (7-DAYS doxycyclin). (ns) = $p > 0.05$. (B) Life-time microscopy images of Flipper-TR probe on SEPT7 KO Hs578T cells before septin 7 knockout (0-DAYS doxycyclin) and after septin 7 knockout (7-DAYS doxycyclin). Color bar (right) for life-time τ. Approximately 5 minutes before the measurement, 1 µM of the Flipper-TR probe in culture medium was added to the cells.

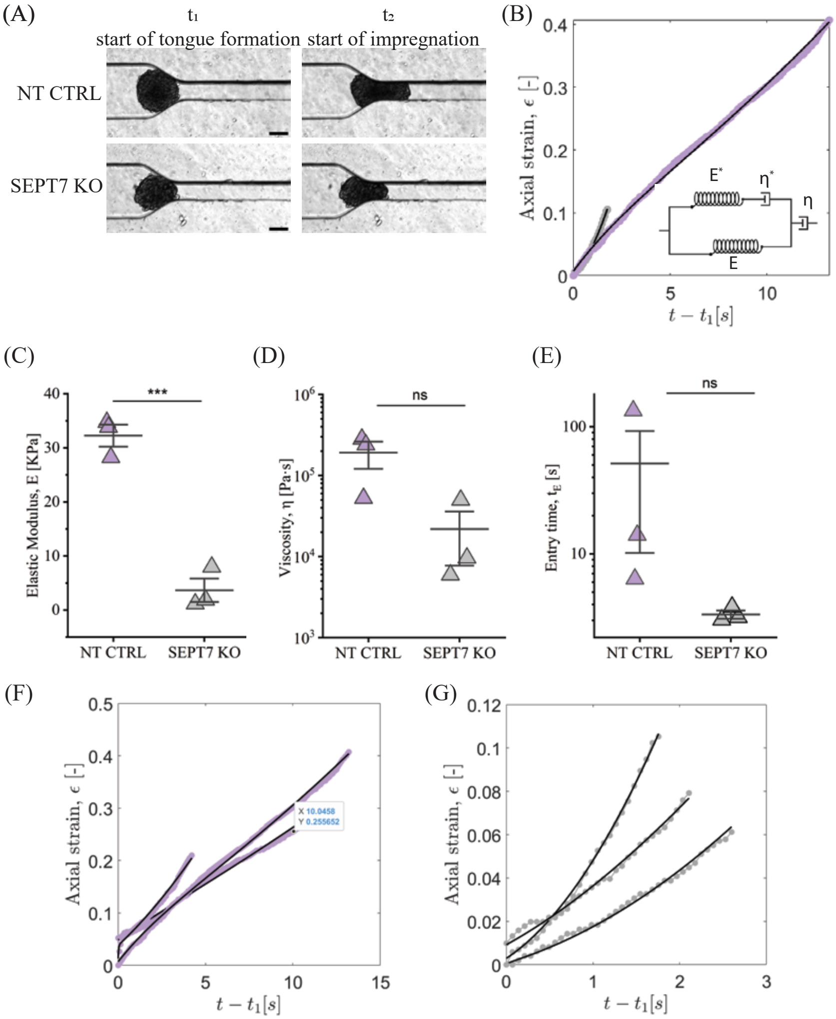

Figure S5.9: Spheroid viscoelasticity. (A) Brightfield images of NT CTRL and SEPT7 KO Hs578T spheroids in the microfluidic constriction channel: snapshots at time t_1 (start of tongue formation) and t_2 (start of compression). Scale bars are 100 µm. (B) Strain curves from NT CTRL and SEPT7 KO Hs578T spheroids shown in panel (A). Strain curves start at the beginning of the tongue formation (t_1) and are fitted to the Dynamic Modified Maxwell Model[516], which is schematically illustrated in the inset. (C) Measurements for spheroid bulk elastic moduli E, (D) viscosity η and (E) entry time t_E. (***) = p < 0.001, (ns) = p > 0.05. Bar and whiskers show the mean and standard error. N = 3 per condition. (F) All individual strain curves from NT CTRL spheroid compressions and (E) SEPT7 KO spheroid compressions.

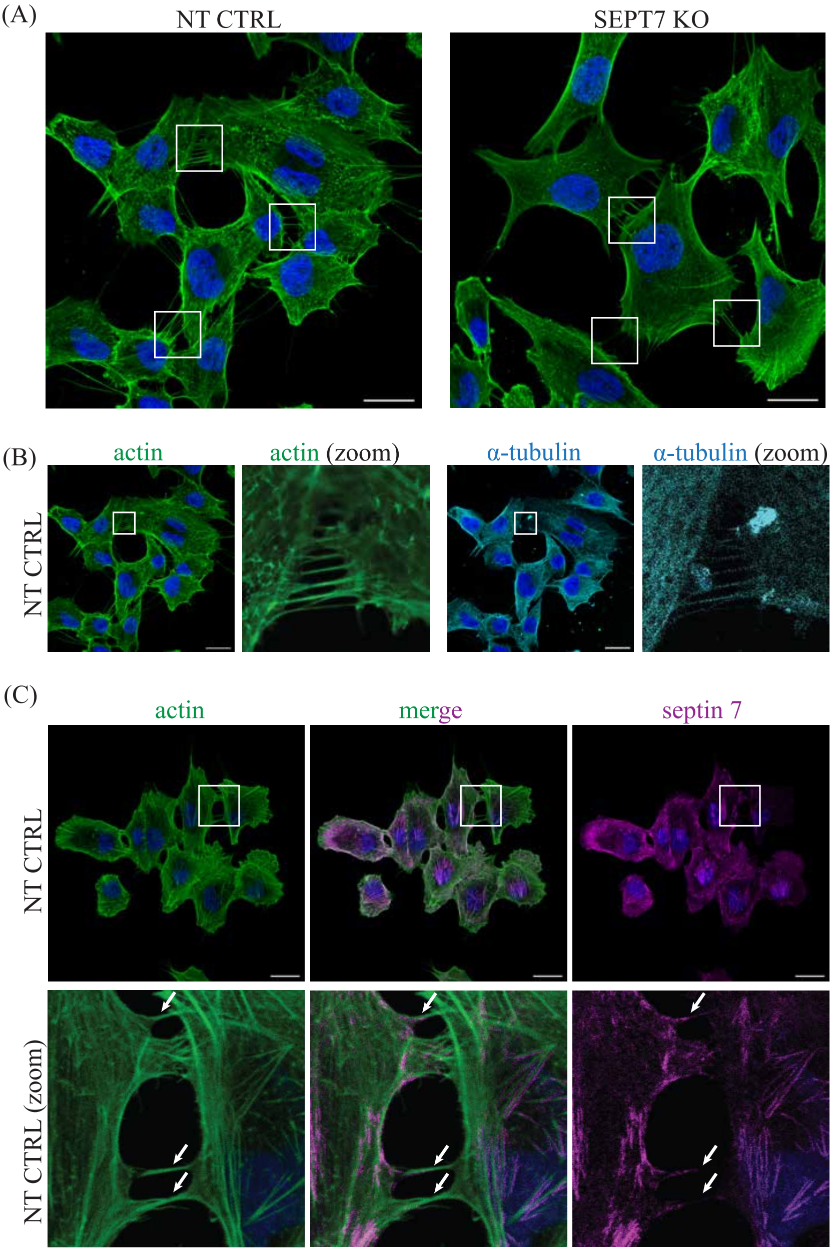

Figure S5.10: Intercellular actin-based protrusions. (A) Immunocytochemistry of NT CTRL and SEPT7 KO Hs578T cells stained for actin (green) and nuclei (blue). Connecting actin protrusions between cells are reduced in SEPT7 KO compared to NT CTRL, as seen in the areas indicated by white squares. (B) Immunocytochemistry of NT CTRL Hs578T cells stained for actin (green), α-tubulin (cyan) and nuclei (blue). Zoom panels are indicated by white squares. Intercellular actin protrusions co-localize with α-tubulin, indicating that these structures are tunneling nanotubes. (C) Immunocytochemistry of NT CTRL Hs578T cells stained for actin (green), septin 7 (magenta) and nuclei (blue). Zoom in panels are indicated by white squares. White arrows indicate the connecting actin protrusions and co-localization with septin 7 signals. Scale bars are 25 µm.

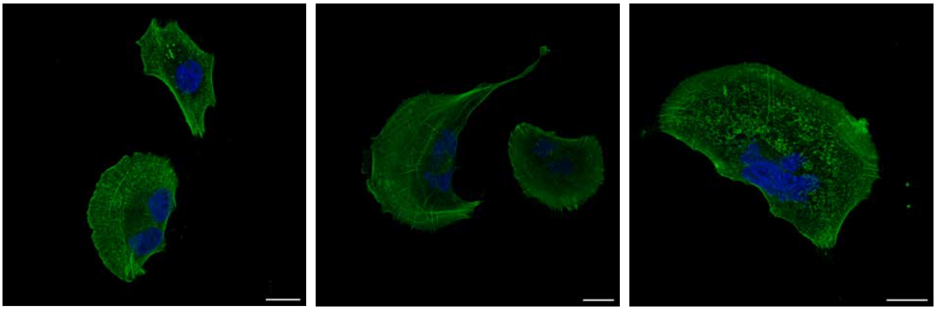

Figure S5.11: Giant multinucleated SEPT7 KO Hs578T cells. Immunocytochemistry of SEPT7 KO cells stained for actin (green) and nuclei (blue). Cells that are shown have an increased size (> 100 µm) and contain multiple nuclei. Scale bars are 25 µm.

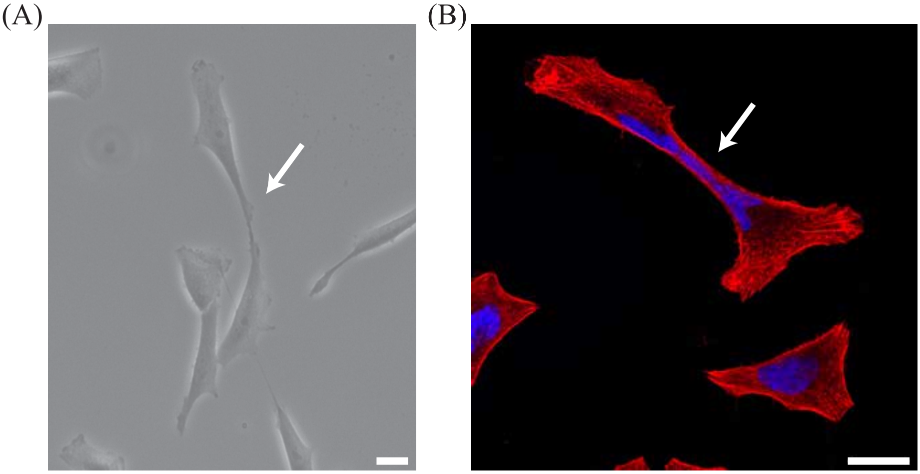

Figure S5.12: Dividing SEPT7 KO Hs5789T cells. (A) Bright-field image of connected SEPT7 KO cells (indicated by white arrow) that are polarized in opposite directions. (B) Immunocytochemistry of SEPT7 KO cells for actin (red) and nuclei (blue). Image shows a multi-nucleated giant cell that appears to divide into two cells that crawl away from each other (indicated by white arrow). Scale bars are 25 µm.

6

OUTLOOK

In this dissertation we explored how biophysical factors play a significant role in controlling the invasion strategies of cancer cells, specifically through cell-matrix interactions and cytoskeletal crosstalk. In this outlook, we further underline the potential of studying cytoskeletal crosstalk in the context of cancer cell invasion. We discuss preliminary work on studying the role of the cytolinker plectin and development of plectin truncation variants to dissect the different cellular functions during invasion. Finally, we show the potential of using new microfluidic migration chips designs as a method to study cancer cell migration modes, in particular collective invasion strategies.

6.1. INTRODUCTION

THE origin of cancer stems from biological processes that cause genomic abnormalities, but evidence is growing that biophysical aspects also play a key role in the initiation of cancer as well as in cancer metastasis. In the first half of this dissertation, we investigated the biophysics behind cell-matrix interactions during cancer cell invasion. In Chapter 2 we specifically looked into cancer cell deformability and how this regulates migration efficacy through confinements using custom-made microfluidic devices. We found that cancer cell deformability correlates with the active migration speed of the cells through narrow constrictions. To further examine the function of cell-matrix interactions during invasion, we explored the role of extracellular matrix properties and the EMT status of the cells in 3D spheroid invasion assays in Chapter 3. Here, we found that matrix porosity and vimentin expression regulate the onset of invasion while MMP1 expression levels correlate with the spheroid expansion rate. Our findings confirm recent models proposing that tumor invasion can be described as a physical unjamming process but highlight that cells actively influence the unjamming process by degrading the matrix. For the second half of this dissertation, we focused our research on cytoskeletal crosstalk as a key regulator of cancer cell migration. In Chapter 4, we summarized current insights in the role of cytoskeletal crosstalk in migration, describing how coupling of filaments through entanglements, crosslinking and bundling regulates cellular mechanics and cytoskeletal dynamics involved in migration strategies. In Chapter 5 we demonstrated that septins, only recently recognized as a central mediator of cytoskeletal crosstalk, strongly impact invasion of breast cancer cells by regulating cell shape and protrusion formation.

Together, the research in this dissertation contributes further to the emerging consensus that biophysics is an important aspect of cancer invasion. Additionally, the work in this dissertation strongly indicates that classical biological perspectives of cancer cell motility and more recent physics-based descriptions of cancer invasion should be integrated to to fully understand the mechanisms driving cancer invasion. Our studies show that cell-matrix interactions and cytoskeletal crosstalk are interesting mechanisms to study the coupling between biology and physics in cancer research. We particularly highlighted this in Chapter 3 by showing that EMT and unjamming transitions are coupled by MMP1-mediated cell-matrix interactions, and in Chapter 4, where we reviewed the role of cytoskeletal crosstalk in cell mechanics during migration. In this Outlook chapter, we aim to further underline the potential of studying cytoskeletal crosstalk in the context of cancer cell invasion, by discussing some preliminary work on plectin knockout cancer cells. In addition, we will also discuss the novel development of variants of plectin that will make it possible to better dissect the different cellular functions of this (and related) cytolinker proteins. Finally, we will show the potential of using microfluidic migration chips as a new method to study cancer cell migration modes, in particular collective invasion strategies.

6.2. PLECTIN-MEDIATED CYTOSKELETAL CROSSTALK IN CANCER INVASION

Plectin is an essential crosslinker in cells that binds to actin filaments, intermediate filaments, microtubules, and the nuclear lamina. As a major cytoskeletal crosslinker, plectin provides structural integrity and mediates mechanotransduction in cells [543, 544]. Therefore, plectin-mediated crosstalk is required for many aspects of cell migration, as described in Chapter 4. In response to acto-myosin contractility, plectin-mediated actin-vimentin coupling is necessary to generate the nuclear piston machine that drives confined cell migration [345, 346]. Actin-intermediate filament linkage by plectin also stabilizes intercellular junctions [274, 545] and microtubule-actin crosslinking in the cortex by plectin influences cell deformability [546]. Because of plectin's broad range of binding partners and involvement in migratory processes, it is not surprising that plectin is also associated with cancer progression. It was recently shown that removing plectin from cancer cells blocks their migration *in vitro* and *in vivo* [547, 548]. Since plectin is strongly upregulated in many types of cancer cells [549], it could be an effective and selective new target for migrastatic drugs. However, further progress is hindered because the mechanisms through which plectin promotes cell migration are poorly understood. Previous research on plectin associated plectin with EMT, where plectin knockdown in hepatocellular carcinoma cells leads to higher E-cadherin and lower N-cadherin and vimentin levels, indicating a more epithelial phenotype [550]. Recent studies showed that plectin regulates invapodia formation by anchoring vimentin to invapodia via F-actin binding and delivering the invadopodia-specific protease MT1-MMP to invapodia [548, 551]. Both mechanisms promote invapodia formation and subsequently increase ECM degradation, which elevates the invasion potential of cancer cells. Another recent study showed that high matrix stiffness can upregulate plectin expression, mediated by integrin $\beta1$, to promote F-actin polymerization and invasion [552], and integrin $\alpha6\beta4$ binds to plectin and vimentin to enhance 3D invasion [553]. Plectin also recruits vimentin filaments to the nucleus, which is implicated in nuclear dysmorphia of breast cancer cells [554].

To further elucidate the role of plectin-mediated cytoskeletal crosstalk in cancer invasion, we performed preliminary experiments with plectin knockout HS578T breast cancer cells, created with a doxycyclin (DOX) inducible CRISPR/CAS9 system using a PkLV-U6-gRNA/PGK-Puro-2A-BFP vector (Addgene, #50946) cloned with plectin (PLEC KO) or a non-targeting control (NT CTRL) single guide RNA sequence. Breast cancer cells often have high levels of plectin [548] and plectin dysregulation is implicated in breast cancer progression [548, 555, 556]. Through immunocytochemistry (Fig. 6.1A) and Western Blot analysis (Fig. 6.1B), we confirmed that we successfully depleted plectin from the HS578T cells, as the plectin signal in the stainings and Western Blots was lost in HS578T PLEC KO cells treated with DOX. Interestingly, lamin A/C stainings in PLEC KO cells were more heterogeneous than control stainings, possibly indicating a dysregulation of the nuclear envelope in response to plectin depletion.

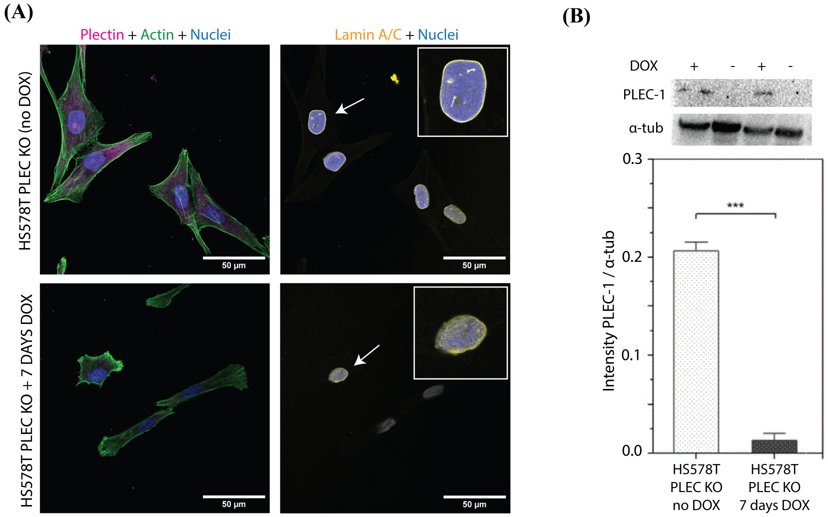

Figure 6.1: Characterization of the extent of doxycyclin (DOX) inducible plectin knockdown in HS578T breast cancer cells. (A) Immunocytochemistry of HS578T plectin knockout cells without (no DOX) and with (+ 7 days DOX) induction of the knockout. Left panels are stained for plectin (magenta), actin (green) and nuclei (blue), right panels are stained for lamin A/C (yellow) and nuclei (blue). Insets of right panels are zoomed-in images of cell nuclei indicated by the white arrows. Scale bars are 50 µm. (B) Western blot analysis of plectin expression levels in HS578T without (no DOX) and with (+ 7 days DOX) induction of the plectin knockout. Bar graph shows the intensities of the plectin bands relative to α-tubulin. (***) = $p < 0.001$. For each condition, $n = 2$ biological replicates, each subtracted from 3 different background spots, resulting in $n = 6$.

To test the effect of the plectin knockout on cancer cell invasion, we next performed single-cell and spheroid migration assays in collagen I gels (Fig. 6.2). The plectin knockout had no effect on single-cell migration, as the number of migrated cells and their distribution in the collagen gel were identical for NT CTRL and PLEC KO cells, as indicated by the population pyramid of invaded cells (Fig. 6.2A-C). Surprisingly, 3D spheroid invasion into collagen gels for 24 hours was enhanced in PLEC KO HS578T spheroids compared to control spheroids (Fig. 6.2D). Invading PLEC KO HS578T cells migrated further from the spheroid within the time-frame of 24 hours and were more heterogeneous in orientation and cell shape compared to NT CTRL cell invasion. This result is contradictory to earlier findings of plectin being upregulated in most types of cancer [549], also breast cancer [548, 556]. However, low expression of plectin was also found to promote breast cancer progression through affecting nuclear centrosome relocalization [555]. The increasing focus on plectin-related cancer research in the last years starts to illuminate the complexity behind studying plectin. We now begin to understand that plectin has a dual role in cancer progression: both high and low plectin expression are found to promote tumor invasion, as further reviewed in Ref. [544]. This complex role of plectin in (breast) cancer is poorly understood, and further investigation of the differ-

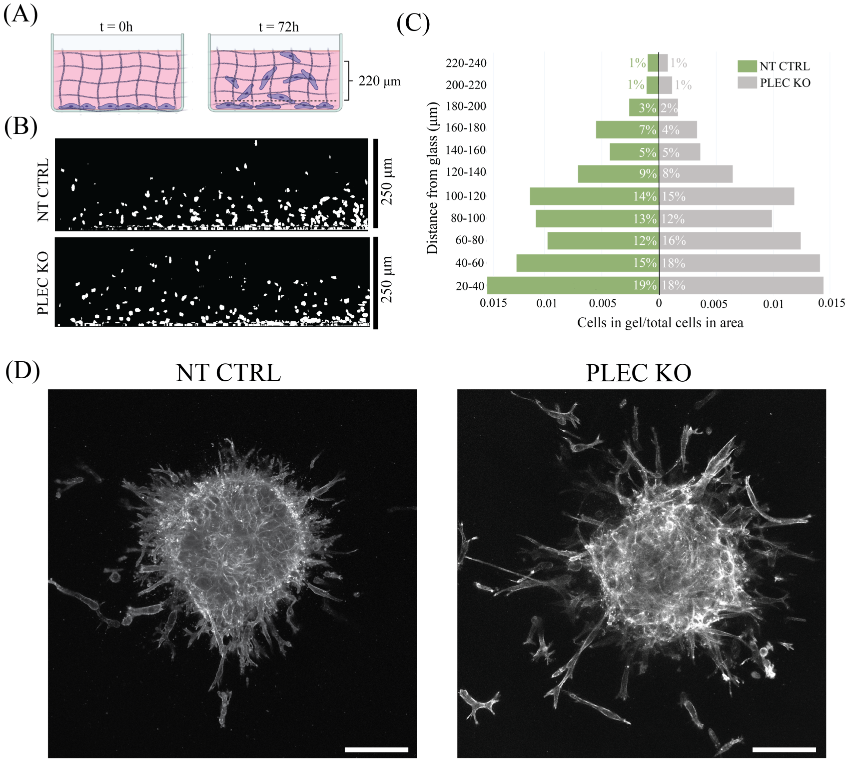

Figure 6.2: Migration assays with plectin knockout cells. (A) Schematic of the assay to quantify single-cell invasion into collagen. HS578T NT CTRL cells or PLEC KO cells (in purple) are seeded on glass. At t = 0 hr, they are overlaid with a collagen gel. At t = 72 hr, we image a confocal z-stack and count the cells remaining on the glass and those that invaded into the collagen gel. (B) Side views (XZ-projections) of 250 µm Z-stacks showing the nuclei (Hoechst label) of NT CTRL cells (top) and PLEC KO cells (bottom). Cells localized within 0-20 µm of the glass are classified as non-invaded. Cells localized between 20-240 µm (220 µm total) are counted as invaded. (C) Quantification of the percentage of invaded cells as a population pyramid, demonstrating the distribution and range of invasion for NT CTRL (green) and PLEC KO (gray). Percentages inside bars show the distribution of invaded cells, binned for 20 µm in Z for gel areas. For the collagen invasion assays, N = 9. (D) Maximum Z-projections of spheroid invasion assays of NT CTRL and PLEC KO spheroids in 2.4 mg/mL bovine type I collagen for 24 hours. Spheroids were stained for actin (gray) with Phalloidin 647. Z-projections were 70 µm upwards from the bottom of the spheroid, with 10 µm steps. N = 3. Scale bars are 100 µm.

ent functions of plectin will help us understand how to target plectin-mediated cancer progression.

6.3. EXPERIMENTAL PATHWAYS TO STUDY PLECTIN-MEDIATED CANCER PROGRESSION

To distinguish between the different functions of plectin and thus better understand the mechanisms behind plectin-mediated cancer progression, we discuss new research pathways below. First of all, we propose using microfluidic migration designs similar to the designs described in Chapter 2, inspired by Refs. [62, 63], in combination with the plectin knockout HS578T cell line. Most of what we currently know about the role of the cytoskeleton in migration is based on *in vitro* migration assays using cells cultured on flat two-dimensional (2D) substrates. However, such unconstrained 2D migration assays fail to mimic the strongly constraining 3D structure of tissues. Tissues impose huge physical barriers on cancer cells because they are densely crowded with cells and extracellular matrix [557]. Invading cancer cells have to squeeze themselves through narrow pores and make directional choices each time they encounter junctions. 3D migration assays based on cancer cell tumoroids embedded in collagen have become a standard assay to simulate 3D tissue invasion [558] (Fig. 6.3A). But this assay poses limitations for fundamental research into the cell migration mechanism because the heterogeneous structure of collagen networks makes it impossible to separate the roles of cell squeezing versus directional decision making. Also it is difficult to image cells in 3D with the subcellular resolution needed to visualize cytoskeletal network remodeling. Microfluidic migration devices are a convenient tool to quantitatively study the impact of confinement on cell migration. It will be interesting to compare wild type and plectin knockout HS578T cells in microfluidic constrictions, in order to analyze the roles of plectin in cell squeezing (Fig. 6.3Bi-ii), decision making (Fig. 6.3Biii-iv) and combinations thereof (Fig. 6.3Bv-vi).

Since plectin is a multidomain protein with many binding partners, an important next step will be to use plectin truncation variants to study the contributions of its different domains (Fig. 6.3C-D). Our group recently developed an engineered variant of plectin called ACTIF, which only has the actin-vimentin crosslinking function of plectin. ACTIF has an actin-binding domain (from MACF) and an intermediate filament-binding domain (from plectin), separated by a coiled-coil linker for dimerisation. Cell-free reconstitution showed that ACTIF indeed efficiently crosslinks actin and vimentin into composite networks and bundles [559]. Furthermore, plectin-1c, a plectin isoform that is known to bind to the nuclear membrane [560], could be used as the basis for an engineered construct that reconstitutes plectin's ability to anchor vimentin to the nucleus. The plectin knockout HS578T cells provide an ideal cellular background to reconstitute the crosslinking (Fig. 6.3F, left panel) or nucleus anchoring (Fig. 6.3F, right panel) functions of plectin using the engineered plectin constructs. To test the importance of plectin as a crosslinker, live-cell confocal imaging of the three cytoskeletal networks (using fluorescent protein tags) during confined migration could help to analyze how each of them redistributes during cell squeezing in constrictions and decision making at junctions. We anticipate that deleting plectin crosslinking will slow down migration and decision making by impairing front-rear polarization. To test the importance of plectin as an anchoring protein, we propose to monitor the shape and integrity of the cell nucleus dur-

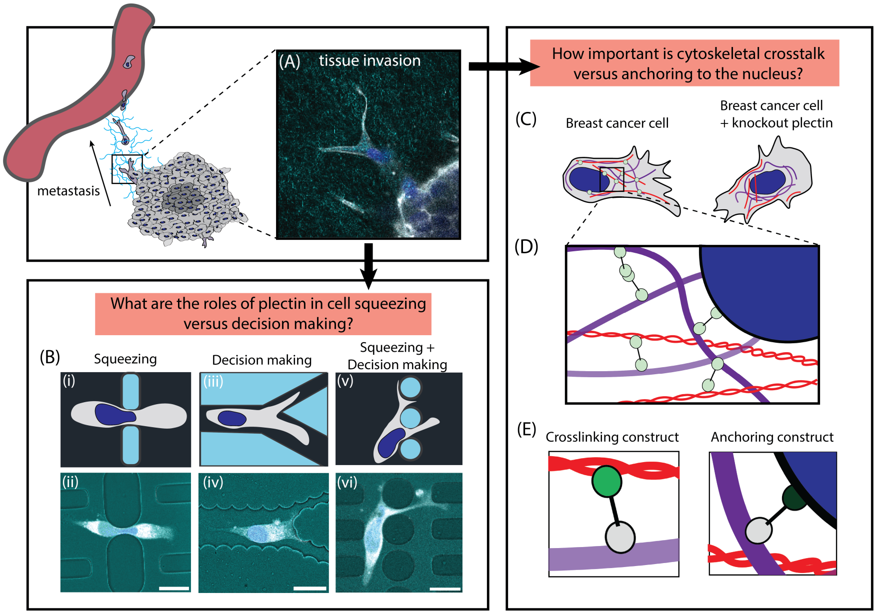

Figure 6.3: Schematic of new experimental pathways to study plectin-mediated cancer cell invasion. (A) 3D spheroid invasion assays in collagen mimic tumor invasion but are difficult to interpret due to the heterogeneous pore structure of collagen networks. (B) Microfluidic channels can be precisely designed to separate the impact of confinement on cancer cell squeezing vs. decision making in constrictions. (C-E) Engineered plectin constructs can be used to separate plectin's crosslinking versus anchoring roles in the cell.

ing migration. We hypothesize that deleting plectin anchoring will make cell squeezing easier by making the nucleus more deformable, but will also make the nucleus prone to rupture.

6.4. COLLECTIVE INVASION DESIGNS FOR MICROFLUIDICS

Clinical studies from the last decade revealed that cancer cells can overcome physical arrest imposed by dense environments by migrating in clusters. Although single cells migrate faster and are more common in cancer, migrating cell clusters have more directional efficiency and result in more metastatic site formations [12, 10]. For example, breast cancer circulating tumor cells (CTCs) in the bloodstream traveling together as clusters have a significantly enhanced metastatic potential compared to individual cells [531]. Cluster CTCs, which undertake the full metastatic cascade of intravasation and circulation as one conserved unit, display a metastatic potential that is up to 50 times larger than for individual CTCs [531, 561]. Although collective migration can protect against programmed cell death and therefore increase survival rates, it remains an open question how cancer cell clusters invade effectively. The increased overall volume, presence of multiple cell nuclei, and requirement for coordination of directionality between cells can pose great physical challenges in the complex microenvironments encountered during metastasis [9].

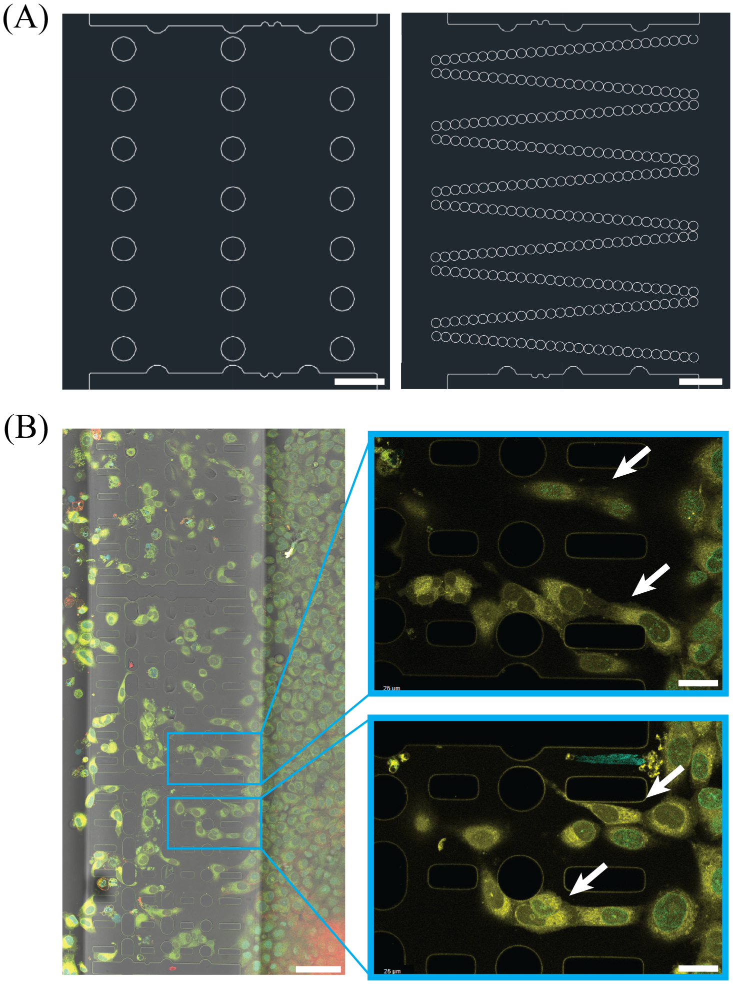

Figure 6.4: Studying collective invasion in custom-designed microfluidic devices. Preliminary experiments with migration devices with constrictions of 30 µm and high cell densities (left panel) to study collective invasion (right, zoomed-in cyan panels). Cells are stained with Cytotracker orange to label the cytoplasm (yellow) and Hoechst (cyan) to label the nucleus. Scale bars are 25 µm.

In order to address these open questions, we designed new constriction areas for the microfluidic migration chip used in Chapter 2 and Chapter 5 of this dissertation, inspired by designs from Ref. [62, 63]. The new designs have wider constrictions regions, allowing for cells to migrate collectively. We designed two new constriction regions; (1) pillars with 30 µm distance (Fig. 6.4A, left panel) and (2) a constriction channel decreasing from 30 µm to 5 µm (Fig. 6.4A, right panel). To induce collective invasion into the constriction areas, we performed preliminary experiments with these chip designs where we seeded cells in high density, creating a monolayer of cells in front of the constriction area. In these experiments (Fig. 6.4B, left panel), we could identify cells migrating collectively into the constriction areas (Fig. 6.4B, right panels) as indicated by the white arrows. These preliminary experiments show great potential for the use and adaptation of existing microfluidic designs to research complicated invasion strategies such as collective invasion in higher resolution compared to 3D-spheroid invasion assays. This will provide more detailed analysis for intercellular processes during collective invasion, for example the remodelling mechanisms of the cytoskeleton, which would be a great step towards finding new molecular targets to block cancer cell invasion.

6.5. ACKNOWLEDGEMENTS

Thanks to Klara Beslmüller and Erik Danen for the creation of the plectin knockout Hs578t cell line. I would also like to thank Irene-Istúriz Petitjean and James Conboy for sharing the ACTIF plasmid, and thanks to Ruben Boot for fabricating the microfluidic designs for collective invasion.

PUBLICATIONS

Included in this thesis:

van der Net, A.[1], Rahman, Z.[1], Bordoloi, A. D., Muntz, I., Ten Dijke, P., Boukany, P. E., Koenderink, G. H. (2024). EMT-related cell-matrix interactions are linked to states of cell unjamming in cancer spheroid invasion. iScience, 27(12).

Conboy, J. P.[2], Istúriz Petitjean, I.[2], **van der Net, A.**[2], Koenderink, G. H. (2024). How cytoskeletal crosstalk makes cells move: Bridging cell-free and cell studies. Biophysics Reviews, 5(2).

van der Net, A.[3], Boot, R. C.[3], van Dijk, I., Conboy, J.P., Boukany, P.E., Koenderink, G.H. (2025). Deformability determines confined cancer cell migration efficiency with limited effect on directionality. (Manuscript in preparation.)

van der Net, A., Beslmüller, K., van Vliet, N., Tavasso, M., Beerens, M., Boot, R. C., Boukany, P.E., Danen, E.H.J., Koenderink, G.H. (2025). Septin promotes breast cancer invasion through actin-based protrusion formation. (Manuscript in preparation.)

Not included in this thesis:

Boot, R. C., **van der Net, A.**, Gogou, C., Mehta, P., Meijer, D. H., Koenderink, G. H., Boukany, P. E. (2024). Cell spheroid viscoelasticity is deformation-dependent. Scientific Reports, 14(1), 20013.

Giubertoni, G., Feng, L., Klein, K., Giannetti, G., Rutten, L., Choi, Y., **van der Net, A.**, Castro-Linares, G., Caporaletti, F., Micha, D. and Hunger, J. (2024). Elucidating the role of water in collagen self-assembly by isotopically modulating collagen hydration. Proceedings of the National Academy of Sciences, 121(11), e2313162121.

---

[1] These authors contributed equally to this work.

[2] These authors contributed equally to this work.

[3] These authors contributed equally to this work.

CURRICULUM VITAE

Anouk van der Net was born in Dordrecht on May 21, 1997, where she lived until 2006. She then moved to Curaçao, part of the Dutch Antilles, before returning to the Netherlands in 2011 to live in Hendrik-Ido-Ambacht. In 2015, she obtained her high school diploma from De Passie Rotterdam and subsequently moved to Eindhoven to begin her studies in Biomedical Engineering at Eindhoven University of Technology. She completed her Bachelor's degree in 2018, with a thesis titled "The involvement of vimentin in the homeostasis of mouse embryonic fibroblasts.". Following this, she enrolled in the Master's program in Biomedical Engineering at the same university, specializing in the Regenerative Medicine and Technology track, which she partially completed at Utrecht University. She graduated in 2021 with a thesis entitled "Researching the interplay between vimentin, Notch signalling, and phenotype that contributes to mechanical homeostasis in vascular smooth muscle cells.". In 2021, she began her PhD research at the Department of Bionanoscience at Delft University of Technology. She moved to Alblasserdam in 2022 and continued her doctoral research until 2025. The results of this work are presented in this thesis.

REFERENCES

[1] Scott Valastyan and Robert A. Weinberg. Tumor metastasis: Molecular insights and evolving paradigms. *Cell*, 147:275–292, 10 2011.

[2] Robert A.. Weinberg, Richard A.. Goldsby, Michael. Hemann, and Tyler. Jacks. *The biology of cancer.* W. W. Norton & Company, Inc., 2023.

[3] Christoph A. Klein. Cancer progression and the invisible phase of metastatic colonization. *Nature Reviews Cancer 2020 20:11*, 20:681–694, 10 2020.

[4] Andrew D. Doyle, Daniel J. Sykora, Gustavo G. Pacheco, Matthew L. Kutys, and Kenneth M. Yamada. 3d mesenchymal cell migration is driven by anterior cellular contraction that generates an extracellular matrix prestrain. *Developmental Cell*, 56:826–841.e4, 3 2021.

[5] Anne J. Ridley, Martin A. Schwartz, Keith Burridge, Richard A. Firtel, Mark H. Ginsberg, Gary Borisy, J. Thomas Parsons, and Alan Rick Horwitz. Cell migration: integrating signals from front to back. *Science (New York, N.Y.)*, 302:1704–1709, 12 2003.

[6] Shailaja Seetharaman and Sandrine Etienne-Manneville. Cytoskeletal crosstalk in cell migration. *Trends in cell biology*, 30:720–735, 9 2020.

[7] Yan Jun Liu, Maël Le Berre, Franziska Lautenschlaeger, Paolo Maiuri, Andrew Callan-Jones, Mélina Heuzé, Tohru Takaki, Raphaël Voituriez, and Matthieu Piel. Confinement and low adhesion induce fast amoeboid migration of slow mesenchymal cells. *Cell*, 160:659–672, 2 2015.

[8] Ryan J. Petrie, Heather M. Harlin, Lulu I.T. Korsak, and Kenneth M. Yamada. Activating the nuclear piston mechanism of 3d migration in tumor cells. *The Journal of Cell Biology*, 216:93, 2017.

[9] Kenneth M. Yamada and Michael Sixt. Mechanisms of 3d cell migration. *Nature Reviews Molecular Cell Biology 2019 20:12*, 20:738–752, 10 2019.

[10] Martin C. Whittle and Sunil R. Hingorani. Disconnect between emt and metastasis in pancreas cancer. *Oncotarget*, 6:30445, 2015.

[11] Olga Ilina, Pavlo G. Gritsenko, Simon Syga, Jürgen Lippoldt, Caterina A.M. La Porta, Oleksandr Chepizhko, Steffen Grosser, Manon Vullings, Gert Jan Bakker, Jörn Starruß, Peter Bult, Stefano Zapperi, Josef A. Käs, Andreas Deutsch, and Peter Friedl. Cell–cell adhesion and 3d matrix confinement determine jamming transitions in breast cancer invasion. *Nature Cell Biology 2020 22:9*, 22:1103–1115, 8 2020.

[12] Joana E. Saraiva and Elias H. Barriga. The basics of collective cell migration: unity makes strength. *Viscoelasticity and Collective Cell Migration: An Interdisciplinary Perspective Across Levels of Organization*, pages 1–19, 1 2021.

[13] Anna Haeger, Stephanie Alexander, Manon Vullings, Fabian M.P. Kaiser, Cornelia Veelken, Uta Flucke, Gudrun E. Koehl, Markus Hirschberg, Michael Flentje, Robert M. Hoffman, Edward K. Geissler, Stephan Kissler, and Peter Friedl. Collective cancer invasion forms an integrin-dependent radioresistant niche. *Journal of Experimental Medicine*, 217, 1 2020.

[14] Aashrith Saraswathibhatla, Dhiraj Indana, and Ovijit Chaudhuri. Cell–extracellular matrix mechanotransduction in 3D. *Nature Reviews Molecular Cell Biology*, 24(7):495–516, 2023.

[15] Juliane Winkler, Abisola Abisoye-Ogunniyan, Kevin J. Metcalf, and Zena Werb. Concepts of extracellular matrix remodelling in tumour progression and metastasis. *Nature Communications*, 11(1):1–19, 2020.

[16] Pahini Pandya, Jose L. Orgaz, and Victoria Sanz-Moreno. Actomyosin contractility and collective migration: may the force be with you. *Current Opinion in Cell Biology*, 48:87–96, 10 2017.

[17] Peter Friedl, Katarina Wolf, and Mirjam M. Zegers. Rho-directed forces in collective migration. *Nature Cell Biology*, 16:208–210, 2014.

[18] Hideki Yamaguchi and John Condeelis. Regulation of the actin cytoskeleton in cancer cell migration and invasion. *Biochimica et Biophysica Acta (BBA) - Molecular Cell Research*, 1773:642–652, 5 2007.

[19] Benjamin P. Bouchet and Anna Akhmanova. Microtubules in 3d cell motility. *Journal of Cell Science*, 130:39–50, 2017.

[20] Gabriel G. Martins and John Kolega. A role for microtubules in endothelial cell protrusion in three-dimensional matrices. *Biology of the cell / under the auspices of the European Cell Biology Organization*, 104:271–286, 5 2012.

[21] Marie Schoumacher, Robert D. Goldman, Daniel Louvard, and Danijela M. Vignjevic. Actin, microtubules, and vimentin intermediate filaments cooperate for elongation of invadopodia. *Journal of Cell Biology*, 189:541–556, 5 2010.

[22] S. Linder, K. Hufner, U. Wintergerst, and M. Aefelbacher. Microtubule-dependent formation of podosomal adhesion structures in primary human macrophages. *Journal of Cell Science*, 113:4165–4176, 2000.

[23] Daniel Irimia and Mehmet Toner. Spontaneous migration of cancer cells under conditions of mechanical confinement. *Integrative Biology*, 1:506–512, 2009.

[24] Alison E. Patteson, Amir Vahabikashi, Katarzyna Pogoda, Stephen A. Adam, Kalpana Mandal, Mark Kittisopikul, Suganya Sivagurunathan, Anne Goldman, Robert D. Goldman, and Paul A. Janmey. Vimentin protects cells against nuclear

rupture and dna damage during migration. *Journal of Cell Biology*, 218:4079–4092, 12 2019.

[25] Alexandra Lynn McGregor, Chieh Ren Hsia, and Jan Lammerding. Squish and squeeze — the nucleus as a physical barrier during migration in confined environments. *Current Opinion in Cell Biology*, 40:32–40, 6 2016.

[26] Alison E. Patteson, Katarzyna Pogoda, Fitzroy J. Byfield, Kalpana Mandal, Zofia Ostrowska-Podhorodecka, Elisabeth E. Charrier, Peter A. Galie, Piotr Deptuła, Robert Bucki, Christopher A. McCulloch, and Paul A. Janmey. Loss of vimentin enhances cell motility through small confining spaces. *Small.*, 15(50):e1903180, dec 2019.

[27] Kevin J. Cheung, Edward Gabrielson, Zena Werb, and Andrew J. Ewald. Collective invasion in breast cancer requires a conserved basal epithelial program. *Cell*, 155:1639–1651, 12 2013.

[28] Arun Satelli and Shulin Li. Vimentin in cancer and its potential as a molecular target for cancer therapy. *Cellular and Molecular Life Sciences*, 68:3033–3046, 9 2011.

[29] Florian Huber, Adeline Boire, Magdalena Preciado López, and Gijsje H. Koenderink. Cytoskeletal crosstalk: When three different personalities team up. *Current Opinion in Cell Biology*, 32:39–47, 2 2015.

[30] Olga C. Rodriguez, Andrew W. Schaefer, Craig A. Mandato, Paul Forscher, William M. Bement, and Clare M. Waterman-Storer. Conserved microtubule-actin interactions in cell movement and morphogenesis. *Nature Cell Biology*, 5:599–609, 7 2003.

[31] Wenxiu Ning, Yanan Yu, Honglin Xu, Xiaofei Liu, Daiwei Wang, Jing Wang, Yingchun Wang, and Wenxiang Meng. The camsap3-acf7 complex couples non-centrosomal microtubules with actin filaments to coordinate their dynamics. *Developmental Cell*, 39:61–74, 10 2016.

[32] Kenneth G. Campellone, Neil J. Webb, Elizabeth A. Znameroski, and Matthew D. Welch. Whamm is an arp2/3 complex activator that binds microtubules and functions in er to golgi transport. *Cell*, 134:148–161, 7 2008.

[33] Yuta Sato, Keiju Kamijo, Motosuke Tsutsumi, Yota Murakami, and Masayuki Takahashi. Nonmuscle myosin iia and iib differently suppress microtubule growth to stabilize cell morphology. *Journal of Infectious Diseases*, 220:25–39, 8 2019.

[34] Naël Osmani, Florent Peglion, Philippe Chavrier, and Sandrine Etienne-Manneville. Cdc42 localization and cell polarity depend on membrane traffic. *The Journal of Cell Biology*, 191:1261, 12 2010.

[35] Brian T. Helfand, Atsushi Mikami, Richard B. Vallee, and Robert D. Goldman. A requirement for cytoplasmic dynein and dynactin in intermediate filament network assembly and organization. *The Journal of Cell Biology*, 157:795, 5 2002.

[36] Caroline Hookway, Liya Ding, Michael W. Davidson, Joshua Z. Rappoport, Gaudenz Danuser, and Vladimir I. Gelfand. Microtubule-dependent transport and dynamics of vimentin intermediate filaments. *Molecular Biology of the Cell*, 26:1675–1686, 5 2015.

[37] Amélie Robert, Harald Herrmann, Michael W. Davidson, and Vladimir I. Gelfand. Microtubule-dependent transport of vimentin filament precursors is regulated by actin and by the concerted action of rho- and p21-activated kinases. *The FASEB Journal*, 28:2879, 7 2014.

[38] Zhuo Gan, Liya Ding, Christoph J. Burckhardt, Jason Lowery, Assaf Zaritsky, Karlyndsay Sitterley, Andressa Mota, Nancy Costigliola, Colby G. Starker, Daniel F. Voytas, Jessica Tytell, Robert D. Goldman, and Gaudenz Danuser. Vimentin intermediate filaments template microtubule networks to enhance persistence in cell polarity and directed migration. *Cell Systems*, 3:252–263.e8, 9 2016.

[39] Serge Mostowy and Pascale Cossart. Septins: The fourth component of the cytoskeleton. *Nature Reviews Molecular Cell Biology*, 13:183–194, 3 2012.

[40] Konstantinos Nakos, Md Noor A. Alam, Megan R. Radler, Ilona A. Kesisova, Changsong Yang, Joshua Okletey, Meagan R. Tomasso, Shae B. Padrick, Tatyana M. Svitkina, and Elias T. Spiliotis. Septins mediate a microtubule–actin crosstalk that enables actin growth on microtubules. *Proceedings of the National Academy of Sciences of the United States of America*, 119, 12 2022.

[41] Rosalind Silverman-Gavrila and Lorelei Silverman-Gavrila. Septins: New microtubule interacting partners. *The Scientific World Journal*, 8:611, 6 2008.

[42] Dimitrios Angelis and Elias T. Spiliotis. Septin mutations in human cancers. *Frontiers in Cell and Developmental Biology*, 4:122, 11 2016.

[43] Christian Poüs, Laurence Klipfel, and Anita Baillet. Cancer-related functions and subcellular localizations of septins. *Frontiers in Cell and Developmental Biology*, 4:126, 11 2016.

[44] Joyce C.M. Meiring, Boris I. Shneyer, and Anna Akhmanova. Generation and regulation of microtubule network asymmetry to drive cell polarity. *Current Opinion in Cell Biology*, 62:86–95, 2 2020.

[45] A. van der Net, R. C. Boot, I. van Dijk, J.P. Conboy, P.E. Boukany, and G.H. Koenderink. Cancer cell deformability impacts the rate of confined migration but not decision making. *bioRxiv*, page 2025.05.12.653524, 5 2025.

[46] Mario Giuliano, Anum Shaikh, Hin Ching Lo, Grazia Arpino, Sabino De Placido, Xiang H Zhang, Massimo Cristofanilli, Rachel Schiff, and Meghana V Trivedi. Perspective on circulating tumor cell clusters: Why it takes a village to metastasize.

[47] Patrick Mehlen and Alain Puisieux. Metastasis: a question of life or death. *Nature Reviews Cancer 2006 6:6*, 6:449–458, 6 2006.

[48] Emily M. Hatch and Martin W. Hetzer. Nuclear envelope rupture is induced by actin-based nucleus confinement. *Journal of Cell Biology*, 215:27–36, 10 2016.

[49] Celine M. Denais, Rachel M. Gilbert, Philipp Isermann, Alexandra L. McGregor, Mariska Te Lindert, Bettina Weigelin, Patricia M. Davidson, Peter Friedl, Katarina Wolf, and Jan Lammerding. Nuclear envelope rupture and repair during cancer cell migration. *Science*, 352:353–358, 4 2016.

[50] Jan Lammerding and Katarina Wolf. Nuclear envelope rupture: Actin fibers are putting the squeeze on the nucleus. *The Journal of Cell Biology*, 215:5, 2016.

[51] Katarina Wolf, Mariska te Lindert, Marina Krause, Stephanie Alexander, Joost te Riet, Amanda L. Willis, Robert M. Hoffman, Carl G. Figdor, Stephen J. Weiss, and Peter Friedl. Physical limits of cell migration: Control by ecm space and nuclear deformation and tuning by proteolysis and traction force. *Journal of Cell Biology*, 201:1069–1084, 6 2013.

[52] Valentina Gifford and Yoshifumi Itoh. Mt1-mmp-dependent cell migration: proteolytic and non-proteolytic mechanisms. *Biochemical Society Transactions*, 47:811–826, 6 2019.

[53] Xiang Qin, Kang Chen, Meng Wang, Ronghua Guo, Yixi Zhang, Ping Li, Ran Yan, Shun Li, Tingting Li, Fengming You, and Yiyao Liu. Nesprin-1/2 facilitates breast cancer cell pore migration via nucleus deformation. *The European Physical Journal Special Topics 2023 232:16*, 232:2739–2749, 7 2023.

[54] Linda Oswald, Steffen Grosser, David M. Smith, and Josef A. Käs. Jamming transitions in cancer. *Journal of Physics D: Applied Physics*, 50:483001, 10 2017.

[55] Anna Haeger, Marina Krause, Katarina Wolf, and Peter Friedl. Cell jamming: Collective invasion of mesenchymal tumor cells imposed by tissue confinement. *Biochimica et Biophysica Acta (BBA) - General Subjects*, 1840:2386–2395, 8 2014.

[56] Jochen Guck, Stefan Schinkinger, Bryan Lincoln, Falk Wottawah, Susanne Ebert, Maren Romeyke, Dominik Lenz, Harold M. Erickson, Revathi Ananthakrishnan, Daniel Mitchell, Josef Kas, Sydney Ulvick, and Curt Bilby. Optical deformability as an inherent cell marker for testing malignant transformation and metastatic competence. *Biophysical Journal*, 88:3689–3698, 5 2005.

[57] Sangwon Byun, Sungmin Son, Dario Amodei, Nathan Cermak, Josephine Shaw, Joon Ho Kang, Vivian C. Hecht, Monte M. Winslow, Tyler Jacks, Parag Mallick, and Scott R. Manalis. Characterizing deformability and surface friction of cancer cells. *Proceedings of the National Academy of Sciences of the United States of America*, 110:7580–7585, 5 2013.

[58] Dong Hee Choi, Hui Wen Liu, Yong Hun Jung, Jinchul Ahn, Jin A. Kim, Dongwoo Oh, Yeju Jeong, Minseop Kim, Hongjin Yoon, Byengkyu Kang, Eunsol Hong, Euijeong Song, and Seok Chung. Analyzing angiogenesis on a chip using deep learning-based image processing. *Lab on a Chip*, 23:475–484, 1 2023.

[59] Se Min Kim, Namu Park, Hye Bin Park, Ju Kyung Lee, Changho Chun, Kyung Hoon Kim, Jong Seob Choi, Hyung Jin Kim, Sekyu Choi, and Jung Hyun Lee. Exploring novel immunotherapy biomarker candidates induced by cancer deformation. *PLOS ONE*, 19:e0303433, 5 2024.

[60] Matthew R. Zanotelli, Aniqua Rahman-Zaman, Jacob A. VanderBurgh, Paul V. Taufalele, Aadhar Jain, David Erickson, Francois Bordeleau, and Cynthia A. Reinhart-King. Energetic costs regulated by cell mechanics and confinement are predictive of migration path during decision-making. *Nature Communications*, 10, 12 2019.

[61] Alexander Hayn, Tony Fischer, and Claudia Tanja Mierke. Inhomogeneities in 3d collagen matrices impact matrix mechanics and cancer cell migration. *Frontiers in Cell and Developmental Biology*, 8, 11 2020.

[62] Sam H. Au, Brian D. Storey, John C. Moore, Qin Tang, Yeng Long Chen, Sarah Javaid, A. Fatih Sarioglu, Ryan Sullivan, Marissa W. Madden, Ryan O'Keefe, Daniel A. Haber, Shyamala Maheswaran, David M. Langenau, Shannon L. Stott, and Mehmet Toner. Clusters of circulating tumor cells traverse capillary-sized vessels. *Proceedings of the National Academy of Sciences of the United States of America*, 113:4947–4952, 5 2016.

[63] Patricia M. Davidson, Gregory R. Fedorchak, Solenne Mondésert-Deveraux, Emily S. Bell, Philipp Isermann, Denis Aubry, Rachele Allena, and Jan Lammerding. High-throughput microfluidic micropipette aspiration device to probe time-scale dependent nuclear mechanics in intact cells. *Lab on a Chip*, 19:3652–3663, 10 2019.

[64] Patricia M. Davidson, Josiah Sliz, Philipp Isermann, Celine Denais, and Jan Lammerding. Design of a microfluidic device to quantify dynamic intra-nuclear deformation during cell migration through confining environments. *Integrative Biology*, 7:1534–1546, 12 2015.

[65] Suraiya Rasheed, Walter A Nelson-Rees, Eva M Toth, Paul Arnstein, and Murray B Gardner. Characterization of a newly derived human sarcoma cell line (ht-1080) ermanent cell lines from animal tissues. *Cancer*, 33:1027–1033, 1974.

[66] Goos N.P. van Muijen, Kees F.J. Jansen, Ine M.H.A. Cornelissen, Dominique F.C.M. Smeets, Johan L.M. Beck, and Dirk J. Ruiter. Establishment and characterization of a human melanoma cell line (mv3) which is highly metastatic in nude mice. *International Journal of Cancer*, 48:85–91, 1991.

[67] Tetsuro Wakatsuki, Bill Schwab, Nathan C. Thompson, and Elliot L. Elson. Effects of cytochalasin d and latrunculin b on mechanical properties of cells. *Journal of Cell Science*, 114:1025–1036, 1 2001.

[68] Johannes Schindelin, Ignacio Arganda-Carreras, Erwin Frise, Verena Kaynig, Mark Longair, Tobias Pietzsch, Stephan Preibisch, Curtis Rueden, Stephan Saalfeld, Benjamin Schmid, Jean Yves Tinevez, Daniel James White, Volker Hartenstein,

Kevin Eliceiri, Pavel Tomancak, and Albert Cardona. Fiji: an open-source platform for biological-image analysis. *Nature Methods 2012 9:7*, 9:676–682, 6 2012.

[69] J. S. Field and M. V. Swain. Determining the mechanical properties of small volumes of material from submicrometer spherical indentations. *Journal of Materials Research*, 10:101–112, 3 1995.

[70] Tomohiro Numata, Takahiro Shimizu, and Yasunobu Okada. Trpm7 is a stretch- and swelling-activated cation channel involved in volume regulation in human epithelial cells. *American Journal of Physiology - Cell Physiology*, 292:460–467, 1 2007.

[71] Panagiotis Mistriotis, Emily O. Wisniewski, Kaustav Bera, Jeremy Keys, Yizeng Li, Soontorn Tuntithavornwat, Robert A. Law, Nicolas A. Perez-Gonzalez, Eda Erdogmus, Yuqi Zhang, Runchen Zhao, Sean X. Sun, Petr Kalab, Jan Lammerding, and Konstantinos Konstantopoulos. Confinement hinders motility by inducing rhoa-mediated nuclear influx, volume expansion, and blebbing. *The Journal of Cell Biology*, 218:4093, 12 2019.

[72] Bettina Weigelin, Gert-Jan Bakker, and Peter Friedl. Intravital third harmonic generation microscopy of collective melanoma cell invasion. *IntraVital*, 1:32–43, 7 2012.

[73] Chieh Ren Hsia, Jawuanna McAllister, Ovais Hasan, Julius Judd, Seoyeon Lee, Richa Agrawal, Chao Yuan Chang, Paul Soloway, and Jan Lammerding. Confined migration induces heterochromatin formation and alters chromatin accessibility. *iScience*, 25, 9 2022.

[74] Kuan Jiang, Su Bin Lim, Jingwei Xiao, Doorgesh Sharma Jokhun, Menglin Shang, Xiao Song, Pan Zhang, Lanfeng Liang, Boon Chuan Low, G. V. Shivashankar, and Chwee Teck Lim. Deleterious mechanical deformation selects mechanoresilient cancer cells with enhanced proliferation and chemoresistance. *Advanced Science*, 10:2201663, 8 2023.

[75] Marta Urbanska, Yan Ge, Maria Winzi, Shada Abuhattum, Syed Shafat Ali, Maik Herbig, Martin Kräter, Nicole Toepfner, Joanne Durgan, Oliver Florey, Martina Dori, Federico Calegari, Fidel-Nicolás Lolo, Miguel Ángel del Pozo, Anna Taubenberger, Carlo Vittorio Cannistraci, and Jochen Guck. De novo identification of universal cell mechanics gene signatures. *eLife*, 12, 2 2025.

[76] Adrien Hallou, Ruiyang He, Benjamin D. Simons, and Bianca Dumitrascu. A computational pipeline for spatial mechano-transcriptomics. *Nature Methods*, 22:737–750, 4 2025.

[77] Yixuan Li, Hui Ting Ong, Hongyue Cui, Xu Gao, Jia Wen Nicole Lee, Yuqi Guo, Rong Li, Fabrizio A. Pennacchio, Paolo Maiuri, Artem K. Efremov, and Andrew W. Holle. Confinement-sensitive volume regulation dynamics via high-speed nuclear morphological measurements. *Proceedings of the National Academy of Sciences of the United States of America*, 121, 12 2024.

[78] Ming Guo, Adrian F. Pegoraro, Angelo Mao, Enhua H. Zhou, Praveen R. Arany, Yulong Han, Dylan T. Burnette, Mikkel H. Jensen, Karen E. Kasza, Jeffrey R. Moore, Frederick C. Mackintosh, Jeffrey J. Fredberg, David J. Mooney, Jennifer Lippincott-Schwartz, and David A. Weitz. Cell volume change through water efflux impacts cell stiffness and stem cell fate. *Proceedings of the National Academy of Sciences of the United States of America*, 114:E8618–E8627, 10 2017.

[79] E. H. Zhou, X. Trepat, C. Y. Park, G. Lenormand, M. N. Oliver, S. M. Mijailovich, C. Hardin, D. A. Weitz, J. P. Butler, and J. J. Fredberg. Universal behavior of the osmotically compressed cell and its analogy to the colloidal glass transition. *Proceedings of the National Academy of Sciences of the United States of America*, 106:10632–10637, 6 2009.

[80] Thomas J. Jentsch. Vracs and other ion channels and transporters in the regulation of cell volume and beyond. *Nature Reviews Molecular Cell Biology 2016 17:5*, 17:293–307, 4 2016.

[81] Kimberly M. Stroka, Hongyuan Jiang, Shih Hsun Chen, Ziqiu Tong, Denis Wirtz, Sean X. Sun, and Konstantinos Konstantopoulos. Water permeation drives tumor cell migration in confined microenvironments. *Cell*, 157:611–623, 4 2014.

[82] Shuyuan Wang, Evgeniy I. Solenov, and Baoxue Yang. Aquaporin inhibitors. *Advances in experimental medicine and biology*, 1398:317–330, 2023.

[83] Kendra D. Nyberg, Kenneth H. Hu, Sara H. Kleinman, Damir B. Khismatullin, Manish J. Butte, and Amy C. Rowat. Quantitative deformability cytometry: Rapid, calibrated measurements of cell mechanical properties. *Biophysical Journal*, 113:1574, 10 2017.

[84] Janina R. Lange, Claus Metzner, Sebastian Richter, Werner Schneider, Monika Spermann, Thorsten Kolb, Graeme Whyte, and Ben Fabry. Unbiased high-precision cell mechanical measurements with microconstrictions. *Biophysical Journal*, 112:1472–1480, 4 2017.

[85] Michael J. Rosenbluth, Wilbur A. Lam, and Daniel A. Fletcher. Analyzing cell mechanics in hematologic diseases with microfluidic biophysical flow cytometry. *Lab on a Chip*, 8:1062–1070, 6 2008.

[86] Sylvain Gabriele, Anne Marie Benoliel, Pierre Bongrand, and Olivier Théodoly. Microfluidic investigation reveals distinct roles for actin cytoskeleton and myosin ii activity in capillary leukocyte trafficking. *Biophysical Journal*, 96:4308, 2009.

[87] Michael Mak and David Erickson. A serial micropipette microfluidic device with applications to cancer cell repeated deformation studies. *Integrative Biology (United Kingdom)*, 5:1374–1384, 2013.

[88] H. W. Hou, Q. S. Li, G. Y.H. Lee, A. P. Kumar, C. N. Ong, and C. T. Lim. Deformability study of breast cancer cells using microfluidics. *Biomedical Microdevices*, 11:557–564, 12 2009.

[89] Alison E. Patteson, Robert J. Carroll, Daniel V. Iwamoto, and Paul A. Janmey. The vimentin cytoskeleton: when polymer physics meets cell biology. *Physical Biology*, 18:011001, 11 2020.

[90] Huayin Wu, Yinan Shen, Suganya Sivagurunathan, Miriam Sarah Weber, Stephen A. Adam, Jennifer H. Shin, Jeffrey J. Fredberg, Ohad Medalia, Robert Goldman, and David A. Weitz. Vimentin intermediate filaments and filamentous actin form unexpected interpenetrating networks that redefine the cell cortex. *Proceedings of the National Academy of Sciences of the United States of America*, 119:e2115217119, 3 2022.

[91] Poonam Sharma, Zachary T. Bolten, Diane R. Wagner, and Adam H. Hsieh. Deformability of human mesenchymal stem cells is dependent on vimentin intermediate filaments. *Annals of Biomedical Engineering*, 45:1365–1374, 5 2017.

[92] M. G. Mendez, D. Restle, and P. A. Janmey. Vimentin enhances cell elastic behavior and protects against compressive stress. *Biophysical Journal*, 107:314–323, 7 2014.

[93] Patricia M Davidson, Celine Denais, Maya C Bakshi, and Jan Lammerding. Nuclear deformability constitutes a rate-limiting step during cell migration in 3-d environments. *Cellular and Molecular Bioengineering*, 7:293306, 6 2014.

[94] Jan Lammerding, Loren G. Fong, Julie Y. Ji, Karen Reue, Colin L. Stewart, Stephen G. Young, and Richard T. Lee. Lamins a and c but not lamin b1 regulate nuclear mechanics. *Journal of Biological Chemistry*, 281:25768–25780, 9 2006.

[95] Sirine Amiri, Inge Bos, Etienne Reyssat, and Cécile Sykes. The nuclear lamin network passively responds to both active or passive cell movement through confinements. *Soft matter*, 21, 12 2025.

[96] Emily S. Bell, Pragya Shah, Noam Zuela-Sopilniak, Dongsung Kim, Alice Anais Varlet, Julien L.P. Morival, Alexandra L. McGregor, Philipp Isermann, Patricia M. Davidson, Joshua J. Elacqua, Jonathan N. Lakins, Linda Vahdat, Valerie M. Weaver, Marcus B. Smolka, Paul N. Span, and Jan Lammerding. Low lamin a levels enhance confined cell migration and metastatic capacity in breast cancer. *Oncogene*, 41:4211–4230, 9 2022.

[97] Katarina Wolf, Irina Mazo, Harry Leung, Katharina Engelke, Ulrich H. Von Andrian, Elena I. Deryugina, Alex Y. Strongin, Eva B. Bröcker, and Peter Friedl. Compensation mechanism in tumor cell migration mesenchymal–amoeboid transition after blocking of pericellular proteolysis. *Journal of Cell Biology*, 160:267–277, 1 2003.

[98] Katarina Wolf, Yi I. Wu, Yueying Liu, Jörg Geiger, Eric Tam, Christopher Overall, M. Sharon Stack, and Peter Friedl. Multi-step pericellular proteolysis controls the transition from individual to collective cancer cell invasion. *Nature Cell Biology 2007 9:8*, 9:893–904, 7 2007.

[99] Steffi Lehmann, Veronika te Boekhorst, Julia Odenthal, Roberta Bianchi, Sjoerd van Helvert, Kristian Ikenberg, Olga Ilina, Szymon Stoma, Jael Xandry, Liying

Jiang, Reidar Grenman, Markus Rudin, and Peter Friedl. Hypoxia induces a hif-1-dependent transition from collective-to-amoeboid dissemination in epithelial cancer cells. *Current Biology*, 27:392–400, 2 2017.

[100] Vinay Swaminathan, Karthikeyan Mythreye, E. Tim O'Brien, Andrew Berchuck, Gerard C. Blobe, and Richard Superfine. Mechanical stiffness grades metastatic potential in patient tumor cells and in cancer cell lines. *Cancer Research*, 71:5075–5080, 8 2011.

[101] Christopher Playter, Rosela Golloshi, Joshua H. Garretson, Alvaro Rodriguez Gonzalez, Taiwo Habeeb Olajide, Ahmed Saad, Samuel John Benson, and Rachel Patton McCord. Deciphering pre-existing and induced 3d genome architecture changes involved in constricted melanoma migration. *iScience*, 28, 5 2025.

[102] Rosela Golloshi, Christopher Playter, Trevor F Freeman, Priyojit Das, Thomas Isaac Raines, Joshua H Garretson, Delaney Thurston, and Rachel Patton McCord. Constricted migration is associated with stable 3d genome structure differences in cancer cells. *EMBO reports*, 23, 10 2022.

[103] Xu Gao, Yixuan Li, Jia Wen Nicole Lee, Jianxuan Zhou, Vaishnavi Rangaraj, Jennifer Marlena, and Andrew W. Holle. Confined migration drives stem cell differentiation. *Advanced Science*, 12, 6 2025.

[104] Jörg Renkawitz, Aglaja Kopf, Julian Stopp, Ingrid de Vries, Meghan K. Driscoll, Jack Merrin, Robert Hauschild, Erik S. Welf, Gaudenz Danuser, Reto Fiolka, and Michael Sixt. Nuclear positioning facilitates amoeboid migration along the path of least resistance. *Nature 2019 568:7753*, 568:546–550, 4 2019.

[105] Asadullah, Sandeep Kumar, Neha Saxena, Madhurima Sarkar, Amlan Barai, and Shamik Sen. Combined heterogeneity in cell size and deformability promotes cancer invasiveness. *Journal of Cell Science*, 134, 4 2021.

[106] Chau Ly, Heather Ogana, Hye Na Kim, Samantha Hurwitz, Eric J. Deeds, Yong Mi Kim, and Amy C. Rowat. Altered physical phenotypes of leukemia cells that survive chemotherapy treatment. *Integrative Biology*, 15, 4 2023.

[107] Maziar Hakim, Farhad Khorasheh, Iran Alemzadeh, and Manouchehr Vossoughi. A new insight to deformability correlation of circulating tumor cells with metastatic behavior by application of a new deformability-based microfluidic chip. *Analytica Chimica Acta*, 1186, 11 2021.

[108] Gray W. Pearson. Control of invasion by epithelial-to-mesenchymal transition programs during metastasis. *Journal of Clinical Medicine*, 8(5), 2019.

[109] Thomas R. Cox. The matrix in cancer. *Nature Reviews Cancer*, 21(4):217–238, 2021.

[110] Erik Henke, Rajender Nandigama, and Süleyman Ergün. Extracellular matrix in the tumor microenvironment and its impact on cancer therapy. *Frontiers in Molecular Biosciences*, 6, 2020.

[111] Kenneth M. Yamada and Michael Sixt. Mechanisms of 3D cell migration. *Nature Reviews Molecular Cell Biology*, 20(12):738–752, 2019.

[112] Anna Haeger, Marina Krause, Katarina Wolf, and Peter Friedl. Cell jamming: Collective invasion of mesenchymal tumor cells imposed by tissue confinement. *Biochimica et Biophysica Acta - General Subjects*, 1840(8):2386–2395, 2014.

[113] Adam Charles Canver, Olivia Ngo, Rebecca Lownes Urbano, and Alisa Morss Clyne. Endothelial directed collective migration depends on substrate stiffness via localized myosin contractility and cell-matrix interactions. *Journal of Biomechanics*, 49:1369–1380, 5 2016.

[114] Maria Parlani, Carolina Jorgez, and Peter Friedl. Plasticity of cancer invasion and energy metabolism. *Trends in Cell Biology*, 33(5):388–402, 2023.

[115] Julia Odenthal, Robert Takes, and Peter Friedl. Plasticity of tumor cell invasion: governance by growth factors and cytokines. *Carcinogenesis*, 37(12):1117–1128, 09 2016.

[116] Sijie Hao, Laura Ha, Gong Cheng, Yuan Wan, Yiqiu Xia, Donna M. Sosnoski, Andrea M. Mastro, and Si Yang Zheng. A Spontaneous 3D Bone-On-a-Chip for Bone Metastasis Study of Breast Cancer Cells. *Small*, 14(12):1–10, 2018.

[117] Jiacheng Huang, Lele Zhang, Dalong Wan, Lin Zhou, Shusen Zheng, Shengzhang Lin, and Yiting Qiao. Extracellular matrix and its therapeutic potential for cancer treatment. *Signal Transduction and Targeted Therapy*, 6(1), 2021.

[118] Jia shun Wu, Jian Jiang, Bing jun Chen, Ke Wang, Ya ling Tang, and Xin hua Liang. Plasticity of cancer cell invasion: Patterns and mechanisms. *Translational Oncology*, 14(1):100899, 2021.

[119] Meng Wang, Bo Cheng, Yaowei Yang, Han Liu, Guoyou Huang, Lichun Han, Fei Li, and Feng Xu. Microchannel stiffness and confinement jointly induce the mesenchymal-amoeboid transition of cancer cell migration. *Nano Letters*, 19:5949–5958, 9 2019.

[120] Andrea Palamidessi, Chiara Malinverno, Emanuela Frittoli, Salvatore Corallino, Elisa Barbieri, Sara Sigismund, Galina V. Beznoussenko, Emanuele Martini, Massimiliano Garre, Ines Ferrara, Claudio Tripodo, Flora Ascione, Elisabetta A. Cavalcanti-Adam, Qingsen Li, Pier Paolo Di Fiore, Dario Parazzoli, Fabio Giavazzi, Roberto Cerbino, and Giorgio Scita. Unjamming overcomes kinetic and proliferation arrest in terminally differentiated cells and promotes collective motility of carcinoma. *Nat. Mat.*, 18(11):1252–1263, nov 2019.

[121] Olga Ilina, Pavlo G. Gritsenko, Simon Syga, Jürgen Lippoldt, Caterina A.M. La Porta, Oleksandr Chepizhko, Steffen Grosser, Manon Vullings, Gert Jan Bakker, Jörn Starruß, Peter Bult, Stefano Zapperi, Josef A. Käs, Andreas Deutsch, and Peter Friedl. Cell–cell adhesion and 3D matrix confinement determine jamming transitions in breast cancer invasion. *Nature Cell Biology*, 22(9):1103–1115, 2020.

[122] Wenying Kang, Jacopo Ferruzzi, Catalina Paula Spatarelu, Yu Long Han, Yasha Sharma, Stephan A. Koehler, Jennifer A. Mitchel, Adil Khan, James P. Butler, Darren Roblyer, Muhammad H. Zaman, Jin Ah Park, Ming Guo, Zi Chen, Adrian F. Pegoraro, and Jeffrey J. Fredberg. A novel jamming phase diagram links tumor invasion to non-equilibrium phase separation. *iScience*, 24(11), 2021.

[123] Kenneth M. Yamada, Andrew D. Doyle, and Jiaoyang Lu. Cell–3D matrix interactions: recent advances and opportunities. *Trends in Cell Biology*, 32(10):883–895, 2022.

[124] Weijing Han, Shaohua Chen, Wei Yuan, Qihui Fan, Jianxiang Tian, Xiaochen Wang, Longqing Chen, Xixiang Zhang, Weili Wei, Ruchuan Liu, Junle Qu, Yang Jiao, Robert H. Austin, and Liyu Liu. Oriented collagen fibers direct tumor cell intravasation. *Proceedings of the National Academy of Sciences of the United States of America*, 113:11208–11213, 10 2016.

[125] Cedric Gaggioli, Steven Hooper, Cristina Hidalgo-Carcedo, Robert Grosse, John F. Marshall, Kevin Harrington, and Erik Sahai. Fibroblast-led collective invasion of carcinoma cells with differing roles for RhoGTPases in leading and following cells. *Nature Cell Biology*, 9(12):1392–1400, 2007.

[126] Lanlan Hui and Ye Chen. Tumor microenvironment: Sanctuary of the devil. *Cancer Letters*, 368(1):7–13, 2015.

[127] Laurent Fattet, Hae Yun Jung, Mike W. Matsumoto, Brandon E. Aubol, Aditya Kumar, Joseph A. Adams, Albert C. Chen, Robert L. Sah, Adam J. Engler, Elena B. Pasquale, and Jing Yang. Matrix Rigidity Controls Epithelial-Mesenchymal Plasticity and Tumor Metastasis via a Mechanoresponsive EPHA2/LYN Complex. *Developmental Cell*, 54(3):302–316, 2020.

[128] Seiichiro Ishihara and Hisashi Haga. Matrix Stiffness Contributes to Cancer Progression by Regulating Transcription Factors. *Cancers*, 14(4), 2022.

[129] Katrina M. Wisdom, Kolade Adebowale, Julie Chang, Joanna Y. Lee, Sungmin Nam, Rajiv Desai, Ninna Struck Rossen, Marjan Rafat, Robert B. West, Louis Hodgson, and Ovijit Chaudhuri. Matrix mechanical plasticity regulates cancer cell migration through confining microenvironments. *Nature Communications*, 9(1), 2018.

[130] Muhammad H. Zaman, Linda M. Trapani, Alisha Siemeski, Drew MacKellar, Haiyan Gong, Roger D. Kamm, Alan Wells, Douglas A. Lauffenburger, and Paul Matsudaira. Migration of tumor cells in 3D matrices is governed by matrix stiffness along with cell-matrix adhesion and proteolysis. *Proceedings of the National Academy of Sciences of the United States of America*, 103(29):10889–10894, 2006.

[131] Katarina Wolf, Mariska te Lindert, Marina Krause, Stephanie Alexander, Joost te Riet, Amanda L. Willis, Robert M. Hoffman, Carl G. Figdor, Stephen J. Weiss, and Peter Friedl. Physical limits of cell migration: Control by ECM space and nuclear deformation and tuning by proteolysis and traction force. *Journal of Cell Biology*, 201(7):1069–1084, 2013.

[132] Shawn P. Carey, Aniqua Rahman, Casey M. Kraning-Rush, Bethsabe Romero, Sahana Somasegar, Olivia M. Torre, Rebecca M. Williams, and Cynthia A. Reinhart-King. Comparative mechanisms of cancer cell migration through 3D matrix and physiological microtracks. *American Journal of Physiology - Cell Physiology*, 308(6):C436–C447, 2015.

[133] Hayri E. Balcioglu, Lakshmi Balasubramaniam, Tomita Vasilica Stirbat, Bryant L. Doss, Marc Antoine Fardin, René Marc Mège, and Benoit Ladoux. A subtle relationship between substrate stiffness and collective migration of cell clusters. *Soft Matter*, 16(7):1825–1839, 2020.

[134] Sjoerd Van Helvert, Cornelis Storm, and Peter Friedl. Mechanoreciprocity in cell migration. *Nature Cell Biology*, 20(1):8–20, 2018.

[135] Raphael Reuten, Sina Zendehroud, Monica Nicolau, Lutz Fleischhauer, Anu Laitala, Stefanie Kiderlen, Denise Nikodemus, Lena Wullkopf, Sebastian Rune Nielsen, Sarah McNeilly, Carina Prein, Maria Rafaeva, Erwin M. Schoof, Benjamin Furtwängler, Bo T. Porse, Hyobin Kim, Kyoung Jae Won, Stefanie Sudhop, Kamilla Westarp Zornhagen, Frank Suhr, Eleni Maniati, Oliver M.T. Pearce, Manuel Koch, Lene Broeng Oddershede, Tom Van Agtmael, Chris D. Madsen, Alejandro E. Mayorca-Guiliani, Wilhelm Bloch, Roland R. Netz, Hauke Clausen-Schaumann, and Janine T. Erler. Basement membrane stiffness determines metastases formation. *Nature Materials*, 20(6):892–903, 2021.

[136] Serenella M. Pupa, Sylvie Ménard, Stefania Forti, and Elda Tagliabue. New insights into the role of extracellular matrix during tumor onset and progression. *Journal of Cellular Physiology*, 192:259–267, 2002.

[137] Catharina Melzer, Ralf Hass, Juliane von der Ohe, Hendrik Lehnert, and Hendrik Ungefroren. The role of TGF-β and its crosstalk with RAC1/RAC1b signaling in breast and pancreas carcinoma. *Cell communication and signaling : CCS*, 15(1):19, 2017.

[138] Bit Na Kim, Dong Hyuck Ahn, Nahyeon Kang, Chang Dong Yeo, Young Kyoon Kim, Kyo Young Lee, Tae Jung Kim, Sug Hyung Lee, Mi Sun Park, Hyeon Woo Yim, Jong Y. Park, Chan Kwon Park, and Seung Joon Kim. TGF-β induced EMT and stemness characteristics are associated with epigenetic regulation in lung cancer. *Scientific Reports*, 10(1):1–11, 2020.

[139] Selcuk Colak and Peter ten Dijke. Targeting TGF-β Signaling in Cancer. *Trends in Cancer*, 3(1):56–71, 2017.

[140] Carl Henrik Heldin, Kohei Miyazono, and Peter Ten Dijke. TGF-β signalling from cell membrane to nucleus through SMAD proteins. *Nature*, 390(6659):465–471, 1997.

[141] Yang Hao, David Baker, and Peter Ten Dijke. TGF-β-mediated epithelial-mesenchymal transition and cancer metastasis. *International Journal of Molecular Sciences*, 20(11), 2019.

[142] Auxtine Micalet, Emad Moeendarbary, and Umber Cheema. 3d in vitro models for investigating the role of stiffness in cancer invasion. *ACS Biomaterials Science Engineering*, 9:3729–3741, 7 2023.

[143] Dharma Pally and Alexandra Naba. Extracellular matrix dynamics: A key regulator of cell migration across length-scales and systems. *Current Opinion in Cell Biology*, 86:102309, 2024.

[144] Mengxiang Zhu, Yingying Wang, Gaia Ferracci, Jing Zheng, Nam-Joon Cho, and Bae Hoon Lee. Gelatin methacryloyl and its hydrogels with an exceptional degree of controllability and batch-to-batch consistency. *Scientific Reports*, 9(1):6863, May 2019.

[145] Iliyana Pepelanova, Katharina Kruppa, Thomas Scheper, and Antonina Lavrentieva. Gelatin-methacryloyl (gelma) hydrogels with defined degree of functionalization as a versatile toolkit for 3d cell culture and extrusion bioprinting. *Bioengineering*, 5(3), 2018.

[146] Henrik S Rasmussen and Peter P Mccann. Matrix metalloproteinase inhibition as a novel anticancer strategy: A review with special focus on batimastat and marimastat. *Pharmacol. Ther*, 75:69–75, 1997.

[147] Marie Nguyen, Adele De Ninno, Arianna Mencattini, Fanny Mermet-Meillon, Giulia Fornabaio, Sophia S. Evans, Mélissande Cossutta, Yasmine Khira, Weijing Han, Philémon Sirven, Floriane Pelon, Davide Di Giuseppe, Francesca Romana Bertani, Annamaria Gerardino, Ayako Yamada, Stéphanie Descroix, Vassili Soumelis, Fatima Mechta-Grigoriou, Gérard Zalcman, Jacques Camonis, Eugenio Martinelli, Luca Businaro, and Maria Carla Parrini. Dissecting Effects of Anti-cancer Drugs and Cancer-Associated Fibroblasts by On-Chip Reconstitution of Immunocompetent Tumor Microenvironments. *Cell Reports*, 25(13):3884–3893, 12 2018.

[148] Vira V. Artym and Kazue Matsumoto. Imaging cells in three-dimensional collagen matrix. *Current Protocols in Cell Biology*, 48:10.18.1–10.18.20, 9 2010.

[149] Abhishek Sinha, Pranav Mehta, Chuannan Fan, Jing Zhang, Dieuwke L. Marvin, Maarten van Dinther, Laila Ritsma, Pouyan E. Boukany, and Peter ten Dijke. *Visualizing Dynamic Changes During TGF-β-Induced Epithelial to Mesenchymal Transition*, pages 47–65. Springer US, New York, NY, 2022.

[150] Zaid Rahman, Ankur Deep Bordoloi, Haifa Rouhana, Margherita Tavasso, Gerard van der Zon, Valeria Garbin, Peter Ten Dijke, and Pouyan E. Boukany. Interstitial flow potentiates TGF-β/Smad-signaling activity in lung cancer spheroids in a 3D-microfluidic chip. *Lab on a Chip*, pages 1037–1043, 2023.

[151] Sanjib Das, Sk Abdul Amin, and Tarun Jha. Inhibitors of gelatinases (mmp-2 and mmp-9) for the management of hematological malignancies. *European Journal of Medicinal Chemistry*, 223:113623, 2021.

[152] Karina M. Lugo-Cintrón, Max M. Gong, José M. Ayuso, Lucas A. Tomko, David J. Beebe, María Virumbrales-Muñoz, and Suzanne M. Ponik. Breast Fibroblasts and ECM Components Modulate Breast Cancer Cell Migration through the Secretion of MMPs in a 3D Microfluidic Co-Culture Model. *Cancers*, 12(5):1173, 5 2020.

[153] Urban Persson, Hiroto Izumi, Serhiy Souchelnytskyi, Susumu Itoh, Susanne Grimsby, Ulla Engström, Carl-Henrik Heldin, Keiko Funa, and Peter ten Dijke. The l45 loop in type i receptors for tgf-b family members is a critical determinant in specifying smad isoform activation. *FEBS Letters*, 434(1-2):83–87, 1998.

[154] Ellen G. Driever, Iain Muntz, Vishal Patel, Jelle Adelmeijer, William Bernal, Gijsje H. Koenderink, and Ton Lisman. Fibrin clots from patients with acute-on-chronic liver failure are weaker than those from healthy individuals and patients with sepsis without underlying liver disease. *Journal of Thrombosis and Haemostasis*, 21(10):2747–2758, 2023.

[155] Stefan Munster and Ben Fabry. Comments to the editor a simplified implementation of the bubble analysis of biopolymer network pores. *Biophys J.*, 104:2774–2775, 2013.

[156] Anil Kokaram. Practical, Unified, Motion and Missing Data Treatment in Degraded Video. *Journal of Mathematical Imaging and Vision*, 20(1):163–177, 2004.

[157] Johannes Schindelin, Ignacio Arganda-Carreras, Erwin Frise, Verena Kaynig, Mark Longair, Tobias Pietzsch, Stephan Preibisch, Curtis Rueden, Stephan Saalfeld, Benjamin Schmid, Jean Yves Tinevez, Daniel James White, Volker Hartenstein, Kevin Eliceiri, Pavel Tomancak, and Albert Cardona. Fiji: An open-source platform for biological-image analysis. *Nature Methods*, 9:676–682, 7 2012.

[158] Eliza Wiercinska, Hildegonda P.H. Naber, Evangelia Pardali, Gabri Van Der Pluijm, Hans Van Dam, and Peter Ten Dijke. The TGF-β/Smad pathway induces breast cancer cell invasion through the up-regulation of matrix metalloproteinase 2 and 9 in a spheroid invasion model system. *Breast Cancer Research and Treatment*, 128(3):657–666, 2011.

[159] Luciana R. Gomes, Letícia F. Terra, Rosângela A. Wailemann, Leticia Labriola, and Mari C. Sogayar. Abstract 5266: TGF-β1 modulates the homeostasis between MMPs and MMPs inhibitors through p38 MAPK and ERK½ in highly invasive human breast cancer cells. *Cancer Research*, 71(8_Supplement):5266–5266, 2011.

[160] W. Thomas Purcell, Michelle A. Rudek, and Manuel Hidalgo. Development of matrix metalloproteinase inhibitors in cancer therapy. *Hematology/Oncology Clinics of North America*, 16(5):1189–1227, 2002.

[161] Bernadette Xin Jie Tune, Maw Shin Sim, Chit Laa Poh, Rhanye Mac Guad, Choy Ker Woon, Iswar Hazarika, Anju Das, Subash C.B. Gopinath, Mariappan Rajan, Mahendran Sekar, Vetriselvan Subramaniyan, Neeraj Kumar Fuloria, Shivkanya Fuloria, Kalaivani Batumalaie, and Yuan Seng Wu. Matrix Metalloproteinases in

Chemoresistance: Regulatory Roles, Molecular Interactions, and Potential Inhibitors. *Journal of Oncology*, 2022, 2022.

[162] Guang Yu Lian, Qing Ming Wang, Thomas Shiu Kwong Mak, Xiao Ru Huang, Xue Qing Yu, and Hui Yao Lan. Inhibition of tumor invasion and metastasis by targeting tgf-β-smad-mmp2 pathway with asiatic acid and naringenin. *Molecular Therapy Oncolytics*, 20:277–289, 3 2021.

[163] Fatemeh Rasti Boroojeni, Sajjad Naeimipour, Philip Lifwergren, Annelie Abrahamsson, Charlotta Dabrosin, Robert Selegård, and Daniel Aili. Proteolytic remodeling of 3d bioprinted tumor microenvironments. *Biofabrication*, 16(2):025002, jan 2024.

[164] Zehuan Liao, Joseph Jing Heng Lim, Jeannie Xue Ting Lee, Damien Chua, Marcus Ivan Gerard Vos, Yun Sheng Yip, Choon Boon Too, Huan Cao, Jun Kit Wang, Yufeng Shou, Andy Tay, Kaisa Lehti, Hong Sheng Cheng, Chor Yong Tay, and Nguan Soon Tan. Attenuating epithelial-to-mesenchymal transition in cancer through angiopoietin-like 4 inhibition in a 3d tumor microenvironment model. *Advanced Healthcare Materials*, 13(10):2303481, 2024.

[165] Hector Castro-Abril, Jónathan Heras, Jesús del Barrio, Laura Paz, Clara Alcaine, Marina Pérez Aliácar, Diego Garzón-Alvarado, Manuel Doblaré, and Ignacio Ochoa. The role of mechanical properties and structure of type i collagen hydrogels on colorectal cancer cell migration. *Macromolecular Bioscience*, 23, 10 2023.

[166] Austin Naylor, Yu Zheng, Yang Jiao, and Bo Sun. Micromechanical remodeling of the extracellular matrix by invading tumors: anisotropy and heterogeneity. *Soft Matter*, 19:9–16, 11 2022.

[167] Alberto Elosegui-Artola, Anupam Gupta, Alexander J. Najibi, Bo Ri Seo, Ryan Garry, Christina M. Tringides, Irene de Lázaro, Max Darnell, Wei Gu, Qiao Zhou, David A. Weitz, L. Mahadevan, and David J. Mooney. Matrix viscoelasticity controls spatiotemporal tissue organization. *Nature Materials*, 22:117–127, 1 2023.

[168] Olga Ilina and Peter Friedl. Mechanisms of collective cell migration at a glance. *Journal of Cell Science*, 122(18):3203–3208, 2009.

[169] Steffen Grosser, Jürgen Lippoldt, Linda Oswald, Matthias Merkel, Daniel M Sussman, Frédéric Renner, Pablo Gottheil, Erik W Morawetz, Thomas Fuhs, Xiaofan Xie, Steve Pawlizak, Anatol W Fritsch, Benjamin Wolf, Lars-Christian Horn, Susanne Briest, Bahriye Aktas, M Lisa Manning, and Josef A Käs. Cell and Nucleus Shape as an Indicator of Tissue Fluidity in Carcinoma. *Phys. Rev. X*, 11(1):011033, 2021.

[170] Jin-Ah Park, Lior Atia, Jennifer A. Mitchel, Jeffrey J. Fredberg, and James P. Butler. Collective migration and cell jamming in asthma, cancer and development. *Journal of Cell Science*, 129(18):3375–3383, 09 2016.

[171] Jennifer A. Mitchel, Amit Das, Michael J. O'Sullivan, Ian T. Stancil, Stephen J. DeCamp, Stephan Koehler, Oscar H. Ocaña, James P. Butler, Jeffrey J. Fredberg, M. Angela Nieto, Dapeng Bi, and Jin Ah Park. In primary airway epithelial cells, the unjamming transition is distinct from the epithelial-to-mesenchymal transition. *Nature Communications*, 11(1):1–14, 2020.

[172] Lianne Beunk, Nan Wen, Sjoerd Van Helvert, Bram Bekker, Lars Ran, Ross Kang, Tom Paulat, Simon Syga, Andreas Deutsch, Peter Friedl, and Katarina Wolf. Cell jamming in a collagen-based interface assay is tuned by collagen density and proteolysis. *Journal of cell science*, 2023.

[173] Andrew W. Holle, Neethu Govindan Kutty Devi, Kim Clar, Anthony Fan, Taher Saif, Ralf Kemkemer, and Joachim P. Spatz. Cancer cells invade confined microchannels via a self-directed mesenchymal-to-amoeboid transition. *Nano Letters*, 19(4):2280–2290, 2019.

[174] Diane Laure Pagès, Emmanuel Dornier, Jean de Seze, Emilie Gontran, Ananyo Maitra, Aurore Maciejewski, Li Wang, Rui Luan, Jérôme Cartry, Canet Jourdan Charlotte, Joël Raingeaud, Grégoire Lemahieu, Marceline Lebel, Michel Ducreux, Maximiliano Gelli, Jean Yves Scoazec, Mathieu Coppey, Raphaël Voituriez, Matthieu Piel, and Fanny Jaulin. Cell clusters adopt a collective amoeboid mode of migration in confined nonadhesive environments. *Science Advances*, 8:8416, 9 2022.

[175] Meghan K. Driscoll, Erik S. Welf, Andrew Weems, Etai Sapoznik, Felix Zhou, Vasanth S. Murali, Juan Manuel García-Arcos, Minna Roh-Johnson, Matthieu Piel, Kevin M. Dean, Reto Fiolka, and Gaudenz Danuser. Proteolysis-free amoeboid migration of melanoma cells through crowded environments via bleb-driven worrying. *Developmental Cell*, 2024.

[176] Haodi Zhao, Jing Wei, and Jian Sun. Roles of tgf-β signaling pathway in tumor microenvirionment and cancer therapy. *International Immunopharmacology*, 89:107101, 2020.

[177] Cecile Dessapt, Marc Olivier Baradez, Anthea Hayward, Alessandra Dei Cas, Stephen M. Thomas, Giancarlo Viberti, and Luigi Gnudi. Mechanical forces and tgfβ1 reduce podocyte adhesion through $\alpha 3\beta 1$ integrin downregulation. *Nephrology Dialysis Transplantation*, 24:2645–2655, 9 2009.

[178] Feng Lin, Haihui Zhang, Jianyong Huang, and Chunyang Xiong. Substrate stiffness coupling tgf-β1 modulates migration and traction force of mda-mb-231 human breast cancer cells in vitro. *ACS Biomaterials Science and Engineering*, 4(4):1337–1345, 2018.

[179] Gaia Cantelli, Jose L. Orgaz, Irene Rodriguez-Hernandez, Panagiotis Karagiannis, Oscar Maiques, Xavier Matias-Guiu, Frank O. Nestle, Rosa M. Marti, Sophia N. Karagiannis, and Victoria Sanz-Moreno. Tgf-β-induced transcription sustains amoeboid melanoma migration and dissemination. *Current Biology*, 25:2899–2914, 11 2015.

[180] David Böhringer, Andreas Bauer, Ivana Moravec, Lars Bischof, Delf Kah, Christoph Mark, Thomas J. Grundy, Ekkehard Görlach, Geraldine M. O'Neill, Silvia Budday, Pamela L. Strissel, Reiner Strick, Andrea Malandrino, Richard Gerum, Michael Mak, Martin Rausch, and Ben Fabry. Fiber alignment in 3d collagen networks as a biophysical marker for cell contractility. *Matrix Biology*, 124:39–48, 12 2023.

[181] Katarzyna S. Kopanska, Yara Alcheikh, Ralitza Staneva, Danijela Vignjevic, and Timo Betz. Tensile forces originating from cancer spheroids facilitate tumor invasion. *PLoS ONE*, 11, 6 2016.

[182] Grace Cai, Anh Nguyen, Yashar Bashirzadeh, Shan Shan Lin, Dapeng Bi, and Allen P. Liu. Compressive stress drives adhesion-dependent unjamming transitions in breast cancer cell migration. *Frontiers in Cell and Developmental Biology*, 10(October):1–17, 2022.

[183] Dongdong Wang, Nayden G. Naydenov, Mikhail G. Dozmorov, Jennifer E. Koblinski, and Andrei I. Ivanov. Anillin regulates breast cancer cell migration, growth, and metastasis by non-canonical mechanisms involving control of cell stemness and differentiation. *Breast Cancer Research*, 22, 1 2020.

[184] Stephan Niland, Andrea Ximena Riscanevo, and Johannes Andreas Eble. Matrix metalloproteinases shape the tumor microenvironment in cancer progression. *International Journal of Molecular Sciences*, 23(1), 2022.

[185] Cristian Scheau, Ioana Anca Badarau, Raluca Costache, Constantin Caruntu, Gratiela Livia Mihai, Andreea Cristiana Didilescu, Carolina Constantin, and Monica Neagu. The role of matrix metalloproteinases in the epithelial-mesenchymal transition of hepatocellular carcinoma. *Analytical Cellular Pathology*, 2019, 2019.

[186] Béatrice Nawrocki-Raby, Christine Gilles, Myriam Polette, Erik Bruyneel, Jean Yves Laronze, Noël Bonnet, Jean Michel Foidart, Marc Mareel, and Philippe Birembaut. Upregulation of mmps by soluble e-cadherin in human lung tumor cells. *International Journal of Cancer*, 105:790–795, 7 2003.

[187] Diana Pinheiro and Jennifer Mitchel. Pulling the strings on solid-to-liquid phase transitions in cell collectives. *Current Opinion in Cell Biology*, 86:102310, 2 2024.

[188] Thomas S. Deisboeck, Yuri Mansury, Caterina Guiot, Piero Giorgio Degiorgis, and Pier Paolo Delsanto. Insights from a novel tumor model: Indications for a quantitative link between tumor growth and invasion. *Medical Hypotheses*, 65(4):785–790, 2005.

[189] Ashleigh J. Crawford, Clara Gomez-Cruz, Gabriella C. Russo, Wilson Huang, Isha Bhorkar, Triya Roy, Arrate Muñoz-Barrutia, Denis Wirtz, and Daniel Garcia-Gonzalez. Tumor proliferation and invasion are intrinsically coupled and unraveled through tunable spheroid and physics-based models. *Acta Biomaterialia*, 175:170–185, 2 2024.

[190] Gaspar Banfalvi. *Overview of Cell Synchronization*, pages 1–23. Humana Press, Totowa, NJ, 2011.

[191] Anna Ligasová and Karel Koberna. Strengths and weaknesses of cell synchronization protocols based on inhibition of dna synthesis. *International Journal of Molecular Sciences*, 22(19), 2021.

[192] Miranda V. Hunter, Emily Montal, Yilun Ma, Reuben Moncada, Itai Yanai, Richard P. Koche, and Richard M. White. Mechanical confinement governs phenotypic plasticity in melanoma. *bioRxiv*, 2024.

[193] Pablo Gottheil, Jürgen Lippoldt, Steffen Grosser, Frédéric Renner, Mohamad Saibah, Dimitrij Tschodu, Anne Kathrin Poßögel, Anne Sophie Wegscheider, Bernhard Ulm, Kay Friedrichs, Christoph Lindner, Christoph Engel, Markus Löffler, Benjamin Wolf, Michael Höckel, Bahriye Aktas, Hans Kubitschke, Axel Niendorf, and Josef A. Käs. State of cell unjamming correlates with distant metastasis in cancer patients. *Physical Review X*, 13, 7 2023.

[194] Elena Scarpa and Roberto Mayor. Collective cell migration in development. *J. Cell Biol.*, 212(2):143–155, 2016.

[195] Laurent Lamalice, Fabrice Le Boeuf, and Jacques Huot. Endothelial cell migration during angiogenesis. *Cir. Res.*, 100(6):782–794, mar 2007.

[196] Peihong Su, Ye Tian, Chaofei Yang, Xiaoli Ma, Xue Wang, Jiawei Pei, and Airong Qian. Mesenchymal Stem Cell Migration during Bone Formation and Bone Diseases Therapy. *Int. J. Mol. Sci.*, 19(8):2343, aug 2018.

[197] Xiaorong Fu, Ge Liu, Alexander Halim, Yang Ju, Qing Luo, and Guanbin Song. Mesenchymal Stem Cell Migration and Tissue Repair. *Cells.*, 8(8):784, aug 2019.

[198] Maria–Graciela Delgado and Ana Maria Lennon-Duménil. How cell migration helps immune sentinels. *Front. Cell Dev. Biol.*, 10:932472, oct 2022.

[199] Juan Liu, Xiaomin Zhang, Yujie Cheng, and Xuetao Cao. Dendritic cell migration in inflammation and immunity. *Cell. Mol. Immunol.*, 18(11):2461–2471, November 2021.

[200] Claudia Tanja Mierke. The matrix environmental and cell mechanical properties regulate cell migration and contribute to the invasive phenotype of cancer cells. *Rep. Prog. Phys.*, 82(6):064602, June 2019.

[201] Vitold E Galkin, Albina Orlova, Matthijn R Vos, Gunnar F Schröder, and Edward H Egelman. Near-atomic resolution for one state of f-actin. *Structure.*, 23(1):173–182, January 2015.

[202] Hyeran Kang, Michael J Bradley, Brannon R McCullough, Anaëlle Pierre, Elena E Grintsevich, Emil Reisler, and Enrique M De La Cruz. Identification of cation-binding sites on actin that drive polymerization and modulate bending stiffness. *Proc. Natl. Acad. Sci. U. S. A.*, 109(42):16923–16927, October 2012.

[203] Peter J Carman, Kyle R Barrie, Grzegorz Rebowski, and Roberto Dominguez. Structures of the free and capped ends of the actin filament. *Science.*, 380(6651):1287–1292, June 2023.

[204] Naoki Watanabe and Timothy J Mitchison. Single-molecule speckle analysis of actin filament turnover in lamellipodia. *Science.*, 295(5557):1083–1086, February 2002.

[205] Marco Fritzsche, Alexandre Lewalle, Tom Duke, Karsten Kruse, and Guillaume Charras. Analysis of turnover dynamics of the submembranous actin cortex. *Mol. Biol. Cell*, 24(6):757, mar 2013.

[206] Michael Murrell, Patrick W Oakes, Martin Lenz, and Margaret L Gardel. Forcing cells into shape: the mechanics of actomyosin contractility. *Nat. Rev. Mol. Cell Biol.*, 16(8):486–498, August 2015.

[207] Rui Zhang, Benjamin LaFrance, and Eva Nogales. Separating the effects of nucleotide and EB binding on microtubule structure. *Proc. Natl. Acad. Sci. U. S. A.*, 115(27):E6191–E6200, July 2018.

[208] Katja M Taute, Francesco Pampaloni, Erwin Frey, and Ernst-Ludwig Florin. Microtubule dynamics depart from the wormlike chain model. *Phys. Rev. Lett.*, 100(2):028102, January 2008.

[209] Gary J Brouhard. Dynamic instability 30 years later: complexities in microtubule growth and catastrophe. *Mol. Biol. Cell*, 26(7):1207–1210, April 2015.

[210] Ulrike Rölleke, Pallavi Kumari, Ruth Meyer, and Sarah Köster. The unique biomechanics of intermediate filaments - from single filaments to cells and tissues. *Curr. Opin. Cell Biol.*, 85(102263):102263, October 2023.

[211] Hyeran Kang, Michael J. Bradley, Wenxiang Cao, Kaifeng Zhou, Elena E. Grintsevich, Alphée Michelot, Charles V. Sindelar, Mark Hochstrasser, and Enrique M. De La Cruz. Site-specific cation release drives actin filament severing by vertebrate cofilin. *Proc. Natl. Acad. Sci. U. S. A.*, 111(50):17821–17826, dec 2014.

[212] Roy Beck, Joanna Deek, Myung Chul Choi, Taiji Ikawa, Osamu Watanabe, Erwin Frey, Philip Pincus, and Cyrus R Safinya. Unconventional salt trend from soft to stiff in single neurofilament biopolymers. *Langmuir.*, 26(24):18595–18599, December 2010.

[213] Bernd Nöding and Sarah Köster. Intermediate filaments in small configuration spaces. *Phys. Rev. Lett.*, 108(8):088101, February 2012.

[214] Paul Pawelzyk, Norbert Mücke, Harald Herrmann, and Norbert Willenbacher. Attractive interactions among intermediate filaments determine network mechanics in vitro. *PLoS One.*, 9(4):e93194, April 2014.

[215] Michael Schopferer, Harald Bär, Bernhard Hochstein, Sarika Sharma, Norbert Mücke, Harald Herrmann, and Norbert Willenbacher. Desmin and vimentin intermediate filament networks: their viscoelastic properties investigated by mechanical rheometry. *J. Mol. Biol.*, 388(1):133–143, April 2009.

[216] N Mücke, L Kreplak, R Kirmse, T Wedig, H Herrmann, U Aebi, and J Langowski. Assessing the flexibility of intermediate filaments by atomic force microscopy. *J. Mol. Biol.*, 335(5):1241–1250, January 2004.

[217] Bernd Nöding, Harald Herrmann, and Sarah Köster. Direct observation of subunit exchange along mature vimentin intermediate filaments. *Biophys. J.*, 107(12):2923–2931, 2014.

[218] Quang D. Tran, Valerio Sorichetti, Gerard Pehau-Arnaudet, Martin Lenz, and Cécile Leduc. Fragmentation and Entanglement Limit Vimentin Intermediate Filament Assembly. *Phys. Rev. X*, 13(1):011014, jan 2023.

[219] Amélie Robert, Molly J Rossow, Caroline Hookway, Stephen A Adam, and Vladimir I Gelfand. Vimentin filament precursors exchange subunits in an ATP-dependent manner. *Proc. Natl. Acad. Sci. U. S. A.*, 112(27):E3505–14, July 2015.

[220] Caroline Hookway, Liya Ding, Michael W Davidson, Joshua Z Rappoport, Gaudenz Danuser, and Vladimir I Gelfand. Microtubule-dependent transport and dynamics of vimentin intermediate filaments. *Mol. Biol. Cell*, 26(9):1675–1686, May 2015.

[221] Klemens Rottner and Matthias Schaks. Assembling actin filaments for protrusion. *Curr. Opin. Cell Biol.*, 56:53–63, February 2019.

[222] Maria F Ullo and Jeremy S Logue. ADF and cofilin-1 collaborate to promote cortical actin flow and the leader bleb-based migration of confined cells. *eLife.*, 10:67856, June 2021.

[223] Anna Akhmanova and Lukas C Kapitein. Mechanisms of microtubule organization in differentiated animal cells. *Nat. Rev. Mol. Cell Biol.*, 23(8):541–558, August 2022.

[224] Alison E. Patteson, Amir Vahabikashi, Katarzyna Pogoda, Stephen A. Adam, Kalpana Mandal, Mark Kittisopikul, Suganya Sivagurunathan, Anne Goldman, Robert D. Goldman, and Paul A. Janmey. Vimentin protects cells against nuclear rupture and DNA damage during migration. *J. Cell Biol.*, 218(12):4079–4092, dec 2019.

[225] Sandrine B Lavenus, Sara M Tudor, Maria F Ullo, Karl W Vosatka, Jeremy S Logue, Enrique M De, and La Cruz. A flexible network of vimentin intermediate filaments promotes migration of amoeboid cancer cells through confined environments. *J. Biol. Chem.*, 295:6700–6709, 2020.

[226] Marileen Dogterom and Gijsje H. Koenderink. Actin–microtubule crosstalk in cell biology. *Nat. Rev. Mol. Cell Biol.*, 20(1):38–54, jan 2019.

[227] Byung Min Chung, Jeremy D. Rotty, and Pierre A. Coulombe. Networking galore: Intermediate filaments and cell migration. *Curr. Opin. Cell Biol.*, 25(5):600–612, oct 2013.

[228] Morgan L Pimm and Jessica L Henty-Ridilla. New twists in actin-microtubule interactions. *Mol. Biol. Cell*, 32(3):211–217, February 2021.

[229] CJ Schmidt and SJ Stehbens. Microtubule control of migration: Coordination in confinement. *Curr. Opin. Cell Biol.*, 86:102289, December 2023.

[230] Andreas Buttenschön and Leah Edelstein-Keshet. Bridging from single to collective cell migration: A review of models and links to experiments. *PLoS Comput. Biol.*, 16(12):e1008411, December 2020.

[231] Shiladitya Banerjee and M Cristina Marchetti. Continuum models of collective cell migration. *Adv. Exp. Med. Biol.*, 1146:45–66, 2019.

[232] Brittany MacTaggart and Anna Kashina. Posttranslational modifications of the cytoskeleton. *Cytoskeleton.*, 78(4):142–173, April 2021.

[233] Shailaja Seetharaman, Benoit Vianay, Vanessa Roca, Aaron J. Farrugia, Chiara De Pascalis, Batiste Boëda, Florent Dingli, Damarys Loew, Stéphane Vassilopoulos, Alexander Bershadsky, Manuel Théry, and Sandrine Etienne-Manneville. Microtubules tune mechanosensitive cell responses. *Nat. Mat.*, 21(3):366–377, mar 2022.

[234] Veronika Te Boekhorst, Luigi Preziosi, and Peter Friedl. Plasticity of cell migration in vivo and in silico. *Annu. Rev. Cell Dev. Biol.*, 32:491–526, October 2016.

[235] Katarina Wolf, Stephanie Alexander, Vivien Schacht, Lisa M Coussens, Ulrich H von Andrian, Jacco van Rheenen, Elena Deryugina, and Peter Friedl. Collagen-based cell migration models in vitro and in vivo. *Semin. Cell Dev. Biol.*, 20(8):931–941, October 2009.

[236] Jochen Guck, Franziska Lautenschläger, Stephan Paschke, and Michael Beil. Critical review: cellular mechanobiology and amoeboid migration. *Integr. Biol.*, 2(11-12):575–583, November 2010.

[237] Zhenhui Liu, Se Jong Lee, Seungman Park, Konstantinos Konstantopoulos, Kristine Glunde, Yun Chen, and Ishan Barman. Cancer cells display increased migration and deformability in pace with metastatic progression. *FASEB J.*, 34(7):9307–9315, July 2020.

[238] Blanca González-Bermúdez, Gustavo V Guinea, and Gustavo R Plaza. Advances in micropipette aspiration: Applications in cell biomechanics, models, and extended studies. *Biophys. J.*, 116(4):587–594, February 2019.

[239] J Guck, R Ananthakrishnan, H Mahmood, T J Moon, C C Cunningham, and J Käs. The optical stretcher: a novel laser tool to micromanipulate cells. *Biophys. J.*, 81(2):767–784, August 2001.

[240] O Thoumine and A Ott. Time scale dependent viscoelastic and contractile regimes in fibroblasts probed by microplate manipulation. *J. Cell Sci.*, 110 (Pt 17)(17):2109–2116, September 1997.

[241] Marta Urbanska, Hector E. Muñoz, Josephine Shaw Bagnall, Oliver Otto, Scott R. Manalis, Dino Di Carlo, and Jochen Guck. A comparison of microfluidic methods for high-throughput cell deformability measurements. *Nat. Methods.*, 17(6):587–593, apr 2020.

[242] P Fernandez, L Heymann, A Ott, N Aksel, and PA Pullarkat. Shear rheology of a cell monolayer. *New J. Phys.*, 9:419, November 2007.

[243] Amy A Sutton, Clayton W Molter, Ali Amini, Johanan Idicula, Max Furman, Pouria Tirgar, Yuanyuan Tao, Ajinkya Ghagre, Newsha Koushki, Adele Khavari, and Allen J Ehrlicher. Cell monolayer deformation microscopy reveals mechanical fragility of cell monolayers following EMT. *Biophys. J.*, 121(4):629–643, February 2022.

[244] Khawaja Muhammad Imran Bashir, Suhyang Lee, Dong Hee Jung, Santanu Kumar Basu, Man-Gi Cho, and Andreas Wierschem. Narrow-gap rheometry: A novel method for measuring cell mechanics. *Cells.*, 11(13):2010, June 2022.

[245] Kellie Beicker, E Timothy O'Brien, 3rd, Michael R Falvo, and Richard Superfine. Vertical light sheet enhanced side-view imaging for AFM cell mechanics studies. *Sci. Rep.*, 8(1):1504, January 2018.

[246] Katarzyna Pogoda, Fitzroy Byfield, Piotr Deptuła, Mateusz Cieśluk, Łukasz Suprewicz, Karol Skłodowski, Jordan L Shivers, Anne van Oosten, Katrina Cruz, Ekaterina Tarasovetc, Ekaterina L Grishchuk, Fred C Mackintosh, Robert Bucki, Alison E Patteson, and Paul A Janmey. Unique role of vimentin networks in compression stiffening of cells and protection of nuclei from compressive stress. *Nano Lett.*, 22(12):4725–4732, June 2022.

[247] B Fabry, G N Maksym, J P Butler, M Glogauer, D Navajas, and J J Fredberg. Scaling the microrheology of living cells. *Phys. Rev. Lett.*, 87(14):148102, October 2001.

[248] Sajedeh Kerdegari, Paolo Canepa, Davide Odino, Reinier Oropesa-Nuñez, Annalisa Relini, Ornella Cavalleri, and Claudio Canale. Insights in cell biomechanics through atomic force microscopy. *Materials.*, 16(8):2980, April 2023.

[249] Frederic Català-Castro, Erik Schäffer, and Michael Krieg. Exploring cell and tissue mechanics with optical tweezers. *J. Cell Sci.*, 135(15):259–355, August 2022.

[250] A R Bausch, F Ziemann, A A Boulbitch, K Jacobson, and E Sackmann. Local measurements of viscoelastic parameters of adherent cell surfaces by magnetic bead microrheometry. *Biophys. J.*, 75(4):2038–2049, October 1998.

[251] A W C Lau, B D Hoffman, A Davies, J C Crocker, and T C Lubensky. Microrheology, stress fluctuations, and active behavior of living cells. *Phys. Rev. Lett.*, 91(19):198101, November 2003.

[252] Porntula Panorchan, Jerry S H Lee, Thomas P Kole, Yiider Tseng, and Denis Wirtz. Microrheology and ROCK signaling of human endothelial cells embedded in a 3D matrix. *Biophys. J.*, 91(9):3499–3507, November 2006.

[253] Jack R Staunton, Bryant L Doss, Stuart Lindsay, and Robert Ros. Correlating confocal microscopy and atomic force indentation reveals metastatic cancer cells stiffen during invasion into collagen I matrices. *Sci. Rep.*, 6(1):19686, January 2016.

[254] Joe Swift, Irena L Ivanovska, Amnon Buxboim, Takamasa Harada, P C Dave P Dingal, Joel Pinter, J David Pajerowski, Kyle R Spinler, Jae-Won Shin, Manorama Tewari, Florian Rehfeldt, David W Speicher, and Dennis E Discher. Nuclear lamin-a scales with tissue stiffness and enhances matrix-directed differentiation. *Science.*, 341(6149):1240104, August 2013.

[255] Andrew D Stephens, Edward J Banigan, Stephen A Adam, Robert D Goldman, and John F Marko. Chromatin and lamin a determine two different mechanical response regimes of the cell nucleus. *Mol. Biol. Cell.*, 28(14):1984–1996, July 2017.

[256] Emily S Bell, Pragya Shah, Noam Zuela-Sopilniak, Dongsung Kim, Alice-Anais Varlet, Julien L P Morival, Alexandra L McGregor, Philipp Isermann, Patricia M Davidson, Joshua J Elacqua, Jonathan N Lakins, Linda Vahdat, Valerie M Weaver, Marcus B Smolka, Paul N Span, and Jan Lammerding. Low lamin a levels enhance confined cell migration and metastatic capacity in breast cancer. *Oncogene.*, 41(36):4211–4230, September 2022.

[257] Haijiao Liu, Jun Wen, Yun Xiao, Jun Liu, Sevan Hopyan, Milica Radisic, Craig A Simmons, and Yu Sun. In situ mechanical characterization of the cell nucleus by atomic force microscopy. *ACS Nano.*, 8(4):3821–3828, April 2014.

[258] Patricia M Davidson, Celine Denais, Maya C Bakshi, and Jan Lammerding. Nuclear deformability constitutes a rate-limiting step during cell migration in 3-D environments. *Cell. Mol. Bioeng.*, 7(3):293–306, September 2014.

[259] Franziska Lautenschläger, Stephan Paschke, Stefan Schinkinger, Arlette Bruel, Michael Beil, and Jochen Guck. The regulatory role of cell mechanics for migration of differentiating myeloid cells. *Proc. Natl. Acad. Sci. U. S. A.*, 106(37):15696–15701, September 2009.

[260] C Rotsch and M Radmacher. Drug-induced changes of cytoskeletal structure and mechanics in fibroblasts: an atomic force microscopy study. *Biophys. J.*, 78(1):520–535, January 2000.

[261] Jan Christian Martens and Manfred Radmacher. Softening of the actin cytoskeleton by inhibition of myosin II. *Pflugers Arch.*, 456(1):95–100, April 2008.

[262] Elisabeth Fischer-Friedrich, Yusuke Toyoda, Cedric J Cattin, Daniel J Müller, Anthony A Hyman, and Frank Jülicher. Rheology of the active cell cortex in mitosis. *Biophys. J.*, 111(3):589–600, August 2016.

[263] Ming Guo, Allen J Ehrlicher, Saleemulla Mahammad, Hilary Fabich, Mikkel H Jensen, Jeffrey R Moore, Jeffrey J Fredberg, Robert D Goldman, and David A Weitz. The role of vimentin intermediate filaments in cortical and cytoplasmic mechanics. *Biophys. J.*, 105(7):1562–1568, October 2013.

[264] M J Brown, J A Hallam, E Colucci-Guyon, and S Shaw. Rigidity of circulating lymphocytes is primarily conferred by vimentin intermediate filaments. *J. Immunol.*, 166(11):6640–6646, June 2001.

[265] Kristin Seltmann, Anatol W. Fritsch, Josef A. Käs, and Thomas M. Magin. Keratins significantly contribute to cell stiffness and impact invasive behavior. *Proc. Natl. Acad. Sci. U. S. A.*, 110(46):18507–18512, nov 2013.

[266] Sandrine B Lavenus, Sara M Tudor, Maria F Ullo, Karl W Vosatka, and Jeremy S Logue. A flexible network of vimentin intermediate filaments promotes migration of amoeboid cancer cells through confined environments. *J. Biol. Chem.*, 295(19):6700–6709, May 2020.

[267] N Wang. Mechanical interactions among cytoskeletal filaments. *Hypertension.*, 32(1):162–165, July 1998.

[268] Yuhui Li, Ondřej Kučera, Damien Cuvelier, David M Rutkowski, Mathieu Deygas, Dipti Rai, Tonja Pavlovič, Filipe Nunes Vicente, Matthieu Piel, Grégory Giannone, Dimitrios Vavylonis, Anna Akhmanova, Laurent Blanchoin, and Manuel Théry. Compressive forces stabilize microtubules in living cells. *Nat. Mater.*, 22(7):913–924, July 2023.

[269] Benjamin P Bouchet, Ivar Noordstra, Miranda van Amersfoort, Eugene A Katrukha, York-Christoph Ammon, Natalie D Ter Hoeve, Louis Hodgson, Marileen Dogterom, Patrick W B Derksen, and Anna Akhmanova. Mesenchymal cell invasion requires cooperative regulation of persistent microtubule growth by SLAIN2 and CLASP1. *Dev. Cell.*, 39(6):708–723, December 2016.

[270] Jan Maarten van Doorn, Luuk Lageschaar, Joris Sprakel, and Jasper van der Gucht. Criticality and mechanical enhancement in composite fiber networks. *Phys. Rev. E.*, 95(4-1):042503, April 2017.

[271] Sihan Chen, Tomer Markovich, and Fred C MacKintosh. Nonaffine deformation of semiflexible polymer and fiber networks. *Phys. Rev. Lett.*, 130(8):088101, February 2023.

[272] Yuan-Chen Chang, Perihan Nalbant, Jörg Birkenfeld, Zee-Fen Chang, and Gary M Bokoch. GEF-H1 couples nocodazole-induced microtubule disassembly to cell contractility via RhoA. *Mol. Biol. Cell*, 19(5):2147–2153, May 2008.

[273] Ernest Latorre, Sohan Kale, Laura Casares, Manuel Gómez-González, Marina Uroz, Léo Valon, Roshna V Nair, Elena Garreta, Nuria Montserrat, Aránzazu Del Campo, Benoit Ladoux, Marino Arroyo, and Xavier Trepat. Active superelasticity in three-dimensional epithelia of controlled shape. *Nature.*, 563(7730):203–208, November 2018.

[274] Magdalena Prechova, Zuzana Adamova, Anna Lena Schweizer, Miloslava Maninova, Andreas Bauer, Delf Kah, Samuel M. Meier-Menches, Gerhard Wiche, Ben Fabry, and Martin Gregor. Plectin-mediated cytoskeletal crosstalk controls cell tension and cohesion in epithelial sheets. *Journal of Cell Biology*, 221, 3 2022.

[275] Moumita Das and F C Mackintosh. Poisson's ratio in composite elastic media with rigid rods. *Phys. Rev. Lett.*, 105(13):138102, September 2010.

[276] M Dogterom and B Yurke. Measurement of the force-velocity relation for growing microtubules. *Science*, 278(5339):856–860, October 1997.

[277] Clifford P Brangwynne, Frederick C MacKintosh, Sanjay Kumar, Nicholas A Geisse, Jennifer Talbot, L Mahadevan, Kevin K Parker, Donald E Ingber, and David A Weitz. Microtubules can bear enhanced compressive loads in living cells because of lateral reinforcement. *J. Cell Biol.*, 173(5):733–741, June 2006.

[278] Patrick Robison, Matthew A Caporizzo, Hossein Ahmadzadeh, Alexey I Bogush, Christina Yingxian Chen, Kenneth B Margulies, Vivek B Shenoy, and Benjamin L Prosser. Detyrosinated microtubules buckle and bear load in contracting cardiomyocytes. *Science.*, 352(6284):aaf0659, April 2016.

[279] N Wang, K Naruse, D Stamenović, J J Fredberg, S M Mijailovich, I M Tolić-Nørrelykke, T Polte, R Mannix, and D E Ingber. Mechanical behavior in living cells consistent with the tensegrity model. *Proc. Natl. Acad. Sci. U. S. A.*, 98(14):7765–7770, July 2001.

[280] Pei Hsun Wu, Dikla Raz Ben Aroush, Atef Asnacios, Wei Chiang Chen, Maxim E. Dokukin, Bryant L. Doss, Pauline Durand-Smet, Andrew Ekpenyong, Jochen Guck, Nataliia V. Guz, Paul A. Janmey, Jerry S.H. Lee, Nicole M. Moore, Albrecht Ott, Yeh Chuin Poh, Robert Ros, Mathias Sander, Igor Sokolov, Jack R. Staunton, Ning Wang, Graeme Whyte, and Denis Wirtz. A comparison of methods to assess cell mechanical properties. *Nat. Methods.*, 15:491–498, 6 2018.

[281] Johanna Block, Hannes Witt, Andrea Candelli, Jordi Cabanas Danes, Erwin J.G. Peterman, Gijs J.L. Wuite, Andreas Janshoff, and Sarah Köster. Viscoelastic properties of vimentin originate from nonequilibrium conformational changes. *Sci. Adv.*, 4(6):aat1161, jun 2018.

[282] Joost van Mameren, Karen C Vermeulen, Fred Gittes, and Christoph F Schmidt. Leveraging single protein polymers to measure flexural rigidity. *J. Phys. Chem. B*, 113(12):3837–3844, March 2009.

[283] R Yasuda, H Miyata, and K Kinosita, Jr. Direct measurement of the torsional rigidity of single actin filaments. *J. Mol. Biol.*, 263(2):227–236, October 1996.

[284] Jeffrey P Bibeau, Nandan G Pandit, Shawn Gray, Nooshin Shatery Nejad, Charles V Sindelar, Wenxiang Cao, and Enrique M De La Cruz. Twist response of actin filaments. *Proc. Natl. Acad. Sci. U. S. A.*, 120(4):e2208536120, January 2023.

[285] L. Kreplak, H. Bär, J. F. Leterrier, H. Herrmann, and U. Aebi. Exploring the mechanical behavior of single intermediate filaments. *J. Mol. Bio.*, 354(3):569–577, dec 2005.

[286] A Kis, S Kasas, B Babić, A J Kulik, W Benoît, G A D Briggs, C Schönenberger, S Catsicas, and L Forró. Nanomechanics of microtubules. *Phys. Rev. Lett.*, 89(24):248101, December 2002.

[287] Laura Schaedel, Karin John, Jérémie Gaillard, Maxence V Nachury, Laurent Blanchoin, and Manuel Théry. Microtubules self-repair in response to mechanical stress. *Nat. Mater.*, 14(11):1156–1163, November 2015.

[288] Y Tsuda, H Yasutake, A Ishijima, and T Yanagida. Torsional rigidity of single actin filaments and actin-actin bond breaking force under torsion measured directly by in vitro micromanipulation. *Proc. Natl. Acad. Sci. U. S. A.*, 93(23):12937–12942, November 1996.

[289] Sharyn A Endow and Piotr E Marszalek. An estimate to the first approximation of microtubule rupture force. *Eur. Biophys. J.*, 48(6):569–577, September 2019.

[290] Charlotta Lorenz, Johanna Forsting, Robert W Style, Stefan Klumpp, and Sarah Köster. Keratin filament mechanics and energy dissipation are determined by metal-like plasticity. *Matter.*, 6(6):2019–2033, June 2023.

[291] Filipe Nunes Vicente, Mickael Lelek, Jean-Yves Tinevez, Quang D Tran, Gerard Pehau-Arnaudet, Christophe Zimmer, Sandrine Etienne-Manneville, Gregory Giannone, and Cécile Leduc. Molecular organization and mechanics of single vimentin filaments revealed by super-resolution imaging. *Sci. Adv.*, 8(8):eabm2696, February 2022.

[292] Margaret L Gardel, Karen E Kasza, Clifford P Brangwynne, Jiayu Liu, and David A Weitz. Chapter 19: Mechanical response of cytoskeletal networks. *Methods Cell Biol.*, 89:487–519, 2008.

[293] Daphne Weihs, Thomas G Mason, and Michael A Teitell. Bio-microrheology: a frontier in microrheology. *Biophys. J.*, 91(11):4296–4305, December 2006.

[294] Yali Yang, Mo Bai, William S Klug, Alex J Levine, and Megan T Valentine. Microrheology of highly crosslinked microtubule networks is dominated by force-induced crosslinker unbinding. *Soft Matter.*, 9(2):383–393, January 2013.

[295] Yi Chia Lin, Gijsje H. Koenderink, Frederick C. MacKintosh, and David A. Weitz. Viscoelastic properties of microtubule networks. *Macromolecules.*, 40(21):7714–7720, oct 2007.

[296] Yali Yang, Jun Lin, Bugra Kaytanli, Omar A. Saleh, and Megan T. Valentine. Direct correlation between creep compliance and deformation in entangled and sparsely crosslinked microtubule networks. *Soft Matter.*, 8(6):1776–1784, jan 2012.

[297] Inka Kirchenbuechler, Donald Guu, Nicholas A Kurniawan, Gijsje H Koenderink, and M Paul Lettinga. Direct visualization of flow-induced conformational transitions of single actin filaments in entangled solutions. *Nat. Commun.*, 5(1):5060, October 2014.

[298] M. L. Gardel, J. H. Shin, F. C. MacKintosh, L. Mahadevan, P. Matsudaira, and D. A. Weitz. Elastic behavior of cross-linked and bundled actin networks. *Science.*, 304(5675):1301–1305, may 2004.

[299] F C MacKintosh, J Käs, and P A Janmey. Elasticity of semiflexible biopolymer networks. *Phys. Rev. Lett.*, 75(24):4425–4428, December 1995.

[300] K. E. Kasza, C. P. Broedersz, G. H. Koenderink, Y. C. Lin, W. Messner, E. A. Millman, F. Nakamura, T. P. Stossel, F. C. MacKintosh, and D. A. Weitz. Actin filament length tunes elasticity of flexibly cross-linked actin networks. *Biophys. J.*, 99(4):1091–1100, aug 2010.

[301] Chase P. Broedersz, Karen E. Kasza, Louise M. Jawerth, Stefan Münster, David A. Weitz, and Frederick C. MacKintosh. Measurement of nonlinear rheology of cross-linked biopolymer gels. *Soft Matter.*, 6(17):4120–4127, aug 2010.

[302] Jan Wilhelm and Erwin Frey. Elasticity of stiff polymer networks. *Phys. Rev. Lett.*, 91(10):108103, September 2003.

[303] David A Head, Alex J Levine, and F C MacKintosh. Deformation of cross-linked semiflexible polymer networks. *Phys. Rev. Lett.*, 91(10):108102, September 2003.

[304] Ovijit Chaudhuri, Sapun H Parekh, and Daniel A Fletcher. Reversible stress softening of actin networks. *Nature.*, 445(7125):295–298, January 2007.

[305] Yi Chia Lin, Norman Y. Yao, Chase P. Broedersz, Harald Herrmann, Fred C. MacKintosh, and David A. Weitz. Origins of elasticity in intermediate filament networks. *Phys. Rev. Lett.*, 104(5):058101, feb 2010.

[306] Norman Y. Yao, Chase P. Braedersz, Yi Chia Lin, Karen E. Kasza, Frederick C. MacKintosh, and David A. Weitz. Elasticity in Ionically cross-linked neurofilament networks. *Biophys. J.*, 98(10):2147–2153, may 2010.

[307] Yi Chia Lin, Chase P. Broedersz, Amy C. Rowat, Tatjana Wedig, Harald Herrmann, Frederick C. MacKintosh, and David A. Weitz. Divalent cations crosslink vimentin intermediate filament tail domains to regulate network mechanics. *J. Mol. Bio*, 399(4):637–644, 2010.

[308] Anders Aufderhorst-Roberts and Gijsje H. Koenderink. Stiffening and inelastic fluidization in vimentin intermediate filament networks. *Soft Matter.*, 15(36):7127–7136, sep 2019.

[309] Harald Bär, Michael Schopferer, Sarika Sharma, Bernhard Hochstein, Norbert Mücke, Harald Herrmann, and Norbert Willenbacher. Mutations in desmin's carboxy-terminal "tail" domain severely modify filament and network mechanics. *J. Mol. Biol.*, 397(5):1188–1198, April 2010.

[310] Huayin Wu, Yinan Shen, Dianzhuo Wang, Harald Herrmann, Robert D Goldman, David A Weitz, and John A Paulson. Effect of Divalent Cations on the Structure and Mechanics of Vimentin Intermediate Filaments. *Biophys. J.*, 119:55–64, 2020.

[311] Kimie Fukuyama, Takashi Murozuka, Russell Caldwell, and William L Epstein. Divalent cation stimulation of in vitro fibre assembly from epidermal keratin protein. *J. Cell Sci*, 33:255–263, 1978.

[312] Anna V. Schepers, Charlotta Lorenz, Peter Nietmann, Andreas Janshoff, Stefan Klumpp, and Sarah Köster. Multiscale mechanics and temporal evolution of vimentin intermediate filament networks. *Proc. Natl. Acad. Sci. U. S. A.*, 118(27):2102026118, jul 2021.

[313] Oliver I. Wagner, Sebastian Rammensee, Neha Korde, Qi Wen, Jean Francois Leterrier, and Paul A. Janmey. Softness, strength and self-repair in intermediate filament networks. *Exp. Cell Res.*, 313(10):2228, jun 2007.

[314] Manuela Denz, Manuel Marschall, Harald Herrmann, and Sarah Köster. Ion type and valency differentially drive vimentin tetramers into intermediate filaments or higher order assemblies. *Soft Matter.*, 17(4):870–878, January 2021.

[315] Tom Golde, Constantin Huster, Martin Glaser, Tina Händler, Harald Herrmann, Josef A. Käs, and Jörg Schnauß. Glassy dynamics in composite biopolymer networks. *Soft Matter.*, 14(39):7970–7978, 2018.

[316] J. Deek, R. Maan, E. Loiseau, and A. R. Bausch. Reconstitution of composite actin and keratin networks in vesicles. *Soft Matter.*, 14(10):1897–1902, March 2018.

[317] Iman Elbalasy, Paul Mollenkopf, Cary Tutmarc, Harald Herrmann, and Jörg Schnauß. Keratins determine network stress responsiveness in reconstituted actin-keratin filament systems. *Soft Matter.*, 17(14):3954–3962, April 2021.

[318] Vincent Pelletier, Naama Gal, Paul Fournier, and Maria L Kilfoil. Microrheology of microtubule solutions and actin-microtubule composite networks. *Phys. Rev. Lett.*, 102(18):188303, May 2009.

[319] I.K. Piechocka. *Biopolymers: from structural hierarchy to nonlinear rheology.* PhD thesis, Vrije Universiteit Amsterdam, 2011.

[320] Osigwe Esue, Ashley A. Carson, Yiider Tseng, and Denis Wirtz. A direct interaction between actin and vimentin filaments mediated by the tail domain of vimentin. *J. Biol. Chem.*, 281(41):30393–30399, oct 2006.

[321] Laura Schaedel, Charlotta Lorenz, Anna V. Schepers, Stefan Klumpp, and Sarah Köster. Vimentin intermediate filaments stabilize dynamic microtubules by direct interactions. *Nat. Commun.*, 12(1):1–12, jun 2021.

[322] Mikkel H Jensen, Eliza J Morris, Robert D Goldman, and David A Weitz. Emergent properties of composite semiflexible biopolymer networks. *Bioarchitecture*, 4(4-5):138–143, 2014.

[323] Yi-Chia Lin, Gijsje H. Koenderink, Frederick C. MacKintosh, and David A. Weitz. Control of non-linear elasticity in f-actin networks with microtubules. *Soft Matter.*, 7:902–906, 2011.

[324] Shea N Ricketts, Jennifer L Ross, and Rae M Robertson-Anderson. Co-entangled actin-microtubule composites exhibit tunable stiffness and power-law stress relaxation. *Biophys. J.*, 115(6):1055–1067, September 2018.

[325] Shea N Ricketts, Madison L Francis, Leila Farhadi, Michael J Rust, Moumita Das, Jennifer L Ross, and Rae M Robertson-Anderson. Varying crosslinking motifs drive the mesoscale mechanics of actin-microtubule composites. *Sci. Rep.*, 9(1):12831, September 2019.

[326] Yinan Shen, Huayin Wu, Peter J. Lu, Dianzhuo Wang, Marjan Shayegan, Hui Li, Weichao Shi, Zizhao Wang, Li Heng Cai, Jing Xia, Meng Zhang, Ruihua Ding, Harald Herrmann, Robert Goldman, Fred C. Mackintosh, Arturo Moncho-Jordá, and David A. Weitz. Effects of Vimentin Intermediate Filaments on the Structure and Dynamics of in Vitro Multicomponent Interpenetrating Cytoskeletal Networks. *Phys. Rev. Lett.*, 127(10):108101, sep 2021.

[327] Huayin Wu, Yinan Shen, Suganya Sivagurunathan, Miriam Sarah Weber, Stephen A Adam, Jennifer H Shin, Jeffrey J Fredberg, Ohad Medalia, Robert Goldman, David A Weitz, and Jennifer Lippincott-Schwartz. Vimentin intermediate filaments and filamentous actin form unexpected interpenetrating networks that redefine the cell cortex. *Proc. Natl. Acad. Sci. U. S. A.*, 119(10):2115217119, 2022.

[328] Magdalena Preciado López, Florian Huber, Ilya Grigoriev, Michel O Steinmetz, Anna Akhmanova, Gijsje H Koenderink, and Marileen Dogterom. Actin-microtubule coordination at growing microtubule ends. *Nat. Commun.*, 5(1):4778, August 2014.

[329] Irene Istúriz Petitjean, Quang D. Tran, Angeliki Goutou, Zima Kabir, Gerhard Wiche, Cécile Leduc, and Gijsje H. Koenderink. Reconstitution of cytolinker-mediated crosstalk between actin and vimentin. *Eur. J. Cell Biol.*, 103(2):151403, 2024.

[330] Shuvasree SenGupta, Carole A Parent, and James E Bear. The principles of directed cell migration. *Nat. Rev. Mol. Cell Biol.*, 22(8):529–547, August 2021.

[331] Ryan J. Petrie and Kenneth M. Yamada. Multiple mechanisms of 3d migration: The origins of plasticity. *Current Opinion in Cell Biology*, 42:7–12, 10 2016.

[332] Sean P. Palecek, Anna Huttenlocher, Alan F. Horwitz, and Douglas A. Lauffenburger. Physical and biochemical regulation of integrin release during rear detachment of migrating cells. *J. Cell Sci.*, 111(7):929–940, 1998.

[333] Robert W. Style, Rostislav Boltyanskiy, Guy K. German, Callen Hyland, Christopher W. Macminn, Aaron F. Mertz, Larry A. Wilen, Ye Xu, and Eric R. Dufresne. Traction force microscopy in physics and biology. *Soft Matter.*, 10(23):4047–4055, 2014.

[334] Ryan J Petrie, Hyun Koo, and Kenneth M Yamada. Generation of compartmentalized pressure by a nuclear piston governs cell motility in a 3D matrix. *Science.*, 345(6200):1062–1065, August 2014.

[335] Ewa K Paluch and Erez Raz. The role and regulation of blebs in cell migration. *Curr. Opin. Cell Biol.*, 25(5):582–590, October 2013.

[336] Yan-Jun Liu, Maël Le Berre, Franziska Lautenschlaeger, Paolo Maiuri, Andrew Callan-Jones, Mélina Heuzé, Tohru Takaki, Raphaël Voituriez, and Matthieu Piel. Confinement and low adhesion induce fast amoeboid migration of slow mesenchymal cells. *Cell.*, 160(4):659–672, February 2015.

[337] Kimberly M Stroka, Hongyuan Jiang, Shih-Hsun Chen, Ziqiu Tong, Denis Wirtz, Sean X Sun, and Konstantinos Konstantopoulos. Water permeation drives tumor cell migration in confined microenvironments. *Cell.*, 157(3):611–623, April 2014.

[338] Mira Krendel, Frank T Zenke, and Gary M Bokoch. Nucleotide exchange factor GEF-H1 mediates cross-talk between microtubules and the actin cytoskeleton. *Nat. Cell Biol.*, 4(4):294–301, April 2002.

[339] Andrew Rape, Wei Hui Guo, and Yu Li Wang. Microtubule depolymerization induces traction force increase through two distinct pathways. *J. Cell Sci.*, 124(24):4233–4240, dec 2011.

[340] Mihai L Azoitei, Jungsik Noh, Daniel J Marston, Philippe Roudot, Christopher B Marshall, Timothy A Daugird, Sidney L Lisanza, María-José Sandí, Mitsu Ikura, John Sondek, Robert Rottapel, Klaus M Hahn, and Gaudenz Danuser. Spatiotemporal dynamics of GEF-H1 activation controlled by microtubule- and src-mediated pathways. *J. Cell Biol.*, 218(9):3077–3097, September 2019.

[341] Jessica N Heck, Suzanne M Ponik, Maria G Garcia-Mendoza, Carolyn A Pehlke, David R Inman, Kevin W Eliceiri, and Patricia J Keely. Microtubules regulate GEF-H1 in response to extracellular matrix stiffness. *Mol. Biol. Cell*, 23(13):2583–2592, July 2012.

[342] Aglaja Kopf, Jörg Renkawitz, Robert Hauschild, Irute Girkontaite, Kerry Tedford, Jack Merrin, Oliver Thorn-Seshold, Dirk Trauner, Hans Häcker, Klaus Dieter Fischer, Eva Kiermaier, and Michael Sixt. Microtubules control cellular shape and coherence in amoeboid migrating cells. *J. Cell Biol.*, 219(6), 2020.

[343] Yaming Jiu, Johan Peränen, Niccole Schaible, Fang Cheng, John E. Eriksson, Ramaswamy Krishnan, and Pekka Lappalainen. Vimentin intermediate filaments control actin stress fiber assembly through GEF-H1 and RhoA. *J. Cell Sci.*, 130(5):892–902, 2017.

[344] Zhuo Gan, Liya Ding, Christoph J. Burckhardt, Jason Lowery, Assaf Zaritsky, Karlyndsay Sitterley, Andressa Mota, Nancy Costigliola, Colby G. Starker, Daniel F. Voytas, Jessica Tytell, Robert D. Goldman, and Gaudenz Danuser. Vimentin Intermediate Filaments Template Microtubule Networks to Enhance Persistence in Cell Polarity and Directed Migration. *Cell Syst.*, 3(3):252–263.e8, sep 2016.

[345] Yaming Jiu, Jaakko Lehtimäki, Sari Tojkander, Fang Cheng, Harri Jäälinoja, Xiaonan Liu, Markku Varjosalo, John E. Eriksson, and Pekka Lappalainen. Bidirectional interplay between vimentin intermediate filaments and contractile actin stress fibers. *Cell reports*, 11:1511–1518, 6 2015.

[346] Pragati C. Marks, Breanne R. Hewitt, Michelle A. Baird, Gerhard Wiche, and Ryan J. Petrie. Plectin linkages are mechanosensitive and required for the nuclear piston mechanism of three-dimensional cell migration. *Molecular Biology of the Cell*, 33, 10 2022.

[347] Csaba Daday, Katra Kolšek, and Frauke Gräter. The mechano-sensing role of the unique sh3 insertion in plakin domains revealed by molecular dynamics simulations. *Sci. Rep.*, 7:11669, 12 2017.

[348] Michael P Murrell and Margaret L Gardel. F-actin buckling coordinates contractility and severing in a biomimetic actomyosin cortex. *Proc. Natl. Acad. Sci. U. S. A.*, 109(51):20820–20825, December 2012.

[349] Viktoria Wollrab, Julio M Belmonte, Lucia Baldauf, Maria Leptin, François Nédeléc, and Gijsje H Koenderink. Polarity sorting drives remodeling of actin-myosin networks. *J. Cell Sci.*, 132(4):jcs219717, December 2018.

[350] José Alvarado, Michael Sheinman, Abhinav Sharma, Fred C. MacKintosh, and Gijsje H. Koenderink. Force percolation of contractile active gels. *Soft Matter.*, 13(34):5624–5644, 2017.

[351] Poul M Bendix, Gijsje H Koenderink, Damien Cuvelier, Zvonimir Dogic, Bernard N Koeleman, William M Brieher, Christine M Field, L Mahadevan, and David A Weitz. A quantitative analysis of contractility in active cytoskeletal protein networks. *Biophys. J.*, 94(8):3126–3136, April 2008.

[352] Kevin Carvalho, Feng C. Tsai, Edouard Lees, Raphaël Voituriez, Gijsje H. Koenderink, and Cecile Sykes. Cell-sized liposomes reveal how actomyosin cortical tension drives shape change. *Proc. Natl. Acad. Sci. U. S. A.*, 110(41):16456–16461, oct 2013.

[353] Etienne Loiseau, Jochen A M Schneider, Felix C Keber, Carina Pelzl, Gladys Massiera, Guillaume Salbreux, and Andreas R Bausch. Shape remodeling and blebbing of active cytoskeletal vesicles. *Sci. Adv.*, 2(4):e1500465, April 2016.

[354] William M McFadden, Patrick M McCall, Margaret L Gardel, and Edwin M Munro. Filament turnover tunes both force generation and dissipation to control long-range flows in a model actomyosin cortex. *PLoS Comput. Biol.*, 13(12):e1005811, December 2017.

[355] Sven K Vogel, Christian Wölfer, Diego A Ramirez-Diaz, Robert J Flassig, Kai Sundmacher, and Petra Schwille. Symmetry breaking and emergence of directional flows in minimal actomyosin cortices. *Cells*, 9(6):1432, June 2020.

[356] Sonal, Kristina A. Ganzinger, Sven K. Vogel, Jonas Mücksch, Philipp Blumhardt, and Petra Schwille. Myosin-II activity generates a dynamic steady state with continuous actin turnover in a minimal actin cortex. *J. Cell Sci.*, 132(4):jcs219899, feb 2019.

[357] Tzer Han Tan, Maya Malik-Garbi, Enas Abu-Shah, Junang Li, Abhinav Sharma, Fred C MacKintosh, Kinneret Keren, Christoph F Schmidt, and Nikta Fakhri. Self-organized stress patterns drive state transitions in actin cortices. Technical Report 6, 2018.

[358] Mathieu Pinot, Villier Steiner, Benoit Dehapiot, Byung-Kuk Yoo, Franck Chesnel, Laurent Blanchoin, Charles Kervrann, and Zoher Gueroui. Confinement induces actin flow in a meiotic cytoplasm. *Proc. Natl. Acad. Sci. U. S. A.*, 109(29):11705–11710, July 2012.

[359] Maya Malik-Garbi, Niv Ierushalmi, Silvia Jansen, Enas Abu-Shah, Bruce L Goode, Alex Mogilner, and Kinneret Keren. Scaling behaviour in steady-state contracting actomyosin networks. *Nat. Phys.*, 15(5):509–516, May 2019.

[360] Ryota Sakamoto, Ziane Izri, Yuta Shimamoto, Makito Miyazaki, and Yusuke T Maeda. Geometric trade-off between contractile force and viscous drag determines the actomyosin-based motility of a cell-sized droplet. *Proc. Natl. Acad. Sci. U. S. A.*, 119(30):e2121147119, July 2022.

[361] Yinan Shen, Huayin Wu, Peter J. Lu, Dianzhuo Wang, Marjan Shayegan, Hui Li, Weichao Shi, Zizhao Wang, Li Heng Cai, Jing Xia, Meng Zhang, Ruihua Ding, Harald Herrmann, Robert Goldman, Fred C. Mackintosh, Arturo Moncho-Jordá, and David A. Weitz. Effects of Vimentin Intermediate Filaments on the Structure and Dynamics of in Vitro Multicomponent Interpenetrating Cytoskeletal Networks. *Phys. Rev. Lett.*, 127(10):108101, sep 2021.

[362] Gloria Lee, Gregor Leech, Michael J Rust, Moumita Das, Ryan J Mcgorty, Jennifer L Ross, and Rae M Robertson-Anderson. Myosin-driven actin-microtubule networks exhibit self-organized contractile dynamics. *Sci. Adv*, 7(6):eabe4334, 2021.

[363] Louise P Cramer. Forming the cell rear first: breaking cell symmetry to trigger directed cell migration. *Nat. Cell Biol.*, 12(7):628–632, July 2010.

[364] Ju M Vasiliev, 1 M Gelfand, L V Domnina, O Y 1vanova, S G Komm, and L V Olshevskaja. Effect of colcemid on the locomotory behaviour of fibroblasts. *Development*, 24:625–640, 1970.

[365] Nadia Efimova, Changsong Yang, Jonathan X Chia, Ning Li, Christopher J Lengner, Kristi L Neufeld, and Tatyana M Svitkina. Branched actin networks are assembled on microtubules by adenomatous polyposis coli for targeted membrane protrusion. *J. Cell Biol.*, 219(9):e202003091, September 2020.

[366] Jessica L Henty-Ridilla, Aneliya Rankova, Julian A Eskin, Katelyn Kenny, and Bruce L Goode. Accelerated actin filament polymerization from microtubule plus ends. *Science*, 352(6288):1004–1009, May 2016.

[367] Atsuko Kodama, Iakowos Karakesisoglou, Ellen Wong, Alec Vaezi, and Elaine Fuchs. ACF7: An Essential Integrator of Microtubule Dynamics. *Cell Press.*, 115:343–354, 2003.

[368] Ksenija Drabek, Marco van Ham, Tatiana Stepanova, Katharina Draegestein, Remco van Horssen, Carmen Laura Sayas, Anna Akhmanova, Timo ten Hagen, Ron Smits, Riccardo Fodde, Frank Grosveld, and Niels Galjart. Role of CLASP2 in Microtubule Stabilization and the Regulation of Persistent Motility. *Curr. Biol.*, 16(22):2259–2264, nov 2006.

[369] Benjamin P Bouchet, Rosemarie E Gough, York-Christoph Ammon, Dieudonnée van de Willige, Harm Post, Guillaume Jacquemet, Af Maarten Altelaar, Albert Heck, Jr, Benjamin T Goult, and Anna Akhmanova. Talin-KANK1 interaction controls the recruitment of cortical microtubule stabilizing complexes to focal adhesions. *eLife.*, 5:e18124, July 2016.

[370] Elvira Infante, Alessia Castagnino, Robin Ferrari, Pedro Monteiro, Sonia Agüera-González, Perrine Paul-Gilloteaux, Mélanie J Domingues, Paolo Maiuri, Matthew Raab, Catherine M Shanahan, Alexandre Baffet, Matthieu Piel, Edgar R Gomes, and Philippe Chavrier. LINC complex-lis1 interplay controls MT1-MMP matrix digest-on-demand response for confined tumor cell migration. *Nat. Commun.*, 9(1):2443, June 2018.

[371] Brian T. Helfand, Melissa G. Mendez, S. N.Prasanna Murthy, Dale K. Shumaker, Boris Grin, Saleemulla Mahammad, Ueli Aebi, Tatjana Wedig, Yi I. Wu, Klaus M. Hahn, Masaki Inagaki, Harald Herrmann, and Robert D. Goldman. Vimentin organization modulates the formation of lamellipodia. *Mol. Biol. Cell*, 22(8):1274–1289, apr 2011.

[372] Yasuhisa Sakamoto, Batiste Boëda, and Sandrine Etienne-Manneville. APC binds intermediate filaments and is required for their reorganization during cell migration. *J. Cell Biol.*, 200(3):249–258, February 2013.

[373] Zhuo Gan, Liya Ding, Christoph J Burckhardt, Jason Lowery, Assaf Zaritsky, Karlyndsay Sitterley, Andressa Mota, Nancy Costigliola, Colby G Starker, Daniel F Voytas, Jessica Tytell, Robert D Goldman, and Gaudenz Danuser. Vimentin intermediate filaments template microtubule networks to enhance persistence in cell polarity and directed migration. *Cell Syst.*, 3(3):252–263.e8, September 2016.

[374] Shagufta H. Shabbir, Megan M. Cleland, Robert D. Goldman, and Milan Mrksich. Geometric control of vimentin intermediate filaments. *Biomaterials.*, 35(5):1359–1366, feb 2014.

[375] Cécile Leduc and Sandrine Etienne-Manneville. Regulation of microtubule-associated motors drives intermediate filament network polarization. *J. Cell Biol.*, 216(6):1689–1703, June 2017.

[376] Nancy Costigliola, Liya Ding, Christoph J. Burckhardt, Sangyoon J. Han, Edgar Gutierrez, Andressa Mota, Alex Groisman, Timothy J. Mitchison, and Gaudenz

Danuser. Vimentin fibers orient traction stress. *Proc. Natl. Acad. Sci. U. S. A.*, 114(20):5195–5200, may 2017.

[377] Yasuhisa Sakamoto, Batiste Boëda, and Sandrine Etienne-Manneville. APC binds intermediate filaments and is required for their reorganization during cell migration. *J. Cell Biol.*, 200(3):249–258, February 2013.

[378] Rudolf E Leube, Marcin Moch, and Reinhard Windoffer. Intermediate filaments and the regulation of focal adhesion. *Curr. Opin. Cell Biol.*, 32:13–20, February 2015.

[379] Magdalena Preciado López, Florian Huber, Ilya Grigoriev, Michel O Steinmetz, Anna Akhmanova, Marileen Dogterom, and Gijsje H Koenderink. In vitro reconstitution of dynamic microtubules interacting with actin filament networks. *Methods Enzymol.*, 540:301–320, 2014.

[380] Daisuke Inoue, Dorian Obino, Judith Pineau, Francesca Farina, Jérémie Gaillard, Christophe Guerin, Laurent Blanchoin, Ana-Maria Lennon-Duménil, and Manuel Théry. Actin filaments regulate microtubule growth at the centrosome. *EMBO J.*, 38(11):e99630, June 2019.

[381] Matthieu Gélin, Alexandre Schaeffer, Jérémie Gaillard, Christophe Guérin, Benoit Vianay, Magali Orhant-Prioux, Marcus Braun, Christophe Leterrier, Laurent Blanchoin, and Manuel Théry. Microtubules under mechanical pressure can breach dense actin networks. *J. Cell Sci.*, 136(22), November 2023.

[382] Dieudonnée van de Willige, Jessica Ja Hummel, Celine Alkemade, Olga I Kahn, Franco Kc Au, Robert Z Qi, Marileen Dogterom, Gijsje H Koenderink, Casper C Hoogenraad, and Anna Akhmanova. Cytolinker Gas2L1 regulates axon morphology through microtubule-modulated actin stabilization. *EMBO Rep.*, 20(11):e47732, November 2019.

[383] Auréliane Elie, Elea Prezel, Christophe Guérin, Eric Denarier, Sacnicte Ramirez-Rios, Laurence Serre, Annie Andrieux, Anne Fourest-Lieuvin, Laurent Blanchoin, and Isabelle Arnal. Tau co-organizes dynamic microtubule and actin networks. *Sci. Rep.*, 5(1):9964, May 2015.

[384] Celine Alkemade. *Reconstituting microtubule-actin coordination by cytolinkers.* PhD thesis, Delft University of Technology, 2021.

[385] N C Rodgers, E J Lawrence, A V Sawant, N Efimova, G Gonzalez-Vasquez, T T Hickman, I Kaverina, and M Zanic. CLASP2 facilitates dynamic actin filament organization along the microtubule lattice. *Mol. Biol. Cell*, 34(3):261a, March 2023.

[386] Celine Alkemade, Harmen Wierenga, Vladimir A. Volkov, Magdalena Preciado López, Anna Akhmanova, Pieter Rein ten Wolde, Marileen Dogterom, and Gijsje H. Koenderink. Cross-linkers at growing microtubule ends generate forces that drive actin transport. *Proc. Natl. Acad. Sci. U. S. A.*, 119(11):1–12, 2022.

[387] Medhavi Vishwakarma, Joachim P Spatz, and Tamal Das. Mechanobiology of leader-follower dynamics in epithelial cell migration. *Curr. Opin. Cell Biol.*, 66:97–103, October 2020.

[388] Anna Haeger, Katarina Wolf, Mirjam M Zegers, and Peter Friedl. Collective cell migration: guidance principles and hierarchies. *Trends Cell Biol.*, 25(9):556–566, 2015.

[389] Jin-Ah Park, Jae Hun Kim, Dapeng Bi, Jennifer A Mitchel, Nader Taheri Qazvini, Kelan Tantisira, Chan Young Park, Maureen McGill, Sae-Hoon Kim, Bomi Gweon, Jacob Notbohm, Robert Steward Jr, Stephanie Burger, Scott H Randell, Alvin T Kho, Dhananjay T Tambe, Corey Hardin, Stephanie A Shore, Elliot Israel, David A Weitz, Daniel J Tschumperlin, Elizabeth P Henske, Scott T Weiss, M Lisa Manning, James P Butler, Jeffrey M Drazen, Jeffrey J Fredberg, CH Analysed, and Nat Mater. Unjamming and cell shape in the asthmatic airway epithelium guided data interpretation on the biological relevance of cellular migration. *Nat Mater*, 14(10):1040–1048, 2015.

[390] Alessandro Mongera, Payam Rowghanian, Hannah J. Gustafson, Elijah Shelton, David A. Kealhofer, Emmet K. Carn, Friedhelm Serwane, Adam A. Lucio, James Giammona, and Otger Campàs. A fluid-to-solid jamming transition underlies vertebrate body axis elongation. *Nature.*, 561(7723):401–405, sep 2018.

[391] Dhananjay T. Tambe, C. Corey Hardin, Thomas E. Angelini, Kavitha Rajendran, Chan Young Park, Xavier Serra-Picamal, Enhua H. Zhou, Muhammad H. Zaman, James P. Butler, David A. Weitz, Jeffrey J. Fredberg, and Xavier Trepat. Collective cell guidance by cooperative intercellular forces. *Nat. Mat.*, 10(6):469–475, 2011.

[392] Tamal Das, Kai Safferling, Sebastian Rausch, Niels Grabe, Heike Boehm, and Joachim P. Spatz. A molecular mechanotransduction pathway regulates collective migration of epithelial cells. *Nat. Cell Biol.*, 17(3):276–287, feb 2015.

[393] O Campàs, I Noordstra, and AS Yap. Adherens junctions as molecular regulators of emergent tissue mechanics. *Nat Rev Mol Cell Biol.*, 1:1–18, December 2023.

[394] Jian Zhang, Kayla F. Goliwas, Wenjun Wang, Paul V. Taufalele, Francois Bordeleau, and Cynthia A. Reinhart-King. Energetic regulation of coordinated leader–follower dynamics during collective invasion of breast cancer cells. *Proc. Natl. Acad. Sci. U. S. A.*, 116:7867–7872, 2019.

[395] Joshua A Broussard, Avinash Jaiganesh, Hoda Zarkoob, Daniel E Conway, Alexander R Dunn, Horacio D Espinosa, Paul A Janmey, and Kathleen J Green. Scaling up single-cell mechanics to multicellular tissues - the role of the intermediate filament-desmosome network. *J. Cell Sci.*, 133(6):jcs228031, March 2020.

[396] M Schmelz and W W Franke. Complexus adhaerentes, a new group of desmoplakin-containing junctions in endothelial cells: the syndesmos connecting retothelial cells of lymph nodes. *Eur. J. Cell Biol.*, 61(2):274–289, August 1993.

[397] Marihan Hegazy, Abbey L Perl, Sophia A Svoboda, and Kathleen J Green. Desmosomal cadherins in health and disease. *Annu. Rev. Pathol.*, 17(1):47–72, January 2022.

[398] Jani E. Lewis, James K. Wahl, Kristin M. Sass, Pamela J. Jensen, Keith R. Johnson, and Margaret J. Wheelock. Cross-talk between adherens junctions and desmosomes depends on plakoglobin. *J. Cell Biol.*, 136(4):919–934, 1997.

[399] Tanmay Sadhanasatish, Katharina Augustin, Lukas Windgasse, Anna Chrostek-Grashoff, Matthias Rief, and Carsten Grashoff. A molecular optomechanics approach reveals functional relevance of force transduction across talin and desmoplakin. *Sci. Adv.*, 9(25):eadg3347, June 2023.

[400] Sandrine Etienne-Manneville. Actin and microtubules in cell motility: Which one is in control?, jul 2004.

[401] Selma Osmanagic-Myers, Stefanie Rus, Michael Wolfram, Daniela Brunner, Wolfgang H. Goldmann, Navid Bonakdar, Irmgard Fischer, Siegfried Reipert, Aurora Zuzuarregui, Gernot Walko, and Gerhard Wiche. Plectin reinforces vascular integrity by mediating crosstalk between the vimentin and the actin networks. *J. Cell Sci.*, 128(22):4138–4150, 2015.

[402] Brett J Roberts, Anjeza Pashaj, Keith R Johnson, and James K Wahl Iii. Desmosome dynamics in migrating epithelial cells requires the actin cytoskeleton. *Exp. cell research*, 317(20):2814–2822, 2011.

[403] Pooja R Sonavane, Chong Wang, Bette Dzamba, Gregory F Weber, Ammasi Periasamy, and Douglas W DeSimone. Mechanical and signaling roles for keratin intermediate filaments in the assembly and morphogenesis of xenopus mesendoderm tissue at gastrulation. *Development*, 144(23):4363–4376, December 2017.

[404] Chiara De Pascalis, Carlos Pérez-González, Shailaja Seetharaman, Batiste Boëda, Benoit Vianay, Mithila Burute, Cécile Leduc, Nicolas Borghi, Xavier Trepat, and Sandrine Etienne-Manneville. Intermediate filaments control collective migration by restricting traction forces and sustaining cell-cell contacts. *J. Cell Biol.*, 217(9):3031–3044, sep 2018.

[405] Sungjun Yoon and Rudolf E Leube. Keratin intermediate filaments: intermediaries of epithelial cell migration. *Essays in Biochemistry*, 63:521–533, 2019.

[406] Anne Marie Fortier, Eric Asselin, and Monique Cadrin. Keratin 8 and 18 loss in epithelial cancer cells increases collective cell migration and cisplatin sensitivity through claudin1 up-regulation. *J. Biol. Chem.*, 288(16):11555–11571, apr 2013.

[407] Anne Kölsch, Reinhard Windoffer, and Rudolf E. Leube. Actin-dependent dynamics of keratin filament precursors. *Cell Motility and the Cytoskeleton*, 66:976–985, 11 2009.

[408] Ekaterina Vasileva and Sandra Citi. The role of microtubules in the regulation of epithelial junctions. *Tissue Barriers*, 6(3):1539596, November 2018.

[409] Marta N. Shahbazi, Diego Megias, Carolina Epifano, Anna Akhmanova, Gregg G. Gundersen, Elaine Fuchs, and Mirna Perez-Moreno. CLASP2 interacts with p120-catenin and governs microtubule dynamics at adherens junctions. *J. Cell Biol.*, 203(6):1043–1061, dec 2013.

[410] Samantha J. Stehbens, Andrew D. Paterson, Matthew S. Crampton, Annette M. Shewan, Charles Ferguson, Anna Akhmanova, Robert G. Parton, and Alpha S. Yap. Dynamic microtubules regulate the local concentration of E-cadherin at cell-cell contacts. *J. Cell Sci.*, 119(9):1801–1811, may 2006.

[411] Xinyu Chen, Shin-Ichiro Kojima, Gary G Borisy, and Kathleen J Green. P120 catenin associates with kinesin and facilitates the transport of cadherin-catenin complexes to intercellular junctions. *J. Cell Biol.*, 163(3):547–557, November 2003.

[412] Lee A. Ligon and Erika L.F. Holzbaur. Microtubules tethered at eepithelial cell junctions by dynein facilitate efficient junction assembly. *Traffic*, 8(7):808–819, jul 2007.

[413] Kazuto Tsukita, Manabu Kitamata, Hiroka Kashihara, Tomoki Yano, Ikuko Fujiwara, Timothy F Day, Tatsuya Katsuno, Jaewon Kim, Fumiko Takenaga, Hiroo Tanaka, Sungsu Park, Makoto Miyata, Hitomi Watanabe, Gen Kondoh, Ryosuke Takahashi, Atsushi Tamura, and Sachiko Tsukita. Phase separation of an actin nucleator by junctional microtubules regulates epithelial function. *Sci. Adv.*, 9(7):eadf6358, February 2023.

[414] Céline Revenu, Sebastian Streichan, Erika Donà, Virginie Lecaudey, Lars Hufnagel, and Darren Gilmour. Quantitative cell polarity imaging defines leader-to-follower transitions during collective migration and the key role of microtubule-dependent adherens junction formation. *Development*, 141(6):1282–1291, mar 2014.

[415] Robert A Law, Alexander Kiepas, Habben E Desta, Emiliano Perez Ipiña, Maria Parlani, Se Jong Lee, Christopher L Yankaskas, Runchen Zhao, Panagiotis Mistriotis, Nianchao Wang, Zhizhan Gu, Petr Kalab, Peter Friedl, Brian A Camley, and Konstantinos Konstantopoulos. Cytokinesis machinery promotes cell dissociation from collectively migrating strands in confinement. *Sci. Adv.*, 9(2):eabq6480, January 2023.

[416] Allison Maker and Barry M. Gumbiner. Reconstitution of the full transmembrane cadherin-catenin complex. *Protein Expression and Purification*, 193:106056, may 2022.

[417] David L. Rimm, Erika R. Koslov, Partow Kebriaei, Carol D. Cianci, and Jon S. Morrow. Alpha 1(E)-catenin is an actin-binding and -bundling protein mediating the attachment of F-actin to the membrane adhesion complex. *Proc. Natl. Acad. Sci. U. S. A.*, 92(19):8813–8817, sep 1995.

[418] Erumbi S Rangarajan, Emmanuel W Smith, and Tina Izard. Distinct inter-domain interactions of dimeric versus monomeric α-catenin link cell junctions to filaments. *Commun. Biol.*, 6(1):276, March 2023.

[419] Soichiro Yamada, Sabine Pokutta, Frauke Drees, William I. Weis, and W. James Nelson. Deconstructing the cadherin-catenin-actin complex. *Cell*, 123(5):889–901, dec 2005.

[420] Craig D. Buckley, Jiongyi Tan, Karen L. Anderson, Dorit Hanein, Niels Volkmann, William I. Weis, W. James Nelson, and Alexander R. Dunn. The minimal cadherin-catenin complex binds to actin filaments under force. *Science*, 346(6209):1254211, oct 2014.

[421] C Arbore, M Sergides, L Gardini, G Bianchi, A V Kashchuk, I Pertici, P Bianco, F S Pavone, and M Capitanio. α-catenin switches between a slip and an asymmetric catch bond with f-actin to cooperatively regulate cell junction fluidity. *Nat. Commun.*, 13(1):1146, March 2022.

[422] Scott D Hansen, Adam V Kwiatkowski, Chung-Yueh Ouyang, Hongjun Liu, Sabine Pokutta, Simon C Watkins, Niels Volkmann, Dorit Hanein, William I Weis, R Dyche Mullins, and W James Nelson. αE-catenin actin-binding domain alters actin filament conformation and regulates binding of nucleation and disassembly factors. *Mol. Bio. of the Cell*, 24(23):3710–3720, 2013.

[423] Oliver J Harrison, Julia Brasch, Gorka Lasso, Phinikoula S Katsamba, Goran Ahlsen, Barry Honig, and Lawrence Shapiro. Structural basis of adhesive binding by desmocollins and desmogleins. *Proc. Natl. Acad. Sci. U. S. A.*, 113(26):7160–7165, June 2016.

[424] Michael Fuchs, Daniela Kugelmann, Nicolas Schlegel, Franziska Vielmuth, and Jens Waschke. Desmoglein 2 can undergo ca2+-dependent interactions with both desmosomal and classical cadherins including e-cadherin and n-cadherin. *Biophys. J.*, 121(7):1322–1335, April 2022.

[425] M Mathur, L Goodwin, and P Cowin. Interactions of the cytoplasmic domain of the desmosomal cadherin dsg1 with plakoglobin. *J. Biol. Chem.*, 269(19):14075–14080, May 1994.

[426] A P Kowalczyk, E A Bornslaeger, J E Borgwardt, H L Palka, A S Dhaliwal, C M Corcoran, M F Denning, and K J Green. The amino-terminal domain of desmoplakin binds to plakoglobin and clusters desmosomal cadherin-plakoglobin complexes. *J. Cell Biol.*, 139(3):773–784, November 1997.

[427] Lionel Fontao, Bertrand Favre, Sara Riou, Dirk Geerts, Fabienne Jaunin, Jean-Hilaire Saurat, Kathleen J Green, Arnoud Sonnenberg, and Luca Borradori. Interaction of the bullous pemphigoid antigen 1 (BP230) and desmoplakin with intermediate filaments is mediated by distinct sequences within their COOH terminus. *Mol. Biol. Cell*, 14(5):1978–1992, May 2003.

[428] Bertrand Favre, Nadja Begré, Jamal-Eddine Bouameur, Prakash Lingasamy, Gloria M Conover, Lionel Fontao, and Luca Borradori. Desmoplakin interacts with the coil 1 of different types of intermediate filament proteins and displays high affinity for assembled intermediate filaments. *PLoS One.*, 13(10):e0205038, October 2018.

[429] Jeffrey W Brown, Charles J Cho, and Jason C Mills. Paligenosis: Cellular Remodeling During Tissue Repair. *Annu. Rev. Physiol.*, 84:461–483, 2021.

[430] Pierre Savagner. Epithelial–Mesenchymal Transitions: From Cell Plasticity to Concept Elasticity. *Curr. Top. Dev. Biol.*, 112:273–300, jan 2015.

[431] V Poltavets, M Kochetkova, Pitson Sm, and M S Samuel. The Role of the Extracellular Matrix and Its Molecular and Cellular Regulators in Cancer Cell Plasticity. *Cancer Cell Plasticity. Front. Oncol*, 8:431, 2018.

[432] Tyler D. Ross, Brian G. Coon, Sanguk Yun, Nicolas Baeyens, Keiichiro Tanaka, Mingxing Ouyang, and Martin A. Schwartz. Integrins in mechanotransduction. *Curr. Opin. Cell Biol.*, 25(5):613–618, oct 2013.

[433] David A Calderwood, Iain D Campbell, and David R Critchley. Talins and kindlins: partners in integrin-mediated adhesion. *Nat. Rev. Mol. Cell Biol.*, 14(8):503–517, 2013.

[434] Julieann I Puleo, Sara S Parker, Mackenzie R Roman, Adam W Watson, Kiarash Rahmani Eliato, Leilei Peng, Kathylynn Saboda, Denise J Roe, Robert Ros, Frank B Gertler, and Ghassan Mouneimne. Mechanosensing during directed cell migration requires dynamic actin polymerization at focal adhesions. *J. Cell Biol.*, 218(12):4215–4235, 2019.

[435] Peter Friedl and Katarina Wolf. Plasticity of cell migration: A multiscale tuning model. *J. Cell Biol.*, 188(1):11–19, dec 2010.

[436] Jennifer M Mataraza, Michael W Briggs, Zhigang Li, Alan Entwistle, Anne J Ridley, and David B Sacks. IQGAP1 Promotes Cell Motility and Invasion. *J. Biol. Chem.*, 278:41237–41245, 2003.

[437] Barbara Belletti, Milena S Nicoloso, Monica Schiappacassi, Stefania Berton, Francesca Lovat, Katarina Wolf, Vincenzo Canzonieri, Antonella Zucchetto, Peter Friedl, Alfonso Colombatti, and Gustavo Baldassarre. Stathmin Activity Influences Sarcoma Cell Shape, Motility, and Metastatic Potential. *Mol. Biol. Cell*, 19:2003–2013, 2003.

[438] Karen M Ridge, John E Eriksson, Milos Pekny, and Robert D Goldman. Roles of vimentin in health and disease. *Genes Dev.*, 36(7-8):391–407, April 2022.

[439] Lei Qi, Teresa Knifley, Min Chen, and Kathleen L. O'Connor. Integrin $\alpha6\beta4$ requires plectin and vimentin for adhesion complex distribution and invasive growth. *J. Cell Sci.*, 135(2):jcs258471, jan 2022.

[440] Herbert B Schiller, Caroline C Friedel, Cyril Boulegue, and Reinhard Fässler. Quantitative proteomics of the integrin adhesome show a myosin II-dependent recruitment of LIM domain proteins. *EMBO Rep.*, 12(3):259–266, March 2011.

[441] Corina Ciobanasu, Bruno Faivre, and Christophe Le Clainche. Actomyosin-dependent formation of the mechanosensitive talin-vinculin complex reinforces actin anchoring. *Nat. Commun.*, 5:3095, 2014.

[442] Florian Franz, Rafael Tapia-Rojo, Sabina Winograd-Katz, Rajaa Boujemaa-Paterski, Wenhong Li, Tamar Unger, Shira Albeck, Camilo Aponte-Santamaria, Sergi Garcia-Manyes, Ohad Medalia, Benjamin Geiger, and Frauke Gräter. Allosteric activation of vinculin by talin. *Nat. Commun.*, 14(1):4311, July 2023.

[443] Rajaa Boujemaa-Paterski, Bruno Martins, Matthias Eibauer, Charlie T. Beales, Benjamin Geiger, and Ohad Medalia. Talin-activated vinculin interacts with branched actin networks to initiate bundles. *eLife.*, 9:1–26, oct 2020.

[444] Derek L. Huang, Nicolas A. Bax, Craig D. Buckley, William I. Weis, and Alexander R. Dunn. Vinculin forms a directionally asymmetric catch bond with F-actin. *Science.*, 357(6352):703–706, aug 2017.

[445] Julien Pernier, Marcelina Cardoso Dos Santos, Mariem Souissi, Adrien Joly, Hemalatha Narassimprakash, Olivier Rossier, Grégory Giannone, Emmanuèle Helfer, Kheya Sengupta, and Christophe Le Clainche. Talin and kindlin cooperate to control the density of integrin clusters. *J. Cell Sci.*, 136(8):jcs260746, April 2023.

[446] Charlotte F Kelley, Thomas Litschel, Stephanie Schumacher, Dirk Dedden, Petra Schwille, and Naoko Mizuno. Phosphoinositides regulate force-independent interactions between talin, vinculin, and actin. *eLife.*, 9:e56110, July 2020.

[447] A J Ehrlicher, F Nakamura, J H Hartwig, D A Weitz, and T P Stossel. Mechanical strain in actin networks regulates FilGAP and integrin binding to filamin A. *Nature.*, 478:260–263, 2011.

[448] Elias T Spiliotis and Michael A McMurray. Masters of asymmetry - lessons and perspectives from 50 years of septins. *Mol. Biol. Cell*, 31(21):2289–2297, October 2020.

[449] Konstantinos Nakos, Md Noor A Alam, Megan R Radler, Ilona A Kesisova, Changsong Yang, Joshua Okletey, Meagan R Tomasso, Shae B Padrick, Tatyana M Svitkina, and Elias T Spiliotis. Septins mediate a microtubule-actin crosstalk that enables actin growth on microtubules. *Proc. Natl. Acad. Sci. U. S. A.*, 119(50):e2202803119, December 2022.

[450] AS Zhovmer, A Manning, C Smith, A Nguyen, O Prince, PJ Sáez, X Ma, D Tsygankov, AX Cartagena-Rivera, NA Singh, RK Singh, and ED Tabdanov. Septins provide microenvironment sensing and cortical actomyosin partitioning in motile amoeboid t lymphocytes. *Sci Adv.*, 10:eadi1788, 2024.

[451] Joanna Kim, Olivia L. Mooren, Michael D. Onken, and John A. Cooper. Septin and actin contributions to endothelial cell–cell junctions and monolayer integrity. *Cytoskeleton*, 80(8):228—241, October 2022.

[452] Xueying Wang, Wenwen Wang, Xiwei Wang, Ming Wang, Lijuan Zhu, Fatima Garba, Chuanhai Fu, Barbara Zieger, Xu Liu, Xing Liu, and Xuebiao Yao. The septin complex links the catenin complex to the actin cytoskeleton for establishing epithelial cell polarity. *Journal of Molecular Cell Biology*, 13:395–408, 6 2021.

[453] Kim J A Vendel, Celine Alkemade, Nemo Andrea, Gijsje H Koenderink, and Marileen Dogterom. In vitro reconstitution of dynamic co-organization of microtubules and actin filaments in emulsion droplets. *Methods Mol. Biol.*, 2101:53–75, 2020.

[454] Orit Siton-Mendelson and Anne Bernheim-Groswasser. Toward the reconstitution of synthetic cell motility. *Cell Adhes. Migr.*, 10(5):461–474, September 2016.

[455] Andreas Fink, Charlotte R Doll, Ana Yagüe Relimpio, Yannik Dreher, Joachim P Spatz, Kerstin Göpfrich, and Elisabetta Ada Cavalcanti-Adam. Extracellular cues govern shape and cytoskeletal organization in giant unilamellar lipid vesicles. *ACS Synth. Biol.*, 12(2):369–374, February 2023.

[456] Torsten Wittmann, Alessandro Dema, and Jeffrey van Haren. Lights, cytoskeleton, action: Optogenetic control of cell dynamics. *Curr. Opin. Cell Biol.*, 66:1–10, October 2020.

[457] Jessica G Bermudez, Alexander Deiters, and Matthew C Good. Patterning microtubule network organization reshapes cell-like compartments. *ACS Synth. Biol.*, 10(6):1338–1350, June 2021.

[458] David B Brückner, Nicolas Arlt, Alexandra Fink, Pierre Ronceray, Joachim O Rädler, and Chase P Broedersz. Learning the dynamics of cell-cell interactions in confined cell migration. *Proc. Natl. Acad. Sci. U. S. A.*, 118(7):e2016602118, February 2021.

[459] Rebecca C Adikes, Ryan A Hallett, Brian F Saway, Brian Kuhlman, and Kevin C Slep. Control of microtubule dynamics using an optogenetic microtubule plus end-f-actin cross-linker. *J. Cell Biol.*, 217(2):779–793, February 2018.

[460] Sorosh Amiri, Camelia Muresan, Xingbo Shang, Clotilde Huet-Calderwood, Martin A Schwartz, David A Calderwood, and Michael Murrell. Intracellular tension sensor reveals mechanical anisotropy of the actin cytoskeleton. *Nat. Commun.*, 14(1):8011, December 2023.

[461] Janik N. Schampera and Carsten Schwan. Septin dynamics and organization in mammalian cells. *Current Opinion in Cell Biology*, 91:102442, 12 2024.

[462] Samed Delic, Brent Shuman, Shoken Lee, Shirin Bahmanyar, Michelle Momany, and Masayuki Onishi. The evolutionary origins and ancestral features of septins. *Frontiers in Cell and Developmental Biology*, 12:1406966, 6 2024.

[463] Deborah C. Mendonça, Joci N. Macedo, Samuel L. Guimarães, Fernando L. Barroso da Silva, Alexandre Cassago, Richard C. Garratt, Rodrigo V. Portugal, and Ana P.U. Araujo. A revised order of subunits in mammalian septin complexes. *Cytoskeleton*, 76:457–466, 9 2019.

[464] Carla Silva Martins, Cyntia Taveneau, Gerard Castro-Linares, Mikhail Baibakov, Nicolas Buzhinsky, Mar Eroles, Violeta Milanović, Shizue Omi, Jean-Denis Pedelacq, Francois Iv, Léa Bouillard, Alexander Llewellyn, Maxime Gomes, Mayssa Belhabib, Mira Kuzmić, Pascal Verdier-Pinard, Stacey Lee, Ali Badache, Sanjay Kumar, Cristel Chandre, Sophie Brasselet, Felix Rico, Olivier Rossier, Gijsje H. Koenderink, Jerome Wenger, Stéphanie Cabantous, and Manos Mavrakis. Human septins organize as octamer-based filaments and mediate actin-membrane anchoring in cells. *Journal of Cell Biology*, 222, 3 2023.

[465] Makoto Kinoshita. Assembly of mammalian septins. *The Journal of Biochemistry*, 134:491–496, 10 2003.

[466] Italo A. Cavini, Diego A. Leonardo, Higor V.D. Rosa, Danielle K.S.V. Castro, Humberto D'Muniz Pereira, Napoleão F. Valadares, Ana P.U. Araujo, and Richard C. Garratt. The structural biology of septins and their filaments: An update. *Frontiers in Cell and Developmental Biology*, 9:765085, 11 2021.

[467] Bradley S. DeMay, Xiaobo Bai, Louisa Howard, Patricia Occhipinti, Rebecca A. Meseroll, Elias T. Spiliotis, Rudolf Oldenbourg, and Amy S. Gladfelter. Septin filaments exhibit a dynamic, paired organization that is conserved from yeast to mammals. *The Journal of Cell Biology*, 193:1065, 6 2011.

[468] Jose M Vargas-Muñiz, Praveen R Juvvadi, and William J Steinbach. Forging the ring: from fungal septins' divergent roles in morphology, septation and virulence to factors contributing to their assembly into higher order structures. *Microbiology*, 162, 9 2016.

[469] Gérard Joberty, Richard R Perlungher, Peter J Sheffield, Makoto Kinoshita, Makoto Noda, Timothy Haystead, and Ian G Macara. Borg proteins control septin organization and are negatively regulated by cdc42. *NATURE CELL BIOLOGY*, 3, 2001.

[470] Peter J Sheffield, Carey J Oliver, Brandon E Kremer, Sitong Sheng, Zhifeng Shao, and Ian G Macara. Borg/septin interactions and the assembly of mammalian septin heterodimers, trimers, and filaments*. *The Journal of Biological Chemistry*, 278:3483–3488, 2002.

[471] Meagan R. Tomasso, Prajakta D. Mehetre, Priyashree Nagarajan, Roshni Ravi, Jennifer Byrnett, Eric Brinckman, Joseph Magliozzi, Bruce L. Goode, and Shae B. Padrick. Cdc42ep3-bound septin scaffolds promote actin polymerization. *The Journal of biological chemistry*, 301, 3 2025.

[472] Danielle K.S.V. Castro, Higor V.D. Rosa, Deborah C. Mendonça, Italo A. Cavini, Ana P.U. Araujo, and Richard C. Garratt. Dissecting the binding interface of the septin polymerization enhancer borg bd3. *Journal of molecular biology*, 435, 7 2023.

[473] Serge Mostowy, Sébastien Janel, Claire Forestier, Charles Roduit, Sandor Kasas, Javier Pizarro-Cerdá, Pascale Cossart, and Frank Lafont. A role for septins in the

interaction between the listeria monocytogenes invasion protein inlb and the met receptor. *Biophysical Journal*, 100:1949–1959, 4 2011.

[474] Christine S. Weirich, Jan P. Erzberger, and Yves Barral. The septin family of gtpases: architecture and dynamics. *Nature Reviews Molecular Cell Biology 2008 9:6*, 9:478–489, 5 2008.

[475] Yohko Tanaka-Takiguchi, Makato Kinoshita, and Kingo Takiguchi. Septin-mediated uniform bracing of phospholipid membranes. *Current Biology*, 19:140–145, 1 2009.

[476] Antonio Casamayor and Michael Snyder. Molecular dissection of a yeast septin: Distinct domains are required for septin interaction, localization, and function. *Molecular and Cellular Biology*, 23:2762–2777, 4 2003.

[477] K. Oegema, M. S. Savoian, T. J. Mitchison, and C. M. Field. Functional analysis of a human homologue of the drosophila actin binding protein anillin suggests a role in cytokinesis. *Journal of Cell Biology*, 150:539–552, 8 2000.

[478] Kinoshita Makato, Field Christine M., Margaret L. Coughlin, Aaron F. Straight, and Timothy J. Mitchison. Self-and actin-templated assembly of mammalian septins. *Cell Press*, 3:791–802, 2002.

[479] Emily Joo, Mark C. Surka, and William S. Trimble. Mammalian sept2 is required for scaffolding nonmuscle myosin ii and its kinases. *Developmental Cell*, 13:677–690, 11 2007.

[480] Manos Mavrakis, Yannick Azou-Gros, Feng-Ching Tsai, José Alvarado, Aurélie Bertin, Francois Iv, Alla Kress, Sophie Brasselet, Gijsje H Koenderink, and Thomas Lecuit. Septins promote f-actin ring formation by crosslinking actin filaments into curved bundles. *NATURE CELL BIOLOGY*, 16, 2014.

[481] Aaron J. Tooley, Julia Gilden, Jordan Jacobelli, Peter Beemiller, William S. Trimble, Makoto Kinoshita, and Matthew F. Krummel. Amoeboid t lymphocytes require the septin cytoskeleton for cortical integrity and persistent motility. *Nature Cell Biology*, 11:17–26, 2009.

[482] Joanna Kim, Olivia L. Mooren, Michael D. Onken, and John A. Cooper. Septin and actin contributions to endothelial cell-cell junctions and monolayer integrity. *Cytoskeleton (Hoboken, N.J.)*, 80:228–241, 7 2023.

[483] Béatrice Benoit, Christian Poüs, and Anita Baillet. Septins as membrane influencers: direct play or in association with other cytoskeleton partners. *Frontiers in Cell and Developmental Biology*, 11, 2023.

[484] Benjamin Targa, Laurence Klipfel, Isabelle Cantaloube, Joëlle Salameh, Béatrice Benoit, Christian Poüs, and Anita Baillet. Septin filament coalignment with microtubules depends on sept9i1 and tubulin polyglutamylation, and is an early feature of acquired cell resistance to paclitaxel. *Cell Death and Disease*, 10:54, 2019.

[485] Mira Kuzmić, Gerard Castro Linares, Jindřiška Leischner Fialová, François Iv, Daniele Salaün, Alex Llewellyn, Maxime Gomes, Mayssa Belhabib, Yuxiang Liu, Keisuke Asano, Magda Rodrigues, Daniel Isnardon, Taro Tachibana, Gijsje H. Koenderink, Ali Badache, Manos Mavrakis, and Pascal Verdier-Pinard. Septin-microtubule association via a motif unique to isoform 1 of septin 9 tunes stress fibers. *Journal of Cell Science*, 135, 1 2022.

[486] Xiaobo Bai, Jonathan R. Bowen, Tara K. Knox, Kaifeng Zhou, Manuela Pendziwiat, Gregor Kuhlenbäumer, Charles V. Sindelar, and Elias T. Spiliotis. Novel septin 9 repeat motifs altered in neuralgic amyotrophy bind and bundle microtubules. *Journal of Cell Biology*, 203:895–905, 12 2013.

[487] Eva P. Karasmanis, Daniel Hwang, Konstantinos Nakos, Jonathan R. Bowen, Dimitrios Angelis, and Elias T. Spiliotis. A septin double ring controls the spatiotemporal organization of the escrt machinery in cytokinetic abscission. *Current biology : CB*, 29:2174–2182.e7, 7 2019.

[488] David Ribet, Serena Boscaini, Clothilde Cauvin, Martin Siguier, Serge Mostowy, Arnaud Echard, and Pascale Cossart. Sumoylation of human septins is critical for septin filament bundling and cytokinesis. *The Journal of Cell Biology*, 216:4041, 2017.

[489] Julia K. Gilden, Sebastian Peck, Yi Chun M. Chen, and Matthew F. Krummel. The septin cytoskeleton facilitates membrane retraction during motility and blebbing. *Journal of Cell Biology*, 196:103–114, 1 2012.

[490] Maxine Lam and Fernando Calvo. Regulation of mechanotransduction: Emerging roles for septins. *Cytoskeleton*, 76:115–122, 1 2019.

[491] Aurosikha Das and Ambarish Kunwar. Septins: Structural insights, functional dynamics, and implications in health and disease. *Journal of Cellular Biochemistry*, 126:e30660, 1 2025.

[492] Song Xu, Zhi Fan Jia, Chunsheng Kang, Qiang Huang, Guangxiu Wang, Xiaozhi Liu, Xuan Zhou, Peng Xu, and Peiyu Pu. Upregulation of sept7 gene inhibits invasion of human glioma cells. *Cancer Investigation*, 28:248–258, 2010.

[493] Hou Mingshan, Liu Xiaobing, Cao Jie, and Chen Bo. Sept7 overexpression inhibits glioma cell migration by targeting the actin cytoskeleton pathway. *Oncology reports*, 35:2003–2010, 2016.

[494] Nianzhu Zhang, Lu Liu, Ning Fan, Qian Zhang, Weijie Wang, Mingnan Zheng, Lingfei Ma, Yan Li, and Lei Shi. The requirement of sept2 and sept7 for migration and invasion in human breast cancer via mek/erk activation. *Oncotarget*, 7:61587–61600, 2016.

[495] Maria E Gonzalez, Esther A Peterson, Lisa M Privette, Janice L Loffreda-Wren, Linda M Kalikin, and Elizabeth M Petty. High sept9v1 expression in human breast cancer cells is associated with oncogenic phenotypes. *Cancer Res*, 67:8554–64, 2007.

[496] Piotr Jędrzejczak, Kamil Saramowicz, Justyna Kuś, Julia Barczuk, Wioletta Rozpędek-Kamińska, Natalia Siwecka, Grzegorz Galita, Wojciech Wiese, and Ireneusz Majsterek. Sept9i1 and septin dynamics in oncogenesis and cancer treatment. *Biomolecules 2024, Vol. 14, Page 1194*, 14:1194, 9 2024.

[497] Jenna Marcus, Michal Bejerano-Sagie, Nicole Patterson, Susmita Bagchi, Vladislav V. Verkhusha, Diana Connolly, Gary L. Goldberg, Aaron Golden, Ved P. Sharma, John Condeelis, and Cristina Montagna. Septin 9 isoforms promote tumorigenesis in mammary epithelial cells by increasing migration and ecm degradation through metalloproteinase secretion at focal adhesions. *Oncogene*, 38:5839–5859, 7 2019.

[498] Yongqiu Zeng, Yang Cao, Lan Liu, Jiao Zhao, Ting Zhang, Lifan Xiao, Man Jia, Qiang Tian, Hong Yu, Shaokun Chen, and Yansen Cai. Sept9i1 regulates human breast cancer cell motility through cytoskeletal and rhoa/fak signaling pathway regulation. *Cell Death and Disease 2019 10:10*, 10:1–16, 9 2019.

[499] Joshua A. Broussard, Donna J. Webb, and Irina Kaverina. Asymmetric focal adhesion disassembly in motile cells. *Current Opinion in Cell Biology*, 20:85–90, 2 2008.

[500] Timo Korb, Kerstin Schlüter, Andreas Enns, Hans Ulrich Spiegel, Norbert Senninger, Garth L. Nicolson, and Jörg Haier. Integrity of actin fibers and microtubules influences metastatic tumor cell adhesion. *Experimental Cell Research*, 299:236–247, 9 2004.

[501] Kristine Østevold, Ana V Meléndez, Friederike Lehmann, Gudula Schmidt, Klaus Aktories, and Carsten Schwan. Septin remodeling is essential for the formation of cell membrane protrusions (microtentacles) in detached tumor cells. *Oncotarget*, 8:76686–76698, 2017.

[502] Monica Charpentier and Stuart Martin. Interplay of stem cell characteristics, emt, and microtentacles in circulating breast tumor cells. *Cancers 2013, Vol. 5, Pages 1545-1565*, 5:1545–1565, 11 2013.

[503] Lee Dolat, John L. Hunyara, Jonathan R. Bowen, Eva Pauline Karasmanis, Maha Elgawly, Vitold E. Galkin, and Elias T. Spiliotis. Septins promote stress fiber-mediated maturation of focal adhesions and renal epithelial motility. *Journal of Cell Biology*, 207:225–235, 2014.

[504] Clayton Smith, Lee Dolat, Dimitrios Angelis, Eva Forgacs, Elias T. Spiliotis, and Vitold E. Galkin. Septin 9 exhibits polymorphic binding to f-actin and inhibits myosin and cofilin activity. *Journal of Molecular Biology*, 427:3273–3284, 10 2015.

[505] David Cohen, Dawn Fernandez, Francisco Lázaro-Diéguez, Beatrix Überheide, and Anne Müsch. Borg5/cdc42ep1 restricts contractility and motility in epithelial mdck cells. 2024.

[506] Daniel Merenich, Konstantinos Nakos, Taylor Pompan, Samantha J. Donovan, Amrik Gill, Pranav Patel, Elias T. Spiliotis, and Kenneth A. Myers. Septins guide noncentrosomal microtubules to promote focal adhesion disassembly in migrating cells. *Molecular Biology of the Cell*, 33, 5 2022.

[507] Stefan Linder, Pasquale Cervero, Robert Eddy, and John Condeelis. Mechanisms and roles of podosomes and invadopodia. *Nature Reviews Molecular Cell Biology 2022 24:2*, 24:86–106, 9 2022.

[508] Michael A. Matrone, Rebecca A. Whipple, Eric M. Balzer, and Stuart S. Martin. Microtentacles tip the balance of cytoskeletal forces in circulating tumor cells. *Cancer Research*, 70:7737–7741, 10 2010.

[509] M. A. Matrone, R. A. Whipple, K. Thompson, E. H. Cho, M. I. Vitolo, E. M. Balzer, J. R. Yoon, O. B. Ioffe, K. C. Tuttle, M. Tan, and S. S. Martin. Metastatic breast tumors express increased tau, which promotes microtentacle formation and the reattachment of detached breast tumor cells. *Oncogene*, 29:3217–3227, 6 2010.

[510] Koyomi Nakazawa, Brieuc Chauvin, Stéphanie Mangenot, and Aurélie Bertin. Reconstituted in vitro systems to reveal the roles and functions of septins. *Journal of cell science*, 136, 10 2023.

[511] Alexandre Beber, Cyntia Taveneau, Manuela Nania, Feng Ching Tsai, Aurelie Di Cicco, Patricia Bassereau, Daniel Lévy, João T. Cabral, Hervé Isambert, Stéphanie Mangenot, and Aurélie Bertin. Membrane reshaping by micrometric curvature sensitive septin filaments. *Nature communications*, 10, 12 2019.

[512] Andrew A. Bridges, Maximilian S. Jentzsch, Patrick W. Oakes, Patricia Occhipinti, and Amy S. Gladfelter. Micron-scale plasma membrane curvature is recognized by the septin cytoskeleton. *The Journal of cell biology*, 213:23–32, 4 2016.

[513] Adeline J. Hackett, Helene S. Smith, E. Louise Springer, Robert B. Owens, Waiter A. Nelson-Rees, John L. Riggs, and Murray B. Gardner. Two syngeneic cell lines from human breast tissue: The aneuploid mammary epithelial (hs578t) and the diploid myoepithelial (hs578bst) cell lines. *JNCI: Journal of the National Cancer Institute*, 58:1795–1806, 6 1977.

[514] Brandon E. Kremer, Laura A. Adang, and Ian G. Macara. Septins regulate actin organization and cell-cycle arrest through nuclear accumulation of nck mediated by socs7. *Cell*, 130:837–850, 9 2007.

[515] Ammar Azioune, Nicolas Carpi, Qingzong Tseng, Manuel Théry, and Matthieu Piel. Protein micropatterns: A direct printing protocol using deep uvs. *Methods in Cell Biology*, 97:133–146, 1 2010.

[516] Margherita Tavasso, Ankur D. Bordoloi, Elsa Tanré, Sanne A.H. Dekker, Valeria Garbin, and Pouyan E. Boukany. Linking metastatic potential and viscoelastic properties of breast cancer spheroids via dynamic compression and relaxation in microfluidics. *Advanced Healthcare Materials*, 3 2024.

[517] Anouk van der Net, Zaid Rahman, Ankur D. Bordoloi, Iain Muntz, Peter ten Dijke, Pouyan E. Boukany, and Gijsje H. Koenderink. EMT-related cell-matrix interactions are linked to states of cell unjamming in cancer spheroid invasion. *iScience*, 27(12):111424, 12 2024.

[518] John H. Henson, Gabriela Reyes, Nina T. Lo, Karina Herrera, Quenelle W. McKim, Hannah Y. Herzon, Maritriny Galvez-Ceron, Alexandra E. Hershey, Rachael S. Kim, and Charles B. Shuster. Cytokinetic contractile ring structural progression in an early embryo: positioning of scaffolding proteins, recruitment of α-actinin, and effects of myosin ii inhibition. *Frontiers in Cell and Developmental Biology*, 12, 2024.

[519] Manoj B. Menon, Akihiro Sawada, Anuhar Chaturvedi, Pooja Mishra, Karin Schuster-Gossler, Melanie Galla, Axel Schambach, Achim Gossler, Reinhold Förster, Michael Heuser, Alexey Kotlyarov, Makoto Kinoshita, and Matthias Gaestel. Genetic deletion of sept7 reveals a cell type-specific role of septins in microtubule destabilization for the completion of cytokinesis. *PLoS Genetics*, 10, 2014.

[520] Mathew P. Estey, Caterina Di Ciano-Oliveira, Carol D. Froese, Margaret T. Bejide, and William S. Trimble. Distinct roles of septins in cytokinesis: Sept9 mediates midbody abscission. *Journal of Cell Biology*, 191:741–749, 11 2010.

[521] Megha Abbey, Cosima Hakim, Roopsee Anand, Juri Lafera, Axel Schambach, Andreas Kispert, Manuel H. Taft, Volkhard Kaever, Alexey Kotlyarov, Matthias Gaestel, and Manoj B. Menon. Gtpase domain driven dimerization of sept7 is dispensable for the critical role of septins in fibroblast cytokinesis. *Scientific Reports*, 6, 1 2016.

[522] Moshe S. Kim, Carol D. Froese, Mathew P. Estey, and William S. Trimble. Sept9 occupies the terminal positions in septin octamers and mediates polymerization-dependent functions in abscission. *Journal of Cell Biology*, 195:815–826, 11 2011.

[523] Cyril Addi, Jian Bai, and Arnaud Echard. Actin, microtubule, septin and escrt filament remodeling during late steps of cytokinesis. *Current Opinion in Cell Biology*, 50:27–34, 2 2018.

[524] Manoj B Menon, Barbara Zieger, Alexandre Benmerah, Oliva Palander, Maha El-Zeiry, and William S Trimble. Uncovering the roles of septins in cilia. *Frontiers in Cell and Developmental Biology | www.frontiersin.org*, 5:36, 2017.

[525] Sven Flemming, Francesc Font, Sergio Alonso, and Carsten Beta. How cortical waves drive fission of motile cells. *Proceedings of the National Academy of Sciences of the United States of America*, 12(117):6330–6338, 3 2020.

[526] Amin Zehtabian, Paul Markus Müller, Maximilian Goisser, Leon Obendorf, Lea Jänisch, Nadja Hümpfer, Jakob Rentsch, and Helge Ewers. Precise measurement of nanoscopic septin ring structures with deep learning-assisted quantitative superresolution microscopy. *Molecular Biology of the Cell*, 33, 7 2022.

[527] P. Verdier-Pinard, D. Salaun, H. Bouguenina, S. Shimada, M. Pophillat, S. Audebert, E. Agavnian, S. Coslet, E. Charafe-Jauffret, T. Tachibana, and A. Badache. Septin 9i2 is downregulated in tumors, impairs cancer cell migration and alters subnuclear actin filaments. *Scientific Reports*, 7:44976, 3 2017.

[528] Giulia Pinto, Christel Brou, and Chiara Zurzolo. Tunneling nanotubes: The fuel of tumor progression? *Trends in Cancer*, 6:874–888, 10 2020.

[529] Stéphanie Légaré, Catherine Chabot, and Mark Basik. Spen, a new player in primary cilia formation and cell migration in breast cancer. *Breast Cancer Research*, 19, 9 2017.

[530] Nataša Resnik, Andreja Erman, Peter Veranič, and Mateja Erdani Kreft. Triple labelling of actin filaments, intermediate filaments and microtubules for broad application in cell biology: uncovering the cytoskeletal composition in tunneling nanotubes. *Histochemistry and Cell Biology*, 152:311–317, 10 2019.

[531] Nicola Aceto, Aditya Bardia, David T. Miyamoto, Maria C. Donaldson, Ben S. Wittner, Joel A. Spencer, Min Yu, Adam Pely, Amanda Engstrom, Huili Zhu, Brian W. Brannigan, Ravi Kapur, Shannon L. Stott, Toshi Shioda, Sridhar Ramaswamy, David T. Ting, Charles P. Lin, Mehmet Toner, Daniel A. Haber, and Shyamala Maheswaran. Circulating tumor cell clusters are oligoclonal precursors of breast cancer metastasis. *Cell*, 158:1110–1122, 8 2014.

[532] Thomas Fuhs, Franziska Wetzel, Anatol W. Fritsch, Xinzhi Li, Roland Stange, Steve Pawlizak, Tobias R. Kießling, Erik Morawetz, Steffen Grosser, Frank Sauer, Jürgen Lippoldt, Frederic Renner, Sabrina Friebe, Mareike Zink, Klaus Bendrat, Jürgen Braun, Maja H. Oktay, John Condeelis, Susanne Briest, Benjamin Wolf, Lars Christian Horn, Michael Höckel, Bahriye Aktas, M. Cristina Marchetti, M. Lisa Manning, Axel Niendorf, Dapeng Bi, and Josef A. Käs. Rigid tumours contain soft cancer cells. *Nature Physics 2022 18:12*, 18:1510–1519, 9 2022.

[533] Wesley Sturgess, Swathi Packirisamy, Rodina Geneidy, Pontus Nordenfelt, Vinay Swaminathan Correspondence, and Vinay Swaminathan. Ecm-dependent regulation of septin 7 in focal adhesions promotes mechanosensing and functional response in fibroblasts. *iScience*, 27:111355, 12 2024.

[534] Jonathan E. Ron, Michele Crestani, Johan M. Kux, Jiayi Liu, Nabil Al-Dam, Pascale Monzo, Nils C. Gauthier, Pablo J. Sáez, and Nir S. Gov. Emergent seesaw oscillations during cellular directional decision-making. *Nature Physics*, 20:501–511, 3 2024.

[535] Joanna Kim and John A. Cooper. Septins regulate junctional integrity of endothelial monolayers. *Molecular Biology of the Cell*, 29:1693, 7 2018.

[536] Tomoe Tamura, Emi Umekawa, Mamiko Mori, Mayuko Otsuki, Yoshio Shibagaki, Seisuke Hattori, Takeyuki Sugawara, Koji Saito, and Yasutaka Ohta. Septin2 regulates arhgap25-mediated suppression of lamellipodia formation and cell spreading. *FEBS Letters*, 2025.

[537] Shayan S. Nazari, Andrew D. Doyle, Christopher K.E. Bleck, and Kenneth M. Yamada. Long prehensile protrusions can facilitate cancer cell invasion through the basement membrane. *Cells*, 12:2474, 10 2023.

[538] Franziska Ragaller, Ellen Sjule, Yagmur Balim Urem, Jan Schlegel, Rojbin El, Dunja Urbancic, Iztok Urbancic, Hans Blom, and Erdinc Sezgin. Quantifying fluorescence lifetime responsiveness of environment-sensitive probes for membrane fluidity measurements. *Journal of Physical Chemistry B*, 128:2154–2167, 3 2024.

[539] Kyungyeun Song, Claudia Gras, Gabrielle Capin, Niclas Gimber, Martin Lehmann, Saif Mohd, Dmytro Puchkov, Maria Rödiger, Ilka Wilhelmi, Oliver Daumke, Jan Schmoranzer, Annette Schürmann, and Michael Krauss. A sept1-based scaffold is required for golgi integrity and function. *Journal of Cell Science*, 132, 2 2019.

[540] Mohyeddine Omrane, Amanda Souza Camara, Cyntia Taveneau, Nassima Benzoubir, Thibault Tubiana, Jinchao Yu, Raphaël Guérois, Didier Samuel, Bruno Goud, Christian Poüs, Stéphane Bressanelli, Richard Charles Garratt, Abdou Rachid Thiam, and Ama Gassama-Diagne. Septin 9 has two polybasic domains critical to septin filament assembly and golgi integrity. *iScience*, 13:138, 3 2019.

[541] Sydney J Conner, Justinne R Guarin, Thanh T Le, Jackson P Fatherree, Charlotte Kelley, Samantha L Payne, Savannah R Parker, Hanan Bloomer, Crystal Zhang, Kenneth Salhany, Rachel A Mcginn, Emily Henrich, Anna Yui, Deepti Srinivasan, Hannah Borges, and Madeleine J Oudin. Cell morphology best predicts tumorigenicity and metastasis in vivo across multiple tnbc cell lines of different metastatic potential. *Breast Cancer Research*, 26:43, 2024.

[542] D. Caballero, A. C. Lima, C. M. Abreu, N. M. Neves, V. M. Correlo, J. M. Oliveira, R. L. Reis, and S. C. Kundu. Quantifying protrusions as tumor-specific biophysical predictors of cancer invasion in in vitro tumor micro-spheroid models. *In vitro models 2022 1:3*, 1:229–239, 5 2022.

[543] Gerhard Wiche, Selma Osmanagic-Myers, and Maria J. Castañón. Networking and anchoring through plectin: a key to if functionality and mechanotransduction. *Current Opinion in Cell Biology*, 32:21–29, 2 2015.

[544] Zhihui Wang, Wenbin Wang, Qing Luo, and Guanbin Song. Plectin: Dual participation in tumor progression. *Biomolecules 2024, Vol. 14, Page 1050*, 14:1050, 8 2024.

[545] Selma Osmanagic-Myers, Stefanie Rus, Michael Wolfram, Daniela Brunner, Wolfgang H. Goldmann, Navid Bonakdar, Irmgard Fischer, Siegfried Reipert, Aurora Zuzuarregui, Gernot Walko, and Gerhard Wiche. Plectin reinforces vascular integrity by mediating crosstalk between the vimentin and the actin networks. *Journal of Cell Science*, 128:4138–4150, 11 2015.

[546] Anahid Amiri, Christian Dietz, Alexander Rapp, M. Cristina Cardoso, and Robert W. Stark. The cyto-linker and scaffolding protein “plectin” mis-localization leads to softening of cancer cells. *Nanoscale*, 15:15008–15026, 9 2023.

[547] Zuzana Outla, Gizem Oyman-Eyrilmez, Katerina Korelova, Magdalena Prechova, Lukas Frick, Lenka Sarnova, Piyush Bisht, Petra Novotna, Jan Kosla, Patricia Bortel, Yasmin Borutzki, Andrea Bileck, Christopher Gerner, Mohammad Rahbari, Nuh Rahbari, Emrullah Birgin, Bibiana Kvasnicova, Andrea Galisova, Katerina Sulkova, Andreas Bauer, Njainday Jobe, Ondrej Tolde, Eva Sticova, Daniel Rösel, Tracy O'Connor, Martin Otahal, Daniel Jirak, Mathias Heikenwälder, Gerhard Wiche, Samuel M. Meier-Menches, and Martin Gregor. Plectin-mediated cytoskeletal crosstalk as a target for inhibition of hepatocellular carcinoma growth and metastasis. *eLife*, 13, 3 2025.

[548] Olivia R. Grafinger, John J. Hayward, Ying Meng, Jennifer Geddes-McAlister, Yan Li, Sara Mar, Minzhi Sheng, Boyang Su, Gobi Thillainadesan, Nir Lipsman, Marc G. Coppolino, John F. Trant, Katarzyna J. Jerzak, and Hon S. Leong. Cancer cell extravasation requires iplectin-mediated delivery of mt1-mmp at invadopodia. *British Journal of Cancer 2024 131:5*, 131:931–943, 7 2024.

[549] Samantha M. Perez, Lindsey T. Brinton, and Kimberly A. Kelly. Plectin in cancer: From biomarker to therapeutic target. *Cells 2021, Vol. 10, Page 2246*, 10:2246, 8 2021.

[550] Rushuang Xu, Shan He, Di Ma, Rui Liang, Qing Luo, and Guanbin Song. Plectin downregulation inhibits migration and suppresses epithelial mesenchymal transformation of hepatocellular carcinoma cells via erk1/2 signaling. *International Journal of Molecular Sciences*, 24:73, 1 2022.

[551] Mihoko Sutoh Yoneyama, Shingo Hatakeyama, Tomonori Habuchi, Takamitsu Inoue, Toshiya Nakamura, Tomihisa Funyu, Gerhard Wiche, Chikara Ohyama, and Shigeru Tsuboi. Vimentin intermediate filament and plectin provide a scaffold for invadopodia, facilitating cancer cell invasion and extravasation for metastasis. *European Journal of Cell Biology*, 93:157–169, 4 2014.

[552] Zhihui Wang, Wenbin Wang, Qing Luo, and Guanbin Song. High matrix stiffness accelerates migration of hepatocellular carcinoma cells through the integrin β1-plectin-f-actin axis. *BMC biology*, 23:8, 12 2025.

[553] Lei Qi, Teresa Knifley, Min Chen, and Kathleen L. O'Connor. Integrin $\alpha 6\beta 4$ requires plectin and vimentin for adhesion complex distribution and invasive growth. *Journal of Cell Science*, 135, 1 2022.

[554] Ke Wei Pan and Hong Chen Chen. Perinuclear assembly of vimentin intermediate filaments induces cancer cell nuclear dysmorphia. *Journal of Biological Chemistry*, 300:107981–107982, 12 2024.

[555] Takayoshi Niwa, Hiroko Saito, Shinobu Imajoh-ohmi, Michio Kaminishi, Yasuyuki Seto, Yoshio Miki, and Akira Nakanishi. Brca2 interacts with the cytoskeletal linker protein plectin to form a complex controlling centrosome localization. *Cancer Science*, 100:2115–2125, 11 2009.

[556] Madhushree M.V. Rao, M. Likith, R. Kavya, and T. P.N. Hariprasad. Plectin as a putative novel biomarker for breast cancer: an in silico study. *Network Modeling Analysis in Health Informatics and Bioinformatics*, 11:1–11, 12 2022.

[557] Junjie Chen, Daniel Yan, and Yun Chen. Understanding the driving force for cell migration plasticity. *Biophysical Journal*, 122:3570–3576, 9 2023.

[558] Katarina Wolf, Stephanie Alexander, Vivien Schacht, Lisa M. Coussens, Ulrich H. von Andrian, Jacco van Rheenen, Elena Deryugina, and Peter Friedl. Collagen-based cell migration models in vitro and in vivo. *Seminars in cell and developmental biology*, 20:931–941, 2009.

[559] Irene Istúriz Petitjean, Quang D. Tran, Angeliki Goutou, Zima Kabir, Gerhard Wiche, Cécile Leduc, and Gijsje H. Koenderink. Reconstitution of cytolinker-mediated crosstalk between actin and vimentin. *European Journal of Cell Biology*, 103:151403, 6 2024.

[560] Kevin Wilhelmsen, Sandy H.M. Litjens, Ingrid Kuikman, Ntambua Tshimbalanga, Hans Janssen, Iman Den Van Bout, Karine Raymond, and Arnoud Sonnenberg. Nesprin-3, a novel outer nuclear membrane protein, associates with the cytoskeletal linker protein plectin. *The Journal of cell biology*, 171:799–810, 12 2005.

[561] Tyler A. Allen, Dana Asad, Emmanuel Amu, M. Taylor Hensley, Jhon Cores, Adam Vandergriff, Junnan Tang, Deliang Shen, Li Qiao, Teng Su, Shiqi Hu, Hongxia Liang, Heather Shive, Erin Harrell, Connor Campbell, Xinxia Peng, Jeffrey A. Yoder, and Ke Cheng. Circulating tumor cells exit circulation while maintaining multicellularity, augmenting metastatic potential. *Journal of Cell Science*, 132, 9 2019.